REDUCED ORDER MODELING AND MULTISCALE INVESTIGATIONS OF HIGH PERFORMANCE ALLOYS UNDER MONOTONIC AND CYCLIC LOADING

By

Xiang Zhang

Dissertation

Submitted to the Faculty of the

Graduate School of Vanderbilt University

in partial fulfillment of the requirements

for the degree of

DOCTOR OF PHILOSOPHY

in

Civil Engineering

September 30, 2017

Nashville, Tennessee

Approved:

Caglar Oskay, Ph.D., Chair

Prodyot Basu, Ph.D.

Ravindra Duddu, Ph.D.

Haoxiang Luo, Ph.D.

Ravinder Chona, Ph.D.

To my family

ACKNOWLEDGMENTS

This dissertation would not have been possible without the support of my advisor Dr. Caglar Oskay, to whom I would like to express my special gratitude. His continuous guidance and support, constant encouragement and enlightening conversations we had on how to conduct quality scientific research over the past five years have greatly helped me winding through the narrows along the research paths, contributed significantly to my professional development and shaped my research interests. I also would like to thank my committee members Dr. Prodyot Basu, Dr. Ravindra Duddu, Dr. Haoxiang Luo and Dr. Ravinder Chona, for their valuable inputs to this research work.

This dissertation is mainly based upon work supported by the US Department of Energy, Nuclear Energy University Program (Grant No: 62-0476822) and the Air Force Office of Science Research Multi-Scale Structural Mechanics and Prognosis Program (Grant No: FA9550-13-1-0104). The technical cooperation with Professor Yongming Liu from Arizona State University, Dr. Richard Wright from Idaho National Laboratory and Dr. Sam Sham from Argonne National Laboratory through the first program, as well as frequent technical discussions with Dr. Ravi Penmetsa from Air Force Strategic Development Planning and Experimentation Office through the second program are greatly acknowledged.

I thank Dr. Albert Cerrone from GE Global Research Center (previously at Cornell University) for sharing his microstructure meshing code PPM and valuable discussions on its extension to insert cohesive zone element along grain boundaries, Dr. Michael Groeber from AFRL and Mr. Michael Jackson from Blue Quartz Software for their help on DREAM.3D software for microstructure reconstruction. Tremendous help I received and knowledge learned from Mr. Andy Richter at Vanderbilt Advanced Computing Center for Research & Education with respect to high performance computing also make my research work smooth and is highly appreciated.

I thank my research group members Mr. Rudraprasad Bhattacharyya, Dr. Michael

Bogdanor, Dr. Robert Crouch, Mr. Ruize Hu, Dr. Tong Hui, Mr. Hao Li, Dr. Yumeng Li, Mr. Yang Liu, Dr. Van-Tung Phan, Dr. Matthew Pike, Mrs. Wendy Paulson, Dr. Paul Sparks, Mr. Scott Williams, Dr. Shuhai Zhang, Dr. Shuiwen Zhu and Mr. Xiaoyu Zhang, for their help on my research and friendship we have that make the past five years joyful. Especially, I would like to acknowledge Dr. Hui and Dr. Yan, for their encouraging conversations and help when I experienced difficulties at the initial stage of my research. I thank my friend Guowei Cai, for the mutual help we have on study and life, especially in the first year of my Ph.D. studies which facilitate the smooth transition to the new environment at Vanderbilt University.

I thank all my colleagues and friends at the Civil and Environmental Engineering Department and the Vanderbilt Multiscale Modeling and Simulation (MuMS) Center for cultivating a joyful and stimulant environment for study and research. Special thanks also go to Mrs. Karen Fuller, Mrs. Hasty Charity, Mrs. Beverly Piatt, Mrs Karen Page and Mrs. Julie Canada for their continuous support in administrative work.

Last but not least, I would like to express my deepest appreciation to my family. I thank my beautiful wife, Yin Guo, for her continuous support, love and company since we first met. I thank our lovely daughter, Amy Yuxi Zhang, for numerous joyful and memorable moments she has brought to us. I thank my parents, for bringing me up, cultivating me with love and trust, granting me the freedom to make my own decisions since I was a kid, all of which shaped the person that I want to be. I thank my sister for her love, support as well as a wonderful childhood we spent together. I also appreciate my parents in law, for their support and trust, that allow me to focus on my research work.

TABLE OF CONTENTS

LIST OF TABLES

Table Page

LIST OF FIGURES

Chapter 1

INTRODUCTION

1.1 Background and Motivation

1.1.1 Challenges in the modeling of polycrystalline materials

Metals and alloys are widely used as structural materials in a wide range of engineering applications. The demand for high performance metallic materials is extremely strong, especially in applications where structures are subjected to extreme environments, such as the Nickel-based alloys in the very high temperature reactor (VHTR, Fig. 1.1(a)) and the Titanium alloys in the hypersonic cruise vehicle (Fig. 1.1(b)). Computational modeling of metals and alloys under various loadings is a challenging task, since the microstructural morphology significantly affects the mechanical performance of structures made of polycrystalline metals and alloys. While modeling the bulk properties of many metals and alloys has been well established, the connection of the mechanical behavior to the material microstructure is being realized relatively recently. This connection is clearly beneficial for physics-based characterization, and ultimately, control of bulk material properties through microstructure design.

Two challenges exist in bridging the material microstructure and bulk properties. The first challenge is the development of sophisticated constitutive models that accurately capture the relevant physical phenomena such as grain boundary slip [168], phase transformation [177], morphological complexity (e.g., [145, 54]) and many others at the microstructure scale (i.e., within a microstructure representative element volume (RVE)). This development is critical as it provides the most accurate representation of the physical process, hence facilitating the discovery and understanding of the causes and consequences of each deformation mechanism, as well as the interactions between them. The second challenge

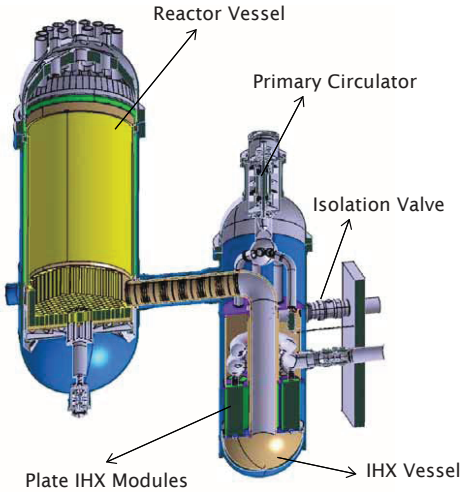

(a)

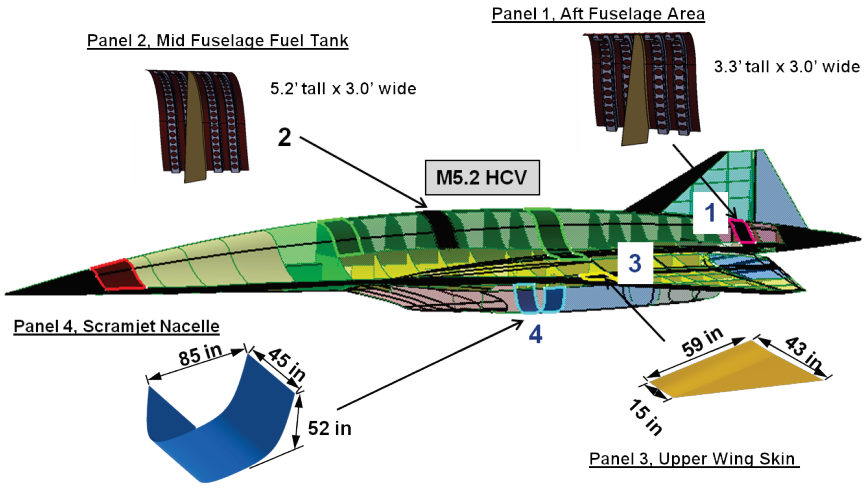

(b)

Figure 1.1: Example high performance alloy applications: (a) very high temperature reactor, picture from [51]; (b) representative hypersonic cruise vehicle, picture from [212].

is the tremendous memory and computational costs associated with the evaluation of complex polycrystalline morphologies, especially in the context of a multiscale analysis. Overcoming this challenge is essential, as it provides the pathways to upscale from the micro structure to the structure or structural component, where the material properties/responses can be directly evaluated.

1.1.2 Microscale modeling of polycrystal plasticity: crystal plasticity finite element method

Evolved from Rice's seminal work on formulations of metal viscoplasticity [148], the crystal plasticity theory describes the deformation mechanisms of metals and alloys by incorporating many microstructural mechanisms including thermal effects [113, 105], mechanical twinning [168], shear band formation [7], martensite formation [177], recrystallization [100], grain boundary slip [38], crack initiation [40] and others (for a comprehensive review, see Ref. [151]). The primary mechanism for plastic deformation remains as the dislocation glide along preferential slip planes, where resolved shear stress acts as the driving force for glide. Finite element analysis of a single crystal was first studied by Peirce, Asaro and Needleman [137, 138] and since then, Crystal Plasticity Finite Element Method (CPFEM) has been developed into a powerful tool that can model the response of polycrystalline microstructures under various loading conditions [179, 104]. Using CPFEM, a wide range of physical mechanisms including (but not limited to) grain boundary evolution [83], damage nucleation [16] and creep [178] can be investigated at the microstructure scale. The CPFEM as a general computational framework has the flexibility to leverage available constitutive formulations that idealize unresolved physical mechanisms, and relies on discretization of the polycrystalline microstructure that allows directly accounting for the stress risers induced by mismatch in grain orientations and other morphological effects.

Hence there is always a clear need to develop relevant constitutive equations for a new metallic material or an existing material that exhibits a different deformation mechanism when subjected to a new environment. One example in this regard is the Nickel-based superalloy IN 617, a candidate structural material for very high temperature reactor (VHTR) intermediate heat exchangers [160] as shown in Fig. 1.1(a). Under the VHTR environment, the material experiences extreme thermal (up to 950°C) and mechanical loadings, including fatigue and creep-fatigue induced by the startup and shutdown cycles. Hence, developing a computational model that incorporates the underlying physics of the plastic deformation, which can lead to the ability to capture the response of IN 617 subjected to the VHTR

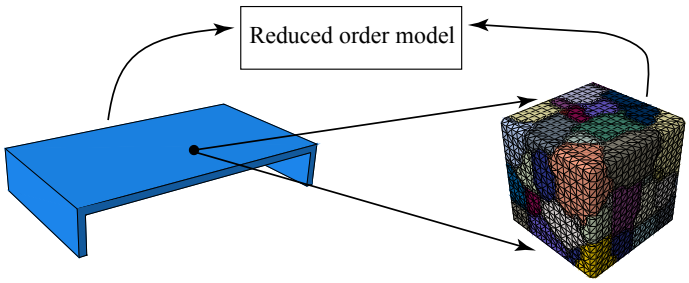

Figure 1.2: Reduced order model bridges the micro- and macroscale.

environment, and ultimately, the capability for life prediction is of significant interest.

1.1.3 Structural scale modeling modeling of polycrystal plasticity

To achieve accurate structural scale modeling of polycrystalline materials, one needs to upscale the microstructural response to that of the structure or structural component. Multiscale computational methods such as computational homogenization [56, 164, 120, 48, 87], variational multiscale enrichment [132, 133, 204], heterogeneous multiscale method [43], multiscale finite element method [62] and others provide the computational framework to realize this upscaling. Unfortunately, the high computational complexity of a CPFEM simulation performed over a representative volume element (RVE) typically prohibits straightforward application of these methods to homogenize polycrystal response. The alternative is reduced order modeling of the RVE simulations that provide an approximation to the microscale problem with orders of magnitude computational efficiency (Fig. 1.2). From the perspective of general heterogeneous media, reduced order methods including the spectral method [3], fast Fourier transform method [126, 116], transformation field analysis [42, 117, 118, 50], proper orthogonal decomposition [89, 200, 59], numerical potentials [201] and the eigendeformation-based homogenization [134, 198, 35, 49, 166], among others have recently been proposed and developed.

Sachs [154] and Taylor [176] models can be viewed as among the earliest attempts of polycrystal plasticity homogenization. Both models disregard grain shapes and interactions, and further assume either iso-stress or iso-strain condition for the grains, which

violate compatibility or equilibrium, respectively. In the context of Taylor model, the spectral crystal plasticity method developed by Knezevic et al. [80] constructs spectral representation of the crystal plasticity constitutive relationship a priori, and retrieves local spectral interpolation using the fast Fourier transformation (FFT) during any specific simulation later on. This approach has been recently embedded into finite element framework and implemented on high performance computer hardware [121, 83]. The grain cluster method [63, 64, 180] relaxes the excessive constraints imposed by the Taylor model by applying the macroscale deformation gradient onto a cluster of grains, thereby accounting for interactions between neighboring grains within the cluster. The grain cluster approach typically restricts grain morphologies to regular geometries, and the elimination of this restriction is an ongoing research topic [190]. Despite a significant improvement, the grain cluster method still includes limited grain-to-grain interactions. Viscoplastic Self-Consistent (VPSC) method, originally suggested by Kroner [88] and later advanced by Molinari et al. [125], Lebensohn and Tome [97] employs the Eshelby solution [46] to approximately account for the microstructural heterogeneity and has been successfully employed to study polycrystalline plasticity and microstructure evolution. Among significant extensions of the VPSC model are the inclusion of finite strain elastoviscoplastic effects [183], embedding into finite element framework [155, 82], and extensions to better account for grain interactions [96, 165]. Despite significant progress, the ellipsoidal representation of the grain morphologies limits accuracy of grain interactions.

The FFT method pioneered by Suquet and coworkers [126, 115] applied to the crystal plasticity problem [95, 98, 44] solves the system using the FFT on regular grids that are often obtained from the voxelized microstructure images. FFT considers full grain interactions and provides high efficiency compared with CPFE. Michel and Suquet extended their non-uniform transformation method [117, 118] into the modeling of polycrystalline materials and reported two orders of magnitude speedup compared with full field simulation using FFT [119]. While the FFT method has seen significant success, employing less

restrictive boundary conditions and loss of accuracy due to the use of regular grids remain open questions.

It is therefore desirable to develop a systematic multiscale homogenization method for polycrystalline materials, which provides efficient structural scale modeling that accounts for the microstructure morphology and is able to retrieve local microscale response for localized phenomenon prediction (i.e., damage initiation). It is also desirable that the developed model can provide a hierarchical model improvement capability to control the resolution as well as the extent of grain interactions to be considered to provide the flexibility of balancing the efficiency and accuracy.

This dissertation is dedicated to the development of multiscale modeling strategies for polycrystalline materials at both micro- and structural scale by addressing the above two challenges in the modeling of metals and alloys. Particularly, the microscale model development is focused on the Nickel-based alloy IN 617 subjected to the VHTR environment, while the reduced order multiscale model development focus more on the reduced order modeling technique development with basic crystal plasticity equations and can be easily generalized to the modeling of any specific high performance alloy. The specific research objectives and associated tasks are summarized below.

Objective 1 Develop an accurate CPFE modeling framework to capture the deformation and failure of IN 617 subjected to the VHTR environment.

Task 1.1: Development of an automatic and robust microstructure reconstruction, meshing, grain boundary interracial elements insertion workflow.

Task 1.2: Development of the CPFE framework and relevant constitutive relationships that characterize the viscoplastic deformation of IN 617.

Task 1.3: Incorporation of intergranular damage into the CPFE framework for the modeling of the creep rupture of IN 617 at high temperature.

Objective 2 Develop efficient reduced order models for polycrystal plasticity to facilitate structural scale modeling of polycrystalline materials.

Task 2.1: Development of eigenstrain-based reduced order modeling technique for polycrystal plasticity.

Task 2.2: Further efficiency improvement of the reduced order model by a grain-clustering enhanced sparse formulation.

1.2 Dissertation Organization

The remainder of this dissertation is organized to present the efforts conducted in achieving the objectives listed above as follows:

- Chapter 2 details the development of a CPFE framework for microscale modeling of IN 617 at high temperature, where dislocation glide is considered as the sole source of viscoplastic deformation within the grains. This chapter covers the work published in Ref. [208].

- Chapter 3 extends the developed CPFE model to a coupled CPFE-CZM model to further incorporate dislocation climb mechanism for the viscoplastic deformation within the grains as well as cohesive-zone based intergranular damage at the grain boundaries. This chapter covers the work published in Refs. [141, 211].

- Chapter 4 introduces the EHM for polycrystal plasticity, where the model development, implementation as well as numerical verification are provided to fully demonstrate the efficiency and accuracy characteristics of EHM in structural scale modeling. This chapter includes the work published in Ref. [207].

- Chapter 5 first identifies the efficiency degradation of EHM as microstructure size increases, and addresses this issue by proposing a sparse EHM formulation. The accuracy and efficiency characteristics are thoroughly probed by comparison with the original full EHM and CPFE simulations. This chapter includes the work published in Refs. [209, 210].

- Chapter 6 summarizes the research work conducted and the overall contribution of this dissertation. Future work that builds upon this dissertation is also discussed.

Chapter 2

POLYCRYSTAL PLASTICITY FINITE ELEMENT MODELING OF NICKEL-BASED SUPERALLOY IN 617 SUBJECTED TO CYCLIC LOADING AT HIGH TEMPERATURE

Nickel-based alloys are widely used as structural materials for turbine engine blades, aircraft engine components, and high temperature power plant steam generators due to their exceptional combination of high temperature strength and creep resistance. In particular, IN 617 is a candidate structural material for very high temperature reactor (VHTR) intermediate heat exchangers [160]. Under these conditions, the material experiences extreme thermal (up to 950°C) and mechanical loadings, including fatigue and creep-fatigue induced by the startup and shutdown cycles. Prediction of failure and life of this alloy under high temperature creep-fatigue conditions is therefore a critical concern. Developing a computational model that incorporates the underlying physics of the plastic deformation, which can lead to the ability to capture the response in cyclic loading, and ultimately, life prediction capability is of significant interest.

IN 617 is a solid solution strengthened nickel-based alloy with coarse Cr and Mo carbides as well as small amount of Ti carbonitrides [181]. γ' phase also exists at relatively low temperatures, but becomes unstable above 650°C [107, 14]. Tensile tests of IN 617 at various temperatures and strain ranges have been studied and it generally exhibits strong temperature and strain rate dependence [189, 147], as well as orientation (between loading direction and sample rolling direction) dependence [124]. Strain controlled fatigue and creep-fatigue tests of IN 617 at 850°C and 950°C have been experimentally studied by several researchers over various strain ranges and hold times [30, 187, 25, 186]. Wright et al. [187] found that under fatigue loading at 850°C, IN 617 deforms by a plastic flow mechanism and shows cyclic hardening, while at 950°C the alloy exhibits softening induced by

solute-drag creep. Introduction of a tensile hold in the creep-fatigue tests significantly decreases the fatigue life compared to that under pure fatigue loading. Microstructure examinations showed failure is controlled by intergranular fracture under creep-fatigue loading, while transgranular cracking dominates when subjected to pure fatigue loads [25]. Further, the microstructure is marked by the formation of dislocation substructures during creep-fatigue testing, which influences the dislocation density and motion within grains [23]. The sensitivity of fatigue and creep-fatigue deformation and failure mechanisms to environmental (e.g., temperature) conditions points to the influence of microstructure on the life of this alloy.

A few viscoplastic constitutive models [156, 144, 127] based on the phenomenological constitutive theories of Robinson [149] and Chaboche [28] have been developed to capture the cyclic response of IN 617 at high temperatures. Chen et al. [30] utilized frequency-modified tensile hysteresis energy to predict the low cycle fatigue and creep-fatigue life of IN 617. While these phenomenological models are successful in capturing the stress-strain loops, they do not provide a direct account of microstructural heterogeneities and their interactions, which may affect the overall long term behavior. Crystal plasticity finite element method (CPFE) is an alternative modeling approach, which is based on full resolution of the representative microstructure of the material. Since its inception [137, 138], CPFE has been developed into a robust numerical strategy to capture the grain level anisotropic deformation of metals and alloys at various loading conditions (see, e.g., Roters et al. [150] for an extensive review). Under the assumption that slip is the dominant carrier of plastic deformation, stress is resolved onto individual slip systems inherent to the lattice structure of the material, which drives dislocation glide and the accumulation of plastic strain. More recent investigations incorporated dislocation climb mechanisms [99], as well as deformation twinning [73] into the CPFE framework to study the high temperature behavior of alloys. A number of numerical investigations employed CPFE to study the cyclic response of various alloys, either to capture the stress-strain response, crack initiation or failure life

prediction [204, 203, 182, 5]. Simulations of the cyclic behavior of nickel-based alloys at intermediate and high temperatures have been performed in Refs. [20, 21, 103], which demonstrated the capability of CPFE to capture hysteresis loops as well as the stress relaxation phenomenon.

Prior experimental studies on the fatigue and creep-fatigue behavior of IN 617 identified a prominent drop in the flow stress (i.e., apparent softening) in the first cycle of both fatigue and creep-fatigue tests. In creep-fatigue testing of IN 617 at 950°C, the apparent softening recurs at every cycle after strain holds as well. These stress drops have been attributed to solute-drag creep [187], which occurs due to the dynamic interactions between dislocations and the solute atoms ([159, 175]). While models of solute-drag creep have been proposed in the literature [175], to the best of the author's knowledge, the modeling of transient phenomena induced by solute-drag creep has not been included into the CPFE framework.

In this chapter, a crystal plasticity model is developed to idealize the fatigue and creep-fatigue cycles of IN 617 at high temperature environment. The CPFE model that incorporates isothermal deformation behavior of the alloy as well as the large deformation kinematics has been formulated, implemented and validated. The proposed CPFE model includes a new slip resistance evolution law that accounts for the solute-drag creep and can capture the transient softening effects observed under fatigue and creep-fatigue tests. Model parameters in the CPFE model are calibrated by employing a model calibration procedure that is based on Gaussian Process modeling to accelerate the process. Simulations were performed using polycrystal morphologies generated using experimental (i.e., EBSD) data along with the calibrated CPFE model. The simulation predictions were found to be in good agreement with all fatigue and creep-fatigue tests at different strain ranges and hold times. The extension of the current model to incorporate the cohesive zone model based intergranular modeling conducted by the author and other collaborators is also presented. The proposed model, although calibrated for 950 °C, is expected to apply within a range of temperature between approximately 900-1000 °C. Within this range, the microstructure of

IN 617 is largely free of γ' precipitates with a relatively stable microstructure [107, 14].

2.1 The Crystal Plasticity Model

A comprehensive review of various crystal plasticity models is provided in Roters et al. [150]. Twinning and dislocation slip have been the most studied deformation mechanism in the context of crystal plasticity and implementation into CPFE framework is readily available. Mechanical twinning preferentially occurs in coarse-grained crystalline metals with low symmetry at low temperature and high strain rate [197, 33, 81, 10]. Furthermore, no significant deformation twinning has been reported in the experimental literature for IN 617 at high temperatures. While evidence of dislocation climb of IN 617 at temperatures between 850 and 1050°C has been reported by Wen [184], it is also pointed out that dislocation glide is still the dominant deformation mechanism. On the other hand, dislocation climb modeling under the context of CPFE has been very recent [52, 99]. In this study, a simplifying assumption is made, where all plastic deformation is modeled as a consequence of dislocation glide. Full traction continuity is assumed along each grain boundary (i.e., the modeling is valid up to the onset of damage initiation). The large deformation formulation is based on the framework of Marin and Dawson [109, 108] and a brief overview of this framework is provided herein for completeness. The kinematic theory implemented in the current CPFE model falls within the theory of Taylor [176] and Hill and Rice [61].

Consider a body that occupies the reference domain $\mathbb{B}_0$ that corresponds to the initial state of the polycrystal microstructure. The current domain is denoted by $\mathbb{B}$ as shown in Fig. 2.1. The motion of the body is described using the deformation map, $\boldsymbol{\phi}(\mathbf{X},t)$:

$$\mathbf{x} = \boldsymbol{\phi}(\mathbf{X},t); \quad \mathbf{X} \in \mathbb{B}_{\mathbf{0}},\ \mathbf{x} \in \mathbb{B} \tag{2.1}$$

where, $\mathbf{x}$ and $\mathbf{X}$ denote the position vectors in the current and reference (initial) configura-

tions, respectively. The displacement field, $\mathbf{u}(\mathbf{X},t)$, is then expressed as:

$$\mathbf{u}(\mathbf{X},t) = \boldsymbol{\phi}(\mathbf{X},t) - \mathbf{X}; \quad \mathbf{X} \in \mathbb{B}_0 \tag{2.2}$$

The deformation gradient, $\mathbf{F} = \partial\boldsymbol{\phi}/\partial\mathbf{X}$, is expressed using the classical multiplicative split into elastic ($\mathbf{F}^e$) and plastic ($\mathbf{F}^p$) contributions as:

$$\mathbf{F} = \mathbf{F}^e \cdot \mathbf{F}^p \tag{2.3}$$

Polar decomposition of the elastic part of the deformation tensor into the left elastic stretch tensor, $\mathbf{V}^e$, and the orthogonal rotation tensor, $\mathbf{R}^e$ (i.e., $\det(\mathbf{R}^e) = 1$ and $\mathbf{R}^{e-1} = \mathbf{R}^{eT}$), allows Eq. (2.3) to be expanded as:

$$\mathbf{F} = \mathbf{V}^e \cdot \mathbf{F}^*, \quad \mathbf{F}^* = \mathbf{R}^e \cdot \mathbf{F}^p \tag{2.4}$$

in which, superscripts -1 and T denotes tensor inverse and transpose, respectively. The above decomposition allows the introduction of two intermediate configurations denoted as $\bar{\mathbb{B}}$ and $\widetilde{\mathbb{B}}$ between the original configuration, $\mathbb{B}_0$, and the current configuration, $\mathbb{B}$, as shown in Fig. 2.1. In what follows, an overbar or tilde indicates the value of a variable at the corresponding intermediate configuration. The current formulation operates in the intermediate configuration, $\widetilde{\mathbb{B}}$, obtained by elastically unloading from the current configuration, $\mathbb{B}$. $\mathbf{F}^p$ is related to the dislocations on crystallographic planes and $\mathbf{V}^e$ is a pure elastic stretching of the lattice, both of which do not change the crystal orientation. $\mathbf{R}^e$ defines the rotation and the reorientation of the grains. By this approach, it is straightforward to incorporate crystal elasticity to CPFE. This is in contrast to formulations based on a single intermediate configuration, where the behavior is often idealized as rigid viscoplastic.

Each slip system α is uniquely defined by its Schmid tensor $\mathbf{Z}^\alpha = \mathbf{m}^\alpha \otimes \mathbf{n}^\alpha$, where $\mathbf{n}^\alpha$ and $\mathbf{m}^\alpha$ are the unit vectors normal to the slip plane and along the slip direction, respec-

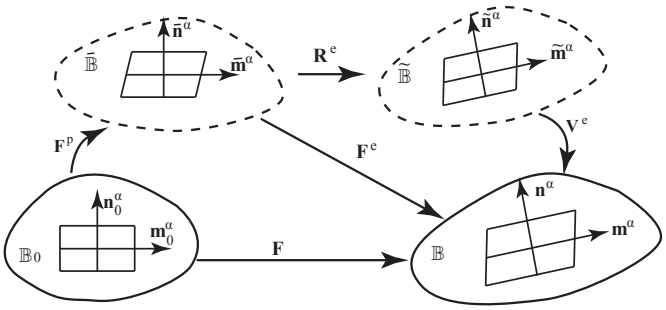

Figure 2.1: Kinematics of the deformation.

tively. Since the lattice orientation is affected only by $\mathbf{R}^e$:

$$\bar{\mathbf{n}}^\alpha = \mathbf{n}_0^\alpha; \quad \bar{\mathbf{m}}^\alpha = \mathbf{m}_0^\alpha; \quad \mathbf{n}^\alpha = \tilde{\mathbf{n}}^\alpha; \quad \mathbf{m}^\alpha = \tilde{\mathbf{m}}^\alpha \tag{2.5}$$

The grain orientation is updated using the rotation tensor $\mathbf{R}^e$:

$$\tilde{\mathbf{n}}^\alpha = \mathbf{R}^e \cdot \bar{\mathbf{n}}^\alpha; \quad \tilde{\mathbf{m}}^\alpha = \mathbf{R}^e \cdot \bar{\mathbf{m}}^\alpha \tag{2.6}$$

which, describes the texture evolution during the deformation process.

The plastic velocity gradients $\bar{\mathbf{L}}^p$ and $\tilde{\mathbf{L}}^p$ in the intermediate configurations $\bar{\mathbb{B}}$ and $\widetilde{\mathbb{B}}$, respectively, are expressed as:

$$\bar{\mathbf{L}}^p = \dot{\mathbf{F}}^p \cdot \mathbf{F}^{p-1} = \sum_{\alpha=1}^{N} \dot{\gamma}^\alpha \bar{\mathbf{m}}^\alpha \otimes \bar{\mathbf{n}}^\alpha \tag{2.7}$$

$$\widetilde{\mathbf{L}}^p = \dot{\mathbf{F}}^* \cdot \mathbf{F}^{*-1} = \widetilde{\Omega}^e + \mathbf{R}^e \cdot \bar{\mathbf{L}}^p \cdot \mathbf{R}^{eT} \tag{2.8}$$

where, $\widetilde{\Omega}^e = \dot{\mathbf{R}}^e \cdot \mathbf{R}^{eT}$ denotes the spin of the lattice in configuration $\widetilde{\mathbb{B}}$, and possesses skew symmetry [12]. The velocity gradient $\mathbf{L}$ in the current configuration $\mathbb{B}$ is expressed as:

$$\mathbf{L} = \dot{\mathbf{F}} \cdot \mathbf{F}^{-1} = \dot{\mathbf{V}}^e \cdot \boldsymbol{V}^{e-1} + \boldsymbol{V}^e \cdot \widetilde{\mathbf{L}}^p \cdot \mathbf{V}^{e-1} \tag{2.9}$$

The velocity gradients $\mathbf{L}$, $\bar{\mathbf{L}}^p$ and $\widetilde{\mathbf{L}}^p$ are decomposed into their symmetric ($\mathbf{D}$, $\bar{\mathbf{D}}^p$, $\widetilde{\mathbf{D}}^p$)

and skew ($\mathbf{W}$, $\bar{\mathbf{W}}^p$, $\widetilde{\mathbf{W}}^p$) components as:

$$\mathbf{L} = \mathbf{D} + \mathbf{W}, \quad \bar{\mathbf{L}}^p = \bar{\mathbf{D}}^p + \bar{\mathbf{W}}^p, \quad \widetilde{\mathbf{L}}^p = \widetilde{\mathbf{D}}^p + \widetilde{\mathbf{W}}^p \tag{2.10}$$

which, together with Eqs. (2.7) and (2.8), yields:

$$\bar{\mathbf{D}}^p = \sum_{\alpha=1}^{N} \dot{\gamma}\big(\bar{\mathbf{m}}^\alpha \otimes \bar{\mathbf{n}}^\alpha\big)_S, \quad \bar{\mathbf{W}}^p = \sum_{\alpha=1}^{N} \dot{\gamma}\big(\bar{\mathbf{m}}^\alpha \otimes \bar{\mathbf{n}}^\alpha\big)_A \tag{2.11}$$

$$\widetilde{\mathbf{D}}^p = \mathbf{R}^e \cdot \bar{\mathbf{D}}^p \cdot \mathbf{R}^e, \quad \widetilde{\mathbf{W}}^p = \widetilde{\Omega}^e + \mathbf{R}^e \cdot \bar{\mathbf{W}}^p \cdot \mathbf{R}^{eT} \tag{2.12}$$

where, the subscripts S and A indicate the symmetric and skew (anti-symmetry) components, respectively (i.e., $(\cdot)_S = \big((\cdot) + (\cdot)^T\big)/2$; $(\cdot)_A = \big((\cdot) - (\cdot)^T\big)/2$).

The stress-strain relationship of the lattice is expressed as:

$$\widetilde{\mathbf{S}} = \widetilde{\mathbb{C}} : \widetilde{\mathbf{E}}^e \tag{2.13}$$

where, $\widetilde{\mathbb{C}}$ is the fourth order anisotropic crystal elasticity tensor, $\widetilde{\mathbf{S}}$ the 2nd Piola-Kirchhoff stress in $\widetilde{\mathbb{B}}$, and $\widetilde{\mathbf{E}}^e$ the Green strain tensor relative to $\widetilde{\mathbb{B}}$, which takes the form:

$$\widetilde{\mathbf{E}}^e = \frac{1}{2}(\mathbf{V}^{eT} \cdot \mathbf{V}^e - \mathbf{I}) \tag{2.14}$$

in which, $\mathbf{I}$ is the second order identity tensor. $\widetilde{\mathbf{S}}$ relates with the Cauchy stress, $\boldsymbol{\sigma}$, and Kirchhoff stress, $\boldsymbol{\tau}$, in the current configuration through the transformations [12]:

$$\widetilde{\mathbf{S}} = \mathbf{V}^{-e} \cdot \boldsymbol{\tau} \cdot \mathbf{V}^{-eT} = \det(\boldsymbol{V}^e)\mathbf{V}^{-e} \cdot \boldsymbol{\sigma} \cdot \mathbf{V}^{-eT} \tag{2.15}$$

The elastic lattice strains are generally orders of magnitude less than the plastic strains in many applications of interest, hence the small elastic strains assumption is adopted for

simplicity [109, 108]:

$$\mathbf{V}^e = \mathbf{I} + \boldsymbol{\epsilon}^e, \quad ||\boldsymbol{\epsilon}^e|| \ll 1 \tag{2.16}$$

in which, $\boldsymbol{\epsilon}^e$ denotes elstic strains. Time differentiation and inverse operation yield:

$$\dot{\mathbf{V}}^e = \dot{\boldsymbol{\epsilon}}^e, \;\; \mathbf{V}^{e-1} = \mathbf{I} - \boldsymbol{\epsilon}^e \tag{2.17}$$

Substituting Eqs. (2.16) and (2.17) into Eq. (2.13)-(2.15), dropping high order terms of $\boldsymbol{\epsilon}^e$, and neglecting terms such as $(\bullet)\boldsymbol{\varepsilon}^e$ and $\boldsymbol{\varepsilon}^e(\bullet)$ in comparison to $(\bullet)$, the stress-strain relationship is expressed as:

$$\boldsymbol{\tau} = \widetilde{\mathbb{C}} : \boldsymbol{\epsilon}^e = \det(\mathbf{I} + \boldsymbol{\epsilon}^e)\boldsymbol{\sigma} \tag{2.18}$$

Following similar procedure and consider Eqs. (2.7) – (2.12) (see [108] for more details), the kinematic equation and the elasticity equation are expressed in a simplified form. Box 1 summarizes the system of equations for the CPFE model with the small elastic strain assumption, together with the plasticity relationships, flow rule, evolution equations, Schmid's law and texture evolution equations discussed below.

2.1.1 Flow rule and evolution equations

A number of flow rules have been used to model the kinematics of slip in alloys at high temperature [138, 20, 158, 106]. The one proposed by Busso to idealize the high temperature behavior of nickel-based alloys [20, 21, 103] is adopted in this study:

$$\dot{\gamma}^\alpha = \dot{\gamma}_0 \exp\left\{ -\frac{F_0}{k\theta}\left\langle 1 - \left\langle \frac{|\tau^\alpha - B^\alpha| - S^\alpha \mu/\mu_0}{\hat{\tau}_0 \mu/\mu_0} \right\rangle^p \right\rangle^q \right\} \mathrm{sgn}(\tau^\alpha - B^\alpha) \tag{2.19}$$

where, k is the Boltzmann constant, θ the temperature in Kelvin, $\dot{\gamma}_0$ the reference shear strain rate, F_0 the activation energy, $\hat{\tau}_0$ the stress at which dislocations can be mobilized without the assistance of thermal activation. p and q are two fitting parameters, μ and μ_0 the

- Equilibrium:

$$\mathrm{div}\boldsymbol{\sigma} = \mathbf{0}$$

- Boundary conditions.:

$$\boldsymbol{u}(\mathbf{x},t) = \bar{\boldsymbol{u}}(\mathbf{x},t),\ \mathbf{x} \in \Gamma^u;\quad \boldsymbol{\sigma}(\mathbf{x},t)\cdot\mathbf{n} = \bar{\mathbf{t}}(\mathbf{x},t),\ \mathbf{x} \in \Gamma^t$$
$$\Gamma^u \cup \Gamma^t = \partial\mathbb{B}_0,\ \Gamma^u \cap \Gamma^t = \emptyset$$

- Kinematics:

$$\mathbf{W} = \widetilde{\boldsymbol{\Omega}}^e + \widetilde{\mathbf{W}}^p,\ \ \widetilde{\boldsymbol{\Omega}}^e = \dot{\mathbf{R}}^e\mathbf{R}^{eT}$$
$$\mathbf{D} = \widetilde{\mathbf{D}}^p + \dot{\boldsymbol{\epsilon}}^e + \boldsymbol{\epsilon}^e\widetilde{\boldsymbol{\Omega}}^e - \widetilde{\boldsymbol{\Omega}}^e\boldsymbol{\epsilon}^e$$

- Elasticity:

$$\boldsymbol{\tau} = \widetilde{\mathbb{C}} : \boldsymbol{\epsilon}^e;\ \ \boldsymbol{\tau} = \det(\mathbf{I} + \boldsymbol{\epsilon}^e)\boldsymbol{\sigma}$$

- Plasticity:

$$\widetilde{\mathbf{W}}^p = \mathbf{R}^e\bar{\mathbf{W}}^p\mathbf{R}^{eT} = \sum_{\alpha=1}^{N}\dot{\gamma}^\alpha(\widetilde{\mathbf{Z}}^\alpha)_A$$
$$\widetilde{\mathbf{D}}^p = \mathbf{R}^e\bar{\mathbf{D}}^p\boldsymbol{R}^{eT} = \sum_{\alpha=1}^{N}\dot{\gamma}^\alpha(\widetilde{\boldsymbol{Z}}^\alpha)_S$$

- Flow rule:

$$\dot{\gamma}^\alpha = \dot{\gamma}_0\exp\left\{-\frac{F_0}{k\theta}\left\langle 1 - \left\langle \frac{|\tau^\alpha - B^\alpha| - S^\alpha\mu/\mu_0}{\hat{\tau}_0\mu/\mu_0}\right\rangle^p\right\rangle^q\right\}\mathrm{sgn}(\tau^\alpha - B^\alpha)$$

- Schmid's law:

$$\tau^\alpha = \boldsymbol{\tau} : \widetilde{\boldsymbol{Z}}^\alpha;\ \widetilde{\boldsymbol{Z}}^\alpha = \widetilde{\boldsymbol{m}}^\alpha \otimes \widetilde{\boldsymbol{n}}^\alpha$$

- Texture evolution:

$$\widetilde{\mathbf{m}} = \mathbf{R}^e\cdot\bar{\mathbf{m}}^\alpha;\ \ \widetilde{\mathbf{n}} = \mathbf{R}^e\cdot\bar{\mathbf{n}}^\alpha$$

- Evolution equations:

$$\dot{S}^\alpha = \left[h_S - d_D(S^\alpha - \bar{S}^\alpha)\right]|\dot{\gamma}^\alpha| - h_2(S^\alpha - S_0^\alpha)H\left(\dot{\gamma}_{\mathrm{th}} - \textstyle\sum_{\alpha=1}^{n}|\dot{\gamma}^\alpha|\right)$$
$$\dot{B}^\alpha = [h_B - D^\alpha B^\alpha\mathrm{sgn}(\dot{\gamma}^\alpha)]\dot{\gamma}^\alpha$$

Box 1: Summary of the CPFE model.

shear moduli at the current temperature and 0 K, respectively, S^α and B^α the slip resistance and backstress in the slip system α, respectively. $\langle\cdot\rangle$ denotes the Macaulay brackets (i.e., $<\cdot>=((\cdot)+|\cdot|)/2$), sgn$(\cdot)$ is the sign function.

The starting point for the evolution equations for the slip resistance (S^α) and the backstress (B^α) for a nickel based alloy is [21, 103]:

$$\dot{S}^\alpha = \left[h_S - d_D(S^\alpha - S_0^\alpha)\right]|\dot{\gamma}^\alpha| \tag{2.20}$$

$$\dot{B}^\alpha = [h_B - D^\alpha B^\alpha \text{sgn}(\dot{\gamma}^\alpha)]\dot{\gamma}^\alpha \tag{2.21}$$

where, S_0^α is the initial slip resistance for slip system α, h_S and d_D are the hardening and dynamic recovery parameters for the slip resistance evolution; h_B and D^α are the hardening and dynamic recovery parameters for the backstress evolution, and D^α is expressed as [103]:

$$D^\alpha = \frac{h_B \mu_0}{S^\alpha}\left\{\frac{\mu_0'}{f} - \mu\right\}^{-1} \tag{2.22}$$

in which, μ_0' is the local slip shear modulus at 0 K and f is a parameter that accounts for the coupling between the internal slip variables as well as the statistical effects.

The slip evolution laws described in Eqs. (2.20) and (2.21) have been used to describe the hardening behavior of nickel-based alloys at different temperatures (see [138, 20, 103]). Fully reversed strain-controlled low cycle fatigue and creep-fatigue tests of IN 617 (with strain profile schematically illustrated in Fig. 2.2) were conducted at total strain ranges of 0.6–2.0% at 950°C. A distinct pattern of stress-strain behavior is observed under high-temperature fatigue and creep-fatigue loading (see Fig. 2.3), featured by: (1) an initial stress drop in the first cycle for both fatigue and creep-fatigue tests; (2) re-emergence of the softening behavior in creep-fatigue tests upon reloading (compression) following a strain hold, which is observed in all cycles until crack initiation. The evolution equations in Eqs. (2.20) and (2.21) do not capture this softening behavior.

The formation of an initial peak followed by an exponential decrease to a stable flow

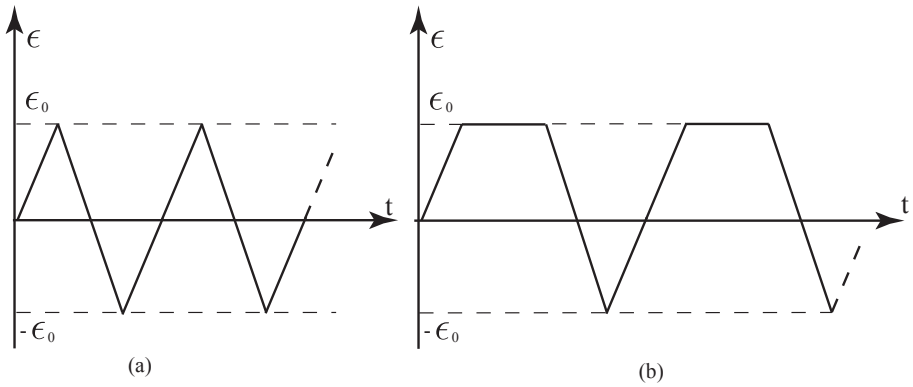

Figure 2.2: Strain profiles: (a) fatigue test; (b) creep-fatigue test.

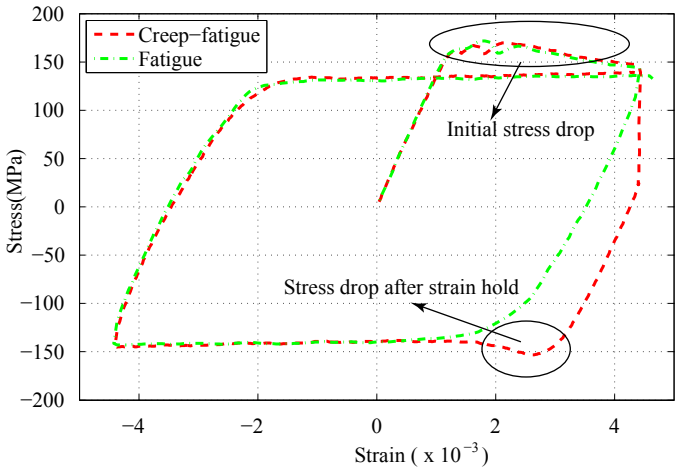

Figure 2.3: Stress drop observed in the stress-strain curve.

stress in IN 617 at high temperatures has been attributed to the solute-drag creep deformation mechanism [187]. Similar behavior has been observed in other alloys (e.g., class I and class A aluminum alloys) that exhibit solute-drag creep at elevated temperatures ([159, 175, 22]). Under pure fatigue, the phenomenon is restricted to the first cycle, whereas under creep-fatigue loading, the transient softening prior to steady state flow is persistent.

While the mechanism of solute-drag creep is known [175], its recurrence under creep-fatigue loading has not been studied in detail to the best of the authors' knowledge. At elevated temperature and applied stress, the solutes hinder dislocation motion resulting in relatively high resistance to plastic flow. At a threshold stress, the dislocations overcome the energy barrier and begin dragging solute atoms, which consequently reduces the flow stress to a steady state. Under sudden load reversal, those solute atoms already dragged

out of their equilibrium state do not contribute to the extra resistance observed in the initial loading. When subjected to a strain-hold with sufficiently long hold time, solutes return to an energetically minimum state. Hence, upon loading reversal, they contribute to added transient resistance to flow.

We model the above interactions by a new evolution law for the slip resistance given as:

$$\dot{S}^{\alpha} = \left[h_S - d_D(S^{\alpha} - \bar{S}^{\alpha})\right]|\dot{\gamma}^{\alpha}| - h_2(S^{\alpha} - S_0^{\alpha})H\left(\dot{\gamma}_{\text{th}} - \sum_{\alpha=1}^{n}|\dot{\gamma}^{\alpha}|\right) \tag{2.23}$$

where, $\dot{\gamma}_{\text{th}}$ is the threshold rate for static recovery, h_2 the rate of static recovery parameter, $\bar{S}^{\alpha}$ the steady state flow strength parameter. $H(\cdot)$ denotes the Heaviside function. The first part of the slip resistance evolution includes the steady state flow strength parameter, $\bar{S}^{\alpha}$, which is typically lower than S_0^{α} - the "initial" slip resistance. The initial slip resistance refers to the energetic configuration with stationary solutes prior to the onset of drag, and corresponds to the threshold stress mentioned above. The second part of the slip resistance evolution accounts for the recovery of strain softening in the form of static recovery. In the present model, the recovery initiation is possible only when dislocation motion reduces significantly, which is a necessary condition to stop the drag process. Considering the Orowan equation:

$$\dot{\gamma}^{\alpha} = \rho_M^{\alpha} b v^{\alpha} \tag{2.24}$$

in which, v^{α} is the average velocity of the mobile dislocations, ρ_M^{α} the density of mobile dislocations and b the length of Burgers vector. We employ the proportionality between the diffusion velocity and the slip rate in Eq. (2.24) to define the recovery term. When magnitude of slip (at all slip systems) drops below a threshold rate, $\dot{\gamma}_{\text{th}}$, static recovery initiates. The rate of recovery is controlled by h_2. At the asymptotic limit, the slip system strength reaches the initial slip system strength (i.e., configuration indistinguishable from the initial state).

The competition between the first and the second components of the strength evolu-

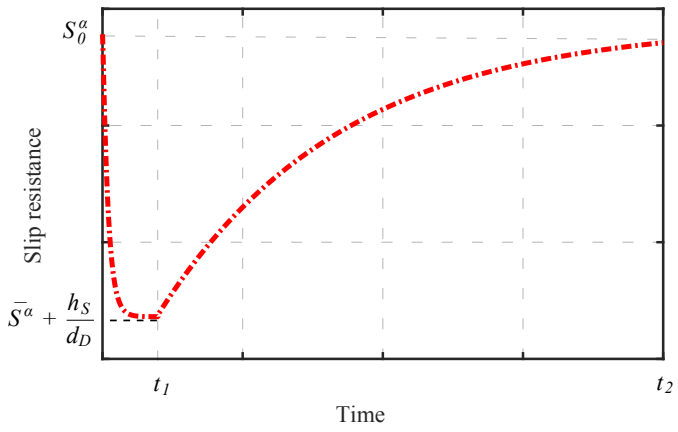

Figure 2.4: Evolution of slip resistance under the prescribed slip rate.

tion equation, which respectively forces a reduction and increase in the slip resistance is explained in the context of a simple example. Consider an arbitrary slip system, α, is subjected to a constant slip rate $\dot{\gamma}^\alpha = \dot{\tilde{\gamma}} > \dot{\gamma}_{\text{th}}$ (with slip in all other slip systems constrained) until time t_1, followed by zero slip rate $\dot{\gamma}^\alpha = 0$ between times t_1 and t_2. The example is set to mimic loading followed by a subsequent strain hold. t_1 and t_2 are sufficiently long such that dynamic and static recovery processes are nearly completed, respectively. Under this prescribed loading condition, the evolution of slip resistance can be evaluated in closed form from Eq. (2.23) as:

$$S^\alpha = \begin{cases} \bar{S}^\alpha + \frac{1}{d_D}\left\{hs - [hs - d_D(S_0^\alpha - \bar{S}^\alpha)]\exp(-d_D|\dot{\gamma}_0^\alpha|t)\right\} & 0 \le t \le t_1 \\ S_0^\alpha - (S_0^\alpha - \bar{S}_\alpha - \frac{h_S}{d_D})\exp(-h_2(t-t_1)) & t_1 \le t \le t_2 \end{cases} \tag{2.25}$$

Equation (2.25) plotted in Fig. 2.4 shows an exponential decay of the slip resistance towards $\bar{S}^\alpha + h_S/dD$ followed by a recovery towards its initial value S_0^α.

2.1.2 Numerical smoothing for convergent stress update

Box 1 summarizes the system of nonlinear equations, which describes the mechanical response based on the crystal plasticity model described above. This system is discretized over the domain of a characteristic microstructure and evaluated numerically us-

ing the finite element method. The stress update at a material point within a grain is performed using an operator split method with a two-level staggering scheme as described in Refs. [109, 108]. In the first level, a Newton-Raphson method is used to solve for stress ($\boldsymbol{\tau}$), while rotations ($\boldsymbol{R}^e$), slip resistances (S^α) and backstress (B^α) are kept constant; In the second level, rotations, slip resistances and backstress are updated for a fixed stress calculated at the first level. Iterations between the two levels continue until changes in the cardinal unknowns (i.e., $\boldsymbol{\tau}$, S^α and B^α) within the increment drop below a threshold value (relative change of the norm is less than 1.0×10^{-4} in the current study). Convergence of the polycrystal plasticity equations summarized in Box 1 using the algorithms defined above is not guaranteed due to the discontinuity in the Jacobian introduced by the presence of Macaulay brackets in the flow rule. This discontinuity typically leads to the oscillation of the iterations without convergence. We employ a simple regularization of this problem, by replacing the Macaulay brackets with a C^1 continuous approximation. Let $\langle f \rangle_c$ be a C^1 continuous functional defined as (Fig. 2.5):

$$\langle f \rangle_c = \begin{cases} f & f > \frac{1}{\sqrt{2}}c \\ r - \sqrt{r^2 - f^2 + 2fc} & -c \leq f \leq \frac{1}{\sqrt{2}}c \\ 0 & f < -c \end{cases} \tag{2.26}$$

where, $r = (\tan\dfrac{3\pi}{8})c$ is the radius of the circle that is used for smoothing. At the limit of $c \to 0$, $\langle f \rangle_c$ approaches $\langle f \rangle$ and c constitutes the numerical regularization parameter. The Macaulay bracket in the slip evolution equation is then replaced with the continuous approximation. In the numerical simulations discussed below c is set to 0.001. By this approach, the system Jacobian remains well-defined and the numerical scheme is convergent for sufficiently small time step size. We note that the convergence is sub-quadratic due to the use of operator split in the evolution of the constitutive equations.

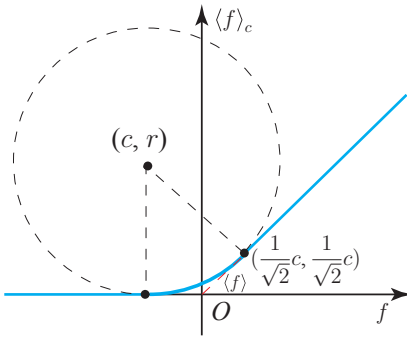

Figure 2.5: "Smoothed" Macaulay bracket to eliminate Jacobian discontinuity and improve stress-update convergence.

2.2 Model Preparation

IN 617 is a solid solution strengthened alloy with face center cubic (FCC) lattice structure, with 12 octahedral $\{111\}\langle 110\rangle$ slip systems. In precipitate strengthened nickel alloys where the γ-γ' phases coexist, the six cubic slip systems $\{100\}\langle 110\rangle$ may also contribute to deformation at high homologous temperatures and high resolved stress (in γ' phase) [158]. γ' phase becomes unstable above 650°C [107, 14]. At temperatures above approximately 750 °C, the microstructure of IN 617 is largely free of γ' precipitates, hence the cubic slip systems remain inactive. Figure 2.6(b) shows a 2-D EBSD scan of IN 617. The microstructure exhibits distinguishable coarse and fine grains and random initial orientations as shown in Fig. 2.6(b). Similar observations have been previously made [122, 123, 111]. Annealing twins are evident in the as-received samples and deformation twinning has not been observed and not considered in the simulations. Annealing twins could serve as sites of strain localization and damage initiation in Ni-based alloys subjected to fatigue loading conditions [170, 171]. The focus of the current investigations is on modeling of the cyclic response prior to the onset of significant microstructural damage, and the presence of annealing twins are not taken into account in the microstructures employed in this study. The microstructure images (Fig. 2.6(a)) also show significant amount of carbides (mainly Mo-rich, Cr-rich carbides and Ti-rich carbonitrides) present within and at grain boundaries. While the presence of carbides may affect the fatigue and creep-fatigue damage, they are

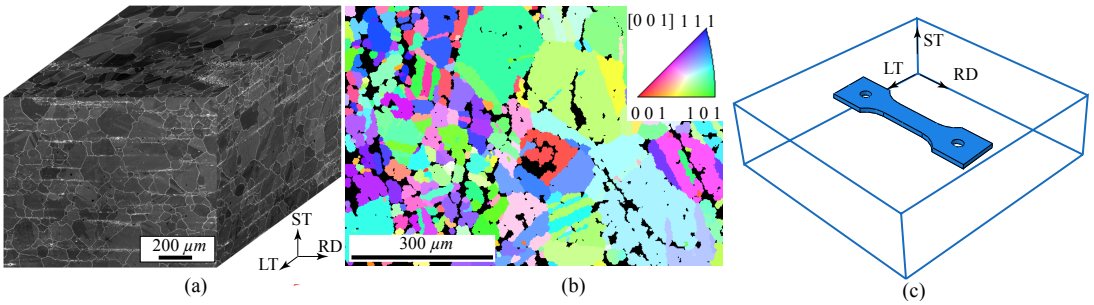

Figure 2.6: IN 617 microstructure: (a) 3-D etched microstructure (reproduced from Ref. [122]; (b) [0 0 1] inverse pole figure (IPF) EBSD map on a short traverse plane of as received IN 617 sample; (c) specimen configuration.

not explicitly modeled in the simulation of the cyclic behavior.

All experimental data used in this study are from specimens machined from the annealed plate produced by ThyssenKrupp VDM and solution annealed at 1175 °C [188]. The compositions of the specimens are given in Table 1 along with the specified ranges in ASTM Standard B168-08 for comparison. The long axis of the specimen is aligned with the rolling direction as schematically demonstrated in Fig. 2.6(c).

Table 2.1: Composition in percentage weight of the IN 617 specimen used in this study.

	Ni	C	Cr	Co	Mo	Fe
ASTM standard	≥ 44.5	0.05-0.15	20.0-24.0	10.0-15.0	8.0-10.0	≤ 3.0
This study	bal	0.05	22.2	11.6	8.6	1.6
	Al	Ti	Si	Cu	Mn	S
ASTM standard	0.8-1.5	≤ 0.6	≤ 1.0	≤ 0.5	≤ 1.0	≤ 0.015
This study	1.1	0.4	0.1	0.04	0.1	≤ 0.02

Fully reversed strain-controlled low cycle fatigue and creep-fatigue tests were conducted at total strain ranges from 0.6-2.0% at 950°C, all with constant strain rate of 1.0×10^{-3}/s. One cycle was defined as the combination of a tension and compression load reversal using a symmetric triangular waveform. During the initial part of most experiments, several cycles with incrementally increasing strain values were used prior to reaching the target strain level to avoid overshooting the target strain, which can occur at high tempera-

ture in the presence of plastic deformation. Table 2.2 summarizes the experiments used in this study.

Table 2.2: Summary of all tests studied.

Specimen	Temperature(°C)	Strain rate ($/s$)	Total Strain (%)	Hold time (s)
B-14	950	0.001	0.6	0
E-11	950	0.001	1.0	0
J-1	950	0.001	2.0	0
A-14	950	0.001	0.6	600
416-18	950	0.001	0.6	1800
B-16	950	0.001	0.6	180
F-5	950	0.001	1.0	180
A-13	950	0.001	1.0	600
E-6	950	0.001	1.0	1800
E-10	950	0.001	1.0	9000

2.2.1 Microstructure reconstruction and meshing

Microstructure generation of IN 617 is conducted using the DREAM.3D software [54], which is capable of creating synthetic microstructures using experimentally determined microstructure morphological and crystallographic statistics. Grain size distribution computed from microstructure observations are employed to generate the synthetic microstructures, as well as their geometry and surface mesh information (see Fig. 2.7(a)). To accurately quantify the bi-modal grain size distribution observed in IN 617, the fine and coarse grains are treated as separate phases during the reconstruction process. The volume fractions of the fine and coarse grains are 75.61% and 24.39%, respectively. Figure 2.8 shows the log-normal distributions fitted to the experimentally observed distributions for both the fine and coarse grains. The Parallelized Polycrystal Mesher (PPM) software developed by Cerrone et al [26] is then used to build a volume mesh of the microstructures. Figure 2.7(b) shows the volume mesh generated using the above-mentioned process, which provides statically equivalent microstructures as the specimen.

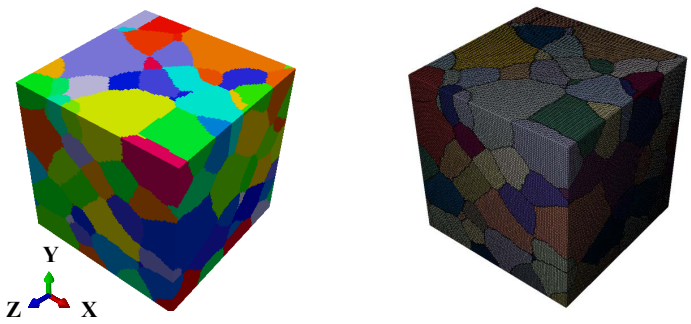

Figure 2.7: Microstructure generation and meshing: (a) microstructure generated in DREAM.3D; (b) volume mesh.

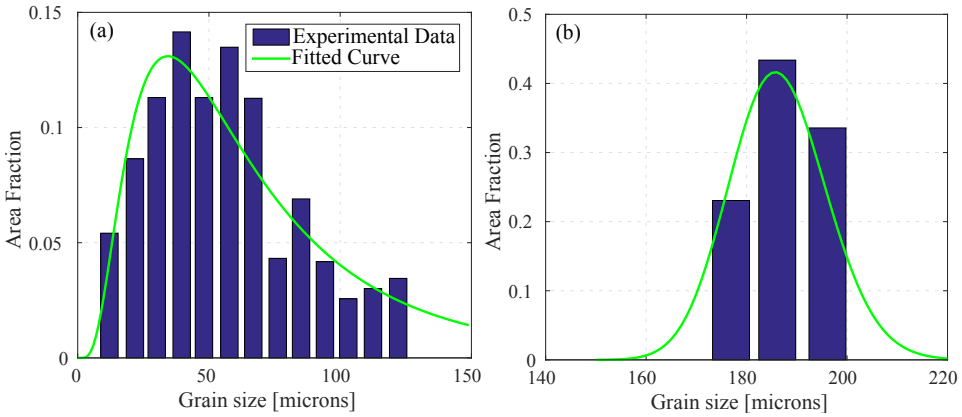

Figure 2.8: Fitted log-normal grain size distribution: (a) fine grains; (b) coarse grains.

2.2.2 Determination of the simulation domain size

In order to identify the appropriate size of the simulation domain that provides converged CPFE simulation results with reasonable computational cost, a parametric study was conducted. The parametric study was performed with respect to the number of grains resolved within the simulated microstructure. Three different cubic simulation cells with edge length of 300 μm, 360 μm and 400 μm are constructed for this purpose. The discretization of the simulation cells are as shown in Fig. 2.9(b)-(d). The boundary conditions are schematically shown in Fig. 2.9(a). The three simulation cells contain 98, 140 and 243 grains, and are discretized using four-noded tetrahedra with 67,689, 113,986 and 243,801 elements, respectively. Each grain is assigned a random initial orientation. The applied strain follows a creep-fatigue test path with 1.0% strain range (R ratio equals to 1), 180 s hold time at the maximum tension and strain rate of 0.001/s.

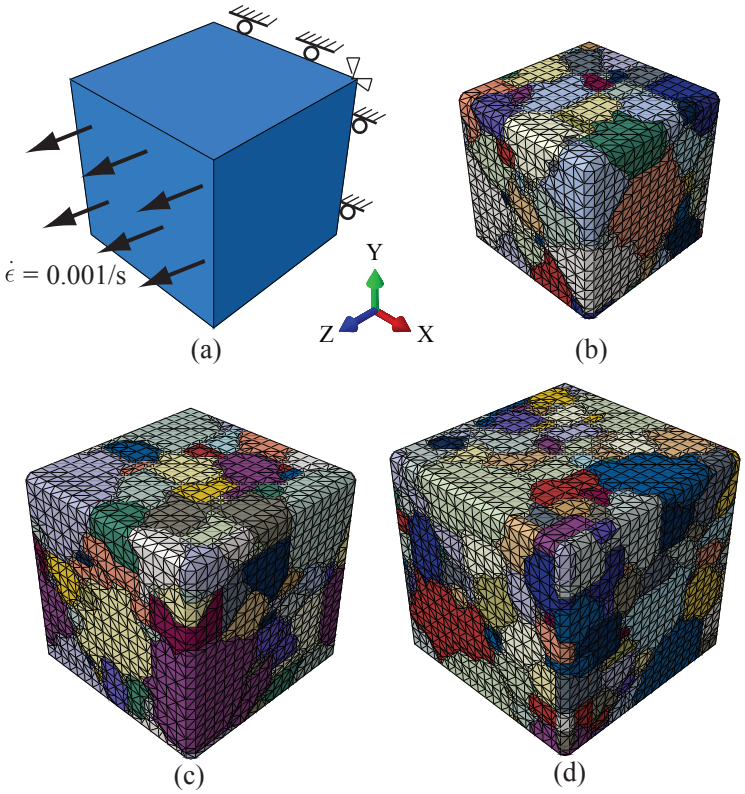

Figure 2.9: (a) Schematic illustration of the boundary conditions and loading used in the microstructure size determination study; (b)-(d) Finite element meshes of the 98-, 140- and 243-grain microstructures.

Figure 2.10 shows the stress-strain responses obtained using the three simulation cells. While the three curves matched well during the elastic region and the stress hold, a noticeable gap between the 98-grain cell and the others is observed after yielding. This observation indicates 98-grain cell is not representative of a converged response while the simulation cell with 140 and 243 grains are sufficiently similar. We further investigate the convergence of the local stress distribution within five microstructures, including a 504- and 769-grain cells (microstructure geometries not plotted for brevity). The stress histograms of the cells at the beginning of the strain hold are plotted in Fig. 2.11. With the exception of the 98-grain cell, the stress distributions with the remainder of the cells are similar with slight variability. The CPFE simulations below are therefore performed using the 140-grain cell. The simulation cell is assigned with random initial texture with the $\{111\}$ pole figure shown in Fig. 2.12.

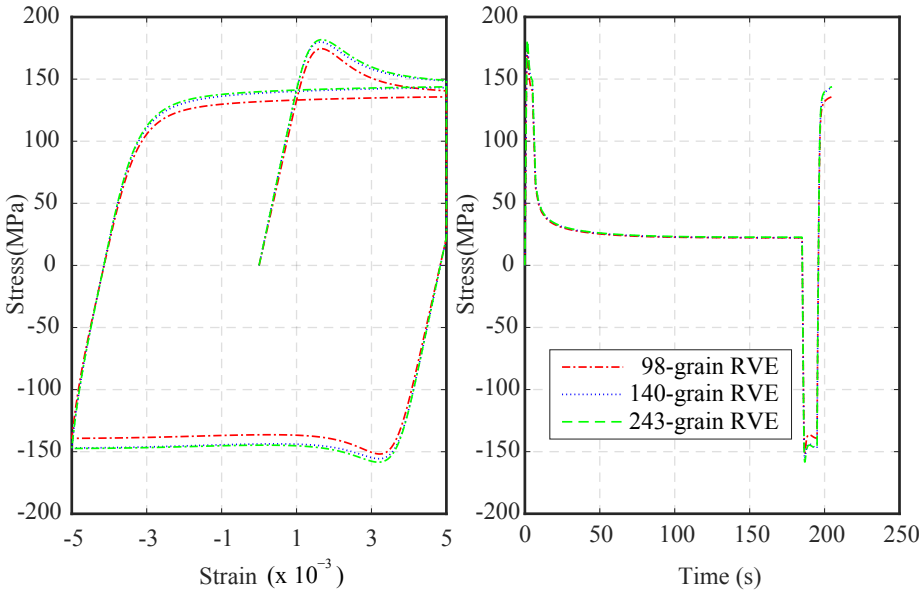

Figure 2.10: Convergence study of microstructure size: (a) stress-strain response; (b) stress-time response.

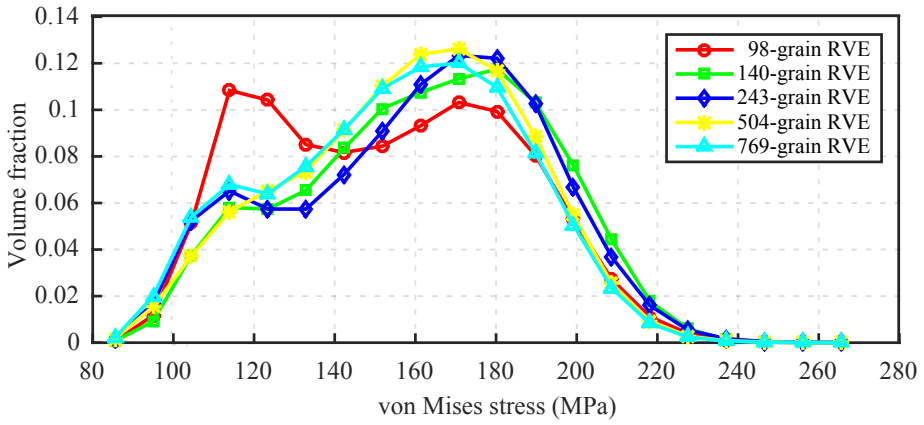

Figure 2.11: von-Mises stress histogram of different RVEs.

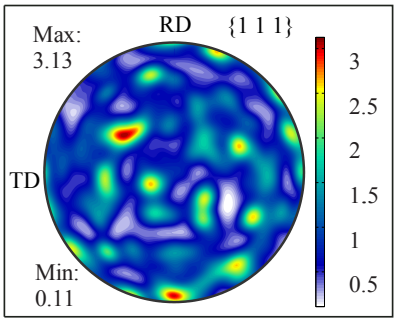

Figure 2.12: {1 1 1} pole figure of the initial texture of the 140-grain microstructure.

2.2.3 Model parameter calibration

The full set of parameter values of the crystal plasticity model for IN 617 described above is not generally available in the literature. Those model parameters not available in the literature are therefore inferred from experimental data. The general calibration approach used in this study is based on optimization through the minimization of an objective function. Let Θ denote the set of all unknown parameters of the model. In the current study, 19 parameters define the model as indicated in Table 2.3. Consider an arbitrary but fixed subset of model parameters, $\hat{\Theta} \subset \Theta$. Each parameter within the parameter set, $\Theta_i \in \Theta$, lies within a range of values $\Theta_i \in [\Theta_i^l, \Theta_i^u]$, where Θ_i^l and Θ_i^u denote the lower and upper bound values of the parameter Θ_i, respectively. These bounds are typically chosen based on physical arguments, (e.g., magnitude of relative yield stress or strain hardening). The optimal set of parameters is achieved by solving the following equation:

$$\hat{\Theta}^{\text{opt}} = \arg\min \left\{ \sum_{i=1}^{M} w_i^t \left[\sum_{j=1}^{N_i} \left(\frac{R_{i,j}^{\text{exp}} - R_{i,j}^{\text{sim}}(\mathbf{X}_k)}{R_{i,j}^{\text{exp}}} \right)^2 \right], \hat{\Theta} \in [\hat{\Theta}^l, \hat{\Theta}^u] \right\} \tag{2.27}$$

in which, M is the total number of experiments used in the calibration process; w_i^t is the weight factor for the i^{th} test used to increase or reduce parameter sensitivity; N_i denotes the number of datasets obtained from test i (e.g., stress-strain, stress time histories); $R_{i,j}^{\text{exp}}$ and $R_{i,j}^{\text{sim}}$ are respectively the experimental and the simulated datasets. Equation (2.27) is written for a subset of parameters only and executed multiple times to calibrate all parameters, since the optimization of the full set of 19 parameters together is computationally prohibitive. At the beginning of the calibration process, each parameter is assigned an initial value, Θ_i^0. During the calibration of the parameter subset $\hat{\Theta}$, all parameters (not being calibrated) are either set to their initial values, or set to their calibrated values at an earlier parameter subset calibration. We further note that a very comprehensive dataset is necessary to uniquely identify all parameters, and experimental data is often quite limited. We therefore seek a set of optimal and physically reasonable parameters that accurately cap-

tures the available calibration data. The calibration is performed by executing the following steps: (1) Determine search range for each parameter (i.e., Θ_i^l and Θ_i^u). (2) Sample parameter subspace and execute CPFE simulations to compute $R_{i,j}^{sim}$. (3) Fit a surrogate model that approximates the response surface (i.e., R_{ij}^{sim}). (4) Solve Eq. (2.27) to obtain optimal parameters set $\hat{\Theta}^{\text{opt}}$. (5) Verify calibration accuracy by running CPFE simulation with $\hat{\Theta}^{\text{opt}}$.

Two out of the 19 parameters are set to fixed values and not calibrated, while three of them are dependent (i.e., can be computed from the remaining 16). The optimizations are therefore performed for 14 parameters only. f is set to 0.36 as suggested by Lin et al. [103] since its effect on the simulation results are found to be small. The lattice friction stress at 0 K, $\hat{\tau}_0$, in Eq. (2.19) is obtained by resolving the difference between the yield strength (at 0.2% offset strain) at 0 K, $\sigma_{0.2}^0$, and the temperature approaching infinity, $\sigma_{0.2}^\infty$ (i.e., see [20]):

$$\hat{\tau}_0 = \frac{\sigma_{0.2}^0 - \sigma_{0.2}^\infty}{2} \tag{2.28}$$

with $\sigma_{0.2}^0$ and $\sigma_{0.2}^\infty$ estimated from Ref. [77], giving $\hat{\tau}_0 = 268.2$ MPa as a constant. This procedure has been previously employed to calibrate lattice friction stress [20]. A fixed anisotropy factor of $A = 2C_{44}/(C_{11} - C_{12}) = 2.5$ which is equal to that of pure nickel is enforced [142], decreasing the number of independent elastic parameters to two. The local shear modulus at 0 K, μ_0', is given by Ref. [20] as:

$$\mu_0' = \frac{C_{11} - C_{12}}{2} \tag{2.29}$$

and the shear modulus μ is equal to the elastic parameter C_{44}.

The search ranges for the remaining 14 parameters of the polycrystal model are established through the literature search on crystal plasticity modeling of similar alloys, and preliminary parametric analysis performed for each parameter. The elastic properties for pure nickel are used as the initial value of the elastic parameter (i.e., $C_{11} = 250$ GPa, $C_{12} = 151$ GPa, $C_{44} = 123$ GPa [142]). By referring to elastic parameters of other nickel-based al-

Table 2.3: Summary of model parameters. (For fixed parameters, only initial value are provided; for dependent parameters, only dependency and calibrated value are provided.)

Parameter	Initial value	Lower bound	Upper bound	Calibrated value	Reference
C_{11} (GPa)	250	150	280	170.64	[142, 158, 103]
C_{12} (GPa)	151	30	160	108.39	[142, 158, 103]
$\dot{\gamma}_0$ (s^{-1})	5×10^{-3}	5×10^{-4}	3×10^{-2}	1.44×10^{-3}	[103]
F_0 (J)	4.98×10^{-19}	4.5×10^{-19}	5.5×10^{-19}	5.148×10^{-19}	[103, 158, 21]
μ_0 (GPa)	200	180	300	265.33	[103, 158, 21]
p	0.3	0.1	0.4	0.181	[86, 103]
q	1.8	1.5	2	1.633	[86, 103]
h_S (MPa)	2000	100	10000	397.73	[103, 21]
d_D (MPa)	100	1000	10000	5073.62	[103, 21]
S_0^α(MPa)	200	50	320	143.41	[103, 21]
$\bar{S}^\alpha$ (MPa)	200	20	S_0^α	18.03	-
h_B (MPa)	5000	10	10000	104.31	[103]
h_2 (MPa)	0	0	0.2	0.015	-
$\dot{\gamma}_{th}$ (s^{-1})	0	0	1×10^{-4}	1×10^{-6}	-
C_{44} (MPa)	$1.25(C_{11}-C_{12})$	-	-	77.82	[142]
μ (GPa)	$1.25(C_{11}-C_{12})$	-	-	77.82	[20]
μ_0' (GPa)	$0.5(C_{11}-C_{12})$	-	-	31.13	[20]
$\hat{\tau}_0$ (MPa)	268.2	-	-	-	[20, 77]
f	0.36	-	-	-	[103]

loys [158, 103] and the observation that bulk moduli of alloy at 950°C is around 140 GPa, the ranges of C_{11} and C_{12} are set to be $150 \leq C_{11} \leq 280$ GPa and $30 \leq C_{12} \leq 160$ GPa, respectively. The activation energy F_0 for various nickel-based alloys was taken to be around 300 KJ/mol (4.98×10^{-19} J) in Refs. [158, 103, 21], which serves as the initial value of F_0 with the range set to be $4.5\times10^{-19} \leq F_0 \leq 5.5\times10^{-19}$J. The initial values for p and q are chosen to be $p = 0.31, q = 1.8$ [103] with recommendation as $0 \leq p \leq 1$ and $1 \leq q \leq 2$ in general by Kothari and Anand [86], while preliminary simulations further constrain them as $0.1 \leq p \leq 0.4$ and $1.5 \leq q \leq 2$. The initial values and ranges of the other parameters are provided in Table 2.3. The initial values used to initiate the optimization process that provided the global minimum are reported in the table.

Since the computational cost of CPFE simulations is high, it is computationally too costly to evaluate the minimization process using CPFE analysis as the forward solver. We rely on a surrogate model (i.e., Gaussian Process model [146]) to approximate the CPFE

simulation for calibration purposes. GP model is a variant of a radial basis function built on Gaussian kernels and provides the fast transform function between the input (parameter set) and output ($R_{i,j}^{\text{sim}}$). The GP model is "trained" using a series of simulations using the CPFE. We employed Latin Hypercube sampling to sample the search space bounded by the parameter ranges. The optimization is performed using a constrained nonlinear multi-variable solver [143], where the objective function evaluations are performed using the GP models [17]. In order to ensure that the global minimum is achieved within the chosen parameter ranges, The optimization process is repeated several times with random initial parameter values. The final step consists of running a CPFE simulation, with optimal parameter set to assess accuracy. If accuracy is deemed insufficient, the GP model is retrained with denser sampling around the optimal point within the parameter space. The optimization procedure is repeated with retrained GP model.

In this study, the calibration is performed for elastic, monotonic and cyclic response in order to limit the number of unknowns (i.e., dimension of parameter space). Since the fatigue and creep-fatigue tests provide the same response of the elastic and monotonic case, only one test (F-5) is used for calibration while a fatigue and creep-fatigue (F-5 and J-1) are used during the cyclic calibration process. In the elastic calibration process, bulk Young's modulus is taken to be $E = 141$ GPa according to the experimental data while Poisson's ratio of the bulk material is reported to be 0.3 at 950°C. The number of variables to be calibrated is equal to the number of properties, leading elastic calibration to a well-posed and unique optimization problem. (i.e., $\mathbf{X}_1 = \{C_{11}, C_{12}\}$, $\mathbf{R}_1 = \{E, \nu\}$).

In the monotonic calibration process, the softening part of the stress-strain curves are not considered at first while the slip resistance and backstress evolution are turned off (i.e., set initial value temporarily as: $h_S = 0$, $d_D = 0$, h_B=0, $h_2 = 0$) in the simulation. $R_{1,j}$ is the j^{th} data point out of the total N_1 data points selected from the tension part of the stress-strain curve with the stress drop region eliminated, while $\mathbf{X}_2 = \{F_0, S_0^\alpha, \mu_0\}$ and $\mathbf{X}_3 = \{S_0^\alpha, \dot{\gamma}_0, p, q\}$ are calibrated successively. Then another set of selected data points from the

tension part of the stress-strain curve that mainly characterizes the initial yield stress, the stress drop speed and the stabilized flow stress are used in the objective function while the parameters set is chosen as $\mathbf{X}_4 = \{\bar{S}^{\alpha}, h_S, d_D, h_B\}$ with the static recovery term turned off (i.e., set initial value temporarily as: $h_2 = 0$).

In the cyclic calibration process, both fatigue test J-1 and creep-fatigue test F-5 are used to define the objective function. Data points that reflect the relaxation, yielding stress at compression, softening after the strain hold in the creep-fatigue test and hardening profile are selected while $\mathbf{X}_5 = \{p, q, \dot{\gamma}_0\ , h_2, \dot{\gamma}_{\text{th}}\}$ are used to match hysteresis response for both the fatigue and creep-fatigue tests. The final calibrated parameters are listed in Table 2.3, while the simulation results together with corresponding experimental tests are plotted in Fig. 2.13. It can be seen that the calibrated parameters can capture the stress-strain and stress-time response for both fatigue test and creep-fatigue tests with good accuracy. Their capability to predict other fatigue and creep-fatigue testes with different strain ranges and hold times is further validated next.

The primary challenges in the proposed optimization strategy, particularly for generalizing beyond the current study, are the identification of the parameter ranges and parameter sensitivity used in the selection of parameter subsets. The sensitivity analysis, which identifies the parameters with similar sensitivity (i.e., the selected parameter subset) to the corresponding experimental data used to calibrate them, depends on the chosen parameter ranges. In the current study the parameter ranges were identified based on a parametric study and values previously reported in the literature as discussed above. These challenges exist because of the large number of parameters to be identified, and because the experiments are performed at the bulk scale to calibrate parameters defined at the grain scale.

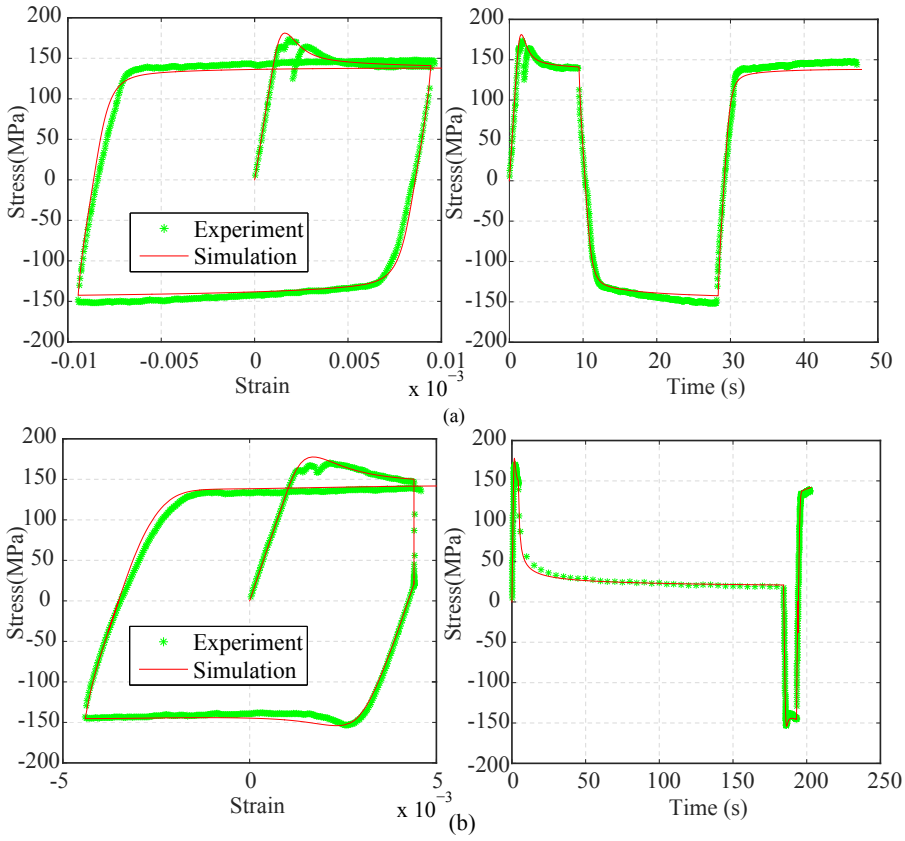

Figure 2.13: Comparison of simulation results using the calibrated parameters with the two experiment tests used for calibration: (a) fatigue test J-1; (b) creep-fatigue test F-5.

2.3 Validation and Analysis of Microstructural Response

The calibrated parameters are further validated by running CPFE simulations to compare the first cycle response with experimental data of the remaining tests. As illustrated in Table 2.2, the tests were performed using various strain ranges and hold times beyond the calibration regime. The comparisons are first focused on the first cycle response. A multiple-cycle analysis and discussion is presented next.

2.3.1 First cycle response

Since the transient stress relaxation phenomenon is most prominent in the first cycle, particularly when subjected to fatigue loading, we first investigate the predictive capability of the proposed model in capturing the hysteresis behavior of the first cycle. In this section,

we also provide a brief analysis of the evolution of the hysteresis behavior through the cycles and an investigation of the evolution of the stress state within the microstructure.

Figure 2.14 shows the first cycle responses of fatigue tests B-14 and E-11, respectively. The creep-fatigue tests B-16, A-14 and A-13 are shown in Fig. 2.15 while creep-fatigue tests 416-18, E-6 and E-10 are shown in Fig. 2.16. The applied strain ranges in B-16, A-14 and 416-18 are small enough such that the stress softening behavior is not significant. The stress softening effect is visible and prominent beyond approximately 0.3% and appears in the other fatigue and creep-fatigue tests. The initial tensile loading part of the stress-strain curves in all experiments is also marked by the presence of serrations induced by the Portevin-Le Chatelier effect [187]. The present approach does not account for this effect and the tensile loading part of the simulations exhibit a smooth loading path.

In view of the above-mentioned points, the simulated overall stress-strain hysteresis curves are in very good agreement with the experiments. In particular, the stress relaxations caused by solute-drag creep are accurately captured as a function of various hold times and strain ranges. Particularly, Fig. 2.16 reveals slight discrepancies in the experimentally observed and simulated compressive flow stresses for creep fatigue tests E-6 and E-10, where the simulations overestimate the flow stress especially during the transient relaxation part. Nevertheless, comparing to the remainder of the creep-fatigue experiments, the simulation results remain within experimental error range.

The evolution of the hysteresis behavior as a function of load cycles are analyzed in the context of experiment F-5, which is a creep-fatigue experiment with applied total strain range of 1% and hold time of 180 s. Figure 2.17 shows the hysteresis loops of the 1st, 50th and 100th cycles from both the experiments and the simulations. The experimentally observed creep-fatigue life of the specimens is 465 cycles. The deformation therefore remains within the viscoplastic regime, with only a small effect of creep processes within the first 100 cycles. The experiment hysteresis loops demonstrate a slightly larger amount of cyclic softening, compared to the simulations. We note that a small amount of cyclic softening is

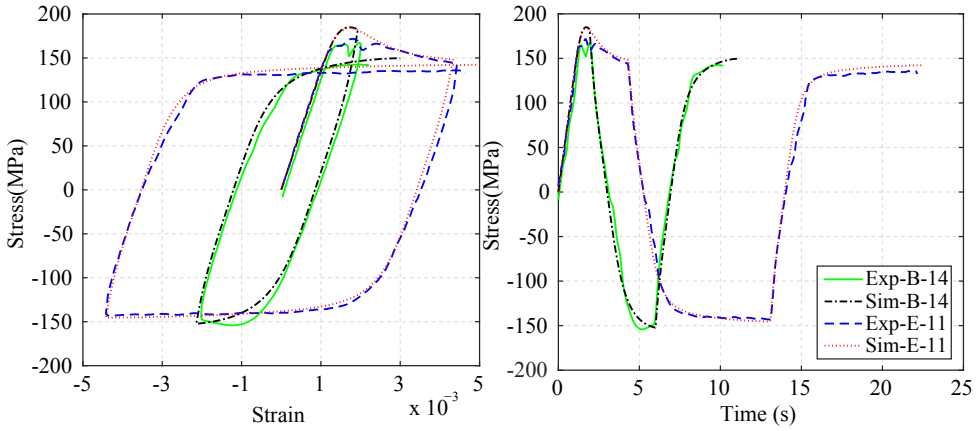

Figure 2.14: First cycle response of fatigue test B-14 and E-11.

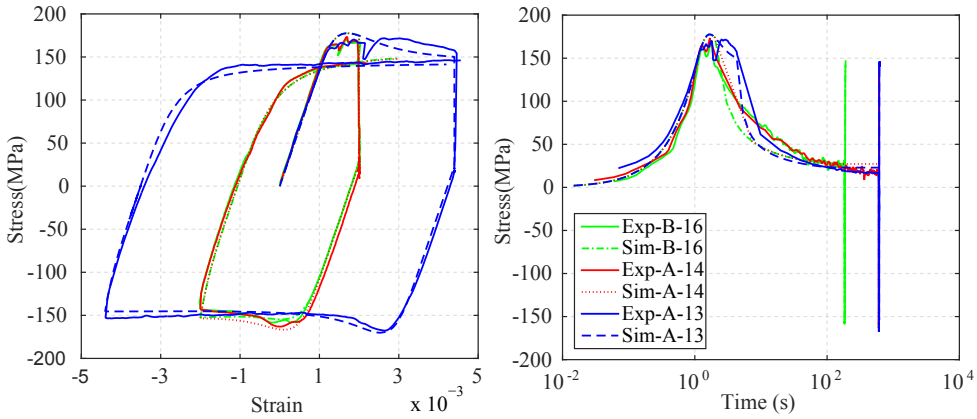

Figure 2.15: First cycle response of creep-fatigue test B-16, A-14 and A-13.

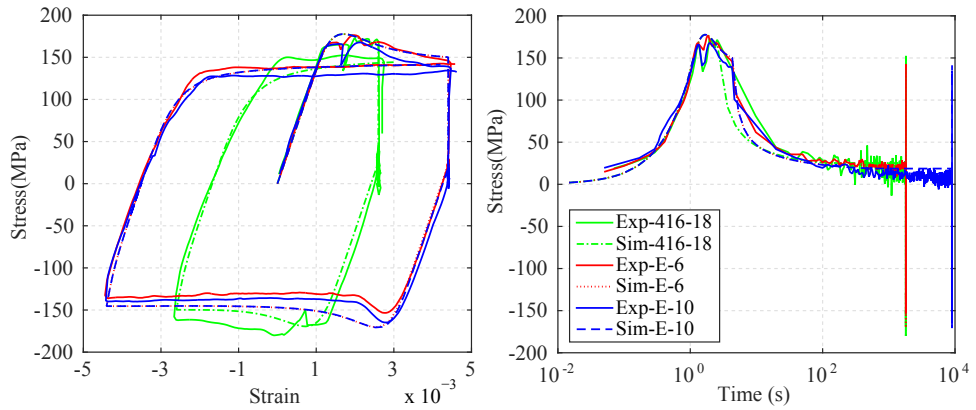

Figure 2.16: First cycle response of creep-fatigue test 416-18, E-6 and E-10.

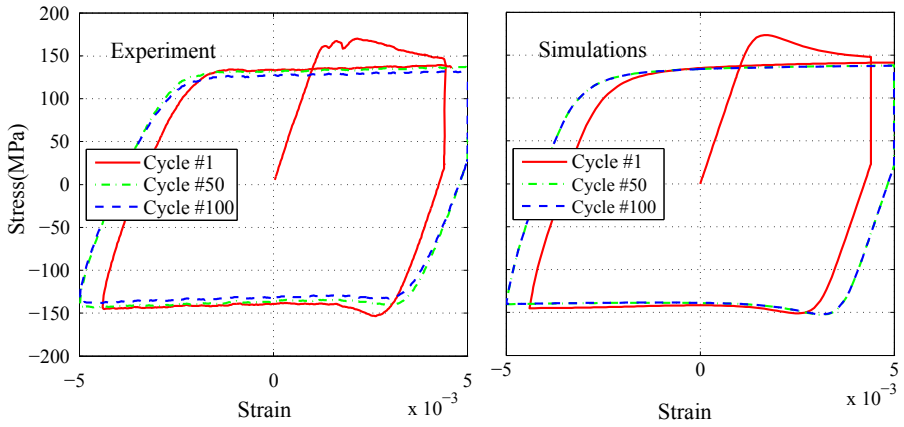

Figure 2.17: Stress-strain curves of different cycles: (a) experiments; (b) simulations.

also observed in simulation results due to the viscoplastic processes modeled in the context of grain deformation. The slight discrepancy between the experimental and simulated cyclic softening is due to the presence of (albeit small) diffusional grain boundary damage (e.g., cavitation) present in the experiments. The current model does not account for creep or fatigue induced damage evolution and these important effects will be investigated in the near future.

2.3.2 Microstructure analysis

The stress distributions within the simulation cell are investigated to gain more understanding of the microstructural aspects of deformation. The analyses are based on the creep-fatigue experiment, F-5. Figure 2.18 shows the stress contour plots over the simulation cell at the beginning, middle and end of hold of the first loading cycle. A complex stress distribution over the microstructure domain is observed with significant stress variations within and between grains, due to differences in grain orientations within the microstructure [31]. Stress concentrations around grain boundaries are also observed, with a naturally higher tendency of stress concentrations with higher misorientation angles. The locations of high stress concentrations (von-Mises stress higher than a threshold magnitude of 280 MPa) are highlighted in Fig. 2.19. It is observed that all of these locations are at

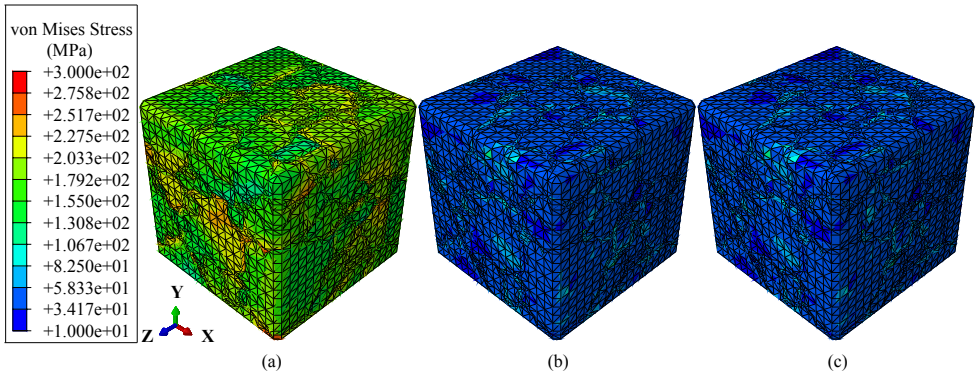

Figure 2.18: Stress contour of the RVE of the first cycle: (a) beginning of hold; (b) middle of hold; (c) end of hold.

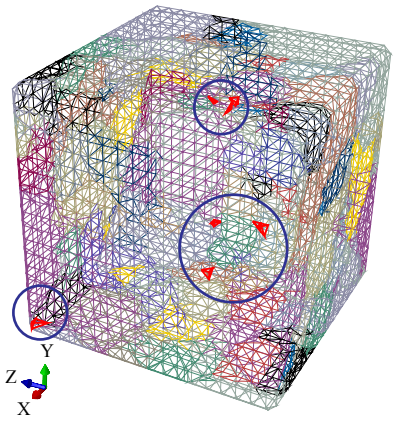

Figure 2.19: Locations with von-Mises Stress higher than 280 MPa at the beginning of hold.

the grain boundaries, and the orientations and misorientations around the locations of high stress are shown in Table 2.4. The misorientation angles are computed using the following equation [85, 31]:

$$\theta = \min \left| \cos^{-1} \left\{ \frac{tr(\mathbf{g}_B \mathbf{g}_A^{-1} \mathbf{O}) - 1}{2} \right\} \right| \tag{2.30}$$

where, $\mathbf{g}_A$ and $\mathbf{g}_B$ are the orientation matrices of adjacent grains A and B, respectively, tr is the trace operator, and $\mathbf{O}$ is the crystal symmetry operator for FCC crystals.

The stress contours also indicate only a small amount stress redistribution occurs at the latter half of the hold (compare Figs. 2.18(b) and (c)) since the stress relaxation process has largely been completed within the first half of the strain hold. The significant stress relaxation observed during the first part of the hold is also associated with a stress redistribution.

Table 2.4: Orientations (Bunge's convention) and misorientations of adjacent grains at the high stress locations.

Orientations of grain A	Orientations of Grain B	Misorientation
(148.51, 61.1, 291.5)	(352.38, 144.74, 242.35)	38.24
(279.2, 44.29, 98.96)	(311.07, 97.24, 264.9)	45.85
(250.05, 44.24, 131.00)	(237.19, 115.02, 41.72)	51.61
(237.19 , 115.02, 41.72)	(67.62, 65.15, 257.39)	34.79
(32.61, 48.65, 182.49)	(354.55, 84.24, 67.38)	57.48
(149.75, 133.74, 160.51)	(207.01, 153.38, 27.1)	37.54

The effect of stress redistribution is further demonstrated using the von-Mises stress histograms as shown in Fig. 2.20 for the first, 50th and 100th cycles. The slight leftward shift of the mean stress at the beginning of strain hold from the first to the 100th cycle indicates the viscoplastic cyclic softening process. The $\{111\}$ pole figure of the microstructure at different stages of the hold (from the first loading cycle) shown in Fig. 2.21 indicates no obvious texture evolution within the cycle. The subsequent loading cycles also did not indicate significant texture evolution.

To further investigate the distribution of stresses within and across grains, stress is plotted along the center line of the simulation cell along the X-direction as shown in Fig. 2.22. The dashed vertical lines indicate the grain boundaries, while each little cube shows the initial orientation of each grain relative to the sample coordinate system (Fig. 2.22(a)). Depending on the orientation of a grain with respect to the loading axis, those exhibit large plastic deformations are denoted as soft grains, and those have little or no plasticity are denoted as hard grains. Hard and soft grains are clearly recognized by different stress levels (approximately 200 MPa for the hard grain and 125 MPa for soft grains at the beginning of hold). At the end of the tensile loading process and the beginning of the hold, the stresses appear quite uniform within grains with sharp stress jumps occurring at the grain boundaries. The relaxation process significantly alters the stress patterns and stress gradients occur within grains. The interaction between neighboring grains that relax at different rates may contribute to the complex stress distributions observed during the creep

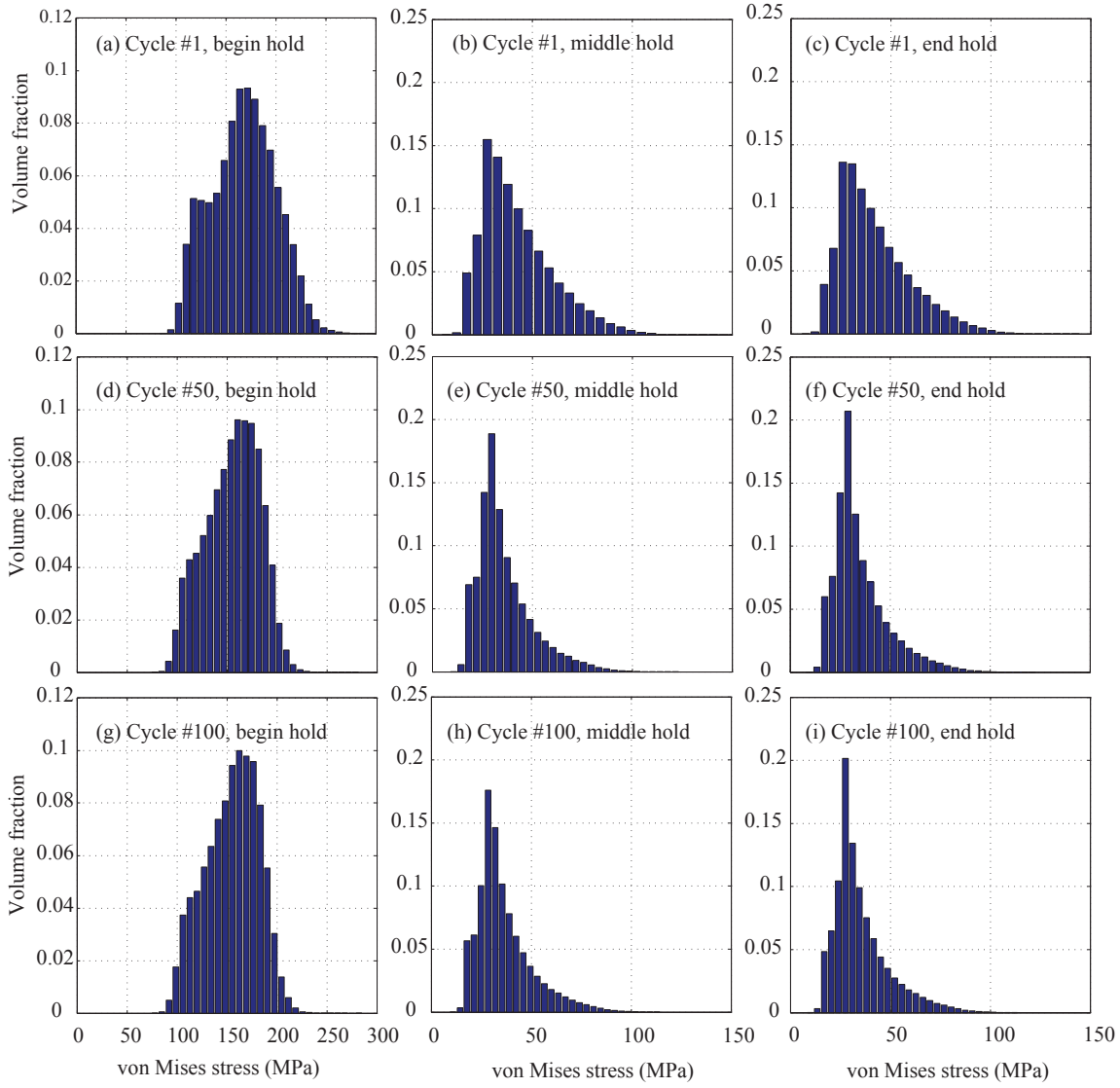

Figure 2.20: Von Mises stress histograms at different stages within the first (a)-(c), 50th (d)-(e) and 100th (g)-(i) cycle.

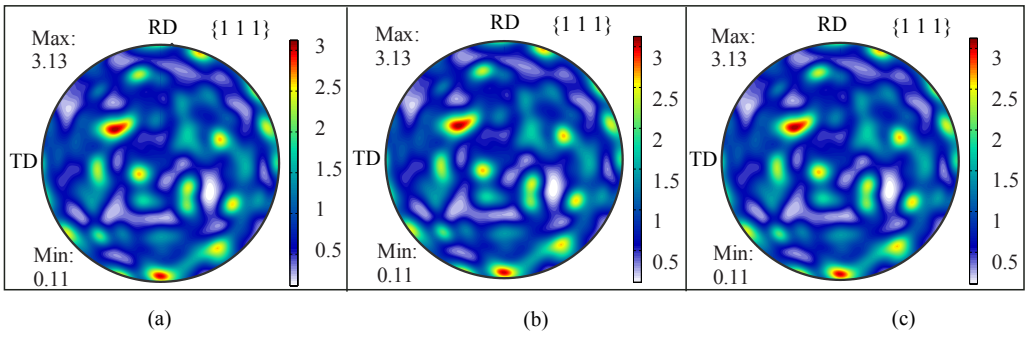

Figure 2.21: {1 1 1} pole figures of the first cycle: (a) beginning of hold; (b) middle of hold; (c) end of hold.

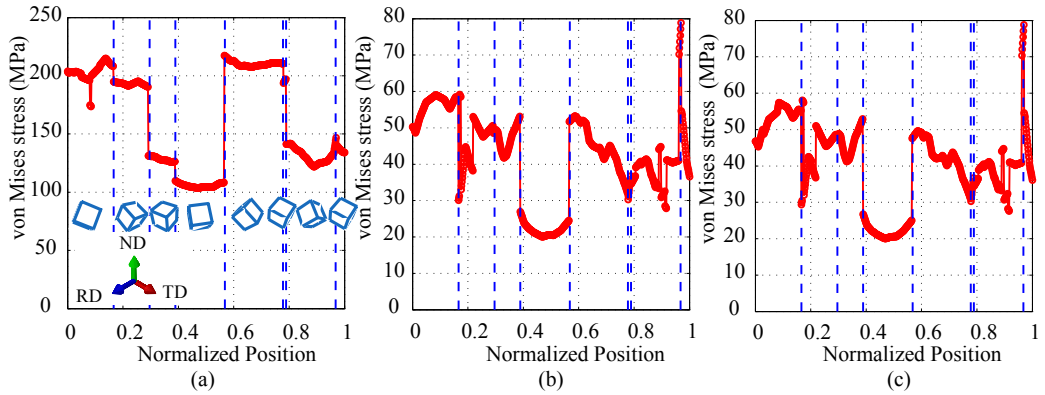

Figure 2.22: Von Mises stress along a line passing the center of the RVE along X direction of the first cycle: (a) beginning of hold; (b) middle of hold; (c) end of hold.

fatigue relaxation process. Within a given cycle, a more uniform stress distribution is observed between hard and soft grains at the end of strain hold compared to the beginning of hold. This is because stresses throughout the microstructure asymptotically reduce, due to the viscoplastic relaxation process under constant macroscopic strain. The simulations do not show a noticeably more uniform stress distribution as a function of cycles (i.e., from cycle 1 to 50 to 100). Furthermore, subgrain formation experimentally observed in creep-fatigue behavior of alloy 617 (see e.g., [24]) may be linked to the formation of persistent intragranular stress jumps and gradients.

2.4 Summary

This chapter presented the formulation, implementation and calibration of a CPFE model for nickel-based alloy IN 617 at high temperature. Model formulation, implementation and model parameters calibration are discussed in detail, and verification against a series of fatigue and creep-fatigue tests with different strain ranges and hold times are conducted. The proposed evolution equation for the slip resistance can well capture the stress drop in the first cycle of both fatigue and creep-fatigue tests, as well as the softening reemerging at every cycle after strain hold in the creep-fatigue tests.

Chapter 3

MICROSCALE MODELING OF CREEP DEFORMATION AND RUPTURE IN NICKEL-BASED SUPERALLOY IN 617 AT HIGH TEMPERATURE

In this chapter, the previously developed CPFE model that considers dislocation glide only is extended to incorporate a dislocation climb model originally proposed by Lebensohn and coworkers [93, 94] for capturing the viscoplastic deformation within the grains while grain boundary damage is modeled by CZM. The CPFE and the CZ models work in tandem to compute the viscoplastic deformation as well as progressive failure in the material microstructure 3.1. This extension is conduced in a collaborative manner by the author with Dr. Van-Tung Phan and Dr. Yumeng Li. The microstructure generation and automatic cohesive zone element insertion tool sets are developed by the author, incorporation of the dislocation climb mechanics is led by Dr. Van-Tung Phan with the author partially involved, the cohesive zone model development is mainly conducted by Dr. Van-Tung Phan and Dr. Yumeng Li. The final simulation and results analysis are completed by the author and Dr. Van-Tung Phan.

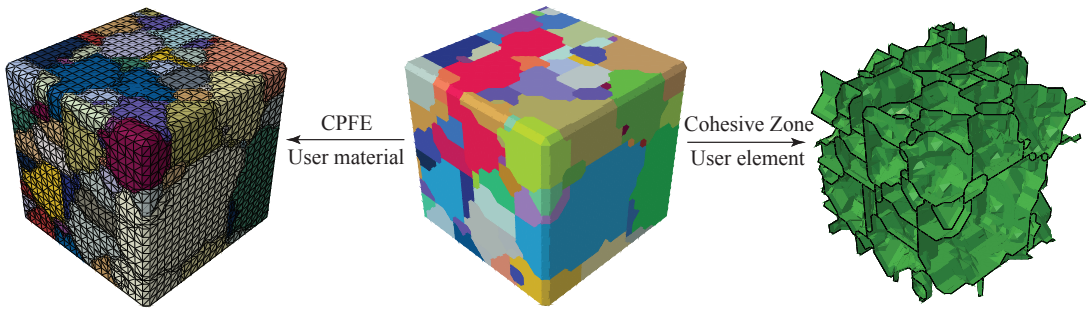

Figure 3.1: A combined CPFE and CZM framework for intergranular damage modeling: the microstructure (b) is discretized into: (a) volume mesh of the grains and (b) cohesive zone element of the grain boundary (c).

3.1 Dislocation Climb and Intergranular Damage in IN 617

Experimental studies by Benz et al. [15], Kim et al. [76, 79], Lillo and Wright [101], Lillo et al. [102], Martino et al. [110], Roy et al. [152], and Wright et al. [185] recently investigated the behavior of IN 617 subjected to creep loads at high temperatures under various levels of applied stresses. Experimental observations of microstructures using optical microscopy show significant atomic mobility and creep deformation even at relatively low stresses. As observed in experimental creep curves [14, 15, 76, 78, 152], a relatively short primary and secondary creep regime is followed by a long tertiary creep regime. In particular, a well-defined secondary creep was not observed. A rapid rise in creep rate caused by an increase in mobile dislocation density can reduce or exclude the secondary creep stage. This is known as sigmoidal creep behavior, and has been observed in Nickel-based alloys [173].

A primary mechanism for creep strains is dislocation climb resulting in a power law creep behavior of metals at high temperatures [128]. Prior experimental observations performed on creep deformation of IN 617 indicate that the minimum creep exponent typically lies between 5-7 within the 850-950°C temperature range [15, 79, 157]. This range indicates the presence of combined dislocation glide and climb [74], typically observed for class II alloys.

Dislocation climb that results from the interactions between dislocations and local non-equilibrium concentrations of point defects at high temperature contributes significantly to the irreversible deformation under creep loads [93, 94]. Therefore, it is necessary to include dislocation climb mechanism into a microstructure model to capture the viscoplastic deformation under high temperature loading conditions. Lebensohn et al. [93] extended their visco-plastic self-consistent (VPSC) formulation to consider coupled glide-climb mechanism and arrived at improved predictions of the behavior of olivine polycrystalline aggregates. Geers et al. [52] proposed an extended strain gradient crystal plasticity model by incorporating the effects of dislocation climb into the plastic strain evolution in the context

of strain gradient plasticity. The coupled glide-climb theory was verified through analysis of dislocation interactions in either bypassing of an elastic precipitate or destruction of dislocation pile-ups at the mesoscale. Huang et al. [67] investigated the influence of dislocation climb on the grain size dependent response and its underlying mechanisms. Other investigations (e.g., [57, 196]) employed discrete dislocation dynamics framework to study single crystal Ni-based superalloys. Vacancy diffusion-induced dislocation climb was found to be critical to describe the strain rate effect on the early plastic behavior of high-temperature and low-stress creep of Ni-based superalloys.

Post-mortem microstructural examinations by Kim et al. [76, 78] revealed that the creep damage and fracture in IN 617 is predominantly intergranular. Creep damage and ultimate rupture have been linked to the formation, growth and coalescence of grain boundary cavities, in addition to oxidation and other mechanisms. The recent experimental study by Tahir et al. [174] also confirms that damage caused by creep is of intergranular in nature.

While the incorporation of the dislocation climb allows modeling of the creep deformations accurately up to the onset of significant intergranular damage, it does not account for the progressive creep damage accumulation at grain boundaries. Cohesive zone modeling (CZM) originally proposed by Barenblatt [11] and Dugdale [39] is an effective approach to model progressive failure (e.g., [66, 72]), particularly in the presence of pre-defined paths of failure (e.g., intergranular fracture). In order to model the intergranular cracking at the microscale, cohesive elements with zero thickness are directly embedded between the adjacent grains to explore normal (i.e., mode I) and normal-and-shear (i.e., mixed mode) damage initiation. The proposed model in this chapter the CZM approach along with CPFE that includes glide-climb mechanisms in predicting the deformation as well as progressive damage accumulation in IN 617 subjected to creep loads.

Some recent numerical investigations employed combined CPFE-CZM approach to model damage behavior at individual grain boundaries in plastically deforming metals [27, 162, 163, 90]. Simonovski and Cizelj [162, 163] demonstrated the initiation and evolution

states of the intergranular cracking using cohesive zone in 3D polycrystalline aggregates for AISI 304 stainless steel. In the work of Kupka and coworkers [90] for an Aluminum-Lithium alloy, a fracture analysis is performed using cohesive zone modeling of the grain boundary, which allows for a mechanism independent description of the fracture process. Gonzalez et al. [53] adopted a CPFE model that embedded isotropic cohesive elements at grain boundaries to examine the effect of elevated grain boundary stresses on fracture behavior. While creep fracture phenomenon observed in experiments [9, 75] were numerically modeled by Onck and van der Giessen [130, 131] for a polycrystalline material at the microscale, a combination of CPFE and CZM has not been used, to the best of the authors' knowledge, in capturing creep deformation and simulating the formation and growth of cavities in polycrystalline aggregates.

3.2 A Coupled CPFE-CZM Framework for IN 617 at High Temperature

Using the virtual work principle, the sum of the strain energy in the domain and the cohesive fracture energy on the intergranular fracture surfaces are equal to the virtual work done by external traction along the boundary (ignoring body forces). The weak form of governing equilibrium equation is expressed as:

$$\int_{\Omega} \mathbf{S} : \delta\mathbf{E} d\Omega + \int_{\Gamma_{\mathrm{GB}}} \mathbf{T} : \delta[\![\mathbf{u}]\!] d\Gamma = \int_{\Gamma_{\mathrm{t}}} \hat{\mathbf{T}} \cdot \delta\mathbf{u} d\Gamma \tag{3.1}$$

in which, $\mathbf{S}$ is the second Piola Kirchhoff stress, $\mathbf{T}$ the tractions along the grain boundaries idealized as sharp interfaces and denoted as Γ_{GB}, and $\hat{\mathbf{T}}$ the prescribed tractions along the Neumann boundaries of the representative volume domain. $\delta\mathbf{u}$, $\delta\mathbf{E}$ and $\delta[\![\mathbf{u}]\!]$ denote the variations of the displacement, Green-Lagrange strain, and grain boundary displacement jump fields, respectively. In the present formulation, the weak form is closed by the stress-strain relationship within the grains and the traction-displacement jump relationship (i.e., cohesive law) across the grain boundaries.

3.2.1 Incorporation of dislocation climb mechanism

To incorporate the dislocation climb mechanism, the velocity gradient has contributions from both dislocation glide (indicated by subscript g) and climb (indicated by subscript c):

$$\begin{aligned} \widetilde{\mathbf{D}}^{\mathrm{p}} &= \widetilde{\mathbf{D}}^{\mathrm{p}}_{\mathrm{g}} + \widetilde{\mathbf{D}}^{\mathrm{p}}_{\mathrm{c}} \\ \widetilde{\mathbf{W}}^{\mathrm{p}} &= \widetilde{\mathbf{W}}^{\mathrm{p}}_{\mathrm{g}} + \widetilde{\mathbf{W}}^{\mathrm{p}}_{\mathrm{c}} \end{aligned} \tag{3.2}$$

The rate of deformation and spin contributions of dislocation climb are expressed as [93]:

$$\begin{aligned} \widetilde{\mathbf{D}}^{\mathrm{p}}_{\mathrm{c}} &= \mathbf{R}^{\mathrm{e}} \cdot \sum_{\alpha=1}^{N} \dot{\gamma}^{\alpha}_{\mathrm{c}} \left(\mathbf{m}^{\alpha}_{0} \otimes \chi^{\alpha}_{0} \right)_{\mathrm{S}} \cdot \mathbf{R}^{\mathrm{e}T} = \sum_{\alpha=1}^{N} \dot{\gamma}^{\alpha}_{\mathrm{c}} (\widetilde{\mathbf{K}}^{\alpha})_{\mathrm{S}} \\ \widetilde{\mathbf{W}}^{\mathrm{p}}_{\mathrm{c}} &= \mathbf{R}^{\mathrm{e}} \cdot \sum_{\alpha=1}^{N} \dot{\gamma}^{\alpha}_{\mathrm{c}} \left(\mathbf{m}^{\alpha}_{0} \otimes \chi^{\alpha}_{0} \right)_{\mathrm{A}} \cdot \mathbf{R}^{\mathrm{e}T} = \sum_{\alpha=1}^{N} \dot{\gamma}^{\alpha}_{\mathrm{c}} (\widetilde{\mathbf{K}}^{\alpha})_{\mathrm{A}} \end{aligned} \tag{3.3}$$

in which, $\dot{\gamma}^{\alpha}_{\mathrm{c}}$ is the shear strain rate as a result of dislocation climb. $\widetilde{\mathbf{K}}^{\alpha} = \widetilde{\mathbf{m}}^{\alpha} \otimes \widetilde{\boldsymbol{\chi}}^{\alpha}$ is the climb tensor associated with the slip system α in the crystal coordinate system [58, 93], and $\widetilde{\chi}^{\alpha}$ the unit vector parallel to the product of normal to the glide plane ($\tilde{\mathbf{n}}^{\alpha}$) and the tangent to the dislocation line ($\tilde{\mathbf{t}}^{\alpha}$) defined as:

$$\widetilde{\chi}^{\alpha} = \tilde{\mathbf{n}}^{\alpha} \times \tilde{\mathbf{t}}^{\alpha} \tag{3.4}$$

It is straightforward to see that the climb tensor depends on the dislocation orientation with respect to the glide coordinate system, and this dependence is expressed in terms of a single parameter ψ (i.e., the angle between $\tilde{\mathbf{t}}^{\alpha}$ and $\tilde{\mathbf{m}}^{\alpha}$).The climb tensor is then expressed as:

$$\widetilde{\mathbf{K}}^{\alpha} = [\widetilde{\mathbf{m}}^{\alpha} \otimes (\widetilde{\mathbf{m}}^{\alpha} \times \widetilde{\mathbf{n}}^{\alpha})] \cos\psi + (\widetilde{\mathbf{m}}^{\alpha} \otimes \widetilde{\mathbf{m}}^{\alpha}) \sin\psi \tag{3.5}$$

which resolves the applied shear stress into an individual climb system as $\tau^{\alpha}_{\mathrm{c}} = \tau : (\widetilde{\mathbf{K}}^{\alpha})_{\mathrm{dev}}$

and accumulates the climb strain based on a climb flow rule given by:

$$\dot{\gamma}_{\mathrm{c}}^{\alpha} = \dot{\gamma}_0 \exp\left(-\frac{F_0}{\kappa\theta}\right)\left(\frac{|\tau_{\mathrm{c}}^{\alpha} - B_{\mathrm{c}}^{\alpha}|}{\hat{\tau}_{0\mathrm{c}}}\right)^{p_{\mathrm{c}}} \mathrm{sgn}(\tau_{\mathrm{c}}^{\alpha} - B_{\mathrm{c}}^{\alpha}) \tag{3.6}$$

where $\dot{\gamma}_0$ denotes the reference shear strain rate, F_0 the activation energy, κ the Boltzmann constant and θ the temperature in Kelvin. $\hat{\tau}_{0\mathrm{c}}$ and p_{c} are the scalar threshold creep stress and the creep exponent, respectively. The evolution of backstress B_{c}^{α} is formulated through a saturation value, B_{∞}, related to the end of the primary creep stage as follows [169]:

$$\dot{B}_{\mathrm{c}}^{\alpha} = C_1\dot{\gamma}_{\mathrm{c}}^{\alpha} - C_2|\dot{\gamma}_{\mathrm{c}}^{\alpha}|B_{\mathrm{c}}^{\alpha} = h_{\mathrm{c}}(\dot{\gamma}_{\mathrm{c}}^{\alpha}B_{\infty} - |\dot{\gamma}_{\mathrm{c}}^{\alpha}|B_{\mathrm{c}}^{\alpha}) \tag{3.7}$$

where, h_{c} is a material parameter.

The numerical implementation of the glide and climb based constitutive model is a straightforward generalization of the glide-only model discussed earlier.

The incorporation of dislocation climb mechanism in Eqs. (3.2)-(3.7) allows the prediction of primary creep deformations. As observed in experimental creep curves of [76, 185], IN 617 does not exhibit a clear secondary creep stage. The extension of the present glide-climb model to capture secondary creep is possible and straightforward for evaluation of the creep response of other alloys that exhibit clear secondary creep.

3.2.2 Incorporation of grain boundary damage model

CZM is a computational approach to track propagation of distinct cracks, where fracture is considered as a gradual process of surface separation that takes place along an extended crack tip (or cohesive zone) resisted by cohesive tractions. Cohesive zone model is advantageous over other fracture mechanics based models, since it does not require the presence of pre-cracks. It can predict the behavior starting from an uncracked configuration, and performs well in the context of nonlinear material behavior. One significant caveat is that, unless coupled with adaptive meshing techniques, the direction of crack propagation is

prescribed by the underlying finite element discretization. The CZM approach is therefore particularly powerful in cases, where the path of crack propagation is known a-priori (e.g., cracking along grain boundaries).

The cohesive law is derived from a damage-based cohesive grain boundary potential defined by:

$$\phi = \frac{1}{2\delta_{\mathrm{c}}}\left(1-\omega_{\mathrm{n}}\right)k_{\mathrm{n}}[\![u_{\mathrm{n}}]\!]^2 + \frac{1}{2\delta_{\mathrm{s}}}\left(1-\omega_{\mathrm{s}}\right)k_{\mathrm{t}}\|[\![\mathbf{u}_{\mathrm{t}}]\!]\|^2 \tag{3.8}$$

where, $[\![u_{\mathrm{n}}]\!]$ and $[\![\mathbf{u}_{\mathrm{t}}]\!]$ denote the normal and tangential separation vectors, respectively, ω_{n} the interface damage induced by creep cavitation, ω_{s} the damage induced by grain boundary sliding, k_{n} and k_{t} are the initial stiffness along the normal and tangential directions, respectively, δ_{c} and δ_{s} are respectively the critical displacement jump in the normal and tangential directions at the point of complete separation when loaded monotonically:

$$\omega_{\mathrm{n}} = 1 \rightarrow [\![u_{\mathrm{n}}]\!] = \delta_{\mathrm{c}}; \quad \omega_{\mathrm{s}} = 1 \rightarrow \|[\![\mathbf{u}_{\mathrm{t}}]\!]\| = \delta_{\mathrm{s}}. \tag{3.9}$$

In order to idealize progressive creep failure, the cohesive law proposed by Bouvard et al. [18] is employed. The cohesive law is built by considering $\delta_{\mathrm{s}} = \delta_{\mathrm{c}}$, $k_{\mathrm{t}} = \alpha k_{\mathrm{n}}$, and:

$$\omega_{\mathrm{c}} := \omega_{\mathrm{n}} = \omega_{\mathrm{s}} \tag{3.10}$$

in which, ω_{c} denotes the creep damage variable. The potential function in Eq. (3.8) then becomes:

$$\phi = \frac{1}{2\delta_{\mathrm{c}}}(1-\omega_{\mathrm{c}})k_{\mathrm{n}}\left([\![u_{\mathrm{n}}]\!]^2 + \alpha\|[\![\mathbf{u}_{\mathrm{t}}]\!]\|^2\right). \tag{3.11}$$

The derivatives of the cohesive potential ϕ with respect to the normal and two tangential separations lead to the normal and shear tractions:

$$T_{\mathrm{n}} = \frac{\partial\phi}{\partial[\![u_{\mathrm{n}}]\!]} = k_{\mathrm{n}}(1-\omega_{\mathrm{c}})\frac{[\![u_{\mathrm{n}}]\!]}{\delta_{\mathrm{c}}} \tag{3.12}$$

$$\mathbf{T}_{\mathrm{t}} = \frac{\partial \phi}{\partial [\![\mathbf{u}_{\mathrm{t}}]\!]} = \alpha k_{\mathrm{n}} (1 - \omega_{\mathrm{c}}) \frac{[\![\mathbf{u}_{\mathrm{t}}]\!]}{\delta_{\mathrm{c}}}. \tag{3.13}$$

When subjected to compression, the normal traction is described as:

$$T_{\mathrm{n}} = k_{\mathrm{c}} \frac{[\![u_{\mathrm{n}}]\!]}{\delta_{\mathrm{c}}} \tag{3.14}$$

where, k_{c} is the penalty parameter. Equation (3.14) ensures that the impenetrability across the cohesive interface is satisfied under compressive loading condition through the penalty method. The magnitude of the penalty parameter is chosen as large as possible to limit interpenetration. Setting this parameter to extremely large values is known to result in numerical convergence difficulties.

Creep damage evolution is idealized using a power law in the following form [18]:

$$\dot{\omega}_{\mathrm{c}} = \frac{1}{(1 - \omega_{\mathrm{c}})^{p}} \left\langle \frac{||\mathbf{T}|| - T_{\mathrm{c}}}{C} \right\rangle^{r} \tag{3.15}$$

where T_{c}, C, p and r are model parameters defining the evolution of the creep damage. T_{c} denotes a threshold traction, above which creep damage accumulates. The norm of traction vector is defined by:

$$||\mathbf{T}|| := \sqrt{\langle T_{\mathrm{n}} \rangle^{2} + \frac{1}{\alpha} ||\mathbf{T}_{\mathrm{t}}||^{2}} \tag{3.16}$$

where $\langle \cdot \rangle = (|\cdot| + (\cdot))/2)$ denotes the Macaulay brackets, which eliminates the compressive grain boundary tractions from contributing to creep damage evolution.

The CZM model has been numerically implemented via a user defined element (UEL) subroutine in the commercial software Abaqus. At each increment of the nonlinear finite element analysis, the UEL is called at each cohesive zone element to solve the separation-traction equation, perform interface element level integration, and update the incremental local force vector and stiffness matrix. In order to evaluate the cohesive law and determine the creep damage state within the cohesive element, the creep damage variable ω_{c} of all Gauss points belonging to each cohesive zone element is solved at each time increment

through a Newton-Raphson method using a creep damage residual function obtained from the creep damage evolution in Eq. (3.15). At each time increment, the nodal displacement fields in the global coordinate system and the cohesive zone model parameters (k_n, α, T_c, δ_c, C, p and r) are considered as inputs while the local force vector and the stiffness matrix of each cohesive element are computed and passed back for the finite element assembly and solver operations. The detailed implementation of CZ elements are provided in Ref. [167].

3.3 Model Preparation

3.3.1 Automatic cohesive elements insertion into the polycrystal microstructure

The cohesive elements are embedded into the microstructure mesh using an automated element insertion methodology that defines the element connectivities for arbitrary 3-D microstructures.

The cohesive element incorporation procedure is implemented consistent with the microstructure morphology and surface mesh generation in DREAM.3D and the insertion process only adds cohesive zone element connectivity using grain boundary nodes, leaving the tetrahedral volume mesh of the grains intact. The surface mesh (triangular facets) of each grain either belongs to an external boundary of the representative volume or to the grain boundaries. Nodes on the surface mesh of each grain are assigned a unique node ID. A k-d tree based search process is then conducted to identify the cohesive node pairs (i.e., nodes sharing the same coordinates but belong to two different grains) and subsequently the cohesive face pairs (i.e., two triangle facets formed by three pairs of cohesive node pairs belonging to two different grains) of each grain boundary facet. Each cohesive face pair is used to define a zero-thickness cohesive zone element.

To guarantee the correct calculation of separation and traction, and a positive element Jacobian within the cohesive element, a set of consistent cohesive zone element connectiv-

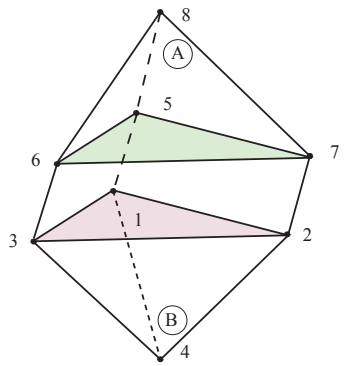

Figure 3.2: Configuration of the cohesive zone element. Thickness is exaggerated to be nonzero for illustration purpose.

ity construction rules as illustrated in Fig. 3.2 is defined as follows:

1. One cohesive zone element is inserted between two adjacent bulk elements that belong to two different adjacent grains. As illustrated in Fig. 3.2, element A and B belong to two different grains with node pairs 6-3, 5-1 and 7-2 being three cohesive node pairs and the red and green faces being a cohesive face pair. A cohesive zone element is inserted between element A and B using nodes 5, 6, 7, 1, 2 and 3.

2. Element connectivity starts from any node that belongs to one of the two cohesive face pairs, loops over all nodes belong to that face and then nodes on the other face. We ensure that the ordering of nodes of the face of the first grain (starting from the chosen node), and the opposing face are identical. For instance, starting from node 1 of grain B, either 1-2-3-5-7-6 or 1-3-2-5-6-7 are the two possible connectivities.

3. The normal direction for the starting grain face using the right-hand rule is taken to point to the opposing grain. For instance, the first element connectivity 1-2-3-5-7-6 yields the normal direction of face 1-2-3 pointing away from the second grain while the second element connectivity 1-3-2-5-6-7 has the normal direction of face 1-3-2 pointing to the second grain. The latter is therefore the valid cohesive element connectivity.

The three rules mentioned above provide a consistent cohesive element connectivity definition methodology. Using this procedure, 22,430 cohesive elements are inserted into the above 144-grain RVE to discretize the grain boundaries, which together with the 133,372 tetrahedral elements form the full discretization of the microstructure.

3.3.2 Model calibration

The parameters of the model associated with the intragranular deformation mechanisms, as well as the intergranular creep damage are calibrated based on experimental data. Model parameters related to the dislocation glide in IN 617 at 950°C have been previously calibrated in chapter 2 and employed as is in this study. Table 1 includes the calibrated parameters that control the dislocation glide. In what follows, the calibration of model parameters related to the dislocation climb and the cohesive grain boundary behavior is discussed. In order to facilitate the calibration process, we first isolate the effects of the dislocation climb parameters by focusing on creep deformation prior to the onset of significant grain boundary damage. The cohesive zone parameters are subsequently calibrated by focusing on creep deformation after grain boundary damage initiation until rupture. Creep tests on IN 617 specimens conducted at Idaho and Argonne National Labs (INL and ANL) have been used to calibrate these parameters [185]. In particular, creep behavior at two applied stress amplitudes of 28.6 and 24 MPa at 950°C are used for calibration.

It is important to note that the number of parameters that describe dislocation climb as well as intergranular damage is high (i.e., 12 parameters). In contrast, only a small number of detailed experiments are available, primarily at the bulk scale. In view of limited calibration data, we rely on: (1) use of previously published data to establish values for some of the parameters and discard them from the calibration set; (2) perform least squares optimization to identify the parameters by minimizing the discrepancy between the experimental and simulated behavior; and (3) ensure that the values of the parameters are within physically meaningful ranges. The third step is necessary, since multiple local minima may

result from the optimization process.

3.3.3 Calibration of dislocation climb parameters

The dislocation climb parameters including the orientation of dislocation climb ψ, the creep exponential parameter p_c, the threshold stress $\hat{\tau}_{0c}$, the saturation stress B_∞ and the primary creep saturation parameter h_c as represented in Eqs. (3.5), (3.6) and (3.7) have been identified. We only focus on the creep-deformation prior to the onset of tertiary creep, where progressive grain boundary damage accumulation using cohesive zone modeling is not included in this calibration step. The calibration process starts with a parametric

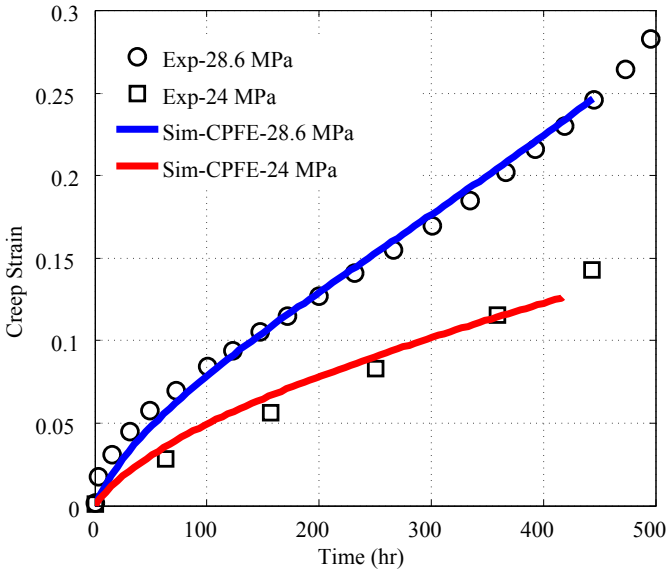

Figure 3.3: Calibrated results of the creep tests to capture the primary creep at two different stress levels.

study to investigate the sensitivity of each parameter in order to identify the ranges for each parameter, where the optimization will be performed. In view of the computational complexity of performing many forward simulations using the CPFE model within an optimization framework, we first performed the optimizations based on Taylor's hypothesis [176] to quickly arrive at a set of parameters that provide an acceptable match for the two calibration tests. The identified parameters are further fine-tuned by performing full CPFE

Table 3.1: Dislocation climb parameters.

$\psi(^\circ)$	p_c	$\hat{\tau}_{0c}$(Pa)	h_c	B_∞(MPa)
$\pi/4$	3	7,750	32	4.7

simulations. The creep exponent value is set to be $p_c = 3$ according to the creep strains controlled mainly by climb at high temperatures [128]. It is difficult to determine experimentally the angle ψ, i.e., the average edge/screw ratio since it is related to the measurement of dislocation motion in each slip system during creep deformation process. Therefore, the angle is assumed to be $\pi/4$ that corresponds to a length equal of edge and screw dislocation lines in each face-centered cubic slip system [19, 93]. The remaining parameters are calibrated by minimizing the discrepancy between the experimental and simulated creep curves in the primary stage. The set of parameters that results from the above-mentioned calibration process is shown in Table 3.1.

The comparisons between simulated creep curves using the calibrated parameters and experimental creep curves for the two different stress levels are shown in Fig. 3.3. It can be seen that a reasonable match is achieved between the simulated and experimentally observed creep strain evolution as a function of time prior to the onset of grain boundary damage. The yield strength of the material at 950°C is approximately 150 MPa and the applied creep stress amplitudes are substantially lower than yield. We note that in the absence of the climb mechanism, CPFE simulations with only the glide do not show any appreciable creep at stress magnitudes lower than yield. The climb mechanism is therefore primarily responsible for creep strain accumulation at low stress levels. .

3.3.4 Calibration of cohesive zone model parameters

The combined CPFE-CZM is employed to capture the creep damage behavior at grain boundaries in the tertiary stage. Two of the cohesive zone parameters (k_n and α) correspond to the elastic behavior of the interface. k_n and α are chosen large enough such that

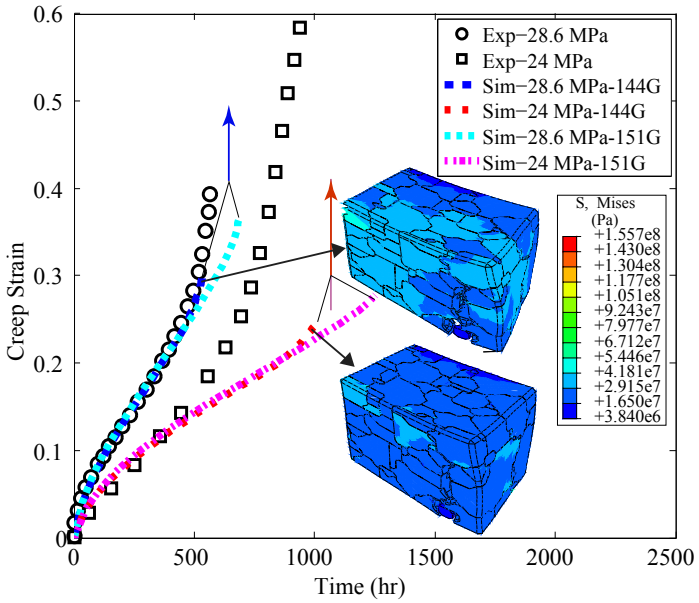

Figure 3.4: Calibrated results of the creep tests in both primary and tertiary stages for two different stress levels. Dotted lines indicate the presence of GB damage.

no significant separation is observed under normal or shear loading in the absence of damage, while keeping the numerical stability in the simulations. k_{n} ($= 10^5$ GPa) is identified through a parameter sensitivity analysis. A lower amplitude of k_n results in softening in the elastic region of the stress-strain curves. α is chosen as 0.5 consistent with the prior studies on Nickel alloy microstructures (e.g., [172]). The penalty parameter is taken as $k_{\mathrm{c}} = 10k_{\mathrm{n}}$ [18] in the numerical simulations to constrain against granular interpenetration. Friction is not considered along the grain boundaries following decohesion.

Table 3.2: Calibrated parameters of the cohesive zone model.

α	k_{n}(Pa)	$\delta_{\mathrm{c}}(\mu\mathrm{m})$	r	p	C(Pa)	T_{c}(Pa)
0.5	10^{14}	450	2.6	3	4.87×10^{10}	8.5×10^{6}

The remainder of the model parameters for the CZM model is calibrated by minimizing the discrepancy between the experimental and simulated creep curves in the tertiary stage. The intrinsic length parameter δ_{c} is identified as 450 μm which lies within the range provided by Bouvard et al. [18] and Sun et al. [172]. The threshold traction T_{c} corresponding

to creep strength is assumed to be 8.5 MPa. The exponent p is 3 consistent with that provided in Ref. [172]. The complete set of calibrated CZM parameters is shown in Table 3.2.

Figure 3.4 shows the comparison between the numerically simulated and experimental creep curves, where two microstructures (the 144-grain and a 151-grain with identical morphological statistics) are considered. The reasonable match between the experimental and simulated curves indicates that CPFE-CZM model can capture the progressive damage evolution and rupture in the specimens at two stress levels. The experimentally observed rupture times for specimens subjected to 24 MPa and 28.6 MPa are 940 and 566 hours, respectively. The simulated rupture times for the two cases are 1010 and 540 hours, respectively with the 144-grain microstructure. Similarly, the corresponding rupture times predicted by the 151-grain simulation are 1,249 and 690 hours, respectively. Rupture is determined when the intergranular separations are fully developed, and when the simulations lose stability under the applied stress amplitude.

The creep damage evolution in the tertiary stage for the specimen subjected to 28.6 MPa has been captured well, whereas the simulated creep strain evolution underpredicts strain rate at the tertiary stage for the 24 MPa case. The simulations also predict a more sudden rupture compared to the experiments.

3.4 Microstructural Analysis

We investigate the state of stress and damage within the microstructure at various creep strain levels to understand the initiation and evolution of grain boundary damage. Figure 3.5 compares the microstructural stress distributions obtained by CPFE-CZM simulation and glide-climb controlled CPFE simulation (without grain boundary damage) at 12% and 19% creep strains under the applied stress of 28.6 MPa. The stress distributions are very similar between the two models at the strain level of 12%, indicating that there is negligible cavitation and/or sliding at the grain boundaries. This observation is consistent with

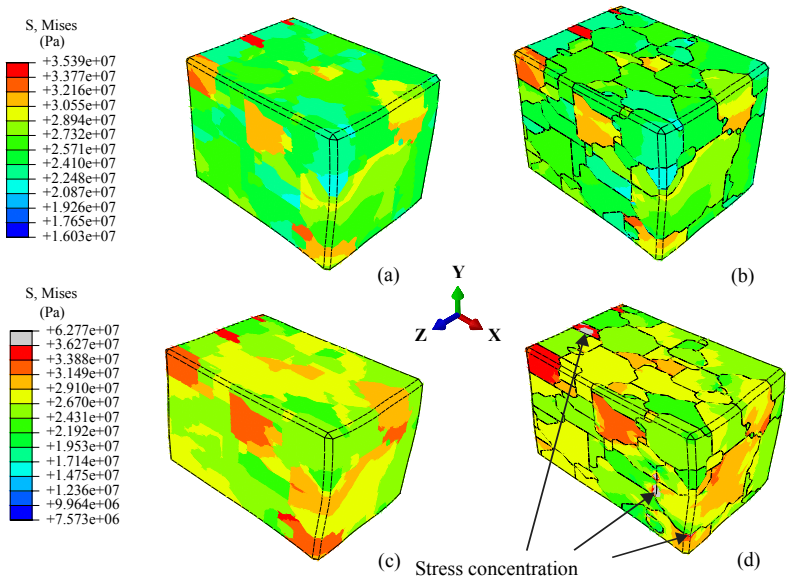

Figure 3.5: Comparison of stress distribution in the microstructure under 28.6 MPa loading. The CPFE (left) and the CPFE-CZM (right): (a-b) 12% and (c-d) 19% of creep strain at 180 and 347 hours, respectively.

experimental investigations on the microstructures of crept IN 617 specimens, which did not show appreciable grain boundary cavitation prior to approximately 12% strain levels as discussed in Ref. [102]. At 19% creep strain, significant grain boundary damage is observed in the CPFE-CZM simulation that results in the formation of stress concentrations shown in Fig. 3.5(d). The stress concentrations in turn accelerate further damage propagation. This behavior is consistent with the observations in the literature [161, 202] on the nucleation of grain boundary cavities for metals and superalloys. Figure 3.6(a)-(b) displays the further growth of grain boundary damage at 25% and 30% creep strains modeled using the CPFE-CZM simulation. The cut views in Fig. 3.6(c)-(d) show the deformation and grain boundary damage in the interior of the microstructure. The stress levels and the grain boundary separations in the interior of the domain are of similar order of magnitude compared with those observed at the exterior of the microstructure. The figure indicates that the separation initiates at the grain boundary and continues to grow until rupture. The extent and magnitude of separation at the strain level of 30% are very significant, which

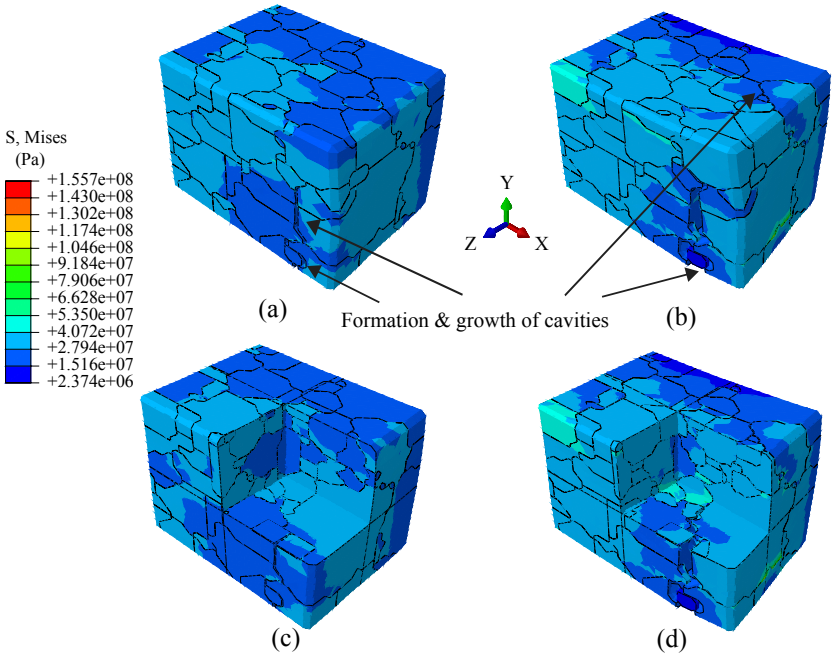

Figure 3.6: Stress distribution in the microstructure applied by 28.6 MPa loading using the CPFE-CZM: (a) 25% and (b) 30% of creep strain at 472 and 540 hours, respectively; (c) and (d) cut views of (a) and (b).

causes an acceleration of the creep strain rate and immediate rupture in the simulation.

Creep deformation causes significant rotations and grain breakup within the microstructure, particularly near fracture point as shown in Fig. 3.6. The rotations and grain separations are primarily caused by cavitation, with a relative minor role of sliding (further discussed below). Local rotations and the breakup of grains increase the stress concentrations near the grain boundaries, which further accelerate cavitation as deformation progresses.

Figure 3.7 shows the deformation of the RVE at the time when the cracks shown in Fig. 3.6 initiate. All cracks initiate at triple junctions, where three or more grains adjoin each other. Furthermore, cracks initiate at the grain boundaries perpendicular to the loading direction (e.g., between grains 93 and 98, 105 and 42, 136 and 42, 136 and 95, 43 and 10, 43 and 42, 29 and 26, 80 and 122 and grains 5 and 122) and later propagate to the boundaries nearby (e.g., between grains 105 and 136 and grains 80 and 5). The misorientations of the grain boundary crack initiation sites in Fig. 3.7 are calculated in Table 3.3 using the

Table 3.3: Orientations (Bunge's convention) and misorientations of grains along the crack initiation sites.

ID of grain A	ID of grain B	Misorientation (degree)
93	98	53.26
105	42	28.78
136	42	36.49
136	95	21.09
43	10	41.83
43	42	45.42
29	26	39.49
80	122	47.37
5	122	60.91

expression in Eq. 2.30.The histogram of misorientations of all grain boundaries within the microstructure are shown in Fig. 3.8. The misorientations on the damage initiation sites are relatively large as shown in Table 3.3.

In order to illustrate damage nucleation and evolution, the creep damage variable ω_c is plotted along all grain boundaries as shown in Fig. 3.9 for various states of creep strain. The grain boundary damage initiates at around 12% creep strain state as shown in Fig. 3.9(a). The growth of damage progresses fairly uniformly across the microstructure (Fig. 3.9(b)) until approximately 25% creep strain, after which damage localizes to a grain boundary that is perpendicular to the load direction (lower left corner in Fig. 3.9(c)). Near the point of rupture (Fig. 3.9(d)) the intergranular crack has propagated significantly. Figure 3.10 further demonstrates the state of intergranular damage from different viewpoints near the rupture time.

Previous investigations generally relied on the assumption that damage predominantly resides on the grain boundaries oriented perpendicular to the loading direction [91]. Considering the applied stress of 28.6 MPa, Figs. 3.11-3.13 illustrate the progressive damage accumulation as a function of creep strain for three different grain boundary orientations. The grain boundary orientation is characterized by the parameter, ϕ, which is the angle between the normal to a cohesive element and the loading direction. In each figure, the evolution of the normalized area fraction of all cohesive elements with angle ϕ are plot-

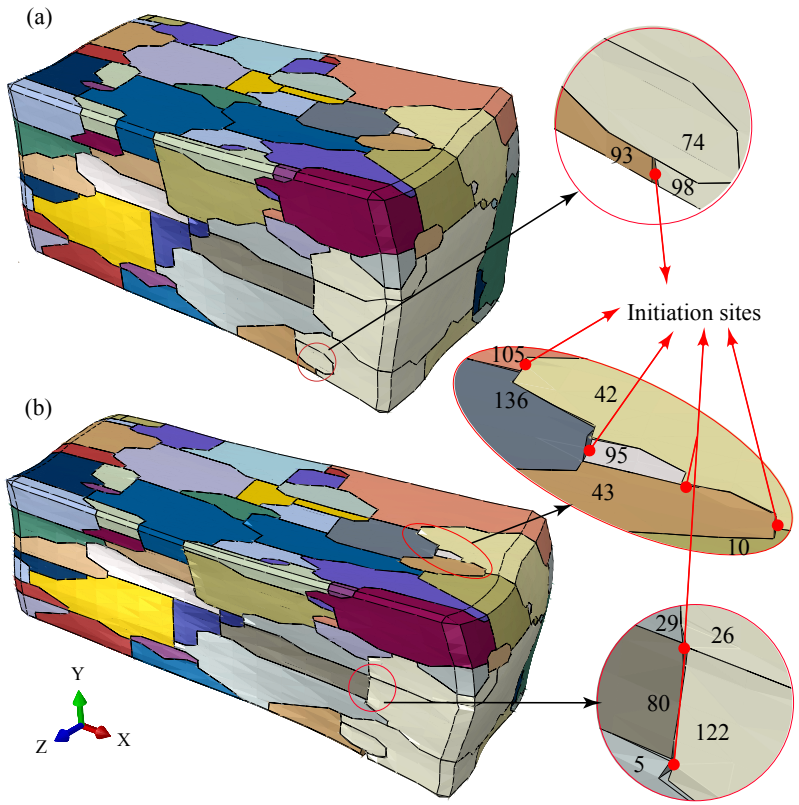

Figure 3.7: Crack initiation sites at: (a) t=220 h and; (b) 355 h. (Different colors indicate different grains with black lines indicating grain boundaries. Numbers indicate grain IDs. Deformation is exaggerated by a factor of 5.)

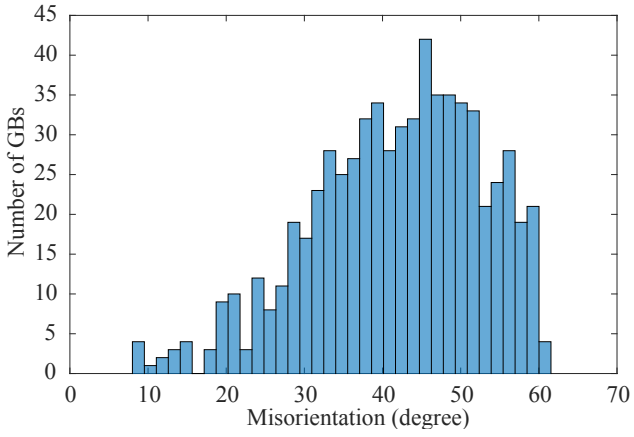

Figure 3.8: Misorientation of all the grain boundaries in the RVE.

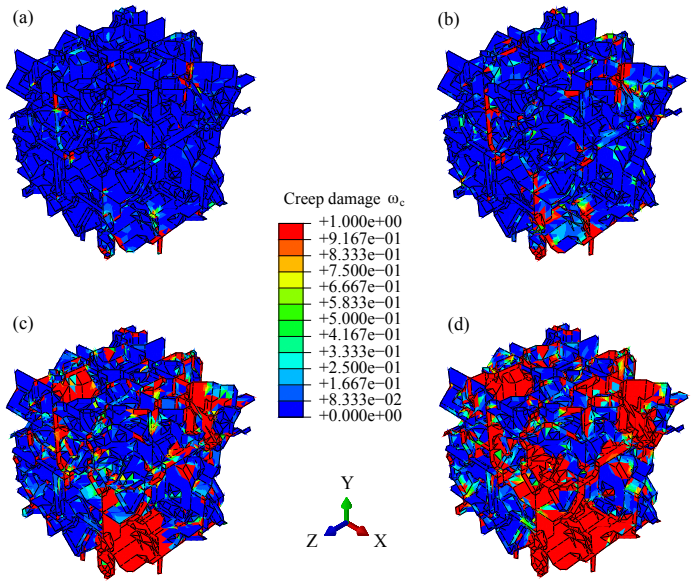

Figure 3.9: Creep damage evolution represented by cohesive elements in the microstructure under 28.6 MPa loading: (a) 12%, (b) 19%, (c) 25%, and (d) 30% of creep strain at 180, 347, 472 and 540 hours, respectively.

ted. $\phi = 0^\circ$ indicates that the cohesive elements are perpendicular to the loading direction, whereas, $\phi = 90^\circ$ indicates the cohesive elements are parallel to the loading direction and primarily undergoes sliding. At early stages of the creep process (5%, 12% and 19% of strain), grain boundaries show little damage for all three orientations. As the creep strain increases, more of the grain boundaries incur damage leading to a higher area fraction of grain boundaries with more damage. Two observations are made: First, a large majority of the cohesive zone elements either display no significant damage or complete failure. This implies a sudden damage accumulation process at the local scale. Second, despite the fact that the grain boundaries perpendicular to the loading direction show a much greater extent of damage, those with different orientations and notably those parallel to the loading direction, also display damage. This indicates the possible presence and role of grain boundary sliding in addition to cavity growth.

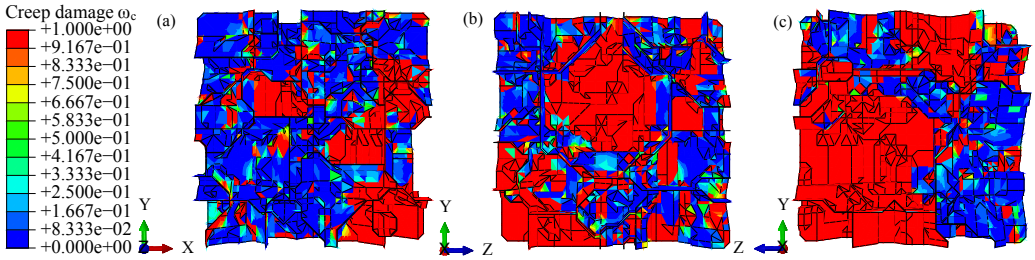

Figure 3.10: Creep damage contour of the microstructure under 28.6 MPa loading at 30% of creep strain: (a) Front view, (b) Left view, and (c) Right view.

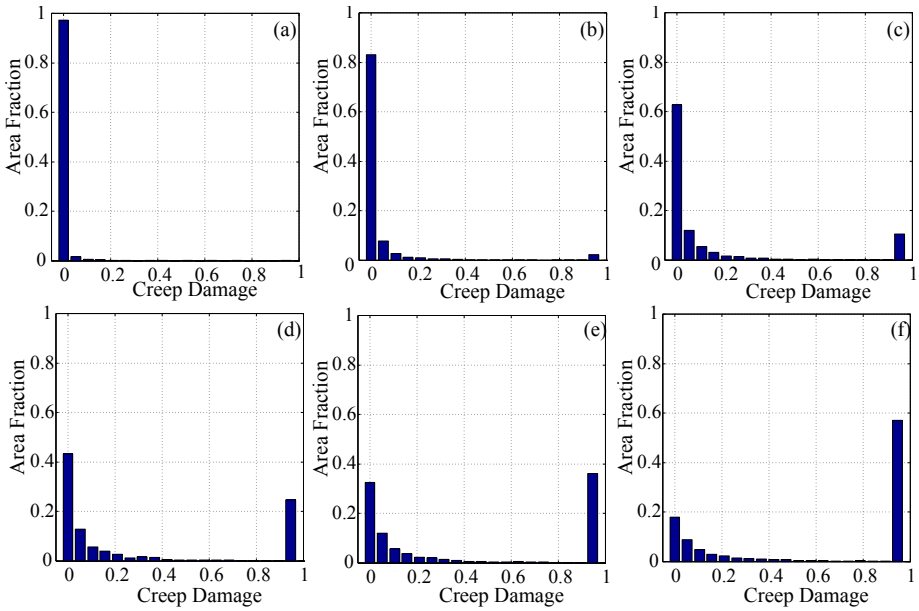

Figure 3.11: Creep damage distribution of cohesive elements with their normal direction parallel to the creep stress axis ($\phi = 0°$): (a) 8%, (b) 12%, (c) 19%, (d) 22.4%, (e) 25%, and (f) 30% of creep strain.

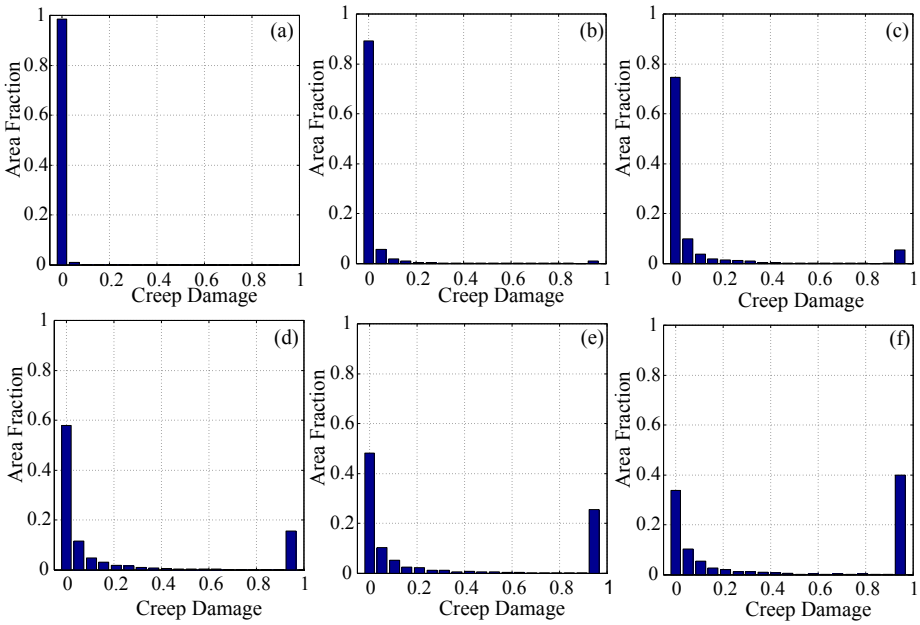

Figure 3.12: Creep damage distribution of cohesive elements with the angle $\phi = 45^\circ$ between their normal direction and the creep stress axis: (a) 8%, (b) 12%, (c) 19%, (d) 22.4%, (e) 25%, and (f) 30% of creep strain.

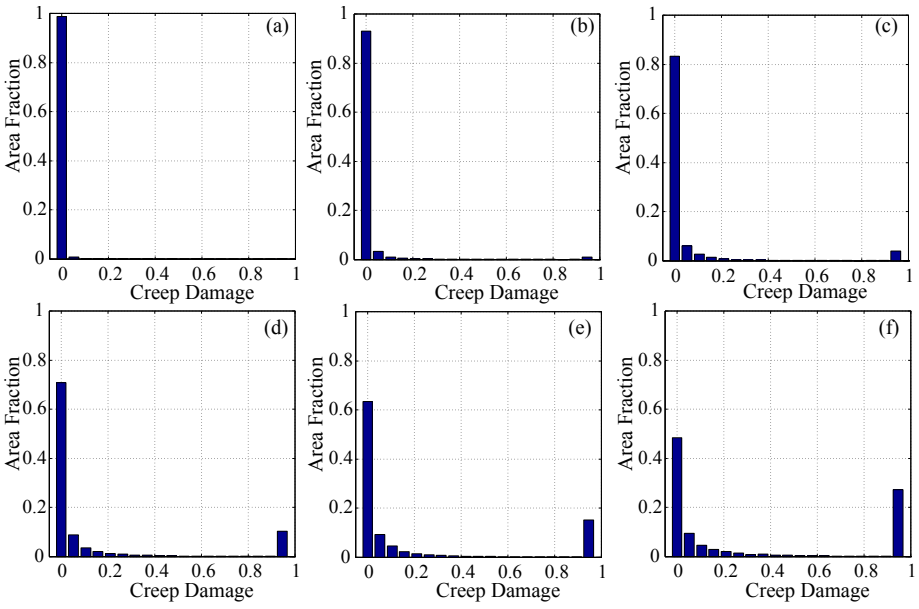

Figure 3.13: Creep damage distribution of cohesive elements with their normal direction perpendicular to the creep stress axis ($\phi = 90^\circ$): (a) 8%, (b) 12%, (c) 19%, (d) 22.4%, (e) 25%, and (f) 30% of creep strain.

3.4.1 Validation of creep strength predictions

In order to further validate the predictive capability of the proposed model against available experimental data, creep rupture times are computed for various stress levels at 950°C. Several numerical calculations with different applied stress amplitudes (i.e., at 18.5 MPa, 24 MPa, 28.6 MPa, 35 MPa, 42 MPa, 52 MPa, 62.55 MPa, 68 MPa and 91 MPa) are performed using several microstructures with identical morphological statistics including the 144-grain case. All experimental and simulated data are plotted together as logarithmic stress versus the Larson-Miller parameter (LMP) [92]. The simulation results are plotted as the mean and variance of the predicted values from several microstructure simulations. The basic equation of the LMP [92] is given by

$$\mathrm{LMP} = T[\log(t) + P] \tag{3.17}$$

where T is the absolute temperature in Kelvin, t is the rupture time in hours, and the constant parameter P is taken as 20. Figure 3.14 shows the comparison between the experimental and predicted creep rupture data at different stress levels at 950°C. The ANL experiments are the rupture data used in the preceding calibration and microstructure analysis (24 MPa and 28.6 MPa), whereas Kim et al. [79] provides the creep rupture data collected from literature for several different stress levels. The mean and variance of the predicted stress rupture times are in reasonable agreement with the experimental data. The predicted rupture data of high stress levels (e.g., 68 MPa and 91 MPa) show a slightly shorter life than the experimental rupture life. A slightly longer rupture life is identified for the stress levels lower than 35 MPa. Some of the discrepancies between the predicted and experimental rupture lives are attributed to the variability in the experiments, possibly due to material processing differences in experiments as they were performed independently. We note that the predictive capability of the proposed microstructural model could be further validated with direct microstructural observations, when such data becomes available.

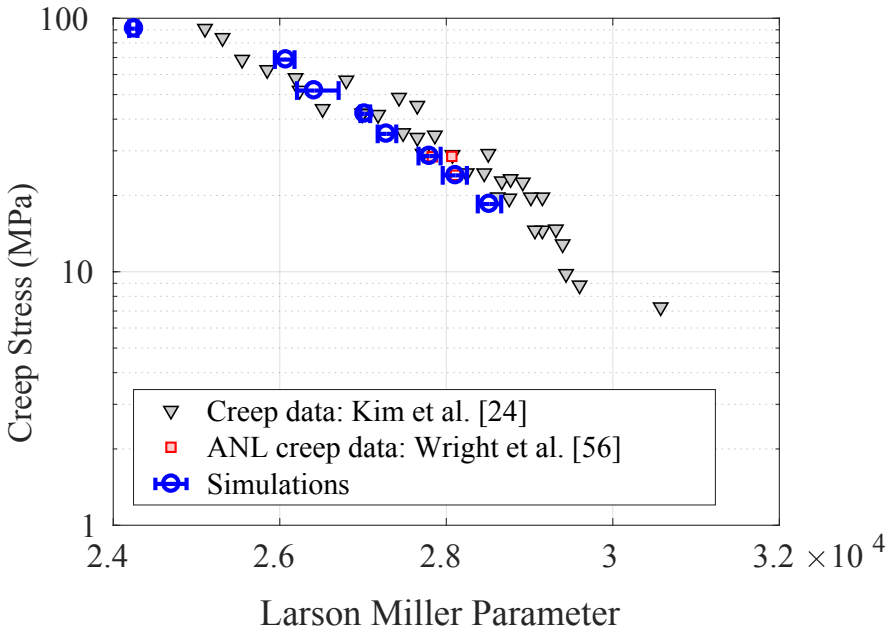

Figure 3.14: Larson-Miller plot: comparison between simulated results and experimental creep data obtained from ANL creep tests and data from literature.

3.5 Summary

In this chapter, we presented extension of the CPFE model in Chapter 2 into a coupled CPFE-CZM modeling framework for creep rupture modeling of IN 617 at high temperature. The proposed model considers the deformation mechanisms of dislocation climb and glide within the grains, along with grain boundary damage. The proposed model accurately captures the creep strain evolution and rupture in IN 617, and provides insight into the microscale stress, grain boundary damage distribution and their evolution. A good agreement is obtained between the experimental creep rupture data and corresponding simulations at several applied stress amplitudes. This illustrates the predictive capability of the proposed model.

Chapter 4

EIGENSTRAIN-BASED REDUCED ORDER HOMOGENIZATION FOR POLYCRYSTAL PLASTICITY

This chapter presents a reduced order homogenization model for polycrystalline materials by extending the eigendeformation-based reduced order homogenization technique to polycrystal plasticity modeling. The proposed model is based on the eigendeformation-based reduced order homogenization approach previously proposed by Oskay and coworkers [134, 198] to study composite materials. A two-scale asymptotic analysis is used to decompose the original equations of polycrystal plasticity into micro- and macroscale problems. Eigenstrain based representation of the inelastic response field is employed to approximate the microscale boundary value problem using an approximation basis of much smaller order. The proposed approach was implemented and its performance was assessed against crystal plasticity finite element simulations. Numerical studies point to the capability to efficiently compute the mechanical response of the polycrystal RVEs with good accuracy and the ability to capture stress risers near grain boundaries. The present model proposed in the chapter presents the following novel contributions: (1) The grain-to-grain interactions are accurately captured through the use of numerical influence functions that directly account for the material microstructure morphology. The use of numerical influence functions (as opposed to those generated through the Eshelby tensor) provides a more accurate distribution of the local stress and strain fields within the microstructure and captures the local variations of the response fields. (2) The modelling approach is enhanced with hierarchical model improvement capability that allows capturing the subgrain stress and deformation states. This information, e.g., elevated stress at grain boundaries may be critical for assessment of fatigue damage initiation. The hierarchical model improvement capability refers to the ability to refine or coarsen the partitioning of the microstructure

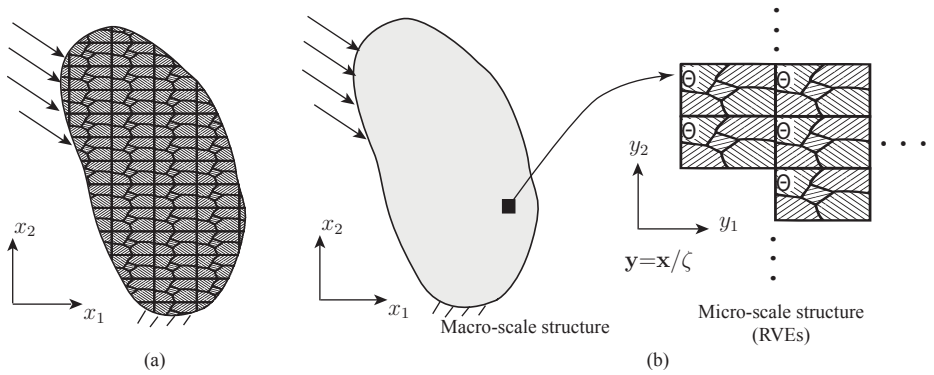

Figure 4.1: A two-scale problem: macro- and microscale structures.

(i.e., increase or decrease the model order in the ROM) to control the accuracy and efficiency characteristics of the reduced order model. The primary reason for choosing the eigenstrain-based model order reduction approach is that, in a straightforward fashion, it allows capturing the grain-to-grain interactions as well as providing the ability to improve the model prediction through its hierarchical structure as explained below.

4.1 Problem Statement

Let $\Omega \subset \mathbb{R}^{n_{sd}}$ denote an open bounded domain occupied by a polycrystalline material as schematically illustrated in Fig. 4.1(a). n_{sd} is the number of space dimensions. The domain is formed by the repetition of a locally periodic, statistically representative volume element (RVE). The material heterogeneity is due to the possible presence of different material phases, constituents, as well as different orientations of grains with otherwise identical molecular composition. The governing equilibrium, stress-strain and kinematic equations that describe the deformation of the polycrystalline domain when subjected to mechanical loading is expressed as ($\mathbf{x} \in \Omega$):

$$\sigma^{\zeta}_{ij,j}(\mathbf{x},t) + b^{\zeta}_{i}(\mathbf{x},t) = 0 \tag{4.1}$$

$$\sigma^{\zeta}_{ij}(\mathbf{x},t) = L^{\zeta}_{ijkl}(\mathbf{x})(\varepsilon^{\zeta}_{kl}(\mathbf{x},t) - \mu^{\zeta}_{kl}(\mathbf{x},t)) \tag{4.2}$$

$$\varepsilon_{ij}^{\zeta}(\mathbf{x},t) = u_{(i,j)}^{\zeta}(\mathbf{x},t) \equiv \frac{1}{2}(u_{i,j}^{\zeta} + u_{j,i}^{\zeta}) \tag{4.3}$$

in which, $\boldsymbol{\sigma}^{\zeta}$ denotes the Cauchy stress, $\mathbf{b}^{\zeta}$ the body force per unit volume, $\mathbf{L}^{\zeta}$ the tensor of elastic moduli, $\mathbf{u}^{\zeta}$ the displacement and ε^{ζ} the total strain that can be additively decomposed into the elastic and viscoplastic ($\boldsymbol{\mu}^{\zeta}$) contributions. A comma in the subscript indicates partial spatial derivative and the superscript ζ indicates the oscillatory behavior of the response field due to the microstructural heterogeneity. $\mathbf{x}$ denotes the position vector and t denotes time. The time dependence of the formulation indicates that the viscous behavior of the material is included. While the inertia term is omitted in Eq. (4.1) for simplicity, the ensuing formulation is also valid for the dynamic response of the polycrystal at the"long" wavelength regime (i.e., when the wavelengths are much longer than the size of the RVE).

It is typical for polycrystalline materials to experience large deformation at the microstructure scale where individual grains significantly deform and rotate, causing texture evolution as a function of applied loads. Large deformation crystal plasticity formulations that capture such texture evolution behavior are readily available (e.g., [138, 109]). The current multiscale formulation is limited to cases in which elastic and inelastic deformations remain small as implicitly implied by Eqs. (4.2)-(4.3). By this assumption, the texture remains static during the deformation process and texture evolution is not considered.

Considering the inelastic deformation within a grain is a consequence of dislocation glide induced crystallographic slip along preferred slip orientations, the inelastic strain rate at a material point within a single grain is expressed as:

$$\dot{\mu}_{ij}^{\zeta} = \sum_{s=1}^{N} \dot{\gamma}^{s,\zeta} Z_{ij}^{s,\zeta} \tag{4.4}$$

where, $\dot{\gamma}^{s,\zeta}$ is the plastic shearing rate on the s^{th} slip system, N the total number of slip systems, $\mathbf{Z}^{s,\zeta}$ is the Schmid tensor uniquely describing the orientation of the s^{th} slip system as the dyadic product of the slip direction, $\mathbf{n}^{s,\zeta}$, and the normal to the slip plane $\mathbf{m}^{s,\zeta}$, (i.e.,

$Z_{ij}^{s,\zeta} = n_i^{s,\zeta} m_j^{s,\zeta}$). The resolved shear stress on a slip system, $\tau^{s,\zeta}$, is computed from the stress tensor using the Schmid tensor as well:

$$\tau^{s,\zeta} = \sigma_{ij}^{\zeta} Z_{ij}^{s,\zeta} \tag{4.5}$$

The shear strain rate is generally formulated by a flow rule as a function of the resolved shear stress and the slip system strength, $g^{s,\zeta}$ [150]:

$$\dot{\gamma}^{s,\zeta} = \dot{\gamma}^{s,\zeta}(\tau^{s,\zeta}, g^{s,\zeta}) \tag{4.6}$$

and the evolution of the slip system strength is described by a hardening rule as a function of the shear strain rate and the strength of all the slip systems:

$$\dot{g}^{s,\zeta} = \dot{g}^{s,\zeta}(g^{1,\zeta}, g^{2,\zeta}, ..., g^{N,\zeta}, \dot{\gamma}^{1,\zeta}, \dot{\gamma}^{2,\zeta}, ..., , \dot{\gamma}^{N,\zeta}) \tag{4.7}$$

which indicates that hardening along a slip system is affected not only by the state on the slip system itself (self-hardening) but all others as well (latent hardening). A number of strength and slip evolution models that specify Eqs. (4.6) and (4.7) has been proposed in the literature (see [150] for a comprehensive review). While the reduced order modeling methodology developed in this dissertation does not depend on the particular forms of the evolution equations of the slip or slip system strength, it is beneficial to demonstrate the formulation in the context of a particular form. Using other hardening laws is straightforward and follows the general steps to be described below. Incorporation of some other mechanisms such as twinning [84], which may involve significant texture evolution, violates the small deformation assumption made in the present formulation. Twinning is therefore not considered. In this dissertation, we choose a frequently used flow rule suggested by Rice

and Peirce [148, 137, 138] for face-centered cubic (FCC) crystals:

$$\dot{\gamma}^{s,\zeta} = \dot{\gamma}_0 \left(\frac{\left| \tau^{s,\zeta} \right|}{g^{s,\zeta}} \right)^{1/m} \operatorname{sgn}(\tau^{s,\zeta}) \tag{4.8}$$

where, $\dot{\gamma}_0$ is the reference shear strain rate, m the rate sensitivity parameter. The strength of each slip system is taken to evolve following the hardening rule proposed by Anand [6]:

$$\dot{g}^{s,\zeta} = h_0 \left(\frac{g_{sa}^{s,\zeta} - g^{s,\zeta}}{g_{sa}^{s,\zeta} - g_0^{s,\zeta}} \right) \sum_{s=1}^{N} |\dot{\gamma}^{s,\zeta}| \tag{4.9}$$

where h_0 is the initial hardening rate, $g_{sa}^{s,\zeta}$ the saturation shear stress, and $g_0^{s,\zeta}$ the initial strength of the s^{th} slip system. The saturation shear stress of the s^{th} slip system is given by:

$$g_{sa}^{s,\zeta} = g_{sa,0}^{s} \left(\sum_{s=1}^{N} |\dot{\gamma}^{s,\zeta}| / \dot{\gamma}_{s0} \right)^{m'} \tag{4.10}$$

in which, $g_{sa,0}^{s}$, $\dot{\gamma}_{s0}$ and m' are material parameters. All the parameters describing the hardening are orientation independent (i.e., same for all slip systems).

The boundary conditions for the boundary value problem are:

$$u_i^{\zeta}(\mathbf{x},t) = \bar{u}_i(\mathbf{x},t) \qquad \mathbf{x} \in \Gamma^u \tag{4.11}$$

$$\sigma_{ij}^{\zeta}(\mathbf{x},t) n_j = \bar{t}_i(\mathbf{x},t) \qquad \mathbf{x} \in \Gamma^t \tag{4.12}$$

in which, $\bar{u}_i(\mathbf{x})$ and $\bar{t}_i(\mathbf{x})$ are the prescribed displacement and traction on the boundaries Γ^u and Γ^t, where $\Gamma^u \cup \Gamma^t = \partial\Omega$ and $\Gamma^u \cap \Gamma^t = \emptyset$. $\mathbf{n}$ is the unit normal to Γ^t.

The system of equations given by Eqs. (4.1)-(4.12) are analyzed using the asymptotic homogenization method with multiple scales. The idea of the homogenization approach is illustrated in Fig. 4.1(b), in which the governing equations are decomposed into a homogenized problem defined over the problem domain, Ω, and parameterized by a macroscale

coordinate vector, $\mathbf{x}$, and microscale problem defined over the representative volume, Θ, and parameterized by the microscale coordinate vector, $\mathbf{y}$. The scaling relation is $\mathbf{y} = \mathbf{x}/\zeta$ with $0 < \zeta \ll 1$ denoting the size scale parameter given as the ratio between the characteristic length of the RVE and the macrostructure. The microstructure is assumed to be infinitesimal compared to the size of the macroscopic domain. $\mathbf{y}$ therefore is the spatial coordinates of the "blown up" version of the microstructure. The asymptotic analysis is consequently performed at the limit where the scaling parameter vanishes (i.e., scale separable limit) [13, 45]. An arbitrary single-scale response field, $f^{\zeta}(\mathbf{x})$, is then expressed using the two spatial coordinates as:

$$f^{\zeta}(\mathbf{x}) = f(\mathbf{x}, \mathbf{y}(\mathbf{x})) \tag{4.13}$$

The macroscopic spatial derivative of the response field is given by the chain rule as:

$$f^{\zeta}_{,x_i}(\mathbf{x}) = f_{,x_i}(\mathbf{x}, \mathbf{y}) + \frac{1}{\zeta} f_{,y_i}(\mathbf{x}, \mathbf{y}) \tag{4.14}$$

using the scaling relationship. All response fields are assumed to remain locally periodic throughout the deformation:

$$f(\mathbf{x}, \mathbf{y})) = f(\mathbf{x}, \mathbf{y} + \mathbf{k}\hat{\mathbf{y}})) \quad \forall \mathbf{x} \in \Omega \tag{4.15}$$

where, $\hat{\mathbf{y}}$ is the period of the RVE and $\mathbf{k}$ is a $n_{sd} \times n_{sd}$ diagonal matrix with integer components.

The domain of the RVE denoted as $\Theta \subset \mathbb{R}^{n_{sd}}$ is composed of n_{grain} grains associated with an orientation, lattice type, slip systems and evolution laws governing the slip along the slip systems. Let $\Theta^{(i)}_{gr}$ denote the i^{th} grain within the polycrystal RVE, then $\cup_{i=1}^{n_{grain}} \Theta^{(i)}_{gr} = \Theta$. In this study, full traction continuity is assumed along each grain boundary. We note that accurate modeling of the response mechanisms within grain boundaries may require

analysis of them as a separate phase (with thickness on the order of nanometers) or as interface (i.e., cohesive behavior). Such effects are beyond the scope of the current model.

4.2 Mathematical Homogenization with Multiple Scales

In this section, the multiscale representations of the response functions are used along with the two-scale asymptotic analysis of the original governing equations defined by Eqs. (4.1)-(4.12) to formulate the micro- and macroscale problems. An eigenstrain based representation of the inelastic response field is employed to express the microscale problem in an integral form, which forms the basis of the reduced order model described in Section 4. Considering a two-scale asymptotic expansion, the displacement field is expressed as:

$$u_i^{\zeta}(\mathbf{x},t) = u_i^0(\mathbf{x},t) + \sum_{a=1}^{m} \zeta^a u_i^a(\mathbf{x},\mathbf{y},t) + \mathrm{O}(\zeta^{m+1}) \tag{4.16}$$

in which, the leading order displacement, $\mathbf{u}^0$, is taken to be independent of the microscale coordinates. Substituting Eq. (4.16) into Eq. (4.3) yields:

$$\varepsilon_{ij}^{\zeta}(\mathbf{x},t) = \sum_{a=0}^{m} \zeta^a \varepsilon_{ij}^a(\mathbf{x},\mathbf{y},t) + \mathrm{O}(\zeta^{m+1}) \tag{4.17}$$

where, the first and second order strain components at each order are defined as:

$$\varepsilon_{ij}^a(\mathbf{x},\mathbf{y},t) = u^a_{(i,x_j)}(\mathbf{x},\mathbf{y},t) + u^{a+1}_{(i,y_j)}(\mathbf{x},\mathbf{y},t);\ a = 0,1,... \tag{4.18}$$

While the first order term of the displacement field in the asymptotic series is independent of the microscale coordinates, the variation of the strain field over the RVE is of order $\mathrm{O}(1)$, as indicated by Eq. (4.17). A comma followed by the micro or macroscale coordinate implies partial derivative with respect to the pertinent coordinate.

Substituting the asymptotic expansion of the strain field (Eq. (4.17)) into the constitu-

tive relationship yields the stress field in the following asymptotic form:

$$\sigma_{ij}^{\zeta}(\mathbf{x},t) = \sum_{a=0}^{m} \zeta^a \sigma_{ij}^{a}(\mathbf{x},\mathbf{y},t) + \mathrm{O}(\zeta^{m+1}) \tag{4.19}$$

in which,

$$\sigma_{ij}^{a}(\mathbf{x},\mathbf{y},t) = L_{ijkl}(\mathbf{y})\left[\varepsilon_{kl}^{a}(\mathbf{x},\mathbf{y},\mathbf{t}) - \mu_{kl}^{a}(\mathbf{x},\mathbf{y},\mathbf{t})\right];\ a = 0,1,... \tag{4.20}$$

The tensor of elastic moduli, L_{ijkl}^{ζ}, is taken to vary locally only (i.e., $L_{ijkl}^{\zeta}(\mathbf{x}) = L_{ijkl}(\mathbf{y})$). This consideration is consistent with the earlier assertion that the body is made of the repetition of an RVE (see Fig. 4.1(a)). The inelastic strain components are the components of the asymptotic series of the form:

$$\mu_{ij}^{\zeta}(\mathbf{x},t) = \sum_{a=1}^{m} \zeta^a \mu_{ij}^{a}(\mathbf{x},\mathbf{y},t) + \mathrm{O}(\zeta^{m+1}) \tag{4.21}$$

To obtain the expressions for the components of the inelastic strain in the asymptotic series, we proceed by substituting Eq. (4.19) into resolved shear stress in Eq. (4.5) and get:

$$\tau^{s,\zeta}(\mathbf{x},t) = \sum_{a=0}^{m} \zeta^a \tau^{s,a}(\mathbf{x},\mathbf{y},t) + \mathrm{O}(\zeta^{m+1}) \tag{4.22}$$

in which,

$$\tau^{s,a}(\mathbf{x},\mathbf{y},t) = \sigma_{ij}^{a}(\mathbf{x},\mathbf{y},t) Z_{ij}^{s}(\mathbf{y}) \tag{4.23}$$

Similar to the tensor of elastic moduli, the Schmid tensor varies with respect to the local coordinates only, due to the periodicity of the underlying microstructure. The Taylor series expansion of the slip rate in Eq. (4.8) about $(\tau^{s,0}, g^{s,0})$ gives:

$$\dot{\gamma}^{s,\zeta} = \sum_{p=0}^{\infty}\sum_{q=0}^{\infty} \frac{(\tau^{s,\zeta} - \tau^{s,0})^p (g^{s,\zeta} - g^{s,0})^q}{p!q!} \left(\frac{\partial^{p+q}\dot{\gamma}^{s,\zeta}}{\partial \tau^{s,\zeta^p} \partial g^{s,\zeta^q}}\right)\Big|_{(\tau^{s,0},\ g^{s,0})} \tag{4.24}$$

$$= \sum_{a=0}^{m} \zeta^a \dot{\gamma}^{s,a} + \mathrm{O}(\zeta^{m+1}) \tag{4.25}$$

where, p and q are integers. The first two terms of the slip strength expression are:

$$\dot{\gamma}^{s,0} = \dot{\gamma}_0 \left(\frac{\left|\tau^{s,0}\right|}{g^{s,0}} \right)^{1/m} \operatorname{sgn}(\tau^{s,0}) \tag{4.26}$$

$$\dot{\gamma}^{s,1} = \frac{\dot{\gamma}_0}{m} \left(\frac{\left|\tau^{s,0}\right|}{g^{s,0}} \right)^{1/m} \left(\frac{\tau^{s,1}}{\tau^{s,0}} - \frac{g^{s,1}}{g^{s,0}} \right) \operatorname{sgn}(\tau^{s,0}) \tag{4.27}$$

which, combined with Eq. (4.25), yields the evolution equation of the components of the inelastic strain tensor:

$$\dot{\mu}_{ij}^{a} = \sum_{s=1}^{N} \dot{\gamma}^{s,a}(\mathbf{x},\mathbf{y},t) Z_{ij}^{s}(\mathbf{y});\ a = 0,1,... \tag{4.28}$$

Similarly, expanding Eq. (4.9) using Taylor series about $(g^{s,0}, \tau^{s,0})$ gives:

$$\dot{g}^{s,\zeta} = \sum_{a=0}^{m} \zeta^{a} \dot{g}^{s,a} + \mathrm{O}(\zeta^{m+1}) \tag{4.29}$$

where, the first two terms are given as:

$$\dot{g}^{s,0} = h_0 \left(\frac{g_{sa}^{s,0} - g^{s,0}}{g_{sa}^{s,0} - g_0^{s,0}} \right) \sum_{s=1}^{N} |\dot{\gamma}^{s,0}| \tag{4.30}$$

$$\dot{g}^{s,1} = \frac{h_0 C}{\tau^{s,0}(g_{sa}^{s,0} - g_0^{s,0})^2} \left(E \frac{\tau^{s,1}}{\tau^{s,0}} - F \frac{g^{s,1}}{g^{s,0}} \right) \tag{4.31}$$

in which,

$$g_{sa}^{s,0} = g_{sa,0}^{s} \left(\sum_{s=1}^{N} |\dot{\gamma}^{s,0}| / \dot{\gamma}_{s0} \right)^{m'} \tag{4.32}$$

and,

$$C := \frac{\dot{\gamma}_0}{m}\left(\frac{\left|\tau^{s,0}\right|}{g^{s,0}}\right)^{1/m}\operatorname{sgn}(\tau^{s,0}) \tag{4.33}$$

$$D := \frac{m'}{\dot{\gamma}_{s0}} g^s_{sa,0}\left(\sum_{s=1}^{N}|\dot{\gamma}^{s,\zeta}|/\dot{\gamma}_{s0}\right)^{m'-1} \tag{4.34}$$

$$E := (1-D)(g^{s,0}_0 - g^{s,0}) + (g^{s,0}_{sa} - g^{s,0})(g^{s,0}_{sa} - g^{s,0}_0) \tag{4.35}$$

$$F := D(g^{s,0}_0 - g^{s,0}) + (g^{s,0}_{sa} - g^{s,0})(g^{s,0}_{sa} - g^{s,0}_0) \tag{4.36}$$

Substituting the asymptotic expansion of the stress field (Eq. (4.19)) into the equilibrium equation (Eq. (4.1)), making use of the chain rule (Eq. (4.14)), and identifying terms with equal order of ζ yields the equilibrium equations at each order of ζ:

$$\mathrm{O}(\zeta^{-1}):\ \sigma^0_{ij,y_j}(\mathbf{x},\mathbf{y},t) = 0 \tag{4.37}$$

$$\mathrm{O}(1):\ \sigma^0_{ij,x_j}(\mathbf{x},\mathbf{y},t) + \sigma^1_{ij,y_j}(\mathbf{x},\mathbf{y},t) + b_i(\mathbf{x},\mathbf{y},t) = 0 \tag{4.38}$$

$$\mathrm{O}(\zeta^a):\ \sigma^a_{ij,x_j}(\mathbf{x},\mathbf{y},t) + \sigma^{a+1}_{ij,y_j}(\mathbf{x},\mathbf{y},t) = 0;\ a = 1,2,... \tag{4.39}$$

The first order homogenization theory employs the $\mathrm{O}(\zeta^{-1})$ equilibrium equation to formulate the microstructural equilibrium, whereas the homogenized macroscale problem follows from the $\mathrm{O}(1)$ equilibrium. It is possible to derive higher order formulations by employing the higher order equilibrium equations (Eq. (4.39)), which may be important in capturing length scale effects, as well as dispersion phenomena under dynamic loads. While higher order methods hold promise, they typically require higher order continuity and may require special treatment of high order boundary conditions [69, 70, 71, 65]. In this dissertation, the focus is on the formulation of the reduced order crystal plasticity equations in the context of first order homogenization.

Integrating the $\mathrm{O}(1)$ equilibrium equation over the RVE domain Θ and exploiting peri-

odicity of stresses over the RVE yields the homogenized equilibrium equation as:

$$\bar{\sigma}_{ij,j}(\mathbf{x},t) + \bar{b}_i(\mathbf{x},t) = 0; \qquad \mathbf{x} \in \Omega \tag{4.40}$$

in which $\bar{b}_i$ is the RVE average body force; and the overbar indicates the averaging operation over the domain of the RVE. For an arbitrary response function, f:

$$\bar{f}(\mathbf{x},t) \equiv \langle f^{\zeta}(\mathbf{x},t)\rangle_{\Theta} = \frac{1}{|\Theta|}\int_{\Theta} f(\mathbf{x},\mathbf{y},t)\,\mathrm{d}\mathbf{y} \tag{4.41}$$

where, $|\Theta|$ denotes the volume of the RVE domain Θ.

We further consider boundary conditions that are smooth (i.e., that do not vary at the scale of the microstructure) over the domain of the microstructure. The resulting governing equations for the macroscale problem are summarized in Box 2. The constitutive behavior is expressed as the volume average of the stress field resolved at the RVE scale (i.e., $\bar{\boldsymbol{\sigma}} = \langle \boldsymbol{\sigma} \rangle_{\Theta}$) and without an explicit constitutive form. The stresses are therefore evaluated at the scale of the RVE, through the microstructure computations as described below. The macroscopic strain provided by the RVE volume averaging is the symmetric gradient of the macroscale displacement (i.e., $\bar{\boldsymbol{\varepsilon}} = \nabla^s \mathbf{u}^0$) due to the periodicity of the displacement field, $\mathbf{u}^1$.

Substituting the first order constitutive equation (Eq. (4.20)) into the $\mathrm{O}(\zeta^{-1})$ equilibrium equation, and using Eq. (4.18) yields:

$$\{L_{ijkl}(\mathbf{y})[\bar{\varepsilon}_{kl}(\hat{\mathbf{x}},t) + u^1_{(k,y_l)}(\hat{\mathbf{x}},\mathbf{y},t) - \mu^0_{kl}(\hat{\mathbf{x}},\mathbf{y},t)]\}_{,y_j} = 0 \tag{4.42}$$

While Eq. (4.42) is specialized to an arbitrary but fixed macroscopic position, $\hat{\mathbf{x}}$, is valid for all positions within the macroscopic domain, Ω.

Eq. (4.42) considered on the domain of an RVE (i.e., $\mathbf{y} \in \Theta$) along with the evolution equations and the periodic boundary condition defined over the RVE boundaries (i.e.,

Given: average body force, $\bar{\mathbf{b}}$, boundary conditions, $\bar{\mathbf{u}}, \bar{\mathbf{t}}$ at time $t \in [0, t_0]$

Find: Macroscopic deformation $\mathbf{u}^0 : \bar{\Omega} \times [0, t_0] \to \mathbb{R}^{n_{\text{sd}}}$

- Equilibrium ($\mathbf{x} \in \Omega; t \in [0, t_0]$)

  $\bar{\sigma}_{ij,j}(\mathbf{x}, t) + \bar{b}_i(\mathbf{x}, t) = 0 \qquad \mathbf{x} \in \Omega$

- Constitutive relation ($\mathbf{x} \in \Omega; t \in [0, t_0]$):

  $\bar{\sigma}_{ij}(\mathbf{x}, t) = \langle \sigma^0_{ij}(\mathbf{x}, \mathbf{y}, t) \rangle_\Theta$

- Kinematics ($\mathbf{x} \in \Omega; t \in [0, t_0]$)

  $\bar{\varepsilon}_{ij}(\mathbf{x}, t) = u^0_{(i,x_j)}(\mathbf{x}, t)$

- Boundary conditions:

  $u^0_i(\mathbf{x}, t) = \bar{u}_i(\mathbf{x}, t) \quad \mathbf{x} \in \Gamma^u, t \in [0, t_0] \qquad \bar{\sigma}_{ij}(\mathbf{x}, t) n_j = \bar{t}_i(\mathbf{x}, t) \quad \mathbf{x} \in \Gamma^t, t \in [0, t_0]$

Box 2: Macroscale problem.

Given: material elastic moduli L_{ijkl} and macroscopic strain, $\bar{\varepsilon}_{kl}$

Find: Microscopic deformation $\mathbf{u}^1 : \bar{\Theta} \times [0, t_0] \to \mathbb{R}^{n_{\text{sd}}}$ defined at a fixed but arbitrary macroscopic position, $\mathbf{x}$, which satisfy:

- Equilibrium:

  $\{L_{ijkl}(\mathbf{y})[\bar{\varepsilon}_{kl}(\mathbf{x}, \mathbf{y}, t) + u^1_{(k,y_l)}(\mathbf{x}, \mathbf{y}, t) - \mu^0_{kl}(\mathbf{x}, \mathbf{y}, t)]\}_{,y_j} = 0, \quad \mathbf{y} \in \Theta$

- Kinematics:

  $\dot{\mu}^0_{ij}(\mathbf{x}, \mathbf{y}, t) = \sum_{s=1}^{N} \dot{\gamma}^{s,0}(\mathbf{x}, \mathbf{y}, t) Z^s_{ij}(\mathbf{y})$

- Flow rule:

  $\dot{\gamma}^{s,0}(\mathbf{x}, \mathbf{y}, t) = \dot{\gamma}_0 \left(\frac{\left| \tau^{s,0}(\mathbf{x}, \mathbf{y}, t) \right|}{g^{s,0}(\mathbf{x}, \mathbf{y}, t)} \right)^{1/m} \operatorname{sgn}\left(\tau^{s,0}(\mathbf{x}, \mathbf{y}, t) \right)$

- Hardening rule:

  $\dot{g}^{s,0}(\mathbf{x}, \mathbf{y}, t) = h_0 \left(\frac{g^{s,0}_{sa} - g^{s,0}(\mathbf{x}, \mathbf{y}, t)}{g^{s,0}_{sa} - g^s_0} \right) \sum_{s=1}^{N} \left| \dot{\gamma}^{s,0}(\mathbf{x}, \mathbf{y}, t) \right|$

- Schmid's law:

  $\tau^{s,0}(\mathbf{x}, \mathbf{y}, t) = \sigma^0_{ij}(\mathbf{x}, \mathbf{y}, t) Z^s_{ij}(\mathbf{y})$

- Θ-periodic boundaries on $\mathbf{y} \in \Gamma_\Theta$

Box 3: Microscale problem based on mathematical homogenization.

$\mathbf{y} \in \partial\Theta$) constitutive a well-defined microscale problem as summarized in Box 3. The microscale problem is evaluated for the microscale displacement field, $\mathbf{u}^1$, considering $\nabla \cdot [\mathbf{L}(\mathbf{y}) : \bar{\varepsilon}(\mathbf{x},t)]$ as a body force.

4.3 Eigenstrain-based Reduced Order Model

The microscale boundary value problem defined over the RVE summarized in Box 3 along with the macroscale boundary value problem defined over the domain of the problem, Ω, is the first order computational homogenization (also called FE^2, see [48, 47]) applied to polycrystalline plasticity. The micro- and macroscale problems are nonlinear and strongly coupled. When the finite element method (FEM) is employed to numerically evaluate the problem, a separate RVE is associated with each quadrature point of the macroscale discretization. The macroscale constitutive response at a quadrature point is computed as the volume averaging of the microscale stress field obtained through the numerical evaluation of the microscale boundary value problem on the RVE of the quadrature point. In view of the fact that many polycrystalline RVEs require a very large degree of freedom (e.g., $O(10^5) - O(10^6)$) to resolve the complicated microstructural topology, direct evaluation of the multiscale system defined in Boxes 2 and 3 is computationally prohibitive. In this study, we employ the eigenstrain idea to develop a reduced order approximation to the microscale boundary value problem, which starts by decomposing the microscale displacement as ([126, 134]):

$$u_i^1(\mathbf{x},\mathbf{y},t) = H_{ikl}(\mathbf{y})\bar{\varepsilon}_{kl}(\mathbf{x},t) + \int_\Theta h_{ikl}(\mathbf{y},\hat{\mathbf{y}})\mu_{kl}^0(\mathbf{x},\hat{\mathbf{y}},t)d\hat{\mathbf{y}} \tag{4.43}$$

where $\mathbf{H}(\mathbf{y})$ and $\mathbf{h}(\mathbf{y},\hat{\mathbf{y}})$ are the elastic and eigenstrain influence functions with symmetry on the second and third indices [70] (i.e., $H_{ikl} = H_{ilk}$, $h_{ikl} = h_{ilk}$). The first component of Eq. 4.43 is due to the classical separation of variables considered in linear elastic computational homogenization [13]. The second component is obtained based on the Green's func-

tion approach, in which the inelastic strain field is viewed as the spatially variable "force" acting on the microstructure [34]. The detailed evaluation of the influence functions are further discussed in Section 4.4.1. Substituting Eq. (4.43) into Eq. (4.42) the microscale equilibrium can be written in the form incorporating the influence functions as:

$$\left\{ L_{ijkl}(\mathbf{y}) \left[A_{klmn}(\mathbf{y}) \bar{\varepsilon}_{mn}(\mathbf{x},t) + \int_{\Theta} a_{klmn}(\mathbf{y},\hat{\mathbf{y}}) \mu^0_{mn}(\mathbf{x},\hat{\mathbf{y}},t) \mathrm{d}\hat{\mathbf{y}}) \right] \right\}_{,y_j} = 0 \tag{4.44}$$

where

$$A_{klmn}(\mathbf{y}) = G_{klmn}(\mathbf{y}) + I_{klmn} \tag{4.45}$$

$$a_{klmn}(\mathbf{y},\hat{\mathbf{y}}) = g_{klmn}(\mathbf{y},\hat{\mathbf{y}}) - I_{klmn}\delta(\mathbf{y}-\hat{\mathbf{y}}) \tag{4.46}$$

with $G_{klmn}(\mathbf{y}) = H_{(k,y_l)mn}(\mathbf{y})$ and $g_{klmn}(\mathbf{y},\hat{\mathbf{y}}) = h_{(k,y_l)mn}(\mathbf{y},\hat{\mathbf{y}})$ being the elastic and eigenstrain polarization functions, respectively. It is straightforward to see that both $\mathbf{G}(\mathbf{y})$ and $\mathbf{g}(\mathbf{y},\hat{\mathbf{y}})$ possess the minor symmetry (i.e., $G_{ijkl} = G_{ijlk}$, $G_{ijkl} = G_{jikl}$, $g_{ijkl} = g_{ijlk}$, $g_{ijkl} = G_{jikl}$) due to the symmetry on the second and third indices of the influence functions. δ is the Dirac delta function, and $\mathbf{I}$ the fourth order identity tensor. Substituting Eq. (4.43) into Eq. (4.18) gives:

$$\varepsilon^0_{ij}(\mathbf{x},\mathbf{y},t) = A_{ijkl}(\mathbf{y})\bar{\varepsilon}_{kl}(\mathbf{x},t) + \int_{\Theta} g_{ijkl}(\mathbf{y},\hat{\mathbf{y}}) \mu^0_{kl}(\mathbf{x},\hat{\mathbf{y}},t)\, \mathrm{d}\hat{\mathbf{y}} \tag{4.47}$$

RVE averaging of Eq. (4.47) shows that the influence functions must satisfy the following constraints:

$$\langle G_{ijkl} \rangle_{\Theta} = 0; \quad \frac{1}{|\Theta|} \int_{\Theta} g_{ijkl}(\mathbf{y},\hat{\mathbf{y}})\, \mathrm{d}\hat{\mathbf{y}} = 0 \tag{4.48}$$

It is trivial to see that Eq. (4.48) is satisfied for periodic influence functions.

The computational complexity of solving the RVE problem is reduced by introducing the following discretization of the first order inelastic strain (i.e., eigenstrain) and stress

fields:

$$\mu_{ij}^{0}(\mathbf{x},\mathbf{y},t) = \sum_{\alpha=1}^{n} N^{(\alpha)}(\mathbf{y})\mu_{ij}^{(\alpha)}(\mathbf{x},t) \tag{4.49}$$

$$\sigma_{ij}^{0}(\mathbf{x},\mathbf{y},t) = \sum_{\alpha=1}^{n} N^{(\alpha)}(\mathbf{y})\sigma_{ij}^{(\alpha)}(\mathbf{x},t) \tag{4.50}$$

where $n \geq n_{grain}$ is an integer that indicates the order of the reduced order model, n_{grain} the number of grains within the RVE, $N^{(\alpha)}$ the shape functions, $\boldsymbol{\mu}^{(\alpha)}$ and $\boldsymbol{\sigma}^{(\alpha)}$ the nonlocal eigenstrain and stress coefficients, respectively. The nonlocal coefficients are expressed in terms of nonlocal weighting functions:

$$\mu_{ij}^{(\alpha)}(\mathbf{x},t) = \int_{\Theta} \psi^{(\alpha)}(\mathbf{y})\mu_{ij}^{0}(\mathbf{x},\mathbf{y},t)\,\mathrm{d}\mathbf{y} \tag{4.51}$$

$$\sigma_{ij}^{(\alpha)}(\mathbf{x},t) = \int_{\Theta} \psi^{(\alpha)}(\mathbf{y})\sigma_{ij}^{0}(\mathbf{x},\mathbf{y},t)\,\mathrm{d}\mathbf{y} \tag{4.52}$$

The shape functions, $N^{(\alpha)}$, differ from the standard finite element shape functions in the level of resolution (i.e., a relatively small number is used in describing the inelastic strain and stress fields) as well as continuity (chosen to be $C^{-1}(\Theta)$ continuous, consistent with the strain and stress continuity in finite elements). The shape functions are taken to satisfy the partition of unity property ($\sum_{\alpha=1}^{N} N^{(\alpha)}(\mathbf{y}) = 1$). The nonlocal weight functions, $\psi^{(\alpha)}$, satisfy positivity and normality, as well as orthonormality with the shape functions:

$$\psi^{(\alpha)}(\mathbf{y}) \geq 0; \quad \int_{\Theta} \psi^{(\alpha)}(\mathbf{y})\,\mathrm{d}\mathbf{y} = 1; \int_{\Theta} \psi^{(\alpha)}(\mathbf{y})N^{(\beta)}(\mathbf{y})\,\mathrm{d}\mathbf{y} = \delta^{(\alpha\beta)} \tag{4.53}$$

where, $\delta^{(\alpha\beta)}$ denotes the Kronecker delta (i.e., $\delta^{(\alpha\beta)} = 1$ if $\alpha = \beta$; $\delta^{(\alpha\beta)} = 0$ if $\alpha \neq \beta$). The orthonormality condition ensures the consistency of the reduced order discretization (i.e., Eqs. (4.49) and (4.50)) with the nonlocal averaging (i.e., Eqs. (4.51) and (4.52)) and can be verified by premultiplying Eqs. (4.49) and (4.50) with $\psi^{(\alpha)}$ and integrating over the RVE domain.

Substituting Eq. (4.49) into Eq. (4.47), premultiplying the resulting equation with $\psi^{(\alpha)}$

integrating over the RVE domain and taking a time derivative yields:

$$\dot{\varepsilon}_{ij}^{(\beta)}(\mathbf{x},t) - \sum_{\alpha=1}^{n} P_{ijkl}^{(\beta\alpha)} \dot{\mu}_{kl}^{(\alpha)}(\mathbf{x},t) = A_{ijkl}^{(\beta)} \dot{\bar{\varepsilon}}_{kl}(\mathbf{x},t) \tag{4.54}$$

in which, $\mathbf{P}^{(\beta\alpha)}$ and $\mathbf{A}^{(\beta)}$ are coefficient tensors expressed as a function of the influence functions as:

$$P_{ijkl}^{(\beta\alpha)} = \int_{\Theta}\int_{\Theta} \psi^{(\beta)}(\mathbf{y}) N^{(\alpha)}(\hat{\mathbf{y}}) g_{ijkl}(\mathbf{y},\hat{\mathbf{y}})\, \mathrm{d}\hat{\mathbf{y}}\, \mathrm{d}\mathbf{y} \tag{4.55}$$

$$A_{ijkl}^{(\beta)} = \int_{\Theta} \psi^{(\beta)}(\mathbf{y}) A_{ijkl}(\mathbf{y})\, \mathrm{d}\mathbf{y} \tag{4.56}$$

and,

$$\varepsilon_{ij}^{(\alpha)}(\mathbf{x},t) \coloneqq \int_{\Theta} \psi^{(\alpha)}(\mathbf{y}) \varepsilon_{ij}^{0}(\mathbf{x},\mathbf{y},t)\, \mathrm{d}\mathbf{y} \tag{4.57}$$

is the nonlocal strain coefficient.

Considering the $\mathrm{O}(1)$ constitutive equation (i.e., Eq. (4.20) with $a = 0$), premultiplying by $\psi^{(\alpha)}$, integrating over the RVE domain and taking the time derivative results in:

$$\dot{\bar{\varepsilon}}_{ij}^{(\beta)}(\mathbf{x},t) = \dot{\mu}_{ij}^{(\beta)}(\mathbf{x},t) + \sum_{\alpha=1}^{n} M_{ijkl}^{(\alpha\beta)} \dot{\sigma}_{kl}^{(\alpha)}(\mathbf{x},t) \tag{4.58}$$

where, $\mathbf{M}^{(\alpha\beta)}$ is expressed as:

$$M_{ijkl}^{(\alpha\beta)} = \int_{\Theta} \psi^{(\beta)}(\mathbf{y}) M_{ijkl}(\mathbf{y}) N^{(\alpha)}(\mathbf{y})\, \mathrm{d}\mathbf{y} = M_{ijkl}^{(\beta)} \delta^{(\alpha\beta)} \tag{4.59}$$

in which, $\mathbf{M}$ is the elastic compliance tensor. Combining Eqs. (4.54) and (4.58) with Eq. 4.59:

$$M_{ijkl}^{(\beta)} \dot{\sigma}_{kl}^{(\beta)}(\mathbf{x},t) - \sum_{\alpha=1}^{n} \left[P_{ijkl}^{(\beta\alpha)} - \delta^{(\alpha\beta)} I_{ijkl} \right] \dot{\mu}_{kl}^{(\alpha)}(\mathbf{x},t) = A_{ijkl}^{(\beta)} \dot{\bar{\varepsilon}}_{kl}(\mathbf{x},t) \tag{4.60}$$

Equation (4.60) along with evolution equations for the eigenstrain coefficients $\mu^{(\alpha)}$ (formulated below) could be evaluated to obtain the microstructure deformation state for a pre-

scribed macroscale strain increment. The macroscale stress is then computed by averaging Eq. (4.50) over the domain of the RVE.

Clearly, the number and form of the shape functions employed in the reduced order discretization of the eigenstrain and stress fields affect the accuracy and efficiency of the resulting model order. It is possible to prescribe piecewise constant or nonuniform variations for the shape functions [126, 134, 117]. In this work, piecewise constant shape functions are employed, which allows achieving evolution functions for the eigenstrain coefficients without further assumptions.

Considering the partitioning of the RVE domain into $n \geq n_{grain}$ nonoverlapping subdomains denoted by $\Theta^{(\alpha)}$ (i.e., $\Theta = \cup_{\alpha=1}^{n} \Theta^{(\alpha)}$ and $\Theta^{(\alpha)} \cap \Theta^{(\beta)} = \emptyset$ for $\alpha \neq \beta$). The partitioning is performed such that each subdomain is allowed to occupy the whole or a part of a single grain within the RVE only (i.e., $\Theta^{(\alpha)} \subseteq \Theta_{gr}^{(i)}$, $1 \leq i \leq n_{grain}$, $\forall \alpha \in \{1,2,...,n\}$). The shape and weighting functions are then chosen as:

$$N^{(\alpha)}(\mathbf{y}) = \begin{cases} 1 & \mathbf{y} \in \Theta^{(\alpha)} \\ 0 & \mathbf{y} \notin \Theta^{(\alpha)} \end{cases} \quad ; \quad \psi^{(\alpha)}(\mathbf{y}) = \frac{1}{|\Theta^{(\alpha)}|} N^{(\alpha)}(\mathbf{y}) \tag{4.61}$$

It is trivial to see that Eq. (4.61) satisfy the partition of unity, positivity, normality and orthonormality properties defined above.

Premultiplying the O(1) evolution laws for the inelastic strain, and the resolved shear stress (Eqs. (4.28) and (4.23), respectively with $a = 0$), and averaging over the domain of the RVE yields:

$$\dot{\mu}_{ij}^{(\alpha)}(\mathbf{x},t) = \sum_{s=1}^{N} \int_{\Theta} \psi^{(\alpha)}(\mathbf{y}) \dot{\gamma}^{s,0}(\mathbf{x},\mathbf{y},t) Z_{ij}^{s}(\mathbf{y}) \, \mathrm{d}\mathbf{y} \tag{4.62}$$

$$\tau^{s(\alpha)}(\mathbf{x},t) = \sigma_{ij}^{(\alpha)}(\mathbf{x},t) Z_{ij}^{s(\alpha)} \tag{4.63}$$

where $\dot{\gamma}^{s(\alpha)}$ and $\tau^{s(\alpha)}$ are the part average of the slip rate and resolved shear stress of the

s^{th} slip system, respectively (i.e., $\dot{\gamma}^{s(\alpha)} = \langle \dot{\gamma}^{s,0} \rangle_{\Theta^\alpha}$ and $\tau^{s(\alpha)} = \langle \tau^{s,0} \rangle_{\Theta^\alpha}$). $\tau^{s(\alpha)}$ denotes the Schmid tensor associated with the grain that contains $\Theta^{(\alpha)}$.

The O(1) evolution of the viscoplastic slip and slip strength (Eqs. (4.26) and (4.30)) are described by the ordinary differential equations as a function of the resolved shear stress. In the general form:

$$\dot{\gamma}^{s,0} = \dot{\gamma}\big(\gamma^{s,0}, \tau^{s,0}\big) \tag{4.64}$$

$$\dot{g}^{s,0} = \dot{g}\big(g^{s,0}, \tau^{s,0}\big) \tag{4.65}$$

Noting that the resolved shear stress in the reduced order model is piecewise uniform by the above arguments (i.e., $\tau^{s,0} = \tau^{s(\alpha)}$ when $y \in \Theta^{(\alpha)}$), considering that the slip and hardening evolve from a uniform reference state, the slip and hardening will evolve as piecewise uniform, which is described using the part averaged counterparts as :

$$\dot{\gamma}^{s(\alpha)}(\mathbf{x},t) = \dot{\gamma}_0 \left(\frac{\left| \tau^{s(\alpha)}(\mathbf{x},t) \right|}{g^{s(\alpha)}(\mathbf{x},t)} \right)^{1/m} \operatorname{sgn}\big(\tau^{s(\alpha)}(\mathbf{x},t)\big) \tag{4.66}$$

$$\dot{g}^{s(\alpha)}(\mathbf{x},t) = h_0 \left(\frac{g_{sa}^{s(\alpha)} - g^{s(\alpha)}(\mathbf{x},t)}{g_{sa}^{s(\alpha)} - g_0^{s(\alpha)}} \right) \sum_{s=1}^{N} |\dot{\gamma}^{s(\alpha)}(\mathbf{x},t)| \tag{4.67}$$

Box 4 summarizes the reduced order microscale problem, which replaces the numerical evaluation of the system described in Box 3. The overall order (i.e., the size of the linear systems evaluated in the context of the nonlinear solver) is $6n$ for a 3-D microstructure, where the unknowns are the nonlocal stress coefficients at each part, Θ^α, while the hardening coefficients evaluated explicitly, as described in Section 5.

4.3.1 Influence functions

The coefficient tensors $\mathbf{A}^{(\alpha)}$ and $\mathbf{P}^{(\alpha\beta)}$ used in the reduced order model are functions of the elastic (i.e., $\mathbf{H}(\mathbf{y})$) and eigenstrain (i.e., $\mathbf{h}(\mathbf{y},\hat{\mathbf{y}})$) influence functions, respectively.

Given: part-wise parameters $M_{ijkl}^{(\alpha\beta)}$, $P_{ijkl}^{(\alpha\beta)}$, $A_{ijkl}^{(\beta)}$, $\mathbf{n}^{s(\alpha)}$, $\mathbf{m}^{s(\alpha)}$, $g_{sa}^{s(\alpha)}$, $\dot{\gamma}_0^{s(\alpha)}$, $h_0^{(\alpha)}$, $g_{s0}^{s(\alpha)}$, $\dot{\gamma}_{s0}^{(\alpha)}$, the macroscale strain $\bar{\varepsilon}_{kl}$ with its increment $\Delta\bar{\varepsilon}_{kl}$

Find: macroscale stress $\bar{\sigma}_{kl}$

- Constitutive equation:

$$M_{ijkl}^{(\beta)}\dot{\sigma}_{kl}^{(\beta)}(\mathbf{x},t) - \sum_{\alpha=1}^{n}\left[P_{ijkl}^{(\beta\alpha)} - \delta^{(\alpha\beta)}I_{ijkl}\right]\dot{\mu}_{kl}^{(\alpha)}(\mathbf{x},t) = A_{ijkl}^{(\beta)}\dot{\bar{\varepsilon}}_{kl}(\mathbf{x},t)$$

$$\bar{\sigma}_{ij} = \sum_{\beta=1}^{n}\frac{|\Theta^{(\beta)}|}{|\Theta|}\sigma_{ij}^{(\beta)}$$

- Kinematics:

$$\dot{\mu}_{ij}^{(\alpha)}(\mathbf{x},t) = \sum_{s=1}^{N}\dot{\gamma}^{s(\alpha)}(\mathbf{x},t)\,Z_{ij}^{s(\alpha)}$$

- Flow rule:

$$\dot{\gamma}^{s(\alpha)}(\mathbf{x},t) = \dot{\gamma}_0\left(\frac{\left|\tau^{s(\alpha)}(\mathbf{x},t)\right|}{g^{s(\alpha)}(\mathbf{x},t)}\right)^{1/m}\operatorname{sgn}\left(\tau^{s(\alpha)}(\mathbf{x},t)\right)$$

- Hardening rule:

$$\dot{g}^{s(\alpha)}(\mathbf{x},t) = h_0\left(\frac{g_{sa}^{s(\alpha)} - g^{s(\alpha)}(\mathbf{x},t)}{g_{sa}^{s(\alpha)} - g_0^{s(\alpha)}}\right)\sum_{s=1}^{N}\left|\dot{\gamma}^{s(\alpha)}(\mathbf{x},t)\right|$$

- Schmid's law:

$$\tau^{s(\alpha)}(\mathbf{x},t) = \boldsymbol{\sigma}^{(\alpha)}(\mathbf{x},t) : \mathbf{Z}^{s(\alpha)} \qquad \mathbf{Z}^{s(\alpha)} = \mathbf{n}^{s(\alpha)} \otimes \mathbf{m}^{s(\alpha)}$$

Box 4: Reduced order microscale problem.

Furthermore, $\mathbf{A}^{(\alpha)}$ and $\mathbf{P}^{(\alpha\beta)}$ inherit minor symmetry from $\mathbf{G}(\mathbf{y})$ and $\mathbf{g}(\mathbf{y},\hat{\mathbf{y}})$.

Considering the microscale equilibrium defined in Eq. (4.44) in the absence of any inelastic strains:

$$\{L_{ijmn}(\mathbf{y})[H_{(m,y_n)kl}(\mathbf{y})+I_{mnkl}]\}_{,y_j}=0; \qquad \mathbf{y}\in\Theta \tag{4.68}$$

is the governing equation for evaluating the elastic influence function. Equation (4.68) is the classical influence function problem of linear elastic mathematical homogenization theory [13] and is well-posed up to rigid body motion when periodicity condition is enforced along the RVE boundaries.

Substituting the eigenstrain discretization (Eq. (4.49)) and (Eq. (4.68)) into Eq. (4.44) and observing that the nonlocal eigenstrain coefficients is a function of the macroscale spatial coordinates only:

$$\left\{L_{ijmn}(\mathbf{y})\left[h^{(\alpha)}_{(m,y_n)kl}(\mathbf{y})-I_{mnkl}N^{(\alpha)}(\mathbf{y})\right]\right\}_{,y_j}=0; \quad \mathbf{y}\in\Theta \tag{4.69}$$

is the governing equation for evaluating the part-wise eigenstrain influence function, $\mathbf{h}^{(\alpha)}$. Equation (4.69) is also well-posed up to rigid body motion when periodicity is imposed along the RVE boundary. It is possible to evaluate $\mathbf{P}^{(\alpha\beta)}$ directly using the part-wise eigenstrain influence functions as:

$$P^{(\beta\alpha)}_{ijkl}=\int_{\Theta}\psi^{(\beta)}(\mathbf{y})h^{(\alpha)}_{(i,y_j)kl}(\mathbf{y},\hat{\mathbf{y}})\,\mathrm{d}\mathbf{y} \tag{4.70}$$

The evaluation of the eigenstrain influence function itself, which is costly from computational and memory standpoints, is therefore not necessary to evaluate coefficient tensors. As a side note, one can realize that the the tensor $\mathbf{P}$ satisfies:

$$c^{(\bar{\beta})}\mathbf{P}^{(\bar{\beta}\bar{\alpha})}=c^{(\bar{\alpha})}\mathbf{P}^{(\bar{\alpha}\bar{\beta})} \tag{4.71}$$

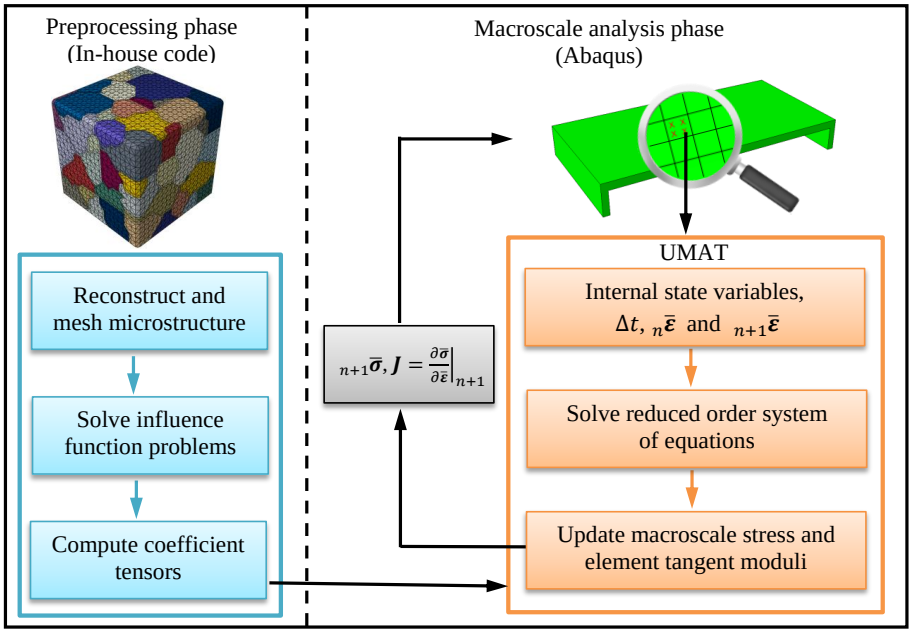

Figure 4.2: Implementation strategy for the reduced order multiscale model.

4.4 Computational Implementation

The proposed reduced order polycrystal plasticity model has been implemented and the implementation details are provided in this section. The overview of the implementation strategy is shown in Fig. 4.2. The evaluation of the multiscale problem is performed in two stages. The preprocessing stage consists of the generation of the RVE and the evaluation of the coefficient tensors. The simulation of the macroscale problem (Box 2) is performed using the commercial finite element analysis package, Abaqus. The evaluation of the reduced order microstructure (Box 4) that constitutes the stress update of the macroscale analysis is incorporated as a user supplied subroutine (i.e., UMAT). In the context of the assumed strain approach, the reduced order model evaluates the reduced order microstructure problem and computes the macroscale stress and tangent stiffness matrix from a given equilibrium state and strain increment at a macroscale quadrature point as described below. In this section, we particularly focus on the evaluation of the part-wise eigenstrain influence functions and the update procedure for the reduced order model.

4.4.1 Evaluation of the influence functions

The elastic and part-wise eigenstrain influence functions are numerically evaluated using the finite element method by solving Eqs. (4.68) and (4.69), respectively. The evaluation of elastic influence functions are standard (see, e.g., [56]) and skipped here for brevity.

Substituting the choice of the reduced order model shape functions into the eigenstrain influence function problem (4.69) and bringing the resulting equation into the weak form using the standard Bubnov-Galerkin procedure:

$$\int_{\Theta} w_{(i,y_j)}(\mathbf{y}) L_{ijmn}(\mathbf{y}) h^{(\alpha)}_{(m,y_n)kl}(\mathbf{y})\,\mathrm{d}\mathbf{y} = \int_{\Theta^{(\alpha)}} w_{(i,y_j)}(\mathbf{y}) L_{ijkl}(\mathbf{y})\,\mathrm{d}\mathbf{y}; \quad \alpha = 1,2,...,n \tag{4.72}$$

where $w(\mathbf{y}) \in \mathscr{W}_{\text{per}} \subset \left[H^1_{\text{per}}(\Theta)\right]^{n_{\text{sd}}}$ is the weight function with sufficient smoothness over the domain of the RVE, $H^1_{\text{per}}(\Theta)$ denotes the Sobolev space of Θ-periodic functions with square integrable values and derivatives defined within the problem domain, Θ. The space of the weight functions and the test functions are taken to be finite dimensional subspaces discretized using the standard finite element shape functions. Following the finite element discretization and assembly procedure, the resulting series of linear systems for the evaluation of the part-wise inelastic influence function becomes:

$$\mathbf{K}\mathbf{d}^{(\alpha)}_K = \mathbf{F}^{(\alpha)}_K; \quad \alpha = 1,2,...,n; K = 1,2,...,6 \tag{4.73}$$

where, $\mathbf{K}$ denotes the stiffness matrix, $\mathbf{F}^{(\alpha)}_K$ and $\mathbf{d}^{(\alpha)}_K$ denote the force vector and the nodal coefficient vector for the K^{th} component of the α^{th} influence function, respectively. Voigt notation is employed to condense the indices (i.e., $ij \rightarrow K$ with $11 \rightarrow 1$, $22 \rightarrow 2$, $33 \rightarrow 3$, $23 \rightarrow 4$, $13 \rightarrow 5$, $12 \rightarrow 6$) and K condenses the free indices in Eq. (4.69). It is important to note that the stiffness matrix, $\mathbf{K}$, is identical for all eigenstrain influence functions and therefore require a single factorization. $\mathbf{d}^{(\alpha)}_K$ denotes the nodal coefficient of the part-wise influence function of α^{th} part and $\mathbf{F}^{(\alpha)}_K$ denotes the corresponding force vector. Figure 4.3

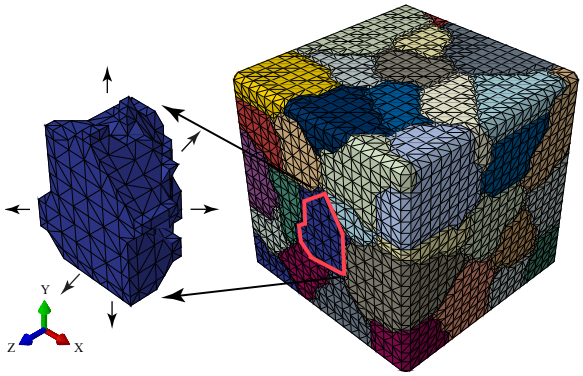

Figure 4.3: Solving influence functions part-by-part (using entire grain as one part as an example).

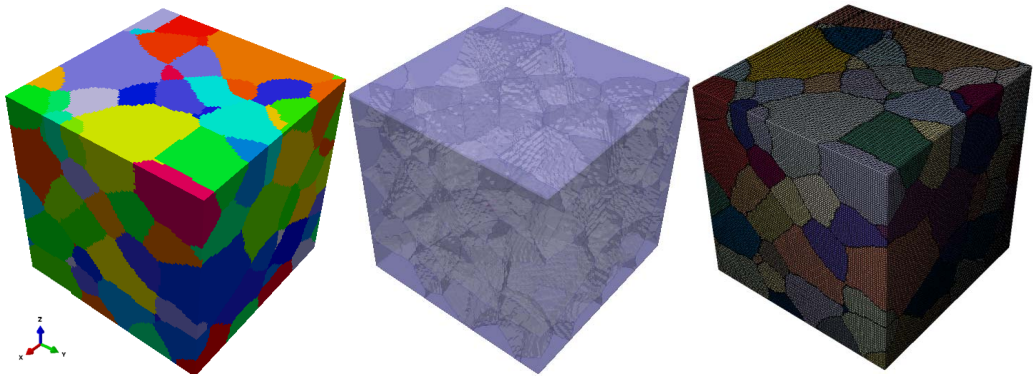

(a) (b) (c)

Figure 4.4: A virtual micro-structure generated from DREAM.3D and Meshed with PPM: (a) synthetic poly-crystal micro-structure; (b) internal grain boundaries based on which meshing of individual grain is conducted; (c) volume mesh.

schematically indicates the part-wise influence function problem, where the RVE subdomain associated with part α is subjected to a spatially uniform body force as expressed on the right-hand side of Eq. (4.72).

Representative polycrystal microstructures are generated using the DREAM.3D software [54], which is capable of creating synthetic RVEs based on microstructure topology metrics such as grain size, orientation and misorientation distributions or reconstruct microstructure directly from sectioned images of real microstructures. The geometry generated with DREAM.3D is discretized using the Parallelized Polycrystal Mesher developed by Cerrone et al. [26]. Figure 4.4 demonstrates the geometry and discretization of a representative microstructure.

The real or reconstructed polycrystal microstructures are often at best close to but not strictly periodic. In strictly periodic microstructure, the periodicity of the influence functions can be enforced by matching the surface nodes along the opposing sides of the RVE, assigning master-slave pairs and constraining the deformation of slave nodes to the deformation of the corresponding master nodes, which is not applicable in polycrystal RVEs. Nguyen et al. [129] proposed interpolating the displacement of two opposite RVE faces by linear combinations of polynomial shape functions for nonmatching RVE mesh. We rely on a similar idea combined with the classic master-slave coupling method to enforce a quasi-periodicity to provide point-wise displacement matching between opposing RVE surfaces with nonmatching meshes. Consider the discretization of the RVE using four-noded tetrahedra. The general treatment of the quasi-periodic mesh applies to hexahedra in a straight forward manner as well. The opposing external surfaces of the RVE are designated as master and slave surfaces. In case of uneven mesh density, slave surface is chosen to be that with the finer mesh density. The system of equations (Eq. (4.73)) is rearranged in the following form:

$$\begin{bmatrix} \mathbf{K}_{ii} & \mathbf{K}_{im} & \mathbf{K}_{is} & \mathbf{K}_{if} \\ \mathbf{K}_{mi} & \mathbf{K}_{mm} & \mathbf{K}_{ms} & \mathbf{K}_{mf} \\ \mathbf{K}_{si} & \mathbf{K}_{sm} & \mathbf{K}_{ss} & \mathbf{K}_{sf} \\ \mathbf{K}_{fi} & \mathbf{K}_{fm} & \mathbf{K}_{fs} & \mathbf{K}_{ff} \end{bmatrix} \begin{Bmatrix} \mathbf{d}^i \\ \mathbf{d}^m \\ \mathbf{d}^s \\ \mathbf{d}^f \end{Bmatrix} = \begin{Bmatrix} \mathbf{F}_1 \\ \mathbf{F}_2 \\ \mathbf{F}_3 \\ \mathbf{F}_4 \end{Bmatrix} \tag{4.74}$$

where $\mathbf{d}^i$, $\mathbf{d}^m$, $\mathbf{d}^s$ and $\mathbf{d}^f$ respectively denote the displacement vector that correspond to the interior, master, slave and fixed nodes respectively. The part and component indicators from the displacement vectors (Eq. (4.73)) are omitted in Eq. (4.74) for simplicity. Due to the symmetry of the stiffness matrix, different components of the stiffness matrix satisfy:

$$\mathbf{K}_{pq} = \mathbf{K}_{qp}^T ; \quad p \in \{i,m,s,f\}, q \in \{i,m,s,f\} \tag{4.75}$$

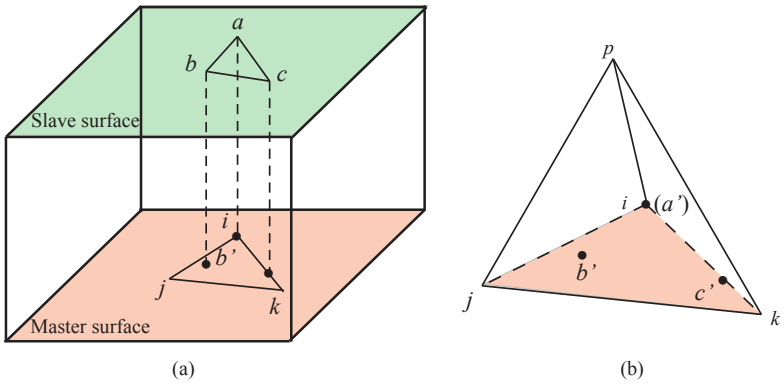

Figure 4.5: Master-Slave relationship for non-periodic mesh RVE.

The corner nodes of the RVE are fixed to prevent rigid body motion, which implies:

$$\mathbf{d}^f = \mathbf{0} \tag{4.76}$$

Every node on the slave surface is associated with a dummy master node, which is a projection of the slave node onto the master surface as illustrated in Fig. 4.5(a). The dummy master node lies on the face, edge or a vertex of a dummy master element as illustrated in Fig. 4.5(b). The displacement of the slave node is expressed as:

$$\mathbf{d}_b = \sum_{p=1}^{4} N_p^e(\hat{\mathbf{y}}_b)\mathbf{d}_p^e \tag{4.77}$$

where $\mathbf{d}_b$ denotes the displacement vector of the slave node, b, $\hat{\mathbf{y}}_b$ denotes the coordinates of the dummy master node, $\mathbf{d}^e$ and $\mathbf{N}^e$ denote the local displacement vector and finite element shape functions of the nodes in the dummy master element, e, respectively. Applying Eq. (4.77) to all nodes on slave surfaces of the RVE boundaries, yields the relationship between the slave and master displacement vectors as:

$$\mathbf{d}^s = \mathbf{C}\mathbf{d}^m \tag{4.78}$$

in which $\mathbf{C}$ is a rectangular matrix that contains the corresponding coefficients from Eq. (4.77).

Lagrange multipliers are used to enforce the boundary constraints. Consider the Lagrangian:

$$\Pi(\mathbf{d}) = \frac{1}{2}\mathbf{d}^T\mathbf{K}\mathbf{d} - \mathbf{d}^T\mathbf{F} + \boldsymbol{\lambda}_1^T(\mathbf{d}^s - \mathbf{C}\mathbf{d}^m) + \boldsymbol{\lambda}_2^T\mathbf{d}^f \tag{4.79}$$

in which, $\boldsymbol{\lambda}_1^T$ and $\boldsymbol{\lambda}_2^T$ are two Lagrange multipliers ensuring the enforcement of the periodic boundary conditions on the RVE boundaries (Eq. (4.78)) and fixed boundary conditions on the corner nodes (Eq. (4.76)). Taking derivative of Π with respect to $\mathbf{d}^i$, $\mathbf{d}^m$, and $\mathbf{d}^s$, and incorporating Eqs. (4.76) and (4.75) gives:

$$\mathbf{K}_{ii}\mathbf{d}^i + \mathbf{K}_{im}\mathbf{d}^m + \mathbf{K}_{is}\mathbf{d}^s - \mathbf{F}_1 = \mathbf{0} \tag{4.80}$$

$$\mathbf{K}_{mi}\mathbf{d}^i + \mathbf{K}_{mm}\mathbf{d}^m + \mathbf{K}_{ms}\mathbf{d}^s - \mathbf{F}_2 - \mathbf{C}^T\boldsymbol{\lambda}_1 = \mathbf{0} \tag{4.81}$$

$$\mathbf{K}_{si}\mathbf{d}^i + \mathbf{K}_{sm}\mathbf{d}^m + \mathbf{K}_{ss}\mathbf{d}^s - \mathbf{F}_3 + \boldsymbol{\lambda}_1 = \mathbf{0} \tag{4.82}$$

Premultiplying Eq. (4.82) with $\mathbf{C}^T$, adding with Eq. (4.81) and considering the periodic boundary condition in Eq. (4.78), yields:

$$\left(\mathbf{K}^{mi} + \mathbf{C}^T\mathbf{K}_{si}\right)\mathbf{d}_i + \left(\mathbf{K}_{mm} + \mathbf{C}^T\mathbf{K}_{sm} + \mathbf{K}_{ms}\mathbf{C} + \mathbf{C}^T\mathbf{K}_{ss}\mathbf{C}\right)d^m - \mathbf{F}_2 - \mathbf{C}^T\mathbf{F}_3 = \mathbf{0} \tag{4.83}$$

Substituting Eq. (4.78) into Eq. (4.80) and combining with Eq. (4.83) gives:

$$\begin{bmatrix} \mathbf{K}_{ii} & \mathbf{K}_{im} + \mathbf{K}_{is}\mathbf{C} \\ \mathbf{K}_{mi} + \mathbf{C}^T\mathbf{K}_{si} & \mathbf{K}_{mm} + \mathbf{C}^T\mathbf{K}_{sm} + \mathbf{K}_{ms}\mathbf{C} + \mathbf{C}^T\mathbf{K}_{ss}\mathbf{C} \end{bmatrix} \begin{Bmatrix} \mathbf{d}^i \\ \mathbf{d}^m \end{Bmatrix} = \begin{Bmatrix} \mathbf{F}_1 \\ \mathbf{F}_2 + \mathbf{C}^T\mathbf{F}_3 \end{Bmatrix} \tag{4.84}$$

The condensed stiffness matrix in Eq. (4.84) is used to solve for the interior and master nodal coordinates. The slave nodal coordinates, $\mathbf{d}^s$, is then computed using Eq. (4.78). It is straightforward to see that the symmetry of the stiffness matrix has been preserved. Equation (4.84) is evaluated for each part for a total of n times.

4.4.2 Evaluation of the reduced order microscale problem

The reduced order system of equations in Box 4 is solved numerically at each macroscale quadrature point to incrementally update the macroscale stress from an equilibrium state for a given increment of macroscopic strain.

The reduced order system is viewed as two sets of coupled nonlinear equations (i.e., the constitutive equations and hardening rules) with $\boldsymbol{\sigma}^{(\beta)}$ and $g^{s(\beta)}$ ($\beta = 1,2,...,n$, $s = 1,2,...,N$) as unknowns, which can be written in the vectorized form as:

$$\boldsymbol{\Sigma} = \left(\boldsymbol{\sigma}_1^{(1)}, \boldsymbol{\sigma}_2^{(1)}, \ldots, \boldsymbol{\sigma}_6^{(1)}, \boldsymbol{\sigma}_1^{(2)}, \ldots, \boldsymbol{\sigma}_6^{(2)}, \ldots, \boldsymbol{\sigma}_1^{(n)}, \ldots, \boldsymbol{\sigma}_6^{(n)}\right)^T \tag{4.85}$$

$$\mathbf{G} = \left(g^{1(1)}, g^{2(1)}, \ldots, g^{N(1)}, g^{1(2)}, \ldots, g^{N(2)}, \ldots, g^{1(n)}, \ldots, g^{N(n)}\right)^T \tag{4.86}$$

A full tight coupled Newton-Raphson (N-R) method [114] or a two-level staggering scheme [109] could be used to solve the reduced order microscale problem. In this work, a staggering scheme is adopted, in which the part-wise stresses and the part-wise strengths are evaluated in a coupled but iterative manner. While the convergence of the system is first order (as opposed to a tight coupled N-R scheme that has second order convergence), the generalization of the implementation of the approach to other evolution laws is somewhat more straightforward using the present formulation. The incremental procedure for evaluating the reduced order microscale problem is shown in Box 5.

To define the residual, we discretize the constitutive equation using a backward Euler scheme. Adopting the Voigt notation:

$$\boldsymbol{\Phi} = \left(\boldsymbol{\phi}_1^{(1)}, \boldsymbol{\phi}_2^{(1)}, \ldots, \boldsymbol{\phi}_6^{(1)}, \boldsymbol{\phi}_1^{(2)}, \ldots, \boldsymbol{\phi}_6^{(2)}, \ldots, \boldsymbol{\phi}_1^{(n)}, \ldots, \boldsymbol{\phi}_6^{(n)}\right)^T = \mathbf{0} \tag{4.87}$$

where,

$$\phi_I^{(\beta)} = \sum_{\alpha=1}^{n} \left(\delta^{(\alpha\beta)} I_{IJ} - P_{IJ}^{(\beta\alpha)}\right)\, {}_{l+1}\dot{\mu}_J^{(\alpha)} + M_{IJ}^{(\beta)} \frac{{}_{l+1}\sigma_J^{(\beta)} - {}_{l}\sigma_J^{(\beta)}}{{}_{l+1}t - {}_{l}t} - A_{IJ}^{(\beta)} \frac{{}_{l+1}\bar{\varepsilon}_J - {}_{l}\bar{\varepsilon}_J}{{}_{l+1}t - {}_{l}t} = 0 \tag{4.88}$$

in which, left subscripts l and $l+1$ indicate the values of the fields at current and next increments, respectively, that correspond to times ${}_{l}t$ and ${}_{l+1}t$. The time increment is: ${}_{l+1}\Delta t = {}_{l+1}t - {}_{l}t$. The Jacobian matrix for the N-R method is expressed as:

$$\frac{\partial \boldsymbol{\Phi}}{\partial \boldsymbol{\Sigma}} = \begin{bmatrix} \frac{\partial \phi_1^{(1)}}{\partial \sigma_1^{(1)}} & \frac{\partial \phi_1^{(1)}}{\partial \sigma_2^{(1)}} & \cdots & \frac{\partial \phi_1^{(1)}}{\partial \sigma_6^{(1)}} & \frac{\partial \phi_1^{(1)}}{\partial \sigma_1^{(2)}} & \cdots & \frac{\partial \phi_1^{(1)}}{\partial \sigma_6^{(n)}} \\ \frac{\partial \phi_2^{(1)}}{\partial \sigma_1^{(1)}} & \frac{\partial \phi_2^{(1)}}{\partial \sigma_2^{(1)}} & \cdots & \frac{\partial \phi_2^{(1)}}{\partial \sigma_6^{(1)}} & \frac{\partial \phi_2^{(1)}}{\partial \sigma_1^{(2)}} & \cdots & \frac{\partial \phi_2^{(1)}}{\partial \sigma_6^{(n)}} \\ \vdots & \vdots & \cdots & \vdots & \ddots & \vdots & \\ \frac{\partial \phi_6^{(1)}}{\partial \sigma_1^{(1)}} & \frac{\partial \phi_6^{(1)}}{\partial \sigma_2^{(1)}} & \cdots & \frac{\partial \phi_6^{(1)}}{\partial \sigma_6^{(1)}} & \frac{\partial \phi_6^{(1)}}{\partial \sigma_1^{(2)}} & \cdots & \frac{\partial \phi_6^{(1)}}{\partial \sigma_6^{(n)}} \\ \frac{\partial \phi_1^{(2)}}{\partial \sigma_1^{(1)}} & \frac{\partial \phi_1^{(2)}}{\partial \sigma_2^{(1)}} & \cdots & \frac{\partial \phi_1^{(2)}}{\partial \sigma_6^{(1)}} & \frac{\partial \phi_1^{(2)}}{\partial \sigma_1^{(2)}} & \cdots & \frac{\partial \phi_1^{(2)}}{\partial \sigma_6^{(n)}} \\ \vdots & \vdots & \cdots & \vdots & \ddots & \vdots & \\ \frac{\partial \phi_6^{(n)}}{\partial \sigma_1^{(1)}} & \frac{\partial \phi_6^{(n)}}{\partial \sigma_2^{(1)}} & \cdots & \frac{\partial \phi_6^{(n)}}{\partial \sigma_6^{(1)}} & \frac{\partial \phi_6^{(n)}}{\partial \sigma_1^{(2)}} & \cdots & \frac{\partial \phi_6^{(n)}}{\partial \sigma_6^{(n)}} \end{bmatrix} \tag{4.89}$$

where each component is expressed as:

$$\frac{\partial \phi_I^{(\beta)}}{\partial \sigma_K^{(\eta)}} = \left(\delta^{(\eta\beta)} I_{IJ} - P_{IJ}^{(\beta\eta)}\right) \sum_{s=1}^{N} \Omega^{s(\eta)} Z_J^{s(\eta)} Z_K^{s(\eta)} + \frac{M_{IK}^{(\beta)}}{{}_{l+1}\Delta t} \tag{4.90}$$

and

$$\Omega^{s(\eta)} = \frac{\dot{\gamma}_0}{m} \frac{1}{g^{s(\eta)}} \left(\frac{|\tau^{s(\eta)}|}{g^{s(\eta)}}\right)^{\frac{1-m}{m}} \tag{4.91}$$

The incremental evaluation of the macroscale equilibrium is performed using the N-R method, in which the tangent moduli is:

$$\frac{\partial_{l+1}\bar{\sigma}_I}{\partial_{l+1}\bar{\varepsilon}_J} = \sum_{\alpha=1}^{N} C^{(\alpha)} \frac{\partial_{l+1}\sigma_I^{(\alpha)}}{\partial_{l+1}\bar{\varepsilon}_J} \tag{4.92}$$

where $C^{(\alpha)}$ is the volume fraction of part α. Eq. (4.92) indicates the need to calculate $\frac{\partial_{l+1}\sigma_I^{(\alpha)}}{\partial_{l+1}\bar{\varepsilon}_J}$ to get the tangent moduli. This term is obtained by taking the derivative of Eq. (4.88) with respect to ${}_{l+1}\bar{\varepsilon}_K$ and considering the chain rule:

$$\sum_{\alpha=1}^{n}\left(\delta^{(\alpha\beta)}I_{IJ}-P_{IJ}^{(\beta\alpha)}\right)\frac{\partial_{l+1}\dot{\mu}_J^{(\alpha)}}{\partial_{l+1}\tau^{s(\alpha)}}\frac{\partial_{l+1}\tau^{s(\alpha)}}{\partial_{l+1}\sigma_L^{(\alpha)}}\frac{\partial_{l+1}\sigma_L^{(\alpha)}}{\partial_{l+1}\bar{\varepsilon}_K}+\frac{M_{IJ}^{(\beta)}}{{}_{l+1}\Delta t}\frac{\partial_{l+1}\sigma_J^{(\beta)}}{\partial_{l+1}\bar{\varepsilon}_K}-\frac{A_{IJ}^{(\beta)}}{{}_{l+1}\Delta t}\frac{\partial_{l+1}\bar{\varepsilon}_J}{\partial_{l+1}\bar{\varepsilon}_K}=0 \tag{4.93}$$

Simplifying the above equation yields:

$$\sum_{\alpha=1}^{n}\left[\left(\delta^{(\alpha\beta)}I_{IJ}-P_{IJ}^{(\beta\alpha)}\right)\varphi_{JL}^{(\alpha)}+M_{IL}^{(\beta)}\delta^{(\alpha\beta)}\right]\frac{\partial_{l+1}\sigma_L^{(\alpha)}}{\partial_{l+1}\bar{\varepsilon}_K}=\frac{A_{IK}^{(\beta)}}{{}_{l+1}\Delta t} \tag{4.94}$$

where,

$$\varphi_{JL}^{(\alpha)}=\sum_{s=1}^{N}\frac{\dot{\gamma}_0}{m}\frac{1}{{}_{l+1}g^{s(\alpha)}}\left(\frac{\left|{}_{l+1}\tau^{s(\alpha)}\right|}{{}_{l+1}g^{s(\alpha)}}\right)^{\frac{1}{m}-1}Z_J^{s(\alpha)}Z_L^{s(\alpha)} \tag{4.95}$$

Equation (4.94) consists of a linear system of equations, from which $\frac{\partial_{l+1}\sigma_L^{(\alpha)}}{\partial_{l+1}\bar{\varepsilon}_K}$ is calculated.

4.5 Numerical Verification

The verification of the proposed reduced order homogenization based crystal plasticity model is performed using three sets of examples. The examples establish the accuracy characteristics of the proposed model as compared to the Crystal Plasticity Finite Element (CPFE) method, in which the microstructure is fully resolved. The first two sets of examples assess the accuracy and efficiency in the context of macroscopic metrics (e.g., homogenized stress-strain behavior) with the first set of example emphasizing on various loading conditions and the second set on different microstructure configurations. The third set of examples demonstrates the importance of employing subgrain partitioning when the local stress fields are of interest. A two-scale analysis of a circular arch subjected to compression is considered at last to further demonstrated the computational capabilities of the proposed

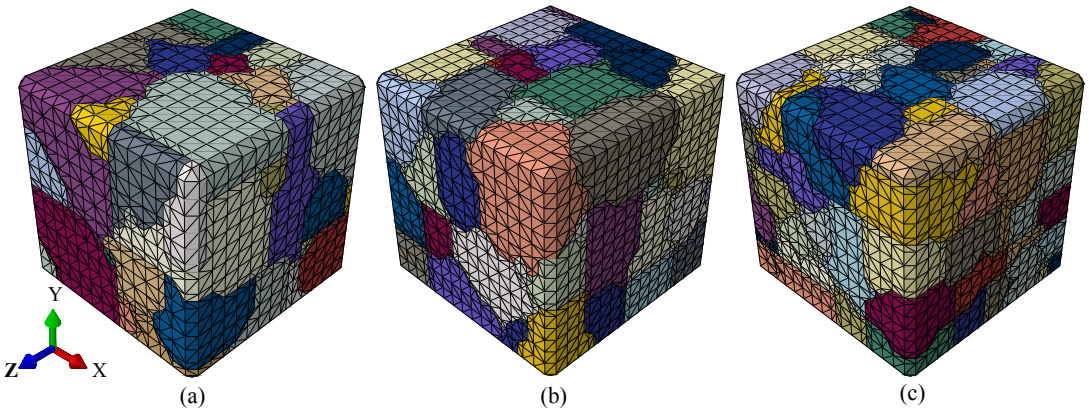

Figure 4.6: Three RVEs of different sizes: (a) small RVE with 52 grains; (b) medium RVE with 73 grains; (c) large RVE with 134 grains.

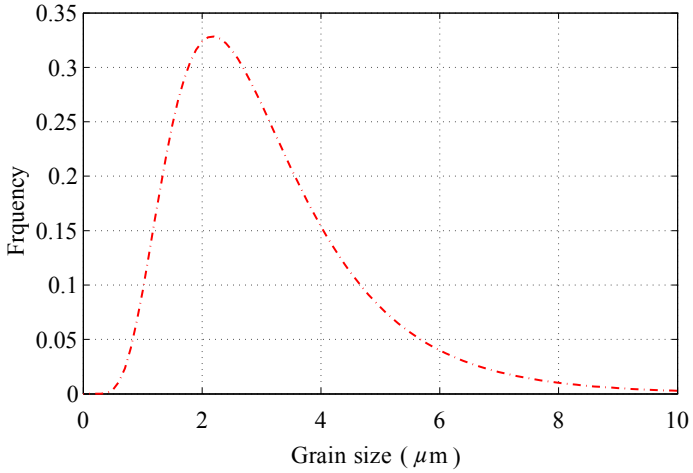

Figure 4.7: Grain size distribution function used in RVE microstructure generation.

reduced order model.

Three polycrystalline microstructural configurations as shown in Fig. 4.6 are investigated during the verification process using the grain size distribution function shown in Fig. 4.7 and equiaxed grain shape. The rolling direction (RD) is along the X axis, while the transverse (TD) and the normal direction (ND) coincides with Y and Z, respectively. The polycrystalline microstructures are taken to consist of 52, 73 and 134 randomly oriented FCC grains of pure aluminum.

The finite element discretizations of the reference CPFE models are composed of trilinear four-noded tetrahedron elements. The three microstructures investigated contained

Table 4.1: Elastic parameters.

C_{11} (GPa)	C_{12} (GPa)	C_{44} (GPa)
108.2	61.3	28.5

Table 4.2: Viscoplasticity parameters.

m	$\dot{\gamma}_0(s^{-1})$	h_0 (MPa)	g_0^s (MPa)	$g_{sa,0}^s$ (MPa)	m'	$\dot{\gamma}_{s0}(s^{-1})$
0.05	1.0	20.4	3.7	30.8	0.0	5.0×10^{10}

50,476, 69,291 and 94,409 elements that correspond to approximately 56,000, 76,000 and 103,000 degrees of freedom, respectively. The partitioning of the proposed reduced order models were performed such that each part coincides with a single grain (i.e., n=52, n =73 and n =134 for the three cases considered) leading to a nonlinear system with 312, 438 and 804 degrees of freedom, respectively. The macroscale discretization of the multiscale model consists of a single tri-linear eight-noded hexahedron element in the three sets of verification examples.

The properties of the material at the reference orientation (taken to be the same as the basis shown in Fig. 4.3) is summarized in Tables 4.1 and 4.2. All 12 $\{111\}\langle 111\rangle$ slip systems are taken to be active in the reference and multiscale simulations.

4.5.1 Effects of loading conditions

Uniaxial, simple shear and biaxial loading conditions are considered to investigate the performance of the ROM as shown in Fig. 4.8 (the illustration is in 2D for simplicity since no loadings are applied along the out-of-plane direction for all cases). Both monotonic and cyclic loading cases are studied under the biaxial tension conditions. For the uniaxial tension and simple shear, a 5% strain is applied with a constant strain rate of 0.05/s. For the monotonic biaxial tension case, a 5% strain is applied at a constant strain rate of 0.05/s along the X direction while a 3% strain is applied at a constant strain rate of 0.03/s along the Y direction. For the cyclic biaxial tension case, a 6% maximum strain is applied along

the X direction with a constant strain rate of 0.04/s. Upon reaching the maximum strain, the loading is held until the end of the simulation. Along the Y direction, the microstructure is cyclically loaded with an R-ratio of one and applied strain range of 4% at constant strain rate 0.04/s. The duration of the cyclic biaxial tension simulation is 2.5 seconds.

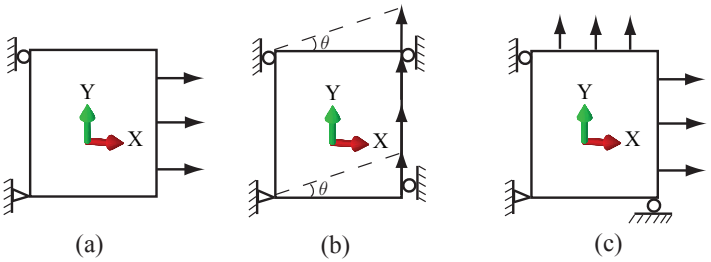

Figure 4.8: Schematic illustration of different boundary and loading conditions investigated: (a) uniaxial tension; (b) simple shear; (c) biaxial tension.

Figure 4.9 shows the comparisons between overall stress-strain behaviors simulated using the proposed reduced order model and the reference model of the 73-grain RVE under above loading conditions with texture given in the $\{111\}$ pole figure in Fig. 4.10. There is a reasonable overall match between the CPFE and the reduced order model behavior for all the loading conditions considered. The proposed model performed slightly stiffer than the reference simulation, which is expected because the proposed model employs a much reduced basis with uniform shape functions within each part. The model therefore does not capture strain/stress gradients within the part. Employing nonuniform shape functions [117, 118] or increasing the number of parts [134] may improve the accuracy. It also should be noted, in all the examples studied, ROM provides approximately two orders of magnitude of efficiency compared with CPFE simulations.

4.5.2 Effects of microstructure configuration

For each microstructure in Fig. 4.6, 32 random grain orientation sets were generated in order to study the error characteristics of the proposed model as a function of the random microstructure geometry. Each microstructure is subjected to uniaxial tension along the

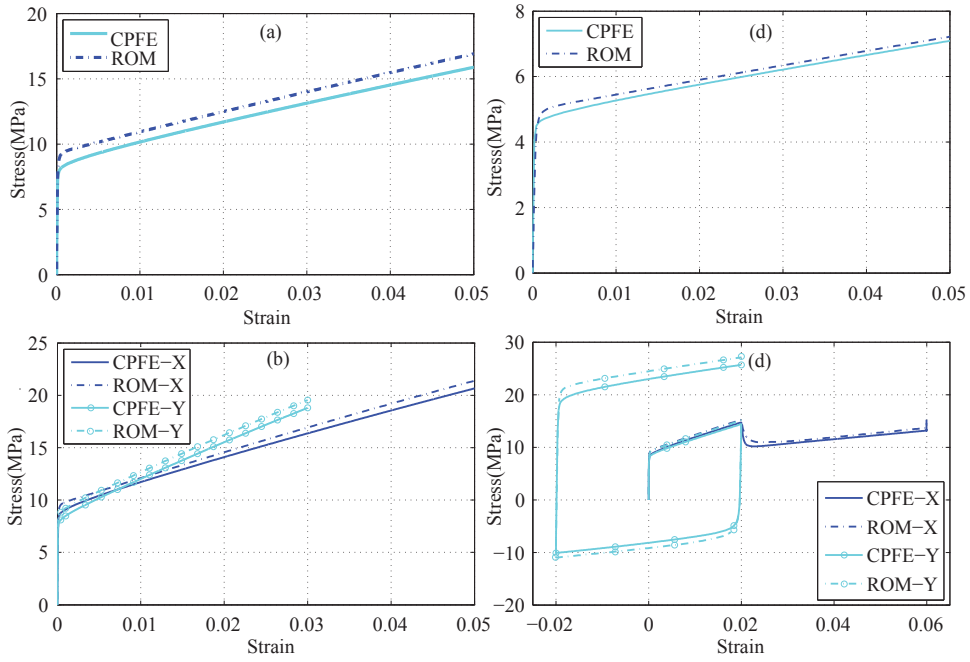

Figure 4.9: Overall constitutive behavior of the 73-grain RVE subjected to: (a) monotonic uniaxial tension; (b) monotonic simple shear; (c) monotonic biaxial tension; (d) cyclic biaxial tension.

X-direction up to 5% macroscopic strain with a strain rate of 0.05/s. All the 96 simulations show similar errors, and in order to give an overall description of the error of all the simulations, we define the overall stress approximation error as:

$$\text{error} = \frac{\int_0^{\varepsilon} |\sigma_{\text{ROM}} - \sigma_{\text{CPFE}}| \, \mathrm{d}\varepsilon}{\int_0^{\varepsilon} \sigma_{\text{CPFE}} \, \mathrm{d}\varepsilon} \tag{4.96}$$

For the simulation shown in Fig. 4.9 (a), this error is calculated as 7.1%. The error distribution functions of the 96 simulations are shown in Fig. 4.11, which demonstrates that the error magnitude is quite stable across random realizations of orientation distributions, as well as microstructure morphologies.

Another RVE with elongated grains along X direction shown in Fig. 4.12) is used to evaluate ROM's performance when the grain shapes are not equiaxed and a preferred orientation exists. The same grain size distribution function is used as in Fig. 4.7 while the aspect ratio of RD/ND and RD/TD is set to 5.0 and 4.0, respectively, to enforce the elon-

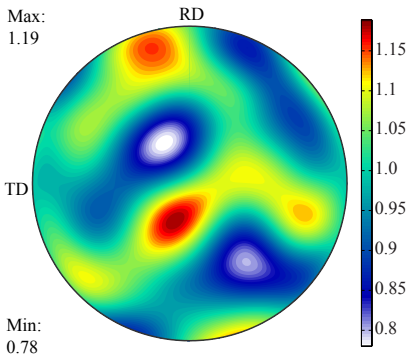

Figure 4.10: {111} pole figure of the initial texture of the 73-grain RVE.

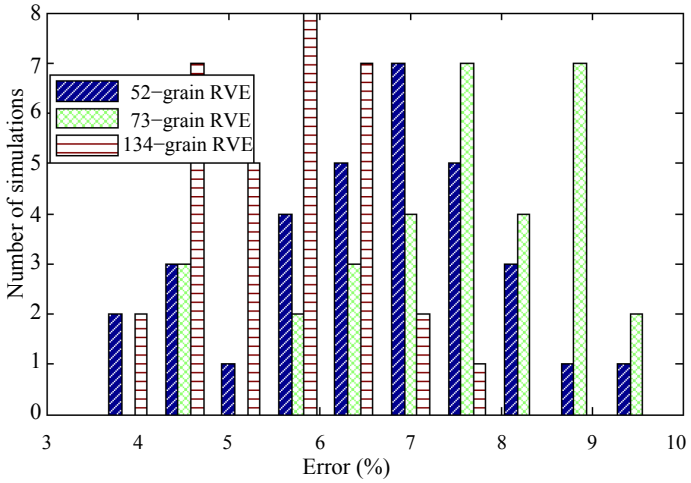

Figure 4.11: Overall stress approximation error distribution functions.

gated grain structure. This RVE consists of 62 grains and the initial texture is chosen such that it follows the pattern of the rolling texture of aluminum as reported in [112]. The {111} pole figure of the initial texture is shown in Fig. 4.13. Figure 4.14 shows the overall constitutive behavior of this RVE subject to uniaxial tension along X and Z direction. ROM performs reasonably well along both loading directions, and, more importantly captures the anisotropic yielding and hardening effects in different loading directions caused by the microstructure anisotropy.

4.5.3 Effect of subgrain partitioning

The reduced order modeling approach, which includes one-part-per-grain partitioning, was demonstrated above to reasonably approximate the overall deformation behavior of the

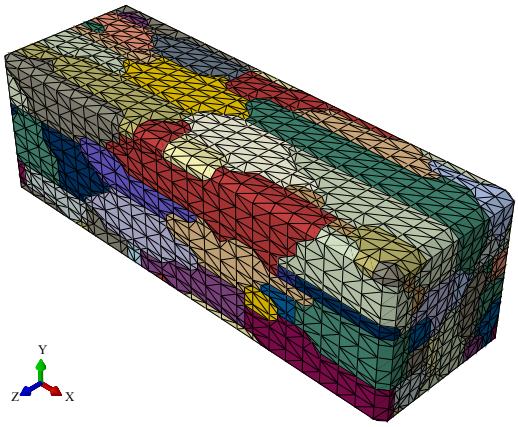

Figure 4.12: RVE with elongated grains along X direction

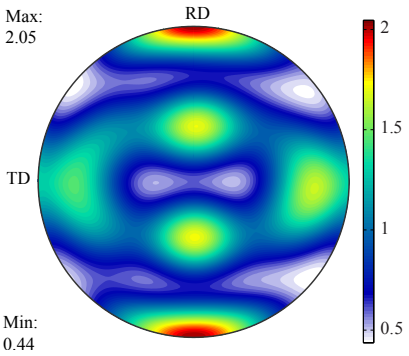

Figure 4.13: $\{111\}$ pole figure of the initial texture of the elongated RVE.

polycrystal. Often times, in addition to the overall constitutive response of the polycrystal, the subgrain stress and strain concentrations are of significant concern. The accurate characterization of stresses along grain boundaries and triple junctions are critical to capturing the damage and crack initiation under fatigue and creep-fatigue loading. It is therefore of interest to demonstrate the capability of the proposed model in capturing the stresses within the grain.

An idealized microstructure with regular, 3×3 cubic grains are considered. The geometry and the discretization of the microstructure is shown in Fig. 4.15(a). Each grain is assigned a random orientation. The microstructure is subjected to uniaxial tension along the X-direction up to 5% macroscopic strain with a strain rate of 0.05/s. The material and properties are taken to be identical to that presented in Section 4.5.2 and summarized in

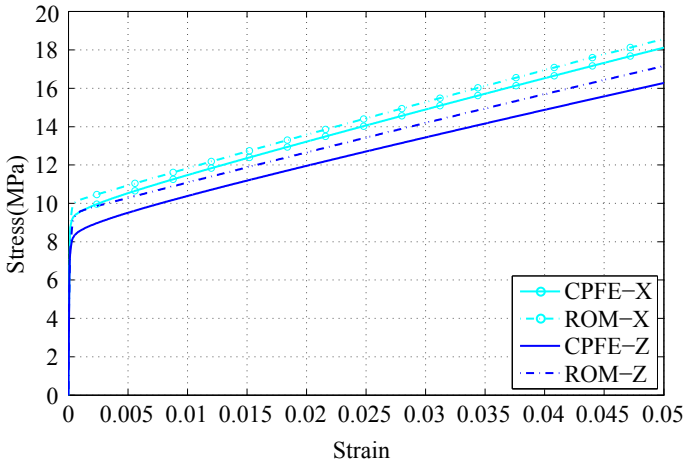

Figure 4.14: Overall constitutive behavior of a RVE with 62 elongated grains subjected to uniaxial tension along different directions.

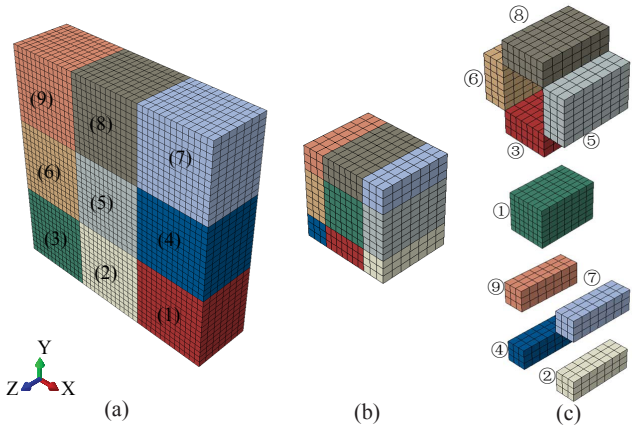

Figure 4.15: Sub-partitioning of the RVE: (a) RVE with grain ID; (b) sub-partitioning of grain No. 5; (c) parts in grain No.5 with part ID.

Tables 4.1 and 4.2. The CPFE discretization consists of 10,647 trilinear hexahedra that corresponds to approximately 76,800 degrees of freedom in the resulting discrete system of equations. Two reduced order models, named ROM1 and ROM2, are considered to approximate the response of the idealized microstructure. ROM1 is generated by assigning a part to each grain in the microstructure ($n = 9$), which leads to a system size of 54. In ROM2, the central grain was further partitioned into nine additional parts (i.e., $n = 17$ with 102 degrees of freedom) as shown in Fig. 4.15(b)-(c). Among the nine additional parts, part (1) approximates the behavior within the interior of the grain, parts (3), (5), (6) and (8)

represent the behavior along the grain boundary and parts (2), (4), (7) and (9) account for the behavior at the triple junctions. The macroscale discretization of the multiscale models consists of a single tri-linear eight-noded hexahedron element.

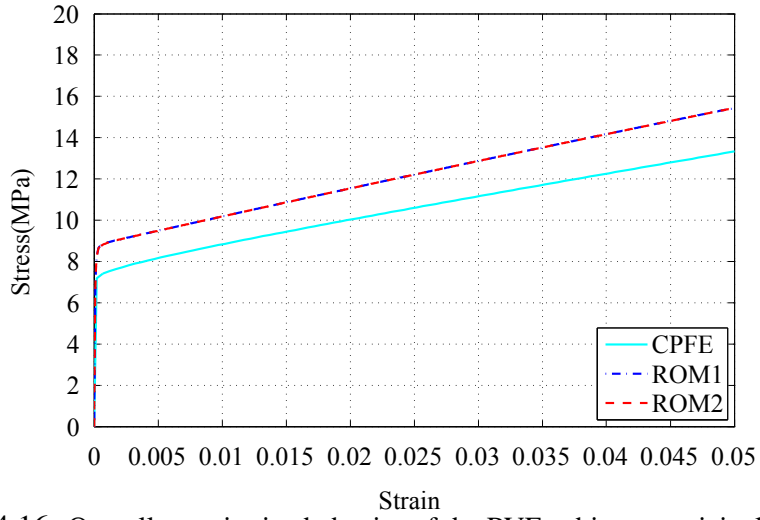

Figure 4.16: Overall constitutive behavior of the RVE subject to uniaixal tension.

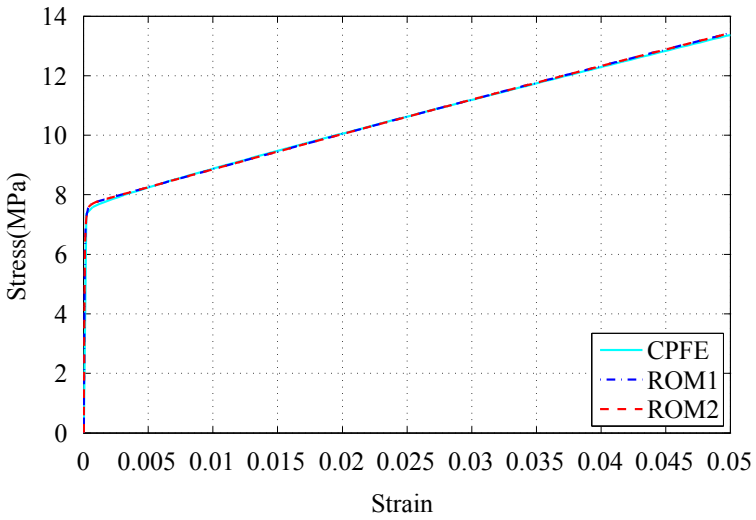

Figure 4.17: Overall constitutive behavior of the RVE subjected to uniaixal tension after parameter scaling.

The homogenized stress-strain curves obtained by the two models and the direct CPFE simulations are shown in Fig. 4.16. The overall constitutive behaviors computed by the two models are virtually identical, which points to the relative invariance of grain decomposition on the overall behavior. Both models slightly overestimate the stress-strain behavior as

compared to the CPFE simulation, but capture the overall deformation behavior with reasonable accuracy. These results also demonstrate that, in this case, the overall stress-strain behavior is not significantly affected by the order of the reduced order model. Additional analysis of the effect of the model order on accuracy is provided in Ref. [134].

A series of simulations using the same microstructure but with different random set of grain orientations show a consistent trend that reduced order models overestimate the overall stress. In order to differentiate the local stress accuracy from the overall stress accuracy, the initial hardening parameter, $\dot{\gamma}_0$, of the reduced order models is scaled such that the discrepancy between the CPFE and the multiscale models are minimized. The initial hardening parameter was shown to affect the yielding stress and hardening slope as suggested in Ref. [55]. We note that this process also resembles calibration based on experimental data, in which, the reduced order model parameters are set to minimize the discrepancy between the experimental observations and the model predictions. Figure 4.17 shows the overall stress-strain curves after $\dot{\gamma}_0$ in the reduced order models is set to $30.0s^{-1}$. The overall stress-strain behaviors of the reduced order models and the reference model are virtually identical following the scaling process.

The stress contours within the microstructure as computed by the CPFE model at an applied overall strain magnitude of 5% is shown in Fig. 4.18. Stresses along the grain boundaries and the triple junctions clearly deviate significantly from the grain interiors, often with significant concentrations at boundaries with high grain orientation mismatch.

Figure 4.19 compares the evolution of average stress along the X-direction within four subgrains (parts (1), (4), (7) and (9) as shown in Fig. 4.15) of the central grain in the idealized microstructure. ROM1, does not distinguish between the subgrains of the central grain since the stress is taken to be spatially uniform within the grain. The stress-strain plots for ROM1 is therefore identical in Figs. 4.19 (a)-(d). The part average stresses of ROM2 are directly tracked in the evaluation of the model, and therefore readily available. The stresses obtained from CPFE were averaged over the relevant subdomains. Within part

Given: Stress and strength of each part at the l^{th} increment, ${}_{l}\boldsymbol{\Sigma}$ and ${}_{l}\mathbf{G}$; macroscale strain and strain increment, ${}_{l+1}\bar{\boldsymbol{\epsilon}}$ and ${}_{l+1}\Delta\bar{\boldsymbol{\epsilon}}$; time and time increment, ${}_{l}t$ and ${}_{l+1}\Delta t$.

Find: Stress and strength of each part at the $l+1^{th}$ increment, ${}_{l+1}\boldsymbol{\Sigma}$ and ${}_{l+1}\boldsymbol{G}$.

- (A) Set iteration number $k = 0$
- (B) Initial guess for stress and strength:

$$ {}^{0}_{l+1}\boldsymbol{\Sigma} = {}_{l}\boldsymbol{\Sigma} \; ; \; {}^{0}_{l+1}\mathbf{G} = {}_{l}\mathbf{G} $$

- (C) Iterate k until convergence:

1) Update the stress using N-R iteration

$$ {}^{k+1}_{l+1}\boldsymbol{\Sigma} = {}^{k}_{l+1}\boldsymbol{\Sigma} - \left(\frac{\partial \boldsymbol{\Phi}}{\partial \boldsymbol{\Sigma}}\right)^{-1}\Bigg|_{({}^{k}_{l+1}\boldsymbol{\Sigma},\, {}^{k}_{l+1}\mathbf{G})} \boldsymbol{\Phi}\Bigg|_{({}^{k}_{l+1}\boldsymbol{\Sigma},\, {}^{k}_{l+1}\mathbf{G})} $$

2) Update the strength explicitly:

$$ {}^{k+1}_{l+1}\mathbf{G} = {}^{k}_{l+1}\mathbf{G} + \dot{\mathbf{G}}\Big|_{({}^{k+1}_{l+1}\boldsymbol{\Sigma},\, {}^{k}_{l+1}\mathbf{G})} {}_{l+1}\Delta t $$

2) $k = k+1$

Box 5: Algorithm for solving the reduced order microscale problem

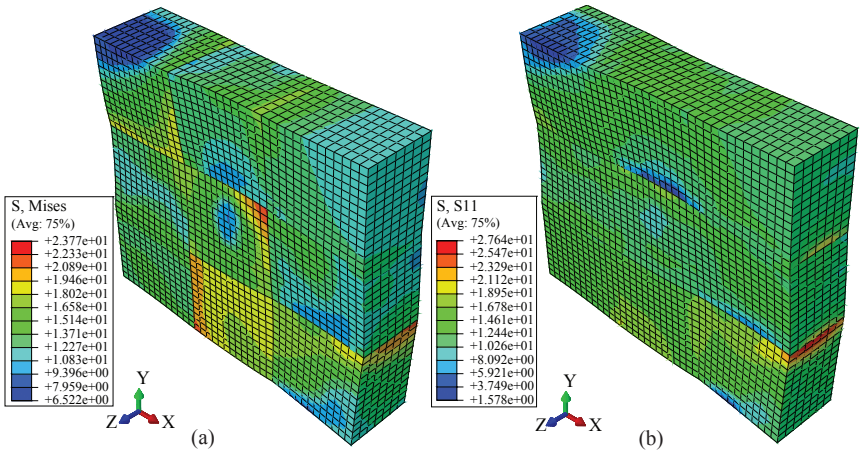

Figure 4.18: Stress contour of the RVE subject to uniaxial tension along the X direction

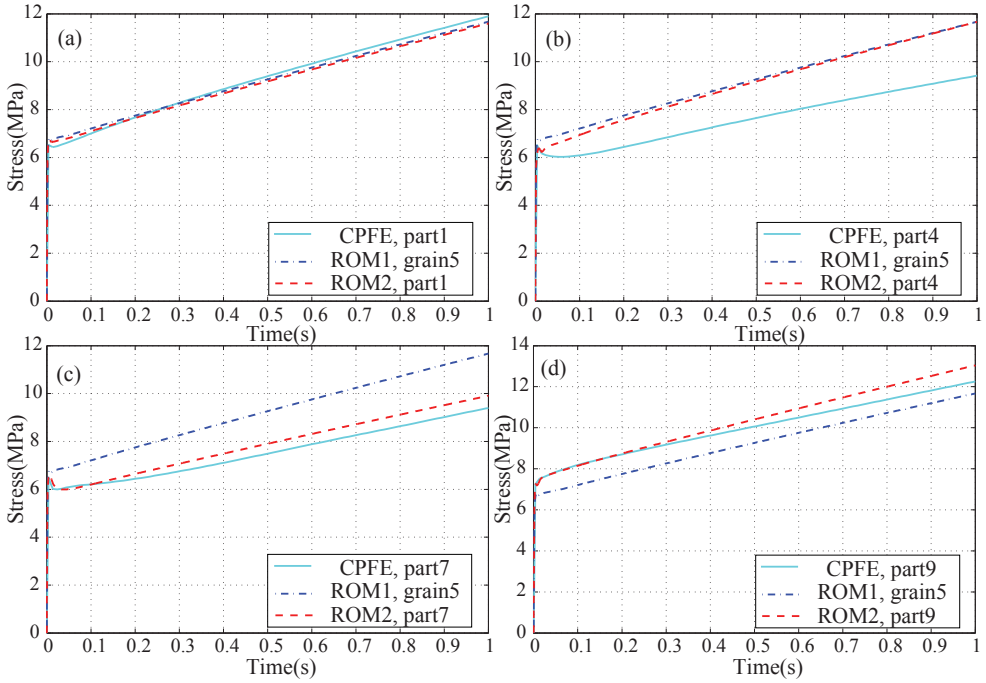

Figure 4.19: σ_{11} of different parts in grain No. 5.

(1) of the central grain that corresponds to the grain interior, the stress evolution is very similar to the average stress and the response of both of the proposed models match very well with the CPFE model. The stress within parts (4), (7) and (9) deviate from the average stresses, which are captured reasonably well with ROM2 particularly in parts (7) and (9). While some deviations exist between the CPFE model and the subgrain partitioned ROM2 model, the relative accuracy of the model points to the capability of the proposed approach in capturing stress concentrations within the material microstructure.

4.5.4 An arch subjected to compression

In this section, a full two-scale analysis is performed to further demonstrate the computational capabilities of the proposed reduced order model. The response of an arch made of aluminum subjected to compressive loading as illustrated in Fig. 4.21(a) is considered. The geometric model is one half of the arch with inner radius of 30 mm, outer radius of 50 mm and thickness of 5 mm. The top of the arch is cut flat, on which the displacement

along the Y direction is applied while the bottom end is fixed. The geometric model is discretized with 56 tri-linear eight-noded hexahedron elements. No comparative analysis based on either direct resolution or computational homogenization could be performed due to prohibitive cost of these approaches.

In order to limit the out-of-plane deformations due to inhomogeneity of the microstructure, a numerical RVE size convergence study is performed. The microstructure characteristics of the arch are taken to be identical to those considered in Section 6.1. Figure 4.20 shows the stress-strain curves of three different microstructures with 134, 242 and 347 grains, respectively, generated by the proposed approach and CPFE. The stress-strain curves are of single microstructures subjected to uniaxial tension. Figure 4.20 clearly demonstrates that the two larger microstructures provide near identical responses, which indicates that the 242-grain microstructure is sufficiently representative. The 242-grain microstructure is therefore used in the analysis of the arch.

Figure 4.21(b) shows the stress contour within the arch at the applied displacement magnitude of 1.425 mm. Under the applied displacement, the structure undergoes significant inelastic deformation as further evidenced by the force-displacement relationship shown in Fig. 4.22. We note that the inhomogeneity of the stress field is due to the onset of inelastic deformations rather than the microstructure inhomogeneity. No significant out-of-plane deformations are observed in the analysis.

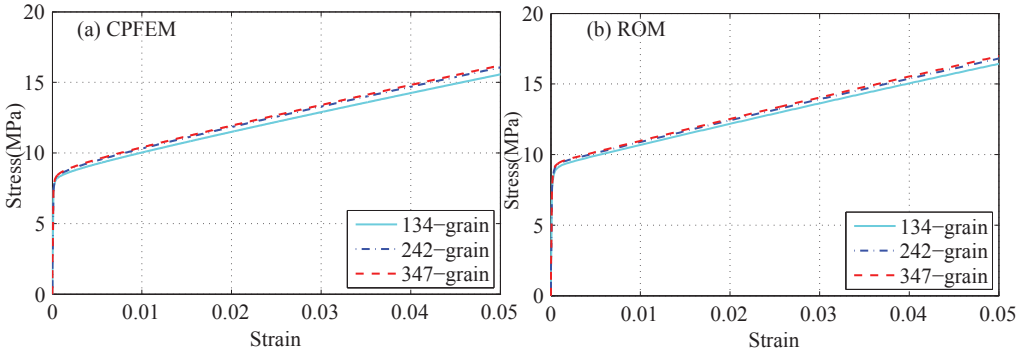

Figure 4.20: Convergence study on the number of grains in the RVE (a) CPFEM; (b) ROM.

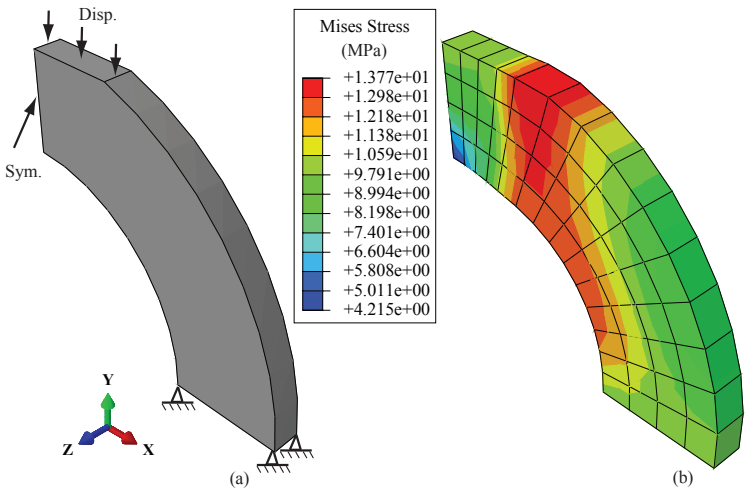

Figure 4.21: Arch: (a) mesh and boundary conditions; (b) von Mises stress contour.

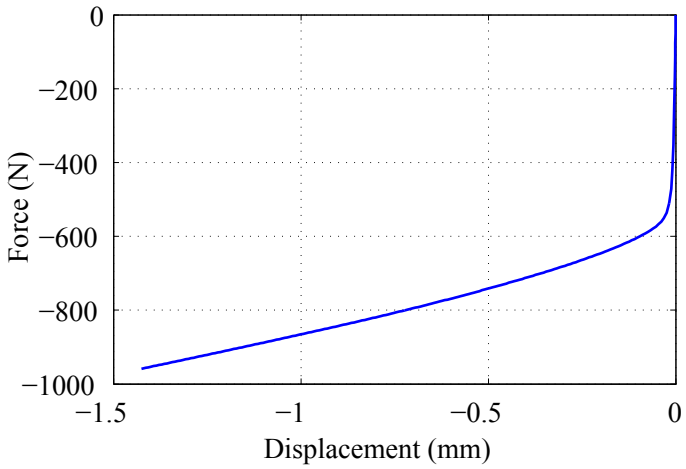

Figure 4.22: Force-displacement curve of the arch example.

4.6 Summary

This chapter presented a mathematical homogenization scheme for polycrystalline materials which is based on a two-scale asymptotic expansion and the transformation field analysis. The model formulation, computational implementation and numerical verifications were conducted to form a computation framework that can provide overall and local predictions with acceptable accuracy. The current model employs a specific flow rule (Eq. 4.8) and hardening rule (Eq. 4.9), however it is straightforward to integrate any other form of flow rule and hardening rule. Depending the partitioning schemes adopted, the model can provide either grain level or sub-grain level resolution and the sub-grain level

resolution is essential in capturing grain boundary stress risers. While utilizing the one-part-per-grain partitioning scheme, the developed model provides approximately two orders of magnitude of efficiency compared with CPFE simulations on the microstructures studied.

Chapter 5

SPARSE AND SCALABLE EIGENSTRAIN-BASED REDUCED ORDER HOMOGENIZATION MODELS FOR POLYCRYSTAL PLASTICITY

The previous chapter described the formulation, implementation and verification of the eigenstrain-based reduced order homogenization (EHM) model for polycrystal plasticity. However, it has been shown in this chapter, that the efficiency characteristics of EHM degrades as larger microstructures are considered in the chapter. Accordingly, an accelerated, sparse and scalable eigenstrain-based reduced order homogenization models for computationally efficient multiscale analysis of polycrystalline materials is proposed in this chapter. The proposed model is based on the EHM approach, and provides significant efficiency in analysis of structures composed of complex polycrystalline microstructures. The grain-cluster concept is used to identify a cluster of neighboring grains for each grain, between which the interactions (i.e., short-range interactions) are considered, whereas the interactions with grains outside the neighborhood (i.e., long-range interactions) are neglected. Computationally, this strategy introduces sparsity into the linearized reduced order system, facilitating the use of sparse solvers to achieve improved efficiency and scalability. This chapter presents the following novel contributions: (1) A sparse EHM has been formulated and a new set of concentration tensors and interaction tensors are derived by only considering interactions between each grain and a cluster of predefined neighboring grains, and enforcing the constraints derived from transformation field analysis; (2) A consistent grain-clustering scheme is proposed to identify grain cluster for each grain. We provide a thorough assessment of the performance of the sparse EHM formulation for a range of microstructure sizes using direct and iterative sparse solvers.

5.1 Analysis of EHM Scalability

Most of the computational cost of solving the reduced order microscale problem comes from constructing and solving the linearized EHM system in each N-R iteration, as well as calculating the tangent moduli by solving the linear system in Eq. (4.94). The computational cost is therefore determined by the size of the linear system (i.e., $6n$). In what follows, we study the efficiency of EHM compared with CPFE as a function of RVE size (or alternatively the order of the EHM model as model order is tied to the number of grains in this study).

In general, the number of grains in an RVE is often on the order of a few hundred depending on the complexity of the constitutive behavior and the microstructure morphology [136, 31, 178, 5, 208]. The EHM efficiency for RVE sizes within this range is evaluated using uniaxial tension test as shown in Fig. 5.1(a). The macroscale mesh consists of a single hexahedron with reduced order integration regularized with hourglass stiffness. The reference CPFE analysis is performed over the fully resolved microstructure discretized with trilinear four-noded tetrahedron elements. A direct solver is used for all reference simulations. Displacement controlled loading with a total applied strain of 5% at a strain rate of 0.05/s is applied to all simulations with the initial time step size 1.0×10^{-6} s and maximum allowable step size of 0.01 s. The investigation is conducted on a series of increasing size RVEs constructed from the same microstructure morphology and discretized using the same mesh size as shown in Fig. 5.1(b)-(h). All simulations were conducted on the same computer (Intel I7 3.0 GHz processor, 16G RAM) without parallelization and all finished in 122 increments.

Information on the number of elements (i.e., n_{element}) and nodes (i.e., n_{node}) in each microstructure as well as the simulation times (i.e., T_{CPFE} and T_{EHM}) are listed in Table 5.1. Since all microstructures are constructed using the same microstructural statistics and meshed with the same element size, number of degrees of freedom (DOF) increases linearly with the total number of grains in the microstructure. For the EHMs, the DOF

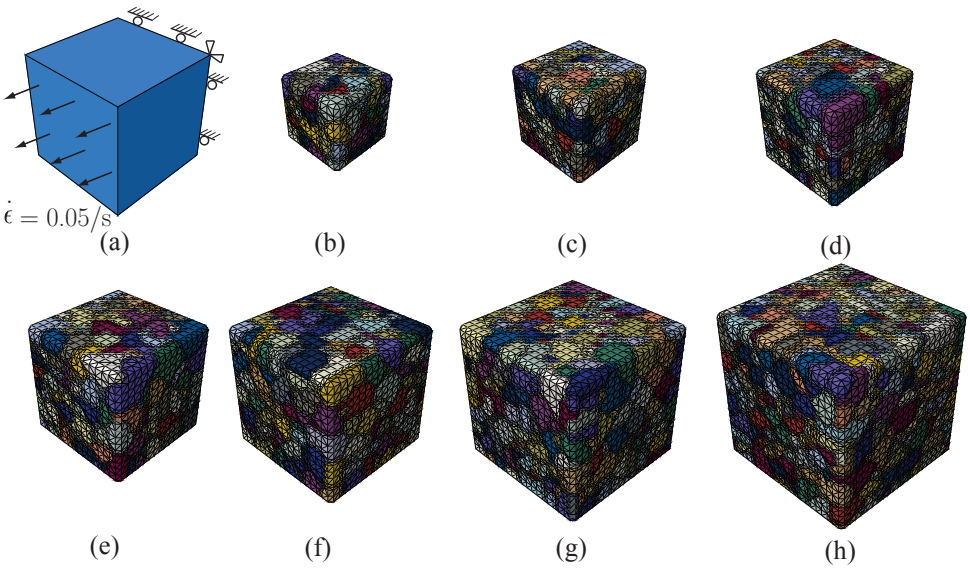

Figure 5.1: Schematic demonstration of (a) the boundary conditions, and (b-h) finite element mesh of RVEs used in the simulation with $n = 85, 154, 242, 347, 487, 629, 938$.

Table 5.1: EHM efficiency compared with direct CPFE.

n	n_{element}	n_{node}	$T_{\text{CPFE}}(s)$	$T_{\text{EHM}}(s)$	R_{DOF}	R_{Time}
85	29,369	5,627	2128.66	19.05	33.11	111.74
154	53,149	9,983	4,034.03	74.85	32.41	53.89
242	84,642	15,583	7,052.75	265.08	32.20	26.61
347	128,716	23,339	10,371.25	662.12	33.63	15.66
487	176,415	31,777	13,998.82	1,671.50	32.63	8.38
629	238,216	42,651	19,435.03	3,434.18	33.90	5.66
938	337,818	60,122	29,451.22	11,240.56	32.05	2.62

associated with the linearized system is $6n$. Since each grain constitutes a part, there is a linear relationship between total number of DOF and number of grains for the EHMs as well. Using the current microstructure statistics and mesh size, each grain is discretized into approximately 350 trilinear tetrahedron elements. The ratio of the number of DOF between CPFE and EHM (i.e., R_{DOF}) is approximately 33 for all microstructures.

The simulation times of CPFE and EHM using different microstructures are compared in Table 5.1 and Fig. 5.2. While the simulation time of CPFE increases roughly linearly with number of grains (since calculations on integration points dominate cost compared with solving the global system in the context of nonlinear FE analysis), simulation time of

EHM scales approximately with n^3. Consequently, the efficiency of EHM compared with CPFE (i.e., speedup of EHM compared to CPFE, defined by the ratio between simulation time of CPFE and EHM, R_{Time}, in Table 5.1) reduces as a function of microstructure size (Fig. 5.3(a)). Clearly, maintaining high efficiency of reduced order models within this range of RVE sizes is critical and motivates the accelerated reduced order model formulation discussed below.

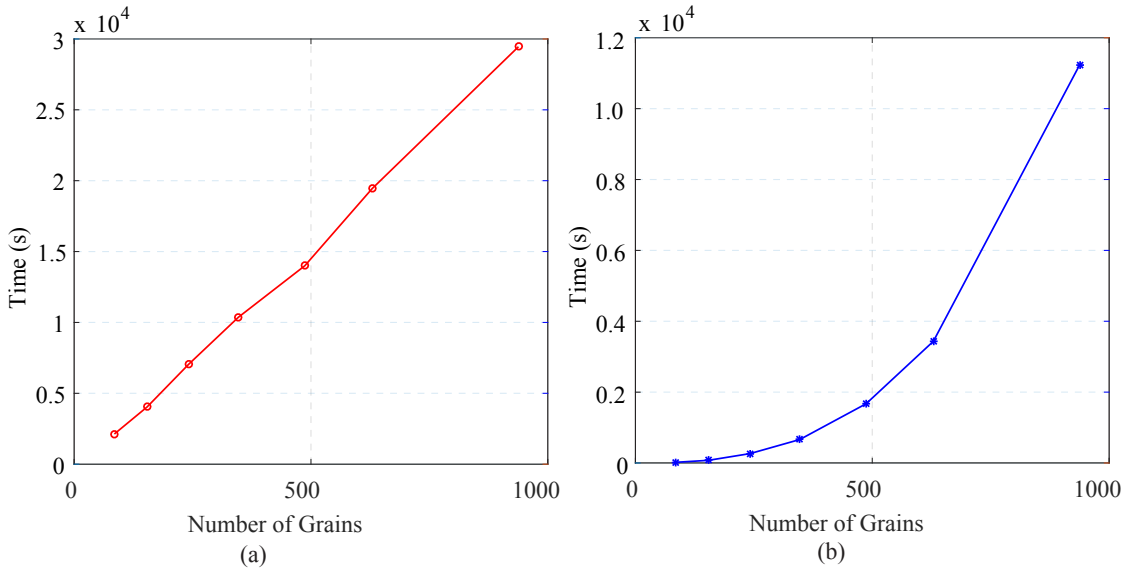

Figure 5.2: Simulation time as a function of microstructure size using (a) CPFE; and (b) EHM models. The ratio of DOF between CPFE and EHM simulations is approximately constant as a function of RVE size (see Table 5.1).

The primary cause for the efficiency degradation with increasing number of grains is the structure of the linear system in N-R iterations when solving the reduced order system and calculating the tangent stiffness. It is straightforward to see that the EHM linear system (Eq. (4.89)) is dense and unsymmetric, with a dimension of $6n$. The number of floating-point operations (FLOPs) of solving a dense unsymmetric linear system of dimension $6n$ using a direct solver (e.g., LAPACK LU decomposition routines) is $0.67(6n)^3 = 144.72n^3$ [8]. This explains the cubic increase in simulation time for the EHM.

Remark 1 *We also investigate the effect of using an iterative solver in the evaluation of the EHM model. Iterative solvers are preferred for large systems, where memory resources are*

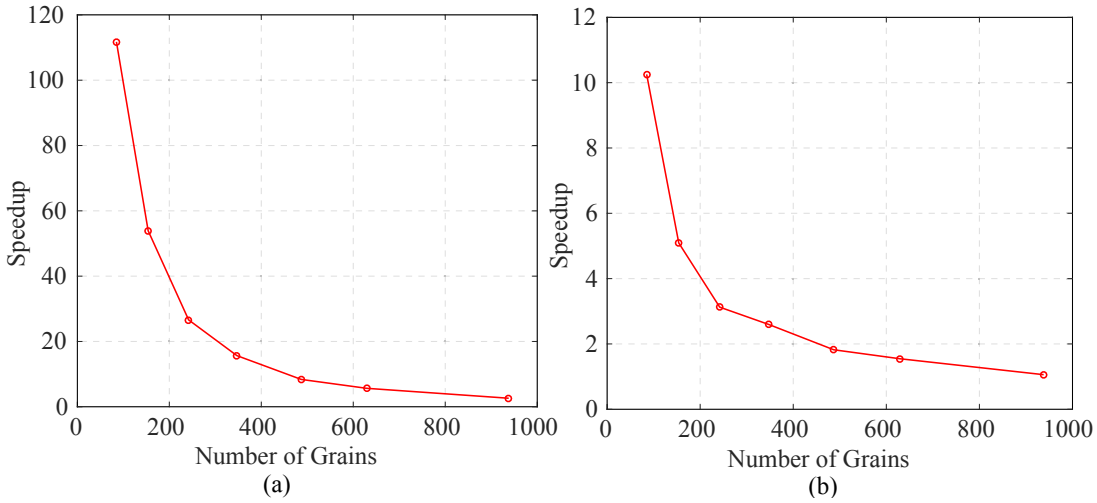

Figure 5.3: Efficiency of EHM compared with CPFE as a function of RVE size using: (a) direct solver; and (b) iterative solver to evaluate the reduced order system.

not sufficient for a direct solver, while direct solvers are advantageous in small and moderate sized problems. Direct solvers are also advantageous for problems with multiple right-hand side vectors since numerical factorization (major computational cost) needs to be conducted only once. In contrast, iterative solvers evaluate each right-hand side as a separate problem and the cost is proportional to the number of right-hand sides. Flexible General Minimum Residual method (FGMRES) [153] implemented in Intel MKL library [2] is employed in this study. The reported results are with Gauss-Seidel pre-conditioning since it provides the highest efficiency among common preconditions (Jacobi, successive over relaxation, symmetric successive over relaxation and incomplete LU decomposition-based pre-conditioning) in the current study.

Simulation time of EHM using FGMRES as linear solver is listed in Table 5.2 and the efficiency of EHM using FGMRES compared with CPFE is plotted in Fig. 5.3(b). EHM using iterative solver is less efficient than direct solver in the current example, but shows similar EHM efficiency degradation as a function of RVE size.

Table 5.2: Simulation time of EHM using FGMRES.

n	85	154	242	347	487	629	938
Time (s)	207.59	792.27	2,255.92	3,992.20	7,686.17	12,566.87	27,820.14

5.2 Sparse EHM Models.

We seek to develop reduced order models that increase efficiency compared with the full EHM, and have better scalability. This is achieved by introducing sparsity into the Jacobian matrix of the linearized EHM system. The off-diagonal components that account for the interaction between two arbitrary grains $\bar{\alpha}$ and $\bar{\beta}$ ($\bar{\beta} \neq \bar{\alpha}$) takes the form:

$$\left(\frac{\partial \phi^{(\bar{\beta})}}{\partial \sigma^{(\bar{\alpha})}}\right)_{IK} = -P_{IJ}^{(\bar{\beta}\bar{\alpha})} \sum_{s=1}^{N} \Omega^{s(\bar{\alpha})} Z_J^{s(\bar{\alpha})} Z_K^{s(\bar{\alpha})}; \;\; \bar{\beta} \neq \bar{\alpha} \tag{5.1}$$

The interaction term vanishes if $\mathbf{P}^{(\bar{\beta}\bar{\alpha})} = \mathbf{0}$ is set to zero (similarly $\frac{\partial \boldsymbol{\phi}^{(\bar{\alpha})}}{\partial \boldsymbol{\sigma}^{(\bar{\beta})}} = \mathbf{0}$ if $\mathbf{P}^{(\bar{\alpha}\bar{\beta})} = \mathbf{0}$). By neglecting the grain-to-grain interaction, two 6×6 zero blocks are introduced into the Jacobian matrix (Fig. (5.4)). A structurally symmetric sparse linear system (zero-valued components distributed symmetrically across the diagonal) is obtained through neglected interactions for a group of selected grain pairs. The sparsity of the resulting system is naturally determined by the extent of neglected interactions. The consequence of partial consideration of grain-to-grain interactions are provided in the next section.

$$\begin{bmatrix}
\frac{\partial \phi^{(1)}}{\partial \sigma^{(1)}} & \frac{\partial \phi^{(1)}}{\partial \sigma^{(2)}} & \cdots & \frac{\partial \phi^{(1)}}{\partial \sigma^{(\bar{\alpha})}} & \cdots & \frac{\partial \phi^{(1)}}{\partial \sigma^{(\bar{\beta})}} & \cdots & \frac{\partial \phi^{(1)}}{\partial \sigma^{(n)}} \\
\frac{\partial \phi^{(2)}}{\partial \sigma^{(1)}} & \frac{\partial \phi^{(2)}}{\partial \sigma^{(2)}} & \cdots & \frac{\partial \phi^{(2)}}{\partial \sigma^{(\bar{\alpha})}} & \cdots & \frac{\partial \phi^{(2)}}{\partial \sigma^{(\bar{\beta})}} & \cdots & \frac{\partial \phi^{(2)}}{\partial \sigma^{(n)}} \\
\vdots & \vdots & \ddots & \vdots & \ddots & \vdots & \ddots & \vdots \\
\frac{\partial \phi^{(\bar{\alpha})}}{\partial \sigma^{(1)}} & \frac{\partial \phi^{(\bar{\alpha})}}{\partial \sigma^{(2)}} & \cdots & \frac{\partial \phi^{(\bar{\alpha})}}{\partial \sigma^{(\bar{\alpha})}} & \cdots & \mathbf{0} & \cdots & \frac{\partial \phi^{(\bar{\alpha})}}{\partial \sigma^{(n)}} \\
\vdots & \vdots & \ddots & \vdots & \ddots & \vdots & \ddots & \vdots \\
\frac{\partial \phi^{(\bar{\beta})}}{\partial \sigma^{(1)}} & \frac{\partial \phi^{(\bar{\beta})}}{\partial \sigma^{(2)}} & \cdots & \mathbf{0} & \cdots & \frac{\partial \phi^{(\bar{\beta})}}{\partial \sigma^{(\bar{\beta})}} & \cdots & \frac{\partial \phi^{(\bar{\beta})}}{\partial \sigma^{(n)}} \\
\vdots & \vdots & \ddots & \vdots & \ddots & \vdots & \ddots & \vdots \\
\frac{\partial \phi^{(n)}}{\partial \sigma^{(1)}} & \frac{\partial \phi^{(n)}}{\partial \sigma^{(2)}} & \cdots & \frac{\partial \phi^{(n)}}{\partial \sigma^{(\bar{\alpha})}} & \cdots & \frac{\partial \phi^{(n)}}{\partial \sigma^{(\bar{\beta})}} & \cdots & \frac{\partial \phi^{(n)}}{\partial \sigma^{(n)}}
\end{bmatrix}$$

Figure 5.4: Zeros blocks in the Jacobian matrix after dropping the interaction between grain $\bar{\alpha}$ and $\bar{\beta}$.

Neglecting all grain interactions (i.e., $\mathbf{P}^{(\alpha\beta)} = \mathbf{0}$ for $\alpha = 1,2,...,n,$, $\beta = 1,2,....,n, \alpha \neq \beta$) results in a diagonal structure, providing the maximum possible computational efficiency. The resulting EHM system has n 6×6 (in 3-D) independent systems, which can be evaluated with $0.67 \times (6)^3 \times n = 144.72n$ FLOPs. The accuracy and efficiency characteristics of this model are similar to the Taylor model. Neglecting p pairs of grain-to-grain interactions results in a sparse system with the sparsity $S = 2p/n^2$.

The goal is to obtain EHM models that exhibit the highest possible sparsity without significantly compromising on the computational accuracy compared to the full EHM model. To this end, we next establish (1) the mathematical and physical consequences of eliminating certain grain-to-grain interactions; (2) the numerical procedures to determine the interactions to keep in the resulting sparse system; and (3) the numerical methodology for efficient evaluation of the sparse EHM models.

5.2.1 Coefficient tensors considering partial interactions

In the context of uniform transformation field analysis, Dvorak and Benveniste [42, 41] derived the following properties for the coefficient tensors:

$$\text{Kinematic consistency} : \sum_{\alpha=1}^{n} \mathbf{P}^{(\beta\alpha)} = \mathbf{I} - \mathbf{A}^{(\beta)} \tag{5.2}$$

$$\text{Simultaneous iso-stress/strain condition} : \sum_{\alpha=1}^{n} \mathbf{P}^{(\beta\alpha)}\mathbf{M}^{(\alpha)} = \mathbf{0} \tag{5.3}$$

$$\text{Elastic reciprocity} : \; c^{(\beta)}\mathbf{P}^{(\beta\alpha)}\mathbf{M}^{(\alpha)} = c^{(\alpha)}\mathbf{M}^{(\beta)}\mathbf{P}^{(\alpha\beta),T} \tag{5.4}$$

$$\text{Strain compatibility} : \sum_{\alpha=1}^{n} c^{(\alpha)}\mathbf{P}^{(\alpha\beta)} = \mathbf{0} \tag{5.5}$$

where, the strain compatibility comes from the requirement that the average of strains in each part is equal to the macroscale strain; the elasticity reciprocity is derived from the elastic reciprocal theorem; and simultaneous iso-stress/strain condition and kinematic consistency are obtained considering a special case where the whole domain is subjected to uniform strain and stress. In addition, the concentration tensors $\mathbf{A}^{(\alpha)}$ satisfy the Hill relation [60]:

$$\sum_{\alpha=1}^{n} c^{(\alpha)} \mathbf{A}^{(\alpha)} = \mathbf{I} \tag{5.6}$$

The new set of coefficient tensors is derived from the coefficient tensors of the full EHM by selectively considering grain-to-grain interactions (setting the transmitted interaction tensors to be zero between grains where interaction are neglected) while adopting the concept of mass lumping in finite element analysis to lump the neglected transmitted interaction tensors onto the self-induced terms (i.e., contributions from the off-diagonal components in Eq. (4.89) are lumped to the diagonal terms) and enforcing some of the constraints in Eqs. (5.2)-(5.6). By this approach, two models that either enforce the kinematic consistency and strain compatibility, or kinematic consistency and simultaneous iso-stress/strain condition are formulated. In what follows, these models are referred to as strain compatibility constrained sparse EHM (ε-EHM) and iso-stress/strain constrained sparse EHM (σ-EHM), respectively.

Below, the lumping procedures to obtain the ε-EHM and σ-EHM by eliminating the interaction between a single pair of reduced model grains ($\bar{\alpha}$ and $\bar{\beta}$) are provided. These procedures are performed for all reduced model grain pairs, whose interactions are to be neglected.

5.2.2 Strain compatibility constrained sparse EHM (ε-EHM)

Consider a pair of grains $\bar{\alpha}$ and $\bar{\beta}$, between which the interaction is to be neglected. Let $\mathbf{P}'^{(\bar{\alpha}\bar{\beta})}$ denote the new sparse set of interaction tensors, which are set to zero:

$$\mathbf{P}'^{(\bar{\alpha}\bar{\beta})} = 0, \quad \mathbf{P}'^{(\bar{\beta}\bar{\alpha})} = 0 \tag{5.7}$$

The compliance tensors remain identical to those in the full EHM:

$$\mathbf{M}'^{(\alpha)} = \mathbf{M}^{(\alpha)}, \ \alpha = 1, 2, ..., n \tag{5.8}$$

To enforce the strain compatibility (Eq. (5.5)), the effect of the neglected transmitted interaction tensors are lumped to the self-induced ones:

$$\mathbf{P}'^{(\alpha\beta)} = \begin{cases} \mathbf{0} & \{\alpha,\beta\} = \{\bar{\alpha},\bar{\beta}\} \text{ or } \{\alpha,\beta\} = \{\bar{\beta},\bar{\alpha}\} \\ \mathbf{P}^{(\bar{\alpha}\bar{\alpha})} + \frac{c^{(\bar{\beta})}}{c^{(\bar{\alpha})}}\mathbf{P}^{(\bar{\beta}\bar{\alpha})} & \{\alpha,\beta\} = \{\bar{\alpha},\bar{\alpha}\} \\ \mathbf{P}^{(\bar{\beta}\bar{\beta})} + \frac{c^{(\bar{\alpha})}}{c^{(\bar{\beta})}}\mathbf{P}^{(\bar{\alpha}\bar{\beta})} & \{\alpha,\beta\} = \{\bar{\beta},\bar{\beta}\} \\ \mathbf{P}^{(\alpha\beta)} & \text{otherwise} \end{cases} \tag{5.9}$$

Substituting Eq. (5.9) into Eq. (5.2), the new concentration tensors are obtained as:

$$\mathbf{A}'^{(\alpha)} = \begin{cases} \mathbf{A}^{(\alpha)} & \alpha \notin \{\bar{\alpha},\bar{\beta}\} \\ \mathbf{A}^{(\bar{\alpha})} + \mathbf{P}^{(\bar{\alpha}\bar{\beta})} - \frac{c^{(\bar{\beta})}}{c^{(\bar{\alpha})}}\mathbf{P}^{(\bar{\beta}\bar{\alpha})} & \alpha = \bar{\alpha} \\ \mathbf{A}^{(\bar{\beta})} + \mathbf{P}^{(\bar{\beta}\bar{\alpha})} - \frac{c^{(\bar{\alpha})}}{c^{(\bar{\beta})}}\mathbf{P}^{(\bar{\alpha}\bar{\beta})} & \alpha = \bar{\beta} \end{cases} \tag{5.10}$$

and it is trivial to verify that Eq. (5.6) holds for the new concentration tensors:

$$\sum_{\alpha=1}^{n} c^{(\alpha)}\mathbf{A}'^{(\alpha)} = \sum_{\alpha=1}^{n} c^{(\alpha)}\mathbf{A}^{(\alpha)} = \mathbf{I} \tag{5.11}$$

We next investigate the impact of the above lumping procedure on the elastic reciprocity and the simultaneous iso-stress/strain condition of the resulting system. Substituting the new coefficient tensors (Eqs. (5.8) and (5.9)) into the elastic reciprocity (Eq. (5.4)), we obtain:

$$c^{(\beta)}\mathbf{P}'^{(\beta\alpha)}\mathbf{M}'^{(\alpha)} = c^{(\beta)}\mathbf{P}^{(\beta\alpha)}\mathbf{M}^{(\alpha)} = c^{(\alpha)}\mathbf{M}^{(\beta)}\mathbf{P}^{(\alpha\beta),T} = c^{(\alpha)}\mathbf{M}'^{(\beta)}\mathbf{P}'^{(\alpha\beta),T}; \quad \alpha \notin \{\bar{\alpha},\bar{\beta}\} \text{ and } \beta \notin \{\bar{\alpha},\bar{\beta}\} \tag{5.12}$$

$$c^{(\bar{\beta})}\mathbf{P}'^{(\bar{\beta}\bar{\alpha})}\mathbf{M}'^{(\bar{\alpha})} = 0 = c^{(\bar{\alpha})}\mathbf{M}'^{(\bar{\beta})}\mathbf{P}'^{(\bar{\alpha}\bar{\beta}),T}; \ \{\alpha,\beta\} = \{\bar{\alpha},\bar{\beta}\} \tag{5.13}$$

However, in the case of $\{\alpha,\beta\} = \{\bar{\alpha},\bar{\alpha}\}$ or $\{\alpha,\beta\} = \{\bar{\beta},\bar{\beta}\}$, the reciprocity condition implies:

$$c^{(\bar{\alpha})}\mathbf{P}'^{(\bar{\alpha}\bar{\alpha})}\mathbf{M}'^{(\bar{\alpha})} = c^{(\bar{\alpha})}\mathbf{M}'^{(\bar{\alpha})}\mathbf{P}'^{(\bar{\alpha}\bar{\alpha}),T} \tag{5.14}$$

$$c^{(\bar{\beta})}\mathbf{P}'^{(\bar{\beta}\bar{\beta})}\mathbf{M}'^{(\bar{\beta})} = c^{(\bar{\beta})}\mathbf{M}'^{(\bar{\beta})}\mathbf{P}'^{(\bar{\beta}\bar{\beta}),T} \tag{5.15}$$

Substituting Eq. (5.9) and the elastic reciprocity into Eqs. (5.14) and (5.15) yields:

$$\begin{aligned} \mathbf{P}^{(\bar{\beta}\bar{\alpha})}\mathbf{M}^{(\bar{\alpha})} - \mathbf{M}^{(\bar{\alpha})}\mathbf{P}^{(\bar{\beta}\bar{\alpha}),T} = 0 \\ \mathbf{P}^{(\bar{\alpha}\bar{\beta})}\mathbf{M}^{(\bar{\beta})} - \mathbf{M}^{(\bar{\beta})}\mathbf{P}^{(\bar{\alpha}\bar{\beta}),T} = 0 \end{aligned} \tag{5.16}$$

which are not guaranteed.

Substituting the new coefficient tensors (Eqs. (5.8) and (5.9)) into the simultaneous iso-stress/strain condition, yields:

$$\sum_{\alpha=1}^{n} \mathbf{P}'^{(\beta\alpha)}\mathbf{M}'^{(\alpha)} = \sum_{\alpha=1}^{n} \mathbf{P}^{(\beta\alpha)}\mathbf{M}^{(\alpha)} = \mathbf{0}; \ \beta \notin \{\bar{\alpha},\bar{\beta}\} \tag{5.17}$$

$$\sum_{\alpha=1}^{n} \mathbf{P}'^{(\bar{\alpha}\alpha)}\mathbf{M}^{(\alpha)} = \frac{1}{c^{(\bar{\alpha})}}\left(c^{(\bar{\beta})}\mathbf{P}^{(\bar{\beta}\bar{\alpha})}\mathbf{M}^{(\bar{\alpha})} - c^{(\bar{\alpha})}\mathbf{P}^{(\bar{\alpha}\bar{\beta})}\mathbf{M}^{(\bar{\beta})}\right) \tag{5.18}$$

$$\sum_{\alpha=1}^{n} \mathbf{P}'^{(\bar{\beta}\alpha)}\mathbf{M}^{(\alpha)} = \frac{1}{c^{(\bar{\beta})}}\left(c^{(\bar{\alpha})}\mathbf{P}^{(\bar{\alpha}\bar{\beta})}\mathbf{M}^{(\bar{\beta})} - c^{(\bar{\beta})}\mathbf{P}^{(\bar{\beta}\bar{\alpha})}\mathbf{M}^{(\bar{\alpha})}\right) \tag{5.19}$$

Substituting the elastic reciprocity into Eqs. (5.18) and (5.19), again leads to Eq. (5.16). Therefore $\varepsilon-$EHM fully satisfies the constraints in Eqs. (5.2) and (5.5), whereas the constraints in Eqs. (5.3) and (5.4) are partially satisfied.

5.2.3 Simultaneous iso-stress/strain constrained sparse EHM (σ-EHM)

In addition to the strain compatibility constrained sparse EHM, we propose an alternative formulation, where the kinematic consistency and simultaneous iso-stress/strain condition are satisfied (denoted as σ-EHM). In σ-EHM, Eqs. (5.2) and (5.3) are retained.

The interaction tensors (after neglecting the interaction between grain $\bar{\alpha}$ and $\bar{\beta}$) are chosen such that the kinetic consistency in Eq. (5.3) is satisfied as:

$$\mathbf{P}'^{(\alpha\beta)} = \begin{cases} \mathbf{0} & \{\alpha,\beta\} = \{\bar{\alpha},\bar{\beta}\} \text{ or } \{\alpha,\beta\} = \{\bar{\beta},\bar{\alpha}\} \\ \mathbf{P}^{(\bar{\alpha}\bar{\alpha})} + \frac{c^{(\bar{\beta})}}{c^{(\bar{\alpha})}}\mathbf{M}^{(\bar{\alpha})}\mathbf{P}^{(\bar{\beta}\bar{\alpha}),T}\mathbf{M}^{(\bar{\alpha}),-1} & \{\alpha,\beta\} = \{\bar{\alpha},\bar{\alpha}\} \\ \mathbf{P}^{(\bar{\beta}\bar{\beta})} + \frac{c^{(\bar{\alpha})}}{c^{(\bar{\beta})}}\mathbf{M}^{(\bar{\beta})}\mathbf{P}^{(\bar{\alpha}\bar{\beta}),T}\mathbf{M}^{(\bar{\beta}),-1} & \{\alpha,\beta\} = \{\bar{\beta},\bar{\beta}\} \\ \mathbf{P}^{(\alpha\beta)} & \text{otherwise} \end{cases} \tag{5.20}$$

Substituting Eq. (5.20) into Eq. (5.2), the new concentration tensors are calculated as:

$$\mathbf{A}'^{(\alpha)} = \begin{cases} \mathbf{A}^{(\alpha)} & \alpha \notin \{\bar{\alpha},\bar{\beta}\} \\ \mathbf{A}^{(\bar{\alpha})} + \mathbf{P}^{(\bar{\alpha}\bar{\beta})} - \frac{c^{(\bar{\beta})}}{c^{(\bar{\alpha})}}\mathbf{M}^{(\bar{\alpha})}\mathbf{P}^{(\bar{\beta}\bar{\alpha})}\mathbf{M}^{(\bar{\alpha}),-1} & \alpha = \bar{\alpha} \\ \mathbf{A}^{(\bar{\beta})} + \mathbf{P}^{(\bar{\beta}\bar{\alpha})} - \frac{c^{(\bar{\alpha})}}{c^{(\bar{\beta})}}\mathbf{M}^{(\bar{\beta})}\mathbf{P}^{(\bar{\alpha}\bar{\beta})}\mathbf{M}^{(\bar{\beta}),-1} & \alpha = \bar{\beta} \end{cases} \tag{5.21}$$

We next investigate the impact of the above lumping procedure on the elastic reciprocity and strain compatibility of the resulting system. Substituting Eqs. (5.20) and (5.21) into

Eq. (5.4) yields:

$$c^{(\beta)}\mathbf{P}'^{(\beta\alpha)}\mathbf{M}^{(\alpha)} - c^{(\alpha)}\mathbf{M}^{(\beta)}\mathbf{P}'^{(\alpha\beta),T} = c^{(\beta)}\mathbf{P}^{(\beta\alpha)}\mathbf{M}^{(\alpha)} - c^{(\alpha)}\mathbf{M}^{(\beta)}\mathbf{P}^{(\alpha\beta),T} = \mathbf{0};\ \beta \notin \{\bar{\alpha},\bar{\beta}\} \tag{5.22}$$

$$\begin{aligned} c^{(\bar{\beta})}\mathbf{P}'^{(\bar{\beta}\bar{\beta})}\mathbf{M}^{(\bar{\beta})} - c^{(\bar{\beta})}\mathbf{M}^{(\bar{\beta})}\mathbf{P}'^{(\bar{\beta}\bar{\beta}),T} &= c^{(\bar{\beta})}(\mathbf{P}^{(\bar{\beta}\bar{\beta})}\mathbf{M}^{(\bar{\beta})} - \mathbf{M}^{(\bar{\beta})}\mathbf{P}^{(\bar{\beta}\bar{\beta}),T}) + \\ & c^{(\bar{\alpha})}\left(\mathbf{M}^{(\bar{\beta})}\mathbf{P}^{(\bar{\alpha}\bar{\beta}),T} - \mathbf{P}^{(\bar{\alpha}\bar{\beta})}\mathbf{M}^{(\bar{\beta})}\right) \end{aligned} \tag{5.23}$$

$$\begin{aligned} c^{(\bar{\alpha})}\mathbf{P}'^{(\bar{\alpha}\bar{\alpha})}\mathbf{M}^{(\bar{\alpha})} - c^{(\bar{\alpha})}\mathbf{M}^{(\bar{\alpha})}\mathbf{P}'^{(\bar{\alpha}\bar{\alpha}),T} &= c^{(\bar{\alpha})}(\mathbf{P}^{(\bar{\alpha}\bar{\alpha})}\mathbf{M}^{(\bar{\alpha})} - \mathbf{M}^{(\bar{\alpha})}\mathbf{P}^{(\bar{\alpha}\bar{\alpha}),T}) + \\ & c^{(\bar{\beta})}\left(\mathbf{M}^{(\bar{\alpha})}\mathbf{P}^{(\bar{\beta}\bar{\alpha}),T} - \mathbf{P}^{(\bar{\beta}\bar{\alpha})}\mathbf{M}^{(\bar{\alpha})}\right) \end{aligned} \tag{5.24}$$

Utilizing the elastic reciprocity, the above equations are written as:

$$\begin{aligned} c^{(\bar{\beta})}\mathbf{P}'^{(\bar{\beta}\bar{\beta})}\mathbf{M}^{(\bar{\beta})} - c^{(\bar{\beta})}\mathbf{M}^{(\bar{\beta})}\mathbf{P}'^{(\bar{\beta}\bar{\beta}),T} &= c^{(\bar{\alpha})}\left(\mathbf{M}^{(\bar{\beta})}\mathbf{P}^{(\bar{\alpha}\bar{\beta}),T} - \mathbf{P}^{(\bar{\alpha}\bar{\beta})}\mathbf{M}^{(\bar{\beta})}\right) \\ c^{(\bar{\alpha})}\mathbf{P}'^{(\bar{\alpha}\bar{\alpha})}\mathbf{M}^{(\bar{\alpha})} - c^{(\bar{\alpha})}\mathbf{M}^{(\bar{\alpha})}\mathbf{P}'^{(\bar{\alpha}\bar{\alpha}),T} &= c^{(\bar{\beta})}\left(\mathbf{M}^{(\bar{\alpha})}\mathbf{P}^{(\bar{\beta}\bar{\alpha}),T} - \mathbf{P}^{(\bar{\beta}\bar{\alpha})}\mathbf{M}^{(\bar{\alpha})}\right) \end{aligned} \tag{5.25}$$

which results in the same constraints as in Eq. (5.16) to ensure reciprocity.

Substituting the new coefficient tensors (Eqs. (5.20) and (5.21)) into the strain compatibility (Eq. (5.5)) yields:

$$\sum_{\alpha=1}^{N} c^{(\alpha)}\mathbf{P}'^{(\alpha\beta)} = \sum_{\alpha=1}^{N} c^{(\alpha)}\mathbf{P}^{(\alpha\beta)} = \mathbf{0};\ \beta \notin \{\bar{\alpha},\bar{\beta}\} \tag{5.26}$$

$$\sum_{\alpha=1}^{N} c^{(\alpha)}\mathbf{P}'^{(\alpha\bar{\beta})} = c^{(\bar{\alpha})}\mathbf{M}^{(\bar{\beta})}\mathbf{P}^{(\bar{\alpha}\bar{\beta}),T}\mathbf{M}^{(\bar{\beta}),-1} - c^{(\bar{\alpha})}\mathbf{P}^{(\bar{\alpha}\bar{\beta})} \tag{5.27}$$

$$\sum_{\alpha=1}^{N} c^{(\alpha)}\mathbf{P}'^{(\alpha\bar{\alpha})} = c^{(\bar{\beta})}\mathbf{M}^{(\bar{\alpha})}\mathbf{P}^{(\bar{\beta}\bar{\alpha}),T}\mathbf{M}^{(\bar{\alpha}),-1} - c^{(\bar{\beta})}\mathbf{P}^{(\bar{\beta}\bar{\alpha})} \tag{5.28}$$

Considering Eq. (4.71) and the elastic reciprocity, the above equations are written as:

$$\begin{aligned} \sum_{\alpha=1}^{N} c^{(\alpha)}\mathbf{P}'^{(\alpha\bar{\beta})} &= c^{(\bar{\beta})}\mathbf{P}^{(\bar{\beta}\bar{\alpha})}(\mathbf{M}^{(\bar{\alpha})}\mathbf{M}^{(\bar{\beta}),-1} - \mathbf{I}) \\ \sum_{\alpha=1}^{N} c^{(\alpha)}\mathbf{P}'^{(\alpha\bar{\alpha})} &= c^{(\bar{\alpha})}\mathbf{P}^{(\bar{\alpha}\bar{\beta})}(\mathbf{M}^{(\bar{\beta})}\mathbf{M}^{(\bar{\alpha}),-1} - \mathbf{I}) \end{aligned} \tag{5.29}$$

which are not guaranteed. Therefore $\sigma-$EHM fully satisfies the constraints in Eqs. (5.2) and (5.3), whereas the constraints in Eqs. (5.4) and (5.5) are partially satisfied.

Remark 2 *ε-EHM can be considered as an intermediate model between the Taylor model and the full EHM. To demonstrate this point, we first consider 0-layer ε-EHM for grain $\bar{\alpha}$ only (i.e., neglect interactions between grain $\bar{\alpha}$ and all other grains while other interactions are retained). Following Eq.* (5.10)*, the concentration tensors not related with part $\bar{\alpha}$ remain unchanged while the one related with part $\bar{\alpha}$ becomes:*

$$\begin{aligned}\mathbf{A}'^{(\bar{\alpha})} =& \mathbf{A}^{(\bar{\alpha})} + \sum_{\beta=1}^{n}\left(\mathbf{P}^{(\bar{\alpha}\beta)} - \frac{c^{(\beta)}}{c^{(\bar{\alpha})}}\mathbf{P}^{(\beta\bar{\alpha})}\right) \\ =& \mathbf{A}^{(\bar{\alpha})} + \sum_{\beta=1}^{n}\mathbf{P}^{(\bar{\alpha}\beta)} - \sum_{\beta=1}^{n}\left(\frac{c^{(\beta)}}{c^{(\bar{\alpha})}}\mathbf{P}^{(\beta\bar{\alpha})}\right)\end{aligned} \tag{5.30}$$

Substituting the kinematic consistency and strain compatibility into the above equation, we have:

$$\mathbf{A}'^{(\bar{\alpha})} = \mathbf{I} \tag{5.31}$$

While the interaction tensors not related with part $\bar{\alpha}$ remain unchanged according to Eq. (5.9)*, the new interactions related with part $\bar{\alpha}$ are calculated as:*

$$\mathbf{P}'^{(\bar{\alpha},\beta)} = \mathbf{P}'^{(\beta,\bar{\alpha})} = \mathbf{0};\ \beta = 1,2,...,\bar{\alpha}-1,\bar{\alpha}+1,...,n \tag{5.32}$$

$$\mathbf{P}'^{(\bar{\alpha},\bar{\alpha})} = \mathbf{P}^{(\bar{\alpha},\bar{\alpha})} + \sum_{\beta=1,\ \beta\neq\bar{\alpha}}^{n}\frac{c^{(\bar{\beta})}}{c^{(\bar{\alpha})}}\mathbf{P}^{(\bar{\beta}\bar{\alpha})} = \sum_{\beta=1}^{n}\frac{c^{(\bar{\beta})}}{c^{(\bar{\alpha})}}\mathbf{P}^{(\bar{\beta}\bar{\alpha})} \tag{5.33}$$

which, by considering the strain compatibility equation leads to:

$$\mathbf{P}'^{(\bar{\alpha},\beta)} = \mathbf{P}'^{(\beta,\bar{\alpha})} = \mathbf{0};\ \beta = 1,2,...,n \tag{5.34}$$

Since the above derivation only employs the kinematic consistency and strain compatibility, which always hold for $\varepsilon-$EHM coefficient tensors, neglecting interaction between

all grains by propagating the above operations on part $\bar{\alpha}$ to all parts leads to:

$$\mathbf{A}'^{(\alpha)} = \mathbf{I};\ \alpha = 1,2,...,n \tag{5.35}$$

and

$$\mathbf{P}'^{(\alpha,\beta)} = \mathbf{0};\ \alpha = 1,2,...,n,\ \beta = 1,2,...,n \tag{5.36}$$

which results in a block diagonal structure in Eq. (4.90) *and recovers the classical Taylor model.*

5.2.4 A consistent grain clustering scheme

The performance of the proposed accelerated EHM models clearly depends on the appropriate choice of the interactions to be kept within the material microstructure. In the current work, we employ a nearest neighbor algorithm to consistently eliminate weak interactions between grains that are far away from each other.

The coefficient tensors $\mathbf{P}^{(\alpha\beta)}$ represent strains in grain α caused by a unit strain applied on grain β. $\mathbf{P}^{(\alpha\beta)}$ is typically larger when the two grains are close to each other and decreases if they are away from each other. Therefore, interactions between those grains that are far from each other are neglected. Two possibilities exist for choosing the interactions to be kept: (1) distance-based; and (2) neighborhood-based. The distance-based selection accounts for the interactions between grains that are within a prescribed distance from each other. In contrast, the neighborhood-based selection relies on grain connectivity. The distance-based and neighborhood-based algorithms are nearly identical when microstructures with uniform grain sizes are considered. Significant differences could exist in microstructures with multi-modal size distributions. It may also be possible to consider a "magnitude-based criterion", where the magnitude of the coefficient tensors (defined, for instance, as the discrete norm of the coefficient tensor) compared to a tolerance determined based on the magnitude of strong interactions). In this study, the neighborhood-based se-

lection strategy is employed as further described below.

Let $\Theta_1^{(\alpha)}$ denote the domain of all grains in the immediate neighborhood of the grain, α, with domain, $\Theta^{(\alpha)}$ and constitutes the primary influence zone of grain α. The immediate neighborhood of $\Theta_1^{(\alpha)}$ is denoted as $\Theta_2^{(\alpha)}$ and constitutes the secondary influence zone of grain α. Following the same argument for higher order influence zones, n_c-layer grain cluster for grain α is defined as:

$$\Omega_{n_c}^{(\alpha)} = \Theta^{(\alpha)} \cup \bigcup_{i=1}^{n_c} \Theta_i^{(\alpha)} \tag{5.37}$$

The algorithm for constructing the grain clusters is schematically illustrated using a simplified 2D microstructure discretization as shown in Fig. 5.5. The index of each grain is illustrated in Fig. 5.5(a). For each grain within the microstructure, the boundary nodes are identified first (Fig. 5.5(b)). An element connectivity-based search is then conducted to identify all grains that contain at least one of the boundary nodes of $\Theta^{(\alpha)}$ to build $\Theta_1^{(\alpha)}$ (Fig. 5.5(c)). To build the second layer of neighbors, $\Theta_2^{(\alpha)}$, the above process is repeated by replacing $\Theta^{(\alpha)}$ with $\Theta_1^{(\alpha)}$ (Fig. 5.5(d)). Due to the periodicity condition, grains that reside near the two opposing sides (2D) or surfaces (3D) of the microstructure are considered as neighbors. Typical grain cluster patterns for different grains of this idealized 2D microstructure are shown in Fig. 5.6. Figure 5.7 illustrates the resulting one-layer and two-layer grain clusters in the context of a more realistic polycrystal microstructure topology.

5.3 Computational Implementation

The nonlinear numerical procedures for the sparse EHM models are similar to the full EHM (detailed in Ref. [207]), where the reduced order system is solved using the N-R process at each increment and each integration point of the macroscale analysis to update the stress and internal state variables (e.g., slip resistance) in each part. The focus of the

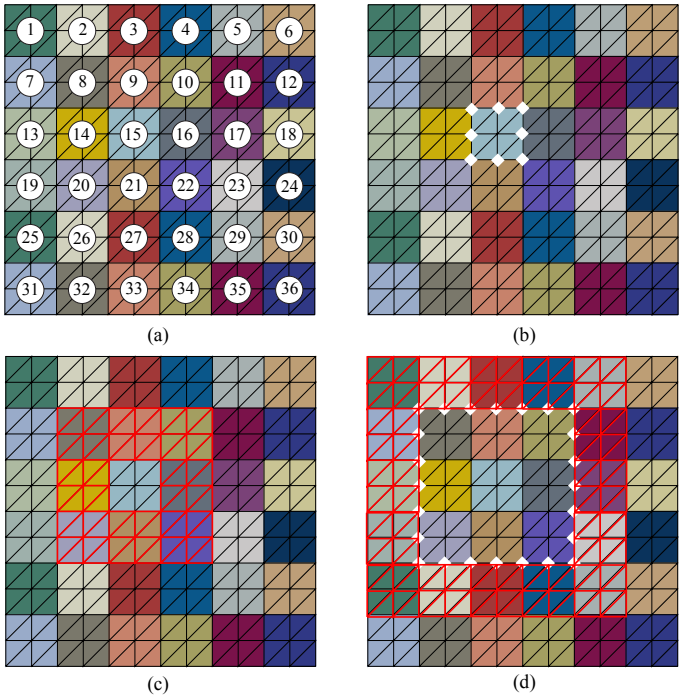

Figure 5.5: Schematic demonstration of the grain-clustering scheme in 2D: (a) mesh of the RVE with grain index; (b) identify the boundary nodes of the target grain, grain 15; (c) identify grains that contains the boundary nodes to identify the first layer of neighbor, $\Theta_1^{(15)}$; (d) find boundary nodes of the first layer neighbor, $\Theta_1^{(15)}$ to identify the second layer neighbor, $\Theta_2^{(15)}$.

current section is efficiently utilizing the sparse solver in the evaluation of the linearized system at each N-R iteration as well as the calculation of the tangent moduli.

5.3.1 Linear solution procedure for accelerated sparse EHMs

The characteristics of the linearized equations of the sparse EHM system are exploited to efficiently evaluate the reduced order models. In particular, we leverage the structural symmetry, sparsity, compressed storage and reordering of the equation system for computational efficiency.

Figures 5.8(a) and (b) show sparsity patterns of the linearized systems for the one-layer and two-layer sparse EHMs using the microstructure with 487 grains (Fig. 5.1(f)). The structural symmetry is clear when we zoom into a small region as shown in Figs. 5.8(c) and (d). This can be easily recognized by observing Eq. (4.90) and considering the fact

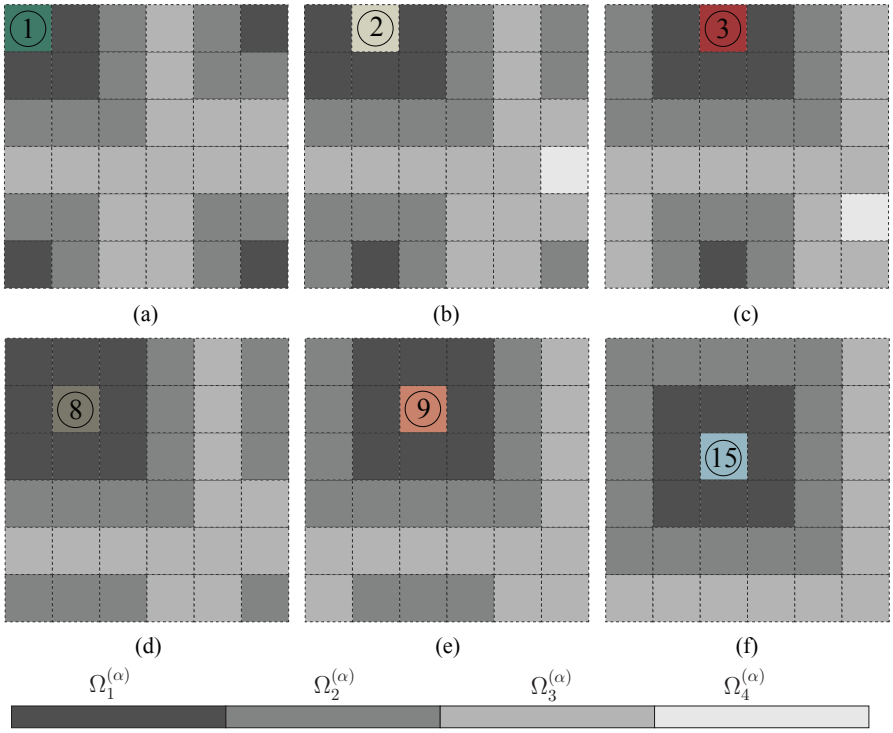

Figure 5.6: Grain clusters for: (a) grain 1; (b) grain 2; (c) grain 3; (d) grain 8; (e) grain 9; (f) grain 15.

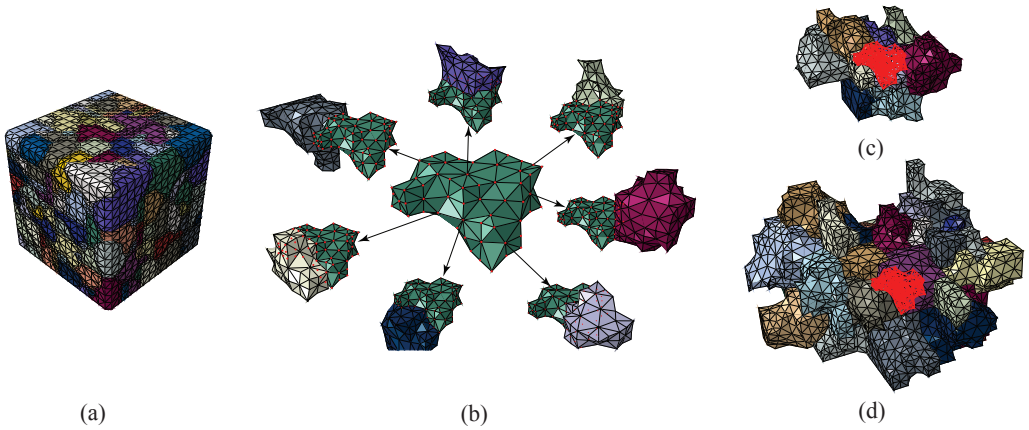

Figure 5.7: Schematic illustration of the grain clustering in 3D: (a) full microstructure; (b) first layer neighbor identification for the center grain (green colored); (c)-(d) identified one-layer and two-layer grain cluster for center grain (red-highlighted).

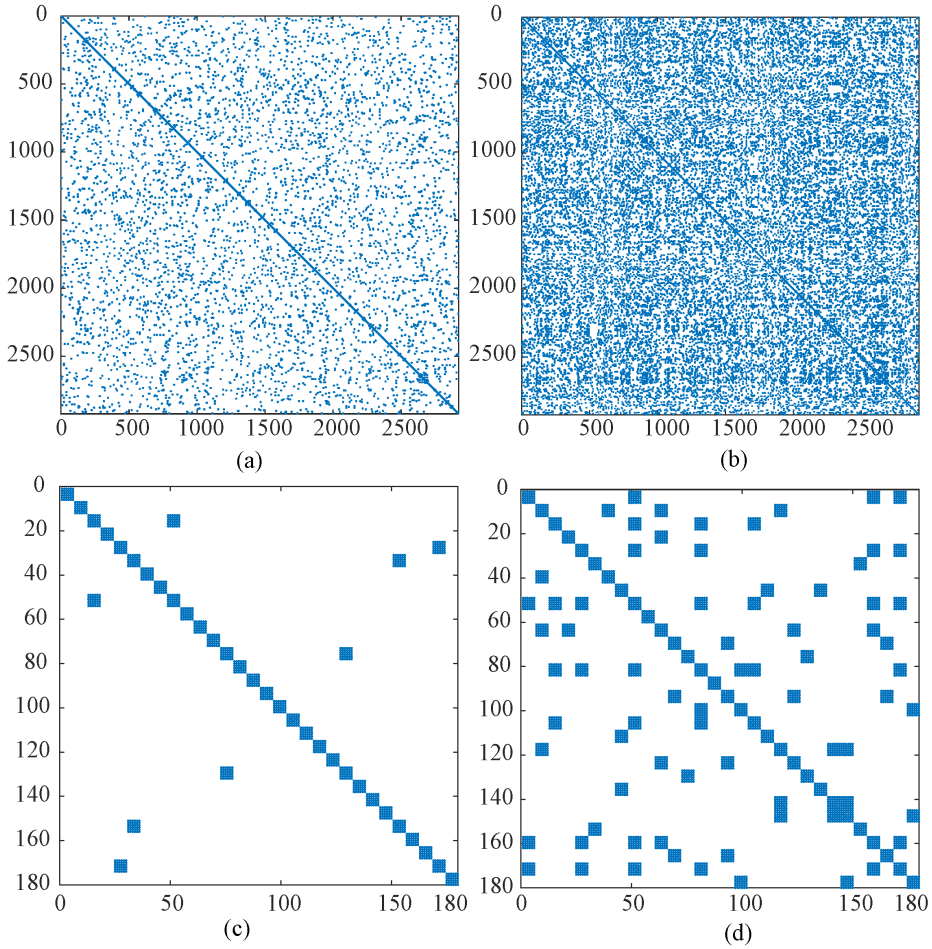

Figure 5.8: Structurally symmetric sparsity pattern of the linearized 487-grain EHM system: (a) one-layer clustering scheme; (b) two-layer clustering scheme; (c)-(d) zoom into the first 180x180 components of (a) and (b).

that $\mathbf{P}^{(\alpha\beta)}$ and $\mathbf{P}^{(\beta\alpha)}$ are simultaneously non-zero or zero at the same time depending on whether the interactions between grain α and β are kept or not.

For a given microstructure, the number of direct neighbor of a grain is independent of the size of microstructure. Given that the sparsity of the proposed models is defined by grain connectivity alone, sparsity increases as the size of the microstructure increases. For example, the above 487-grain microstructure gives sparsity of $S = 0.9764$ for the 1-layer sparse EHM and $S = 0.8906$ for the 2-layer sparse EHM. For the 938-grain microstructure (Fig. 5.1(h)), $S = 0.9875$ for the 1-layer sparse EHM and $S = 0.9397$ for the 2-layer sparse EHM. The increasing sparsity as a function of microstructure size indicates higher effi-

$$\mathbf{A} = \begin{bmatrix} a_{11} & a_{12} & 0 & a_{14} \\ 0 & a_{22} & a_{23} & 0 \\ a_{31} & 0 & a_{33} & a_{34} \\ a_{41} & 0 & 0 & a_{44} \end{bmatrix} CRS \begin{cases} Column\ index: & ja(nnz) = & 1 & 2 & 4 & 2 & 3 & 1 & 3 & 4 & 1 & 4 \\ Values: & a(nnz) = & a_{11} & a_{12} & a_{14} & a_{22} & a_{23} & a_{31} & a_{33} & a_{34} & a_{41} & a_{44} \\ Row\ pointer: & ia(N+1) = & 1 & 4 & 6 & 9 & 11 & & & & & \\ & N = 4 \;\; nnz = 10 & & & & & & & & & & \end{cases}$$

Figure 5.9: Illustration of the CRS format of a sparse matrix.

ciency of the sparse EHM at larger microstructure sizes, which is discussed further below.

Figure 5.9 demonstrates the compressed row storage (CRS) format of a sparse matrix employed in this study, which significantly decreases the storage requirements proportional to the system sparsity. Figure 5.10 shows the reordered one-layer and two-layer sparse EHM systems for the 487-grain microstructure (Fig. 5.8) using the reverse Cuthill-McKee ordering and approximate minimum degree ordering schemes. While the former is intended to reduce the bandwidth of the matrix [37], the latter aims at producing factors with relatively low fill-in operations for efficient calculation [4] and is employed in the current study. Since the system sparsity structure remains unchanged throughout the multiscale analysis, the CRS format construction and reordering of the sparse linear system is performed only once at the beginning of the analysis.

Both direct and iterative solvers are available for sparse systems. For the direct sparse solver, PARDISO ([140, 139]) is used. PARDISO stands for Parallel Sparse Direct Solver and is an LU decomposition-based high-performance linear solver for solving large sparse linear system of equations. PARDISO splits the solving process into four sequential tasks: analysis and symbolic factorization, numerical factorization, forward and backward substitution and a final termination to release all internal solver memory. These four separate procedures allow the flexibility to conduct certain operations only once and to be used multiple times later on as discussed next since the sparsity pattern of the linear system remains unchanged throughout the macroscale analysis. For the iterative solver, we use FGMRES and GS preconditioning as discussed in Section 2. While direct sparse solvers can save some operations when solving different systems (e.g., linear system from different N-R

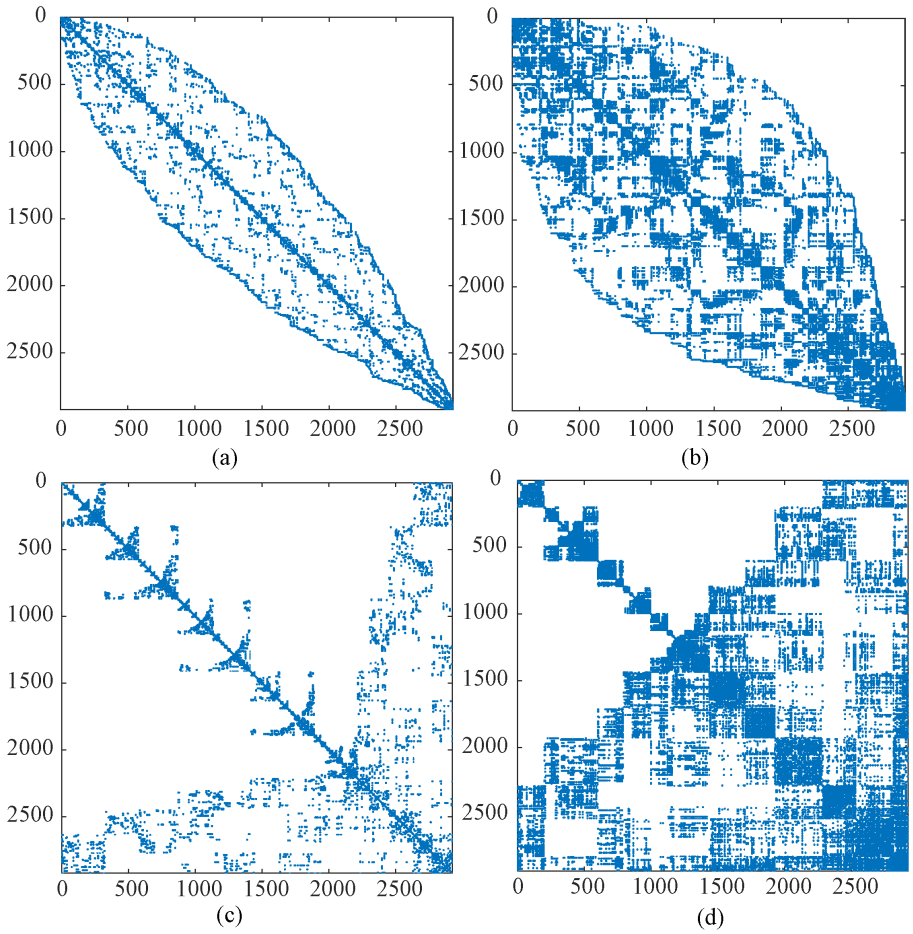

Figure 5.10: Reordering of the sparse EHM system: (a)-(b) reverse Cuthill-Mckee ordering of the one-layer and two-layer sparse EHM system; (c)-(d) approximate minimum degree ordering of the one-layer and two-layer sparse EHM system.

iterations) with the same sparsity pattern, iterative sparse solvers could not. This requires different treatment when embedding the direct and iterative sparse solvers into EHM for maximum efficiency. Since the focus in this work is to introduce and leverage the sparsity, we do not employ the parallelism in either solvers and only use them as serial solvers.

5.3.2 Efficient embedding of direct sparse solver into EHM

Figure 5.11 shows the implementation strategy for the sparse EHM approach using the sparse linear solvers discussed above. The implementation is performed in two stages (1) preprocessing; and (2) multiscale analysis. In the preprocessing stage, the grain clus-

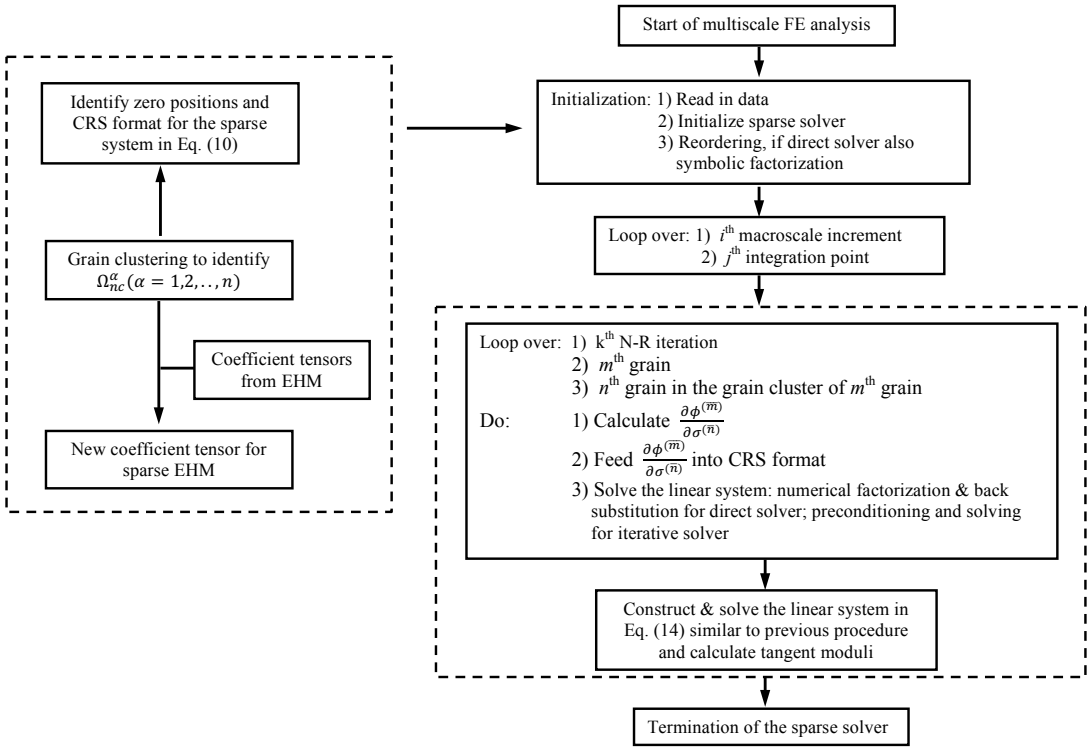

Figure 5.11: Schematic demonstration of the embedding of the sparse solver: left, preprocessing and right, multiscale analysis.

tering procedure is conducted on the microstructure to identify the grain cluster, Ω_{nc}^{α}, for each grain. The lumping procedures elaborated in Section 3 are performed for each grain to obtain the coefficient tensors for the sparse EHM. The grain clustering information is further utilized to identify sparsity pattern of the linear system and construct the CRS.

At the onset of the multiscale analysis, all material data is read and the sparse solver is initialized. At each integration point of each increment of the multiscale analysis, the reduced order system is solved using the N-R procedure and the tangent moduli is calculated (right dashed box in Fig. 5.11). At the end of the multiscale analysis, the sparse solver is terminated.

When initializing the sparse solver, the sparsity pattern of the system is used to identify the positions of non-zero blocks of the linear system and to conduct the reordering of the system. In the case of direct solver, symbolic factorization is also conducted once since it only depends on the sparsity pattern. At each N-R iteration (right dashed box in Fig. 5.11),

only non-zero blocks of the Jacobian (Eq. (4.89)) are calculated to directly feed the CRS, and passed to the linear solver. While the number of FLOPs for constructing a full EHM system scales with $(6n)^2$, the number of FLOPs for constructing a sparse EHM system scales with $(6n)^2 * (1 - S)$.

In the case of direct solver, only numerical factorization and back substitutions are needed to solve the system at each iteration, allowing computational cost savings on the analysis, reordering and symbolic factorization. The number of FLOPs needed for numerical factorization and back substitution in the full EHM is $O((6n)^3)$. Number of FLOPs needed for the same operations on the sparse EHM, while dependent on the level and pattern of sparsity, is typically far less than $O((6n)^3)$. In the case of iterative solver, a complete preconditioning and solving is necessary for each N-R iteration to obtain the solution. While it is generally difficult to theoretically estimate the number of FLOPs of an iterative solver, system sparsity contributes to the overall efficiency as demonstrated by the numerical examples below.

Upon convergence, a similar procedure is taken to evaluate Eq. (4.94) for the tangent moduli calculation. Although Eq. (4.94) has six right-hand side vectors, one numerical factorization (major computation cost) and six back-substitutions (minor computation cost) are performed in the direct solver. In the case of iterative solver, computational cost is directly proportional to the number of right-hand side vectors.

5.4 Numerical Verification

The verification of the sparse reduced order homogenization based crystal plasticity model is performed using two sets of examples. The examples aim at probing the accuracy and efficiency characteristics of the proposed sparse EHM models as compared with CPFE as well as full EHM. The first set of examples compare different sparse EHM models (one-layer and two-layer, strain compatibility or simultaneous iso-stress/strain constrained) with CPFE and full EHM on single phase polycrystal microstructures. While the accuracy

Table 5.3: Inelastic parameters [108].

m	$\dot{\gamma}_0(s^{-1})$	h_0 (MPa)	g_0^s (MPa)	$g_{sa,0}^s$ (MPa)	m'	$\dot{\gamma}_{s0}(s^{-1})$
0.05	1.0	20.4	3.7	30.8	0.0	5.0×10^{10}

of different sparse EHM models are evaluated in terms of overall stress-strain response and local stress distributions, we particularly focus on the assessment of efficiency of the proposed models. The second set of examples evaluate the performance of sparse EHM on two-phase polycrystal microstructures in order to quantify accuracy in the presence of high phase property contrast. A multiscale example is also provided to demonstrate the capability of sparse EHM in solving a large polycrystalline structure.

5.4.1 Single phase polycrystals

The material considered is pure aluminum which has FCC lattice and 12 $\{111\}\langle 111\rangle$ slip systems. The elastic parameters are $C_{11} = 108.2$ GPa, $C_{12} = 61.3$ GPa, $C_{44} = 28.5$ GPa, while the remainder of the inelastic parameters are listed in Table 5.3. The RVE is taken to consist of 487 grains and the microstructure is shown in Fig. 5.1(f). The microstructure is loaded uniaxially along X direction up to 5% strain at strain rate of 0.05/s. The finite element discretization of the reference CPFE model is composed of 176,415 trilinear four-noded tetrahedron elements with 31,777 nodes, resulting in a system with 95,331 DOF. The CPFE models with tri-linear tetrahedral elements are known to exhibit some volumetric locking [32]. The CPFE simulations were checked for the existence of checkerboard patterning in the pressure contours [1]. The checkerboard patterning was observed to be very small indicating a minor effect of volumetric locking. The partitioning of the proposed reduced order models were performed such that each part coincides with a single grain (i.e., n= 487) leading to a nonlinear system with 2,922 degrees of freedom. The macroscale discretization of the multiscale model consists of a single tri-linear eight-noded hexahedron element.

The overall stress-strain response obtained by the CPFE, full EHM and the ε-EHM

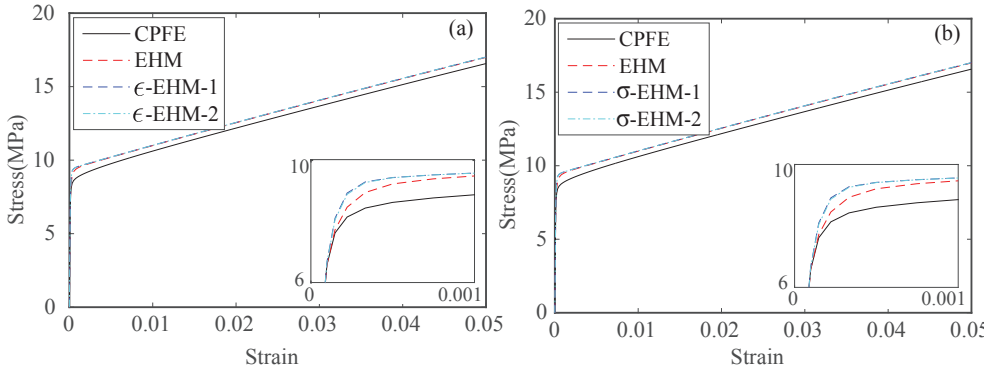

Figure 5.12: Overall stress-strain response comparison between CPFE, EHM and: (a) ε-EHMs; (b) σ-EHMs.

models are shown in Fig. 5.12(a), in which -1 and -2 indicate the 1-layer and 2-layer sparse EHM, respectively. The comparison between CPFE, full EHM and σ-EHM models are shown in Fig. 5.12(b). Under the uniaxial loading, both ε-EHM and σ-EHM models provide almost identical results to the full EHM model, indicating the relative insignificance of the grain interactions on the overall response in this example. The discrepancy between the EHM and CPFE models is about 3% at the end of the simulation.

The normalized stress distributions at the grain-scale, computed with the CPFE and the EHM models are shown in Fig. 5.13. The normalized stress refers to the Von Mises stress within a grain normalized with the initial strength, g_0 in Fig. 5.13(a,b). Similarly, the normalized stresses transverse to the loading direction (σ_{22}/g_0) are compared in Fig. 5.13(c,d). The figures display the volume fraction of grains within the microstructure as a function of the normalized stress experienced by the grains, in the form of a histogram. For clarity, the bin plot representation is included only for the CPFE model. The data points on the line plots for the EHM models refer to the mid-point of the stress range associated with each bin of the histogram plot. The ε-EHM-0 is identical to the Taylor model as stated in Remark 2. The local normalized stress distributions predicted by ε-EHM-0 have a larger error compared to the other EHM models, especially in the transverse direction. The stress distributions for the remainder of the EHM models match the CPFE results with reasonable accuracy. While the Von-Mises stresses for the ε-EHM-1,2 and σ-EHM-1,2 models

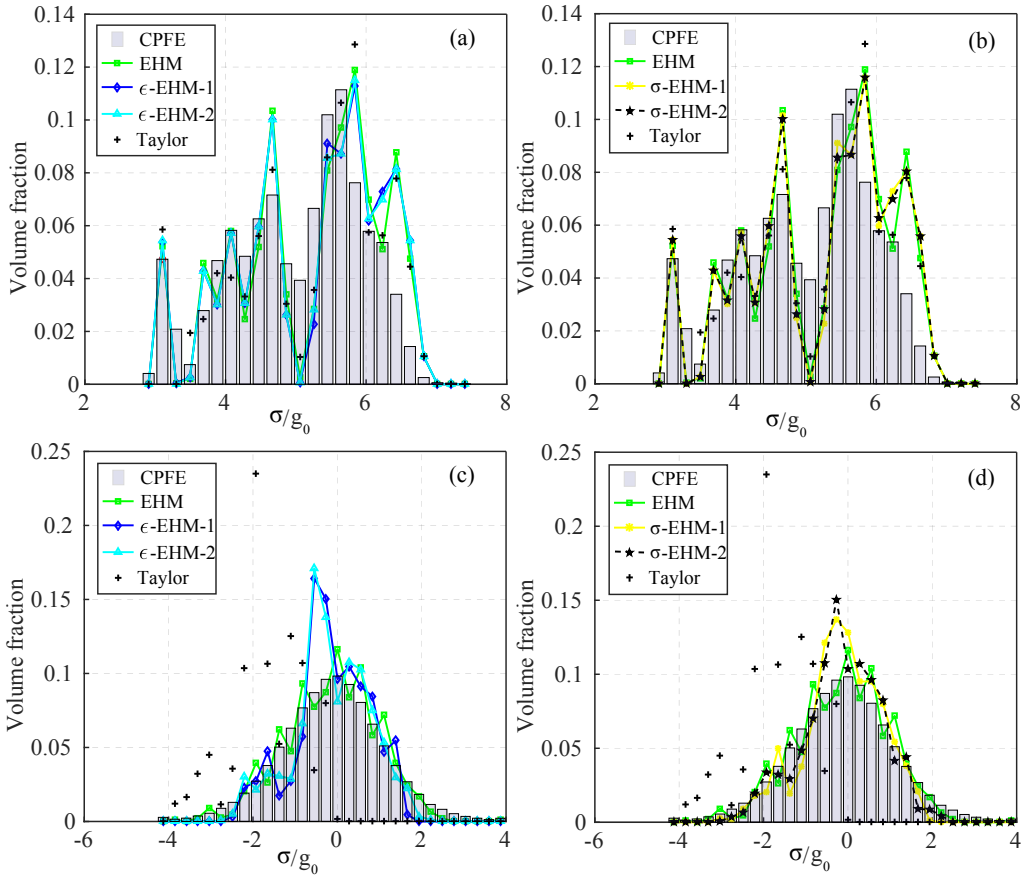

Figure 5.13: Local normalized stress distribution: (a)-(b) Von Mises stress; (c)-(d) stress component σ_{22}.

are very similar, transverse stresses indicate some variation with slightly better accuracy in the σ-EHM models. The accuracy of the EHM models in capturing the local stress distributions could be further improved by increasing the reduced model order by partitioning the grains with more than a single part as discussed in Ref. [207].

We also compared the response of different EHM models and the CPFE model under simple shear loading up to 5% strain loaded at a strain rate of 0.05/s. The overall stress-strain responses are shown in Fig. 5.14(a) and the local responses are shown in Fig. 5.14(b). The behavior and accuracy characteristics of the EHM models are similar to the cases discussed above. For the overall response, the discrepancy between the stress magnitudes computed by the full EHM and the CPFE models at the end of the simulation is approximately 2.5%, while ε-EHM-1 and ε-EHM-2 results show a discrepancy of 2.7% compared

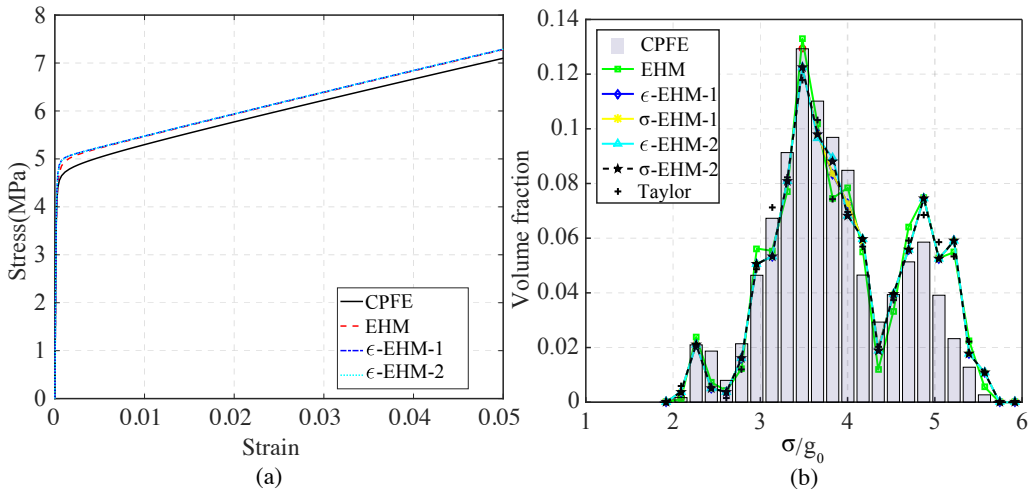

Figure 5.14: The 487-grain under simple shear: (a) Overall stress strain response; (b) Normalized Von Mises stress distribution.

with the CPFE results.

The efficiency characteristics of the EHM models are assessed by performing simulations with varying microstructural complexity (parameterized by the RVE size) as shown in Fig. 5.1(b)-(h). The speedup of different EHM models compared with CPFE are listed in Table 5.4 and plotted in Fig. 5.15. One-layer sparse EHM models (i.e., ϵ-EHM-1 and σ-EHM-1) provide significant speedup compared with full EHM and a much slower efficiency degradation as the microstructure size increases. From the 85-grain to the 938-grain RVE, speedup of full EHM reduces by a factor of 44.1, while the ϵ-EHM-1 only reduces by a factor of 5.8 and theϵ-EHM-2 reduces by a factor of 8.4. For a 938-grain microstructure, the one-layer sparse EHM models provide speedup of 48 compared with the direct CPFE simulation.

To investigate the effect of sparsity, we compare the efficiency of different sparse EHM compared with the full EHMs. To ensure a fair comparison between full EHM and different sparse EHM models, we first confirmed that all models compared have similar number of load increments and iterations at the micro- and macroscopic scales. All analyses consist of approximately 122 load increments, and 246 macroscale iterations, resulting in a total of 2050 microscale iterations. The fluctuations in number of iterations in different models

Table 5.4: Speedup of EHM and sparse EHM models compared with CPFE.

n	R_{EHM}	$R_{\epsilon\text{-EHM-1}}$	$R_{\sigma\text{-EHM-1}}$	$R_{\epsilon\text{-EHM-2}}$	$R_{\sigma\text{-EHM-2}}$
85	111.74	279.35	258.96	120.13	118.46
154	53.89	200.20	197.26	68.40	67.45
242	26.61	164.51	166.06	64.66	64.50
347	15.66	116.05	113.69	45.11	43.92
487	8.38	85.08	83.72	34.96	34.55
629	5.66	70.24	68.22	26.11	25.67
938	2.62	48.15	48.36	14.31	14.72

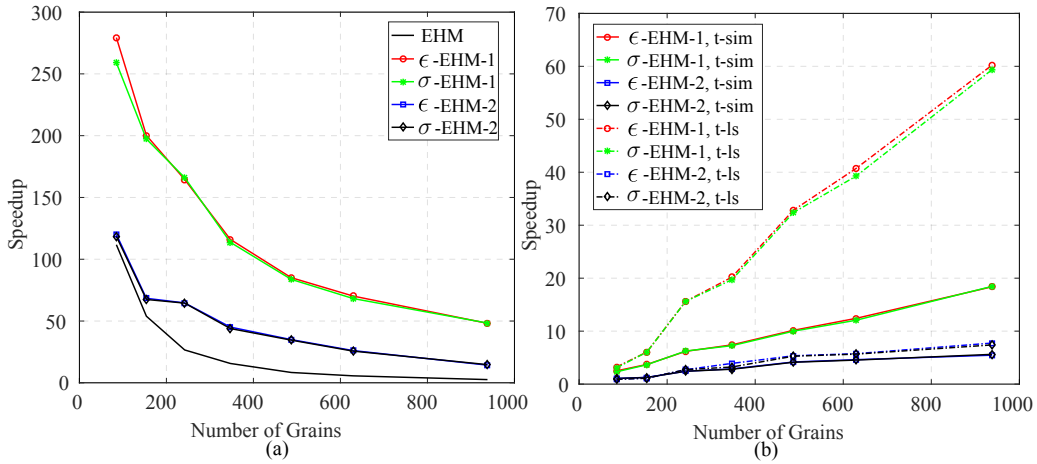

Figure 5.15: Speedup of: (a) EHM and sparse EHM models compared with the CPFE model; (b) sparse EHM models compared with the full EHM model.

are within 5% compared with the above values. The speedup of sparse EHMs compared with the full EHM (defined by the ratio between simulation time of full EHM and sparse EHM models) are plotted in Fig. 5.15(b), together with the speedup of linear solver portion (accumulated CPU time spent for linear solver in N-R iterations). It is observed that the speedup of one-layer sparse EHM compared with full EHM increases linearly as the number of grains increases. The speedup of the two-layer sparse EHM compared with EHM, shows a sub-linear relationship with number of grains. This is because sparsity decreases fast from the one-layer sparse EHM to the two-layer sparse EHM, and the FLOPs for solving a sparse linear system increase fast with decrease in sparsity. The behavior of speedup for the linear solver portion is generally similar to the total simulation times, the curves display much higher slopes. This is because the other procedures (i.e. computation of slip

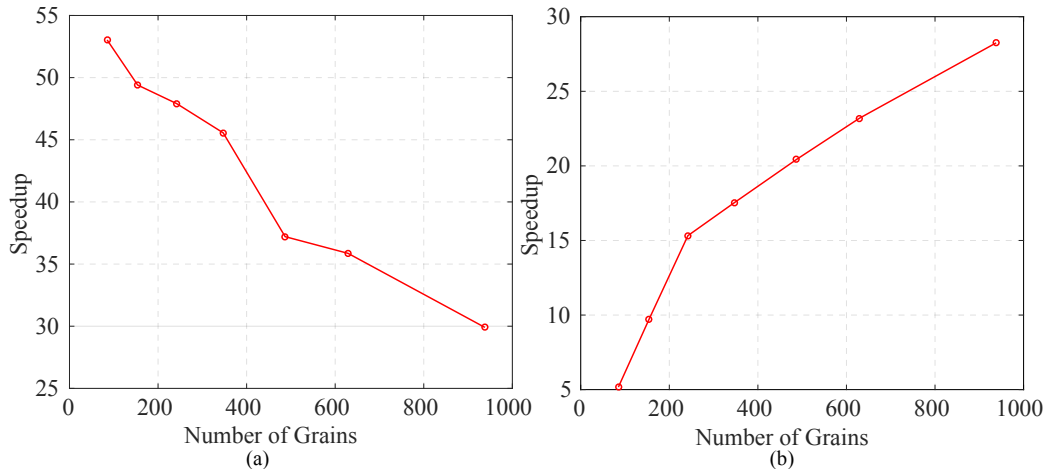

Figure 5.16: Speedup of ε-EHM-1 using iterative solver compared with: (a) CPFE model and (b) full EHM model using iterative solver.

and hardening evolution, matrix constructions etc.) are of similar order for all models, including the full EHM and sparse EHM.

Figure 5.16 shows the efficiency of ε-EHM-1 using the iterative solver as a function of RVE size. It clearly shows that sparsity also significantly increases the efficiency of EHM when using the iterative solver, while the speedup is less than that of direct solver in the cases we studied. For both direct and iterative solvers, the sparse EHM scales larger than $O(n)$ observed in the CPFE model. This implies that there may exist a trade-off point, for which the sparse EHM model performance could degrade below the performance of the CPFE model. However, the number of grains to reach this trade-off point is beyond microstructure sizes typically needed to define a representative volume.

5.4.2 Two-phase polycrystals

The accuracy characteristics of the reduced order microstructure models degrade as a function of the property contrast between constituents. For example, Taylor's hypothesis generally performs well in single-phase materials exhibiting moderate crystal anisotropy, but yields too stiff response for multiphase materials with higher anisotropy or hexagonal symmetry [96]. In single phase materials such as discussed in the above example, the

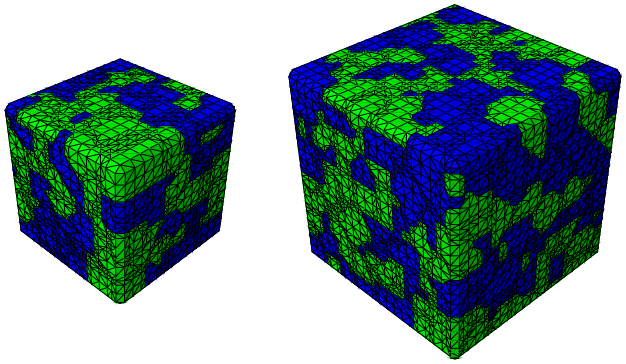

(a) (b)

Figure 5.17: Two-phase microstructures with: (a) 242-grain microstructure; (b) 629-grain microstructure rendered with green for phase 1 and blue for phase 2.

material property contrasts are relatively small. In the current example we consider a two-phase FCC material where the two phases have significant property contrast.

Figure 5.17 illustrates the morphology of the two microstructures employed in this example. The microstructures consist of 242 and 629 grains. Each grain within the microstructures is randomly assigned to one of the two phases. The volume fraction of each phase is approximately 0.5. The material parameters of the two phases are listed in Table 5.5. In all simulations considered below, phase 1 parameters are fixed (first row in Table 5.5). Two cases of simulations are considered, in which all the grains in phase 2 are assigned either the "low contrast" parameters (second row in Table 5.5) or the "high contrast" parameters (third row in Table 5.5).

To evaluate the accuracy of different sparse EHM formulations (i.e., ε-EHM and σ-EHM) in the two-phase polycrystal case, we first use the 242-grain microstructure as shown in Fig. 5.17(a). The material properties for phase two are taken to have the smaller phase contrast (row 2 of Table 5.5). The microstructure is loaded uniaxially along the X direction up to 5% strain at a strain rate of 0.05/s. The overall stress-strain response of the two different formulations compared with CPFE and full EHM are shown in Fig. 5.18, which shows increasing predicted stress from CPFE to full EHM to one-layer and two-layer sparse EHM. The discrepancies between the full EHM and the sparse EHM are more

Table 5.5: Inelastic parameters for different phases.

Phase ID	m	$\dot{\gamma}_0(s^{-1})$	h_0 (MPa)	g_0^s (MPa)	$g_{sa,0}^s$ (MPa)	m'	$\dot{\gamma}_{s0}(s^{-1})$
1	0.05	1.0	20.4	3.7	30.8	0.0	5.0×10^{10}
2 (low contrast)	0.05	1.0	50.0	10.0	30.8	0.0	5.0×10^{10}
2 (high contrast)	0.05	1.0	200.0	30.0	50.0	0.0	5.0×10^{10}

distinguishable in the two-phase microstructure, while they are nearly identical in the case of single phase polycrystals. The local response in terms of the spatial distribution of the Von Mises stress computed with, sparse EHM, CPFE and full EHM are shown in Fig. 5.19. The predictions from ϵ-EHM and σ-EHM are very similar and closely match those of the CPFE and full EHM. While the differences between one-layer sparse EHM and full EHM are relatively larger than that in the single phase microstructure, the differences between one-layer sparse EHM and two-layer EHM are still very small. The full EHM, one-layer and two-layer sparse EHM all provide better local stress predictions than Taylor model compared with CPFE simulation.

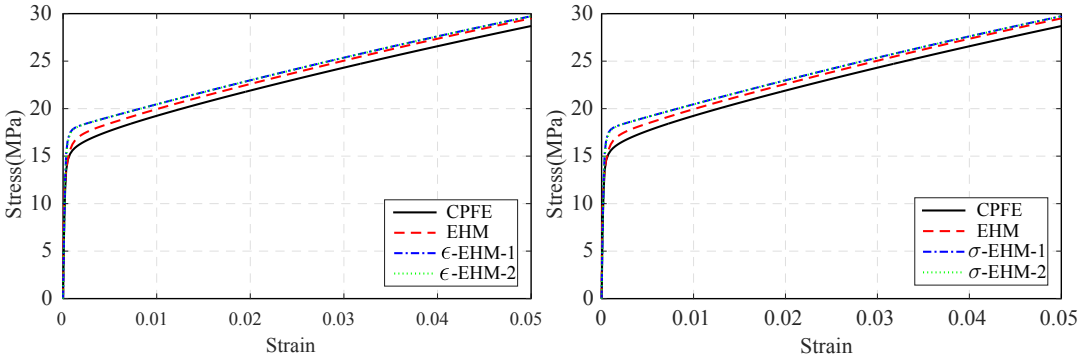

Figure 5.18: Overall response comparison of the low phase contrast 242-grain microstructure between CPFE, full EHM and: (a) ϵ-EHMs; (b) σ-EHMs.

The above mentioned investigation is repeated in the presence of a higher phase contrast (i.e., material properties of phase two taken to be row 3 of Table 5.5). The stress-strain response of the higher phase contrast case is shown in Fig. 5.20(a), along with the corresponding local stress distributions (Fig. 5.20(b)). The one-layer and two-layer sparse EHM provide almost identical results, yet the discrepancies between the sparse EHMs,

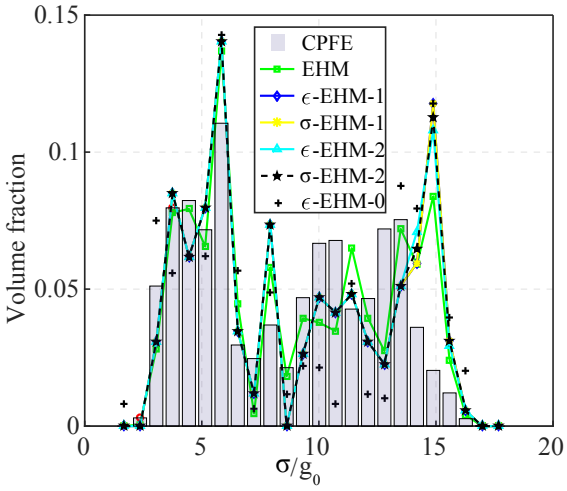

Figure 5.19: Von Mises stress distribution comparison of the 242-grain microstructure with low phase contrast.

full EHM and CPFE are more distinguishable. The stress level from full EHM is 6.4% higher than the CPFE, whereas one-layer and two-layer sparse EHMs are 8.3% higher than CPFE. Similar discrepancies between the sparse EHMs, full EHM and CPFE in the local stress distributions are observed. At the end of the analyses of the low contrast case shown in Fig. 5.18, the stress magnitude from full EHM is 2.8% higher than the CPFE, whereas one-layer and two-layer sparse EHMs are 3.6% higher than CPFE. In the higher phase contrast case shown in Fig. 5.20, the stress magnitude from full EHM is 5.8% higher than the CPFE, whereas one-layer and two-layer sparse EHM models are 8.3% higher than the CPFE. This comparison indicates that higher phase contrast increases the discrepancy between full EHM and CPFE as well as the discrepancy between full EHM and sparse EHMs. Increase in the property contrast has been previously shown to degrade the full EHM accuracy (Ref. [205]). The current results indicate that the accuracy of sparse EHMs also degrades compared to the full EHM as a function of property contrast. The reduction in the accuracy of sparse EHMs compared to the full EHM is attributed to the increasing role of grain interactions (i.e., longer range stresses within the microstructure), which are partly neglected in the sparse EHM models.

Fig. 5.21 illustrates the accuracy characteristics of the proposed models under different

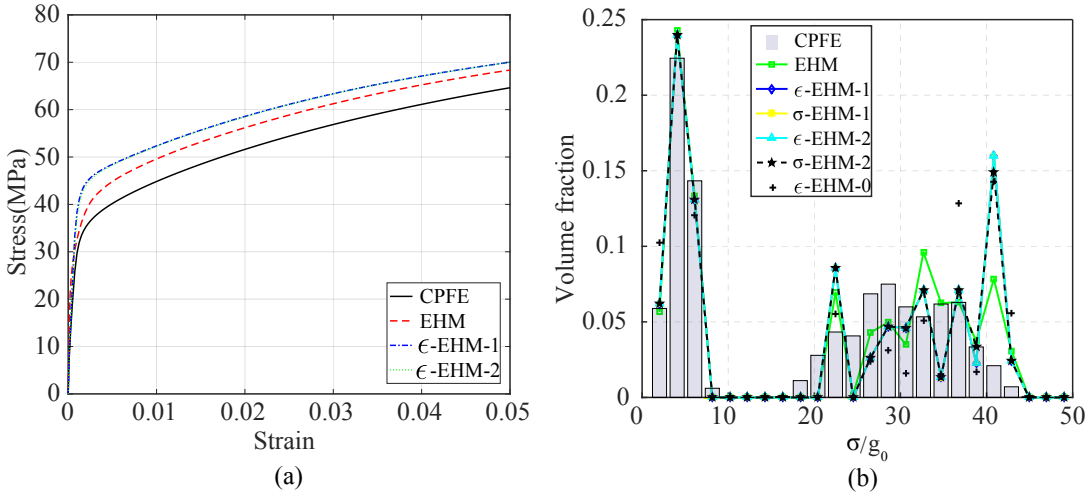

Figure 5.20: Response of the 242-grain microstructure with high phase contras: (a) overall stress-strain; (b) local Von Mises stress distribution.

loading conditions. We consider biaxial tension with either monotonic loading or cyclic loading conditions for the 629-grain microstructure (Fig. 5.17(b)) using the above higher contrast two-phase material. The figure shows the overall stress-strain response along the X and Y directions. For the biaxial monotonic tension with proportional loading, 5% strain is applied along the X direction with a strain rate of 0.005/s, while a 3% strain is applied along the Y direction with a strain rate 0.003/s (Fig. 5.21(a,b)). Compared with the CPFE, the full EHM exhibits errors of 9.36% and 14.13% at 1% strain for X and Y directions, respectively. ε-EHM-1 and ε-EHM-2 show similar accuracy with the full EHM with 11.01% and 15.06% error. At the end of the simulation, the full EHM as well as the sparse EHM models display stress errors less than 1% and 6.5% along the X and Y directions, respectively. For the non-proportional biaxial loading case, 6% maximum strain is applied along the X direction with a constant strain rate of 0.04/s. Upon reaching the maximum strain, the loading is held constant at 6% until the end of the simulation. Along the Y direction, the microstructure is cyclically loaded with an R-ratio of -1 and applied strain range of 4% at constant strain rate 0.04/s (Fig. 5.21(c,d)). The duration of the cyclic biaxial tension simulation is 2.5 s. Compared with the CPFE, the full EHM exhibits errors of 9.61% and 14.29% at 1% strain for X and Y directions, respectively. ε-EHM-1 and ε-EHM-2 show similar accuracy with

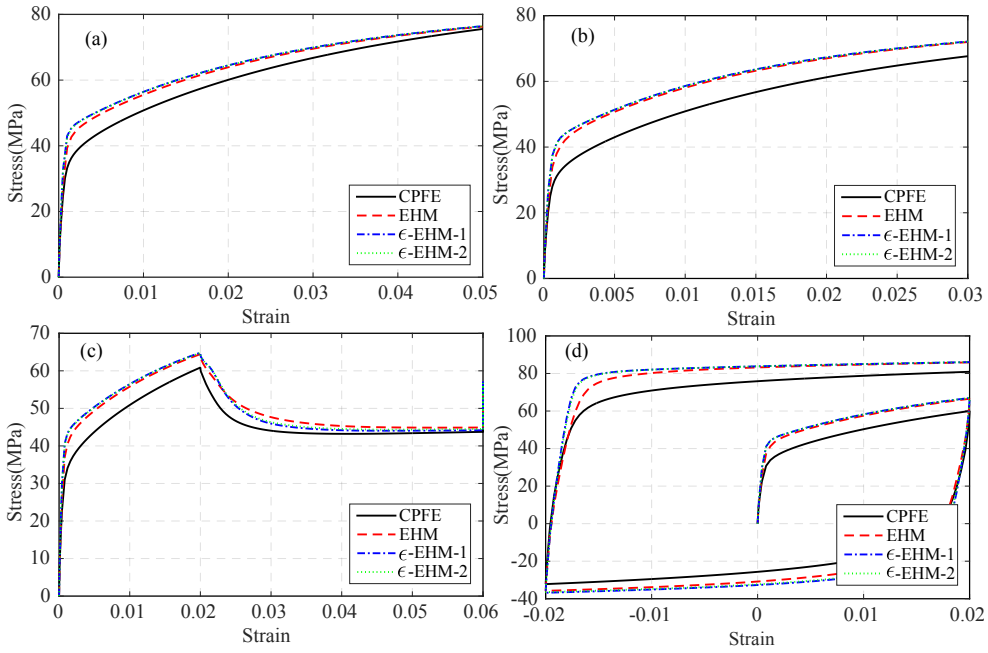

Figure 5.21: Stress-strain response of: (a) proportional biaxial loading, X direction; (b) proportional biaxial loading, Y direction; (c) non-proportional biaxial loading, X direction; (d) non-proportional biaxial loading, Y direction.

the full EHM with 10.76% and 15.66% error. At the end of simulation, the full EHM as well as the sparse EHM models display stress errors less than 6.5% and 6.9% along the X and Y directions, respectively.

While some discrepancy between the CPFE and the EHM models exists, the errors introduced by the proposed sparse formulation are small. The accuracy characteristics of the full EHM method compared to the CPFE has been presented in Ref. [207]. Additional assessment of accuracy in the context of damage mechanics has been provided in Refs. [134, 198, 194, 68, 36, 199].

5.4.3 A macroscale example: plate with hole under bolt pressure

To demonstrate the capability of the sparse EHM in solving structural scale problems, we investigated the response of a thick plate subjected to bolt pressure. The geometry and dimensions of the plate are shown in Fig. 5.22. The bold load is applied as tractions at the

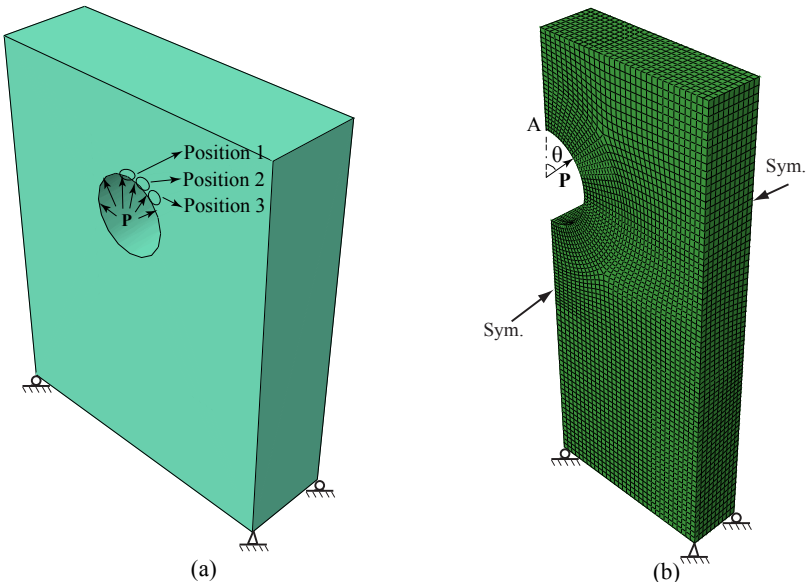

Figure 5.22: A plate under bolt pressure: (a) geometry and loading conditions of the plate; (b) finite element mesh.

inner surface of the hole with a spatially varying form [29]:

$$\mathbf{T}_i = -\frac{4P}{\pi D}\mathbf{n}_i \cos\theta \tag{5.38}$$

in which, D is the diameter of the hole (50 mm), $\mathbf{T}_i$ denotes the traction distribution inside the hole at point i, which is characterized by angle θ that measure clockwise from point A as shown in Fig. 5.22(b); $\mathbf{n}_i$ is the unit normal of the hole surface at point i; and P=350 N/mm.

Half of the plate is discretized due to symmetry with 27,680 tri-linear eight-noded hexahedron elements as shown in Fig. 5.22(b). The microstructure is the 938-grain RVE as shown in Fig. 5.1 (h). The simulation therefore tracks 25,963,840 grains throughout the domain of the specimen. Clearly, such a simulation is computationally prohibitive using the direct CPFE simulation and the classical computational homogenization. The full EHM is also expensive due to the size of the system associated with the model. In this study, the one-layer ε-EHM and zero-layer ε-EHM (i.e., Taylor model) are used to model the response of the plate.

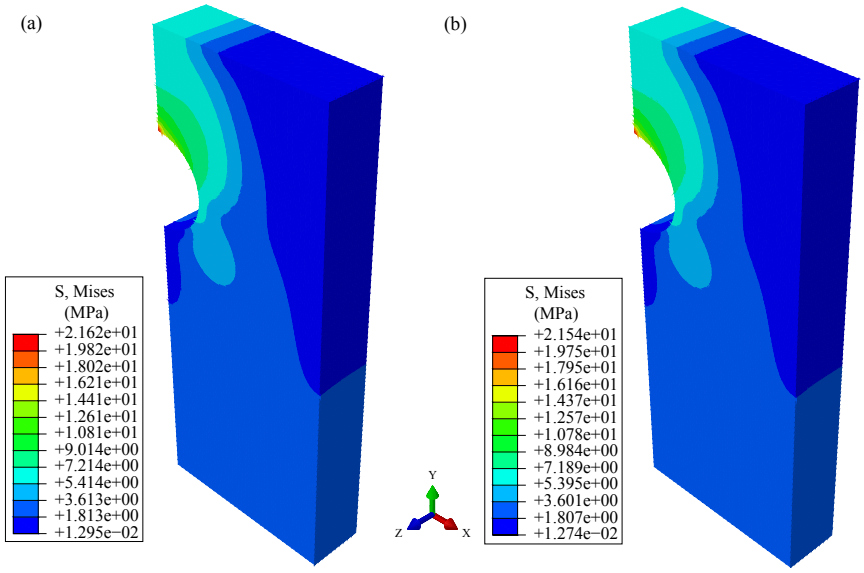

Figure 5.23: Von Mises stress contour at the end of simulation: (a) ε-EHM-1 model; (b) ε-EHM-0 model.

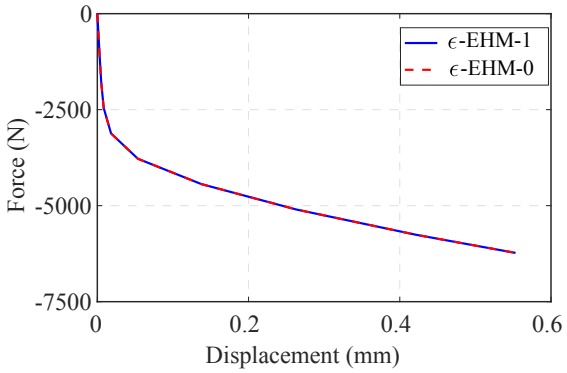

Figure 5.24: Bearing force-displacement curve of the plate.

The stress-contours of the plate at the end of loading using the zero- and one-layer ε-EHM are shown in Fig. 5.23. The macroscopic stresses are close between the two models. The overall bearing force versus the displacement at the far end of the hole (point A) predicted using the two models are identical and shown in Fig. 5.24. Plastic deformations near stress concentration around the hole are responsible for the nonlinearity in the force-displacement behavior.

To better understand the microscale stress variations at the grain level, three different positions around the hole are probed as shown in Fig. 5.22(a). 12 elements at each position

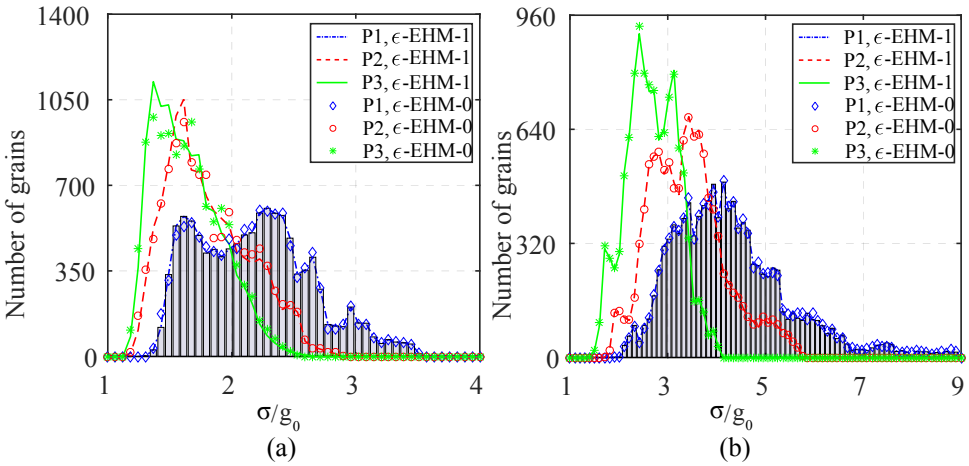

Figure 5.25: Normalized Von Mises stress histogram of the three positions at: (a) middle; (b) end of the simulation.

are selected (probing $938 \times 12 = 11,256$ grains at each position), and the normalized Von Mises stress distributions of the microscale grains at each position are plotted in Fig. 5.25 at the middle and end of the simulation, respectively. The figures clearly show an increase in the local stress as deformation continues. Microscale stress histograms also show a decreasing grain level Von Mises stress from position 1, 2 to 3, which is in accordance with the macroscale stress at position 1, 2 and 3 as shown in Fig. 5.22. In contrast to the global behavior, the ε-EHM-0 and ε-EHM-1 models demonstrate variations in local stresses as shown in Figs. 5.23 and 5.24. The variations are relatively more significant during the elastic-plastic transition. Once most of the grains within the localized regions start to undergo fully plastic deformations, the variations between the two models decrease in magnitude.

5.5 Summary

This chapter presents a grain-cluster accelerated eigenstrain-based reduced-order homogenization model for computationally efficient modeling of complex polycrystal microstructures. The efficiency gain is obtained through introducing sparsity into the linear system associated with full EHM formulation by selectively considering grain-to-grain in-

teractions. A neighborhood-based grain-clustering scheme is developed to consistently identify grain neighborhoods for each grain, between which interactions are considered. The proposed model introduces a hierarchy of reduced models that recovers eigenstrain-based homogenization when full range of interactions are considered. The proposed sparse EHM maintains high efficiency as the RVE size increases with negligible reduction in accuracy compared to the full EHM approach. The proposed sparse EHM models open the possibility of performing relatively large scale structural simulations, in which the grain level information can be directly tracked throughout the structural domain and throughout the duration of a structural analysis.

Chapter 6

CONCLUSION AND FUTURE WORK

6.1 Conclusion

This dissertation has focused on advancing the multiscale modeling of high performance alloys. The development of the microscale modeling is devoted to a CPFE framework for accurate modeling of deformation and failure for IN 617 at high temperature. The multiscale model development is focused on the method development of the eigenstrain-based reduced order modeling for viscoplastic deformation. The key contributions of this dissertation are concluded as follows:

1. *Development of a CPFE framework for the modeling of Nickel-based alloy IN 617 subjected to fatigue, creep-fatigue and creep loading at high temperature.* A crystal plasticity finite element (CPFE) model considering isothermal, large deformation and cyclic loading conditions has been formulated and employed to investigate the mechanical response of nickel-based alloy IN 617 at high temperature. The investigations first focus on fatigue and creep-fatigue hysteresis response of IN 617 subjected to fatigue and creep-fatigue cycles. A new slip resistance evolution equation is proposed to account for cyclic transient features induced by solute drag creep that occur in IN 617 at 950°C. The crystal plasticity model parameters are calibrated against the experimental fatigue and creep-fatigue data based on an optimization procedure that relies on a surrogate modeling (i.e., Gaussian Process) technique to accelerate multi-parameter optimizations. The model predictions are validated against experimental data, which demonstrates the capability of the proposed model in capturing the hysteresis behavior for various hold times and strain ranges in the context of fatigue and creep-fatigue loading. Base on this framework, a collaborative work is

also conducted to include cohesive zone model based intergranular damage modeling. The coupled CPFE-CZM model accurately captures the creep strain evolution and rupture in IN 617, and provides insight into the microscale stress, grain boundary damage distribution and their evolution.

2. *Development of the eigestrain-based reduced order models (EHM) for polycrystal plasticity to facilitate the efficient modeling of viscoplastic response at structural scale.* A reduced order modeling approach has been developed to very efficiently perform crystal plasticity analysis at the scale of the material mesostructure and tightly couple the response at the mesoscale to a structural scale analysis. EHM is based on the transformation field theory and operates in the context of computational homogenization. EHM pre-computes certain microstructure information (i.e., concentration tensors, interaction tensors) and approximates the microscale problem using a much smaller basis by prescribing spatial variation of inelastic response fields over the microstructure. A significant benefit of the EHM approach is that it numerically approximates the influence functions using actual grain morphologies. Depending on order reduction strategy used, EHM can provide either sub-grain level or grain-level resolution. To further improve the efficiency of EHM, the accelerated, sparse and scalable eigenstrain-based reduced order homogenization models have been introduced to address the efficiency degradation of EHM as microstructure size increases. This strategy introduces sparsity into the linearized reduced order system facilitating the use of sparse solvers. A thorough assessment of the performance of the sparse EHM formulation for a range of microstructure sizes using direct and iterative sparse solvers is conducted and the capability of the sparse EHM for solving large scale problem while simultaneously tracking the local response has been demonstrated.

6.2 Recommendations for the Future Work

The contributions of the work presented in this dissertation are twofold. Firstly, this work provides a coupled CPFE-CZM framework that can accurately capture the deformation and intergranular damage within the microstructure of IN 617 at hight temperature. This model is beneficial for microscale deformation mechanism understanding, and facilitates the life prediction of IN 617 serving at the VHTR environment. Secondly, this work establishes the connections between microscale morphology and structural scale response and this development is crucial for efficient structural scale prediction. EHM is developed for structural scale analysis that consider viscoplastic deformation only and can retrieve local response simultaneously. EHM provides a hierarchy of reduced order models that provides different resolutions (grain level or subgrain level) as well as accounting for different levels of grain interactions (i.e., full, partial or none).

For the CPFE-CZM modeling framework, while it accurately captures the viscoplastic deformation within the grains as well as intergranular damage under creep loading, it currently does not account for fatigue damage which might be pronounced in the fatigue or fatigue dominated creep-fatigue tests. The modeling framework is also computationally expensive, which makes the modeling of cyclic tests with large number of cycles impractical at its current stage. In order to capture the damage in the fatigue or fatigue-dominated creep-fatigue tests, and accurately simulate the cyclic softening due to damage in an time efficient manner, the following future development is recommended:

1. Speedup of the current CPFE-CZM model to facilitate structural response modeling. While the current model can accurately capture the deformation and failure at the microstructure scale, the very expensive computational cost still make the multiple-cycle fatigue or creep-fatigue tests modeling unpractical. Hence a reduced modeling technique is needed and a possible solution is a lattice-spring type of reduced order model for the coupled CPFE-CZM modeling as schematically demonstrated in

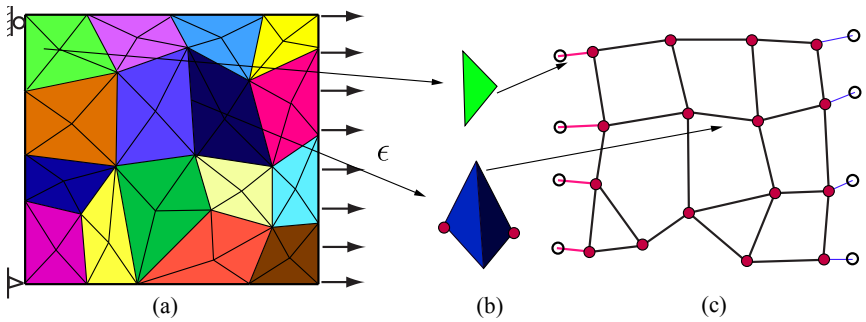

Figure 6.1: Schematic illustration of a lattice-spring system representation of a polycrystal microstructure in 2D.

Fig. 6.1. The basic idea toward this development is to discretize the polycrystalline microstructure using a lattice-spring network to arrive at a reduced order representation of the microstructure. The lattice nodes are chosen to be the centroids of the grains and the springs between lattices are approximated using a small scale CPFE-CZM model.

2. Incorporation of fatigue damage together with the creep damage in the current model. While the current model considers only creep damage, fatigue damage can potentially be activated and interact with the creep damage under the creep-fatigue tests [174]. As experiments suggest a strong interaction between fatigue and creep damage, the interaction mechanism need to be understood and incorporated into the current modeling framework to achieve accurate life prediction of IN 617 under creep-fatigue loading.

For the EHM models, while it opens the doors for structural scale polycrystal plasticity analysis and paves the pathways to a larger picture of a computational framework for damage prognosis as shown in Fig. 6.2, a few future work is recommended, particularly for the goal of facilitating the modeling and damage initiation prediction of hypersonic structure subjected to combined acoustic and thermal loading:

1. Incorporation of other lattice structures and dislocation density based crystal plasticity constitutive laws will enable physical-based modeling of a wider range of poly-

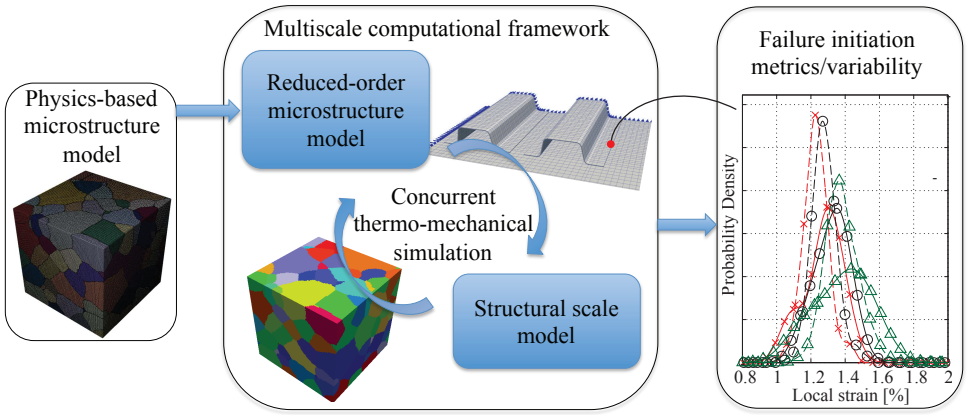

Figure 6.2: A concurrent multiscale computational framework for damage prognosis.

crystalline materials, including FCC, BCC and HCP single phase or multiphase materials. Given the existing EHM framework, this implementation is straightforward.

2. Incorporation of thermal effects into the EHM framework to enable the structure response prediction under thermal-mechanical loading. The importance of accounting for thermal effects for metallic materials has already been revealed in the literature [206, 191, 192, 195, 193, 135]. In order to generalize the EHM approach for thermo-mechanical problems, the effects of (1) the presence of thermal expansion strains and consequent stresses, (2) the variation of the elastic properties of the constituent grains, and (3) the variation of the viscoplastic slip evolution as a function of temperature need to be accounted for.

3. Development of a damage initiation indicator that relies on the microscale response retrieved from the EHM for structural scale damage initiation prediction. Except for the structural response, EHM also provides the local response at every material point of the macroscale model, which is crucial in localized response prediction (e.g., damage initiation). The development of a damage initiation indicator, together with the EHM modes forms the backbone of the damage prognosis framework in Fig. 6.2

BIBLIOGRAPHY

[1] ABAQUS Documentation. Dassault Systemes, Providence, RI, USA.

[2] *Intel(R) Math Kernel Library 11.3.2 Update 1 for Linux*. Intel, MKL 2016 edition, 2015.

[3] J. Aboudi. A continuum theory for fiber-reinforced elastic-viscoplastic composites. *Int. J. Eng. Sci.*, 20:605–621, 1982.

[4] P. R. Amestoy, T. A. Davis, and I. S. Duff. An approximate minimum degree ordering algorithm. *SIAM J. Matrix Anal. Appl.*, 17:886–905, 1996.

[5] M. Anahid, M. K. Samal, and S. Ghosh. Dwell fatigue crack nucleation model based on crystal plasticity finite element simulations of polycrystalline titanium alloys. *J. Mech. Phys. Solids*, 59:2157–2176, 2011.

[6] L. Anand. Constitutive equations for the rate-dependent deformation of metals at elevated temperatures. *J. Eng. Mater. Technol.*, 104:12–17, 1982.

[7] L. Anand and C. Su. A theory for amorphous viscoplastic materials undergoing finite deformations, with application to metallic glasses. *J. Mech. Phys. Solids*, 53: 1362–1396, 2005.

[8] E. Anderson, Z. Bai, C. Bischof, S. Blackford, J. Demmel, J. Dongarra, J. Du Croz, A. Greenbaum, S. Hammarling, A. McKenney, and D. Sorensen. *LAPACK Users' Guide*. Society for Industrial and Applied Mathematics, Philadelphia, PA, third edition, 1999.

[9] A. Argon. Mechanisms and mechanics of fracture in creeping alloys. *Recent Advances in Creep and Fracture of Engineering Materials and Structures. Pineridge press, Swansea*, pages 1–52, 1982.

[10] L. Balogh, S.R. Niezgoda, A.K. Kanjarla, D.W. Brown, B. Clausen, W. Liu, and C.N. Tom. Spatially resolved in situ strain measurements from an interior twinned grain in bulk polycrystalline AZ31 alloy. *Acta Mater.*, 61:3612–3620, 2013.

[11] G. Barenblatt. The formation of equilibrium cracks during brittle fracture. General ideas and hypotheses. axially-symmetric cracks. *J. Appl. Math. Mech.*, 23:622–636, 1959.

[12] T. Belytschko, W.K. Liu, B. Moran, and K. Eikhodary. *Nonlinear Finite Elements for Continua and Structures*. John Wiley and Sons, New York, 2nd edition, 2014.

[13] A. Bensoussan, J.-L. Lions, and G. Papanicolaou. *Asymptotic analysis for periodic structures*. North-Holland, Amsterdam, 1978.

[14] J. Benz, T. Lillo, and R. Wright. Aging of Alloy 617 at 650 and 750°C. Technical report, Idaho National Laboratory, 2013.

[15] J. Benz, L. Carroll, J. Wright, R. Wright, and T. Lillo. Threshold stress creep behavior of Alloy 617 at intermediate temperatures. *Metall. Trans. A*, 45:3010–3022, 2014.

[16] T.R. Bieler, P. Eisenlohr, F. Roters, D. Kumar, D.E. Mason, M.A. Crimp, and D. Raabe. The role of heterogeneous deformation on damage nucleation at grain boundaries in single phase metals. *Int. J. Plast.*, 25:1655–1683, 2009.

[17] M. Bogdanor, S. Mahadevan, and C. Oskay. Uncertainty quantification in damage modeling of heterogeneous materials. *Int. J. Multisc. Comp. Eng.*, 11:289–307, 2013.

[18] J. Bouvard, J. Chaboche, F. Feyel, and F. Gallerneau. A cohesive zone model for fatigue and creepfatigue crack growth in single crystal superalloys. *Int. Journal of Fatigue*, 31:868–879, 2009.

[19] V.V. Bulatov and W. Cai. *Computer Simulations of Dislocations*. Oxford University Press, Oxford, 2006.

[20] E. P. Busso and F. A. McClintock. A dislocation mechanics-based crystallographic model of a B2-type intermetallic alloy. *Int. J. Plast.*, 12:1–28, 1996.

[21] E.P. Busso, F.T. Meissonnier, and N.P. O'Dowd. Gradient-dependent deformation of two-phase single crystals. *J. Mech. Phys. Solids*, 48:2333–2361, 2000.

[22] R. Carmona, Q. Zhu, C.M. Sellars, and J.H. Beynon. Controlling mechanisms of deformation of AA5052 aluminium alloy at small strains under hot working conditions. *Mater. Sci. Eng. A*, 393:157–163, 2005.

[23] L. Carroll. Creep-fatigue behavior of Alloy 617 at 850 and 950°C. Technical report, Idaho National Laboratory, 2015.

[24] M. Carroll and L. Carroll. Developing dislocation subgrain structures and cyclic softening during high-temperature creepfatigue of a Nickel alloy. *Metall. Trans. A*, 44:3592–3607, 2013.

[25] L. Carrolla, C. Cabetb, M. Carrolla, and R. Wright. The development of microstructural damage during high temperature creepfatigue of a nickel alloy. *Int. J. Fatigue*, 47:115–125, 2013.

[26] A. Cerrone, J. Tucker, C. Stein, A. Rollett, and A. Ingraffea. Micromechanical modeling of RENE88DT: From characterization to simulation. In *2012 Joint Conference of the Engineering Mechanics Institute and the 11th ASCE Joint Specialty Conference on Probabilistic Mechanics and Structural Reliability*, 2012.

[27] A. Cerrone, P. Wawrzynek, A. Nonn, G. Paulino, and A. Ingraffea. Implementation and verification of the Park-Paulino-Roesler cohesive zone model in 3D. *Eng. Fract. Mech.*, 120:26–42, 2014.

[28] J.L. Chaboche. Constitutive equations for cyclic plasticity and cyclic viscoplasticity. *Int. J. Plast.*, 5:247–302, 1989.

[29] F.-K. Chang and R. Scott. Strength of mechanically fastened composite joints. *J. Compos. Mater.*, 16:470–494, 1982.

[30] X. Chen, M. A. Sokolov, S. Sham, D. L. Erdman III, Jeremy T. Busby, Kun Mo, and James F. Stubbins. Experimental and modeling results of creep-fatigue life of Inconel 617 and Haynes 230 at 850 °C. *J. Nucl. Mater.*, 432:94–101, 2013.

[31] J. Cheng and S. Ghosh. A crystal plasticity FE model for deformation with twin nucleation in magnesium alloys. *Int. J. Plast.*, 67:148–170, 2015.

[32] J. Cheng, A. Shahba, and S. Ghosh. Stabilized tetrahedral elements for crystal plasticity finite element analysis overcoming volumetric locking. *Comput. Mech.*, 57: 733–753, 2016.

[33] J.W. Christian and S. Mahajan. Deformation twinning. *Prog. Mater. Sci.*, 39:1–157, 1995.

[34] R. Courant and D. Hilbert. *Methods of Mathematical Physics*, volume 1. Wily-VCH, 1991.

[35] R. Crouch and C. Oskay. Symmetric mesomechanical model for failure analysis of heterogeneous materials. *Int. J. Multiscale Com. Eng.*, 8:447–461, 2010.

[36] R. D. Crouch, S. B. Clay, and C. Oskay. Experimental and computational investigation of progressive damage accumulation in CFRP composites. *Compos. Part B-Eng.*, 48:59–67, 2013.

[37] E. Cuthill and J. McKee. Reducing the bandwidth of sparse symmetric matrices. In *In Proceedings of the 1969 ACM 24th national conference*, pages 157–172. ACM, 1969.

[38] C. F.O. Dahlberg, J. Faleskog, C. F. Niordson, and B. N. Legarth. A deformation mechanism map for polycrystals modeled using strain gradient plasticity and interfaces that slide and separate. *Int. J. Plast.*, 43:177–195, 2013.

[39] D. Dugdale. Yielding of steel sheets containing slits. *J. Mech. Phys. Solids*, 8: 100–104, 1960.

[40] F.P.E. Dunne, A.J. Wilkinson, and R. Allen. Experimental and computational studies of low cycle fatigue crack nucleation in a polycrystal. *Int. J. Plast.*, 23:273–295, 2007.

[41] G. J. Dvorak and Y. Benveniste. On transformation strains and uniform fields in multiphase elastic media. *Proc. Math. Phys. Eng. Sci.*, 437:291–310, 1992.

[42] G.J. Dvorak and Y. Benveniste. On transformation strains and uniform fields in multiphase elastic media. *Proc. R. Soc. Lond. A*, 437:291–10, 1992.

[43] W. E and B. Engquist. The heterognous multiscale methods. *Commun. Math. Sci.*, 1:87 –132, 2003.

[44] P. Eisenlohr, M. Diehl, R.A. Lebensohn, and F. Roters. A spectral method solution to crystal elasto-viscoplasticity at finite strains. *Int. J. Plast.*, 46:37–53, 2013.

[45] E.Sanchez-Palencia. Lecture notes in physics, 1980.

[46] J. D. Eshelby. The determination of the elastic field of an ellipsoidal inclusion, and related problems. *Proc. R. Soc. Lond. A*, 241:376–396, 1957.

[47] F. Feyel. A multilevel finite element method (FE2) to describe the response of highly non-linear structures using generalized continua. *Comput. Methods Appl. Mech. Engrg.*, 192:3233–3244, 2003.

[48] F. Feyel and J.-L. Chaboche. FE2 multiscale approach for modelling the elasto-viscoplastic behaviour of long fibre SiC/Ti composite materials. *Comput. Methods Appl. Mech. Engrg.*, 183:309–330, 2000.

[49] J. Fish, V. Filonova, and Z. Yuan. Reduced order computational continua. *Comput. Methods Appl. Mech. Engrg.*, 221-222:104–116, 2012.

[50] F. Fritzen and M. Leuschner. Reduced basis hybrid computational homogenization based on a mixed incremental formulation. *Comput. Methods Appl. Mech. Engrg.*, 260:143–154, 2013.

[51] J.-C. Gauthier, G. Brinkmann, B. Copsey, and M. Lecomte. Antares: The HTR/VHTR project at Framatome ANP. *Nucl. Eng. Des.*, 2006.

[52] M.G.D. Geers, M. Cottura, B. Appolaire, E.P. Busso, S. Forest, and A. Villani. Coupled glide-climb diffusion-enhanced crystal plasticity. *J. Mech. Phys. Solids*, 70:136 – 153, 2014.

[53] D. Gonzalez, I. Simonovski, P.J. Withers, and J. Quinta da Fonseca. Modelling the effect of elastic and plastic anisotropies on stresses at grain boundaries. *Int. J. Plast.*, 61:49–63, 2014.

[54] M. Groeber and M. Jackson. Dream.3D: A digital representation environment for the analysis of microstructure in 3d. *Integr. Mater. Manuf. Innov.*, 3:5–19, 2014.

[55] S. Groh, E.B. Marin, M.F. Horstemeyer, and H.M. Zbib. Multiscale modeling of the plasticity in an aluminum single crystal. *Int. J. Plast.*, 25:1456–1473, 2009.

[56] J. Guedes and N. Kikuchi. Preprocessing and postprocessing for materials based on the homogenization method with adaptive finite element methods. *Comput. Methods Appl. Mech. Engrg.*, 83:143–198, 1990.

[57] S. Hafez Haghighat, G. Eggeler, and D. Raabe. Effect of climb on dislocation mechanisms and creep rates in $\gamma'-$strengthened Ni base superalloy single crystals: A discrete dislocation dynamics study. *Acta Mater.*, 61:3709–3723, 2013.

[58] Craig S. Hartley. A method for linking thermally activated dislocation mechanisms of yielding with continuum plasticity theory. *Phil. Mag.*, 83:3783–3808, 2003.

[59] J.A. Hernndez, J. Oliver, A.E. Huespe, M.A. Caicedo, and J.C. Cante. High-performance model reduction techniques in computational multiscale homogenization. *Comput. Methods Appl. Mech. Engrg.*, 276:149–189, 2014.

[60] R. Hill. Elastic properties of reinforced solids: Some theoretical principles. *J. Mech. Phys. Solids*, 11:357–372, 1963.

[61] R. Hill and J.R. Rice. Constitutive analysis of elastic-plastic crystals at arbitrary strain. *J. Mech. Phys. Solids*, 20:401–413, 1972.

[62] T. Y. Hou and X. Wu. A multiscale finite element method for elliptic problems in composite materials and porous media. *J. Comput. Phys.*, 134:169–189, 1997.

[63] P. V. Houtte. On the equivalence of the relaxed Taylor theory and the Bishop-Hill theory for partially constrained plastic deformation of crystals. *Mater. Sci. Eng*, 55: 69–77, 1982.

[64] P. V. Houtte, S. Li, M. Seefeldt, and L. Delannay. Deformation texture prediction: from the Taylor model to the advanced Lamel model. *Int. J. Plast.*, 21:589–624, 2005.

[65] R. Hu and C. Oskay. Nonlocal homogenization model for wave dispersion and attenuation in elastic and viscoelastic periodic layered media. *J. Appl. Mech.*, 84: 031003, 2017.

[66] R. Hu, C. Prakash, V. Tomar, M. Harr, I. Emre Gunduz, and C. Oskay. Experimentally-validated mesoscale modeling of the coupled mechanical-thermal response of ap-htpb energetic material under dynamic loading. *Int. J. Fract.*, 203: 277–298, 2017.

[67] M. Huang, Z. Lia, and J. Tong. The influence of dislocation climb on the mechanical behavior of polycrystals and grain size effect at elevated temperature. *Int. J. Plast.*, 61:112–127, 2014.

[68] T. Hui and C. Oskay. Computational modeling of polyurea-coated composites subjected to blast loads. *J. Compos. Mater.*, 46:2167–2178, 2012.

[69] T. Hui and C. Oskay. A nonlocal homogenization model for wave dispersion in dissipative composite materials. *Int. J. Solids Struct.*, 50:38–48, 2013.

[70] T. Hui and C. Oskay. A high order homogenization model for transient dynamics of heterogeneous media including micro-inertia effects. *Comput. Methods Appl. Mech. Engrg.*, 273:181–203, 2014.

[71] T. Hui and C. Oskay. Laplace-domain, high-order homogenization for transient dynamic response of viscoelastic composites. *Int. J. Numerical Methods Eng.*, 103: 937–957, 2015.

[72] S. Jimenez and R. Duddu. On the parametric sensitivity of cohesive zone models for high-cycle fatigue delamination of composites. *Int. J. Solids and Struct.*, 82: 111–124, 2016.

[73] S. R. Kalidindi. Incorporation of deformation twinning in crystal plasticity models. *J. Mech. Phys. Solids*, 46:267–290, 1998.

[74] M.E. Kassner. *Fundamentals of Creep in Metals and Alloys 3rd Edition*. Butterworth-Heinemann, 2015.

[75] M.E. Kassner and T.A. Hayes. Creep cavitation in metals. *Int. J. Plast.*, 19:1715–1748, 2003.

[76] W.-G. Kim, S.-N. Yin, G.-G. Lee, Y.-W. Kim, and S.J. Kim. Creep oxidation behavior and creep strength prediction for Alloy 617. *Int. J. Press. Vessels Pip.*, 87: 289–295, 2010.

[77] W.-G. Kim, S.-N. Yin, J.-Y. Park, S.-D. Hong, and Y.-W. Kim. An improved methodology for determining tensile design strengths of Alloy 617. *J. Mech. Sci. Technol.*, 26:379–387, 2012.

[78] W.-G. Kim, J.-Y. Park, I.M.W. Ekaputra, M.-H. Kim, and Y.-W. Kim. Analysis of creep behavior of Alloy 617 for use of VHTR system. *Procedia Mater. Sci.*, 3: 1285–1290, 2014.

[79] W.-G. Kim, J.-Y. Park, I.M.W. Ekaputra, S.-J. Kim, M.-H. Kim, and Y.-W. Kim. Creep deformation and rupture behavior of Alloy 617. *Eng. Fail. Anal.*, 58:441–451, 2015.

[80] M. Knezevic, S. R. Kalidindi, and D. Fullwood. Computationally efficient database and spectral interpolation for fully plastic taylor-type crystal plasticity calculations of face-centered cubic polycrystals. *Int. J. Plast.*, 24:1264–1276, 2008.

[81] M. Knezevic, A. Levinson, R. Harris, R.K. Mishra, R.D. Doherty, and S.R. Kalidindi. Deformation twinning in AZ31: Influence on strain hardening and texture evolution. *Acta Mater.*, 58:6230–6242, 2010.

[82] M. Knezevic, R. J. McCabe, R. A. Lebensohn, C. N. Tome, C. Liu, M. L. Lovato, and B. Mihaila. Integration of self-consistent polycrystal plasticity with dislocation density based hardening laws within an implicit finite element framework: Application to low-symmetry metals. *J. Mech. Phys. Solids*, 61:2034–2046, 2013.

[83] M. Knezevic, B. Drach, M. Ardeljan, and I.J. Beyerlein. Three dimensional predictions of grain scale plasticity and grain boundaries using crystal plasticity finite element models. *Comput. Methods Appl. Mech. Engrg.*, 277:239–259, 2014.

[84] M. Knezevic, M. Zecevic, I. J. Beyerlein, J. F. Bingert, and R. J. McCabe. Strain rate and temperature effects on the selection of primary and secondary slip and twinning systems in HCP Zr. *Acta Mater.*, 88:55–73, 2015.

[85] U. F. Kocks, C. N. Tome, and H. R. Wenk. *Texture and Anisotropy: Preferred Orientations in Polycrystals and Their Effect on Materials Properties*. Cambridge University Press, Cambridge, 1998.

[86] M. Kothari and L. Anand. Elasto-viscoplastic constitutive equations for polycrystalline metals: Application to tantalum. *J. Mech. Phys. Solids*, 46:51–83, 1998.

[87] V. Kouznetsova, W. A. M. Brekelmans, and F. P. T. Baaijens. An approach to micro-macro modeling of heterogeneous materials. *Comput. Mech.*, 27:37–48, 2001.

[88] E. Kroner. Berechnung der elastischen konstanten des vielkristalls aus den konstanten des einkristalls. *Z. Phys [in German]*, 151:504–18, 1958.

[89] P. Krysl, S. Lall, and J. E. Marsden. Dimensional model reduction in non-linear finite element dynamics of solids and structures. *Int. J. Numerical Methods Eng.*, 51:479–504, 2001.

[90] D. Kupka, N. Huber, and E.T. Lilleodden. A combined experimental-numerical approach for elasto-plastic fracture of individual grain boundaries. *J. Mech. Phys. Solids*, 64:455–467, 2014.

[91] M. Carroll L. Carroll. Creep-fatigue behavior of Alloy 617 at 850 and 950°C. Technical report, Idaho National Laboratory, 2013.

[92] F.R. Larson and J. Miller. A time-temperature relationship for rupture and creep stresses. *Trans. ASME*, 74:765–771, 1952.

[93] R. Lebensohn, C. Hartley, C. Tomé, and O. Castelnau. Modeling the mechanical response of polycrystals deforming by climb and glide. *Philos. Mag.*, 90:567–583, 2010.

[94] R. Lebensohn, R. Holt, A. Caro, A. Alankar, and C. Tomé. Recent advances in micromechanics of materials: Improved constitutive description of single crystal viscoplastic deformation by dislocation climb. *C. R. Mécanique*, 340:289–295, 2012.

[95] R.A. Lebensohn. N-site modeling of a 3D viscoplastic polycrystal using Fast Fourier Transform. *Acta Mater.*, 49:2723–2737, 2001.

[96] R.A. Lebensohn and G.R. Canova. A self-consistent approach for modelling texture development of two-phase polycrystals: Application to titanium alloys. *Acta Mater.*, 45:3687–3694, 1997.

[97] R.A. Lebensohn and C.A. Tome. A self-consistent anisotropic approach for the simulation of plastic deformation and texture development of polycrystals: Application to zirconium alloys. *Acta Metall. Mater.*, 41:2611–2624, 1993.

[98] R.A. Lebensohn, A.K. Kanjarla, and P. Eisenlohr. An elasto-viscoplastic formulation based on fast fourier transforms for the prediction of micromechanical fields in polycrystalline materials. *Int. J. Plast.*, 3233:59–69, 2012.

[99] Rl A. Lebensohn, C. S. Hartley, C. N. Tome, and O. Castelnau. Modeling the mechanical response of polycrystals deforming by climb and glide. *Philos. Mag.*, 90: 567–583, 2010.

[100] H. Li, C. Wu, and H. Yang. Crystal plasticity modeling of the dynamic recrystal-

lization of two-phase titanium alloys during isothermal processing. *Int. J. Plast.*, 51: 271–291, 2013.

[101] T. Lillo and R. Wright. Microstructural characterization of Alloy 617 crept into the tertiary regime. *Proceedings of the ASME 2015 Pressure Vessels and Piping Conference, PVP2015*, 2015.

[102] Thomas Lillo, James Cole, Megan Frary, and Scott Schlegel. Influence of grain boundary character on creep void formation in Alloy 617. *Metall. Trans. A*, 40: 2803–2811, 2009. ISSN 1073-5623.

[103] B. Lin, L.G. Zhao, J. Tong, and H.J. Christ. Crystal plasticity modeling of cyclic deformation for a polycrystalline nickel-based superalloy at high temperature. *Mater. Sci. Eng. A*, 527:3581–3587, 2010.

[104] Q. Liu, A. Roy, S. Tamura, T. Matsumura, and V. V. Silberschmidt. Micro-cutting of single-crystal metal: Finite-element analysis of deformation and material removal. *Int. J. Mech. Sci.*, 118:135–143, 2016.

[105] Q. Liu, A. Roy, and V. V. Silberschmidt. Temperature-dependent crystal-plasticity model for magnesium: A bottom-up approach. *Mech. Mater.*, 113:44–56, 2017.

[106] A. Ma and F. Roters. A constitutive model for FCC single crystals based on dislocation densities and its application to uniaxial compression of aluminium single crystals. *Acta Mater.*, 52:3603–3612, 2004.

[107] W.L. Mankins, J.C. Hosier, and T.H. Bassford. Microstructure and phase stability of INCONEL Alloy 617. *Metall. Trans.*, 5:2579–2590, 1974.

[108] E. B. Marin. On the formulation of a crystal plasticity model. Technical report, Sandia National Laboratories, 2006.

[109] E.B. Marin and P.R. Dawson. On modelling the elasto-viscoplastic response of metals using polycrystal plasticity. *Comput. Methods Appl. Mech. Engrg.*, 165:1–21, 1998.

[110] S.F. Di Martino, R.G. Faulkner, S.C. Hogg, S. Vujic, and O. Tassa. Characterisation of microstructure and creep properties of Alloy 617 for high-temperature applications. *Mater. Sci. Eng. A*, 619:77–86, 2014.

[111] S.F. Di Martino, R.G. Faulkner, S.C. Hogg, S. Vujic, and O. Tassa. Characterisation of microstructure and creep properties of Alloy 617 for high-temperature applications. *Mater. Sci. Eng. A*, 619:77–86, 2014.

[112] K. Mathur and P. Dawson. On modeling the development of crystallographic texture in bulk forming processes. *Int. J. Plast.*, 5:67–94, 1989.

[113] F. Meier., C. Schwarz, and E. Werner. Crystal-plasticity based thermo-mechanical modeling of Al-components in integrated circuits. *Comput. Mater. Sci.*, 94:122–131, 2014.

[114] F.T. Meissonnier, E.P. Busso, and N.P. O'Dowd. Finite element implementation of a generalised non-local rate-dependent crystallographic formulation for finite strains. *Int. J. Plast.*, 17:601–640, 2001.

[115] H. Michel, J.C. Moulinec and P. Suquet. Effective properties of composite materials with periodic microstructure: a computational approach. *Comput. Methods Appl. Mech. Engrg.*, 172:109–143, 1999.

[116] J. C. Michel, H. Moulinec, and P. Suquet. A computational scheme for linear and non-linear composites with arbitrary phase contrast. *Int. J. Numer. Methods Eng.*, 52:139–160, 2001.

[117] J.C. Michel and P. Suquet. Nonuniform transformation field analysis. *International Journal of Solids and Structures*, 40:6937–6955, 2003.

[118] J.C. Michel and P. Suquet. Computational analysis of nonlinear composite structures using the nonuniform transformation field analysis. *Comput. Methods Appl. Mech. Engrg.*, 193:5477–5502, 2004.

[119] J.C. Michel and P. Suquet. A model-reduction approach to the micromechanical analysis of polycrystalline materials. *Comput. Mech.*, 57:483–508, 2016.

[120] C. Miehe, J. Schrder, and J. Schotte. Computational homogenization analysis in finite plasticity simulation of texture development in polycrystalline materials. *Comput. Methods Appl. Mech. Engrg.*, 171:387–418, 1999.

[121] B. Mihaila, M. Knezevic, and A. SCardenas. Three orders of magnitude improved efficiency with high-performance spectral crystal plasticity on gpu platforms. *Int. J. Numer. Meth. Engng*, 83:785798, 2014.

[122] K. Mo. *Microstructural Evolution and Mechanical Behavior in Nickel based Alloy for Very High Temperature Reactor*. PhD thesis, University of Illinois at Urbana-Champaign, 2011.

[123] K. Mo, G. Lovicu, X. Chen, H.-M. Tung, J. B. Hansen, and J. F. Stubbins. Mechanism of plastic deformation of a ni-based superalloy for VHTR applications. *J. Nucl. Mater.*, 441:695 – 703, 2013.

[124] K. Mo, G. Lovicu, H.-M. Tung, X. Chen, Y. Miao, J. B. Hansen, and J. F. Stubbins. Effect of orientation on plastic deformations of Alloy 617 for VHTR applications. *J. Nucl. Mater.*, 443:366–377, 2013.

[125] A. Molinari, G.R. Canova, and S. Ahzi. A self consistent approach of the large deformation polycrystal viscoplasticity. *Acta Metall.*, 35:2983–2994, 1987.

[126] H. Moulinec and P. Suquet. A numerical method for computing the overall response of nonlinear composites with complex microstructure. *Comput. Methods Appl. Mech. Engrg.*, 157:69–94, 1998.

[127] S. Quayyum N. Islam and T. Hassan. A unified constitutive model for high temperature multiaxial creep-fatigue and ratcheting response simulation of Alloy 617. In *ASME Proceedings 22nd Scavuzzo Student Paper Symposium and Competition*, 2014.

[128] F.R.N Nabarro. Steady-state diffusional creep. *Philos. Mag.*, 16:231, 1967.

[129] V.D. Nguyen, E. Bechet, C. Geuzaine, and L. Noels. Imposing periodic boundary condition on arbitrary meshes by polynomial interpolation. *Comput Mater Sci*, 55: 390–406, 2012.

[130] P. Onck and E. van der Giessen. Microstructurally-based modelling of intergranular creep fracture using grain elements. *Mech. Mater.*, 26:109–126, 1997.

[131] P. Onck and E. van der Giessen. Micromechanics of creep fracture: simulation of intergranular crack growth. *Comput. Mater. Sci.*, 13:90–102, 1998.

[132] C. Oskay. Variational multiscale enrichment for modeling coupled mechano-diffusion problems. *Int. J. Numer. Methods Eng.*, 89:686–705, 2012.

[133] C. Oskay. Variational multiscale enrichment method with mixed boundary conditions for modeling diffusion and deformation problems. *Comput. Methods Appl. Mech. Engrg.*, 264:178–190, 2013.

[134] C. Oskay and J. Fish. Eigendeformation-based reduced order homogenization for failure analysis of heterogeneous materials. *Comput. Methods Appl. Mech. Engrg.*, 196:1216–1243, 2007.

[135] C. Oskay and M. Haney. Computational modeling of titanium structures subjected to thermo-chemo-mechanical environment. *Int. J. Solids Struct.*, 47:3341–3351, 2010.

[136] T. Ozturk, C. Stein, R. Pokharel, C. Hefferan, H. Tucker, S. Jha, R. John, R. A. Lebensohn, P. Kenesei, R. M. Suter, and A. D. Rollett. Simulation domain size requirements for elastic response of 3d polycrystalline materials. *Modelling Simul. Mater. Sci. Eng.*, 24:015006, 2016.

[137] R.J. Peirce, D. Asaro and A. Needleman. An analysis of nonuniform and localized deformation in ductile single crystals. *Acta Metall.*, 30:1087–1119, 1982.

[138] R.J. Peirce, D. Asaro and A. Needleman. Material rate dependence and localized deformation in crystalline solids. *Acta Metall.*, 31:1951–1976, 1983.

[139] C. G. Petra, O. Schenk, and M. Anitescu. Real-time stochastic optimization of complex energy systems on high-performance computers. *IEEE Comput. Sci. Eng.*, 16: 32–42, 2014.

[140] C. G. Petra, O. Schenk, M. Lubin, and K. Gärtner. An augmented incomplete factorization approach for computing the schur complement in stochastic optimization. *SIAM J. Sci. Comput.*, 36:C139–C162, 2014.

[141] V.-T. Phan, X. Zhang, Y. Li, and C. Oskay. Microscale modeling of creep deformation and rupture in nickel-based superalloy in 617 at high temperature. *Mech. Mater.*, 114:215–227, 2017.

[142] Neite G. Pottebohm, H. and E. Nembach. Elastic properties (the stiffness constants, the shear modulus and the dislocation line energy and tension) of Ni-Al solid-solutions and of the Nimonic alloy PE16. *Mater. Sci. Eng.*, 60:189–194, 1983.

[143] M.J.D. Powell. A fast algorithm for nonlinearly constrained optimization calcula-

tions. In G.A. Watson, editor, *Numerical Analysis*, volume 630 of *Lecture Notes in Mathematics*, pages 144–157. Springer Berlin Heidelberg, 1978.

[144] P.G. Pritchard, L. Carroll, and T. Hassan. Constitutive modeling of high temperature uniaxial creep-fatigue and creep-ratcheting responses of Alloy 617. In *Proceedings of the ASME 2013 Pressure Vessels and Piping Conference*, 2013.

[145] R. Quey, P.R. Dawson, and F. Barbe. Large-scale 3d random polycrystals for the finite element method: Generation, meshing and remeshing. *Comput. Methods Appl. Mech. Engrg.*, 200:1729–1745, 2011.

[146] C. Rasmussen and C. Williams. *Gaussian Processes for Machine Learning*. Springer, New York, 2006.

[147] W. Ren and R. W. Swindeman. A review on current status of Alloys 617 and 230 for Gen IV nuclear reactor internals and heat exchangers. *ASME. J. Pressure Vessel Technol.*, 131, 2009.

[148] J.R. Rice. Inelastic constitutive relations for solids: An internal-variable theory and its application to metal plasticity. *J. Mech. Phys. Solids*, 19:433–455, 1971.

[149] D.N. Robinson. Constitutive relationships for anisotropic high-temperature alloys. *Nucl. Eng. Des.*, 83:389–396, 1984.

[150] F. Roters, P. Eisenlohr, L. Hantcherli, D.D. Tjahjanto, T.R. Bieler, and D. Raabe. Overview of constitutive laws, kinematics, homogenization and multiscale methods in crystal plasticity finite-element modeling: Theory, experiments, applications. *Acta Mater.*, 58:1152–1211, 2010.

[151] F. Roters, P. Eisenlohr, T.R. Bieler, and D. Raabe. *Crystal Plasticity Finite Element Methods*. John Wiley and Sons, New York, 1st edition, 2013.

[152] A. Roy, M. Hasan, and J. Pal. Deformation of Alloys 617 and 276 at $750-950^{\circ}$C. *Mater. Sci. Eng. A*, 520:184–188, 2009.

[153] Y. Saad. *Iterative Methods for Sparse Linear Systems*. Society for Industrial and Applied Mathematics, 2nd edition, 2003.

[154] G. Sachs. Zur ableitung einer fliessbedingung. *Ver. Dtsch. Ing.*, 72:734–736, 1928.

[155] J. Segurado, R. A. Lebensohn, J. LLorca, and C. N. Tom. Multiscale modeling of plasticity based on embedding the viscoplastic self-consistent formulation in implicit finite elements. *Int. J. Plast.*, 28:124–140, 2012.

[156] T.-L. Sham and Kevin P. Walker. Preliminary development of a unified viscoplastic constitutive model for Alloy 617 with special reference to long term creep behavior. In *ASME Proceedings, Materials and Components*, 2008.

[157] S.K. Sharma, G.D. Ko, F.X. Li, and K.J. Kang. Oxidation and creep failure of Alloy 617 foils at high temperature. *J. Nucl. Mater*, 378:144–152, 2008.

[158] M.M. Shenoy, A.P. Gordon, D.L. McDowell, and R.W. Neu. Thermomechanical fatigue behavior of a directionally solidified Ni-base superalloy. *J. Eng. Mater. Technol.*, 127:325–336, 2005.

[159] O.D. Sherby and P.M. Burke. Mechanical behavior of crystalline solids at elevated temperature. *Prog. Mater. Sci.*, 13:323–390, 1968.

[160] Y. Shi, K. Yuan, X. Zhao, and Y. Wu. Study on comparison between Inconel 617 and Gh3128 as structural material candidates for intermediate heat exchanger. In *Proceedings of the 2013 21st International Conference on Nuclear Engineering ICONE21*. ASME, 2013.

[161] K. Shiozawa and J. Weertman. Studies of nucleation mechanisms and the role of

residual stresses in the grain boundary cavitation of a superalloy. *Acta Metall.*, 31, 1983.

[162] I. Simonovski and L. Cizelj. Cohesive element approach to grain level modelling of intergranular cracking. *Engng. Fract. Mech.*, 110:364–377, 2013.

[163] I. Simonovski and L. Cizelj. Cohesive zone modeling of intergranular cracking in polycrystalline aggregates. *Nucl. Eng. Des.*, 283:139–147, 2015.

[164] R.J.M. Smit, W.A.M. Brekelmans, and H.E.H. Meijer. Prediction of the mechanical behavior of nonlinear heterogeneous systems by multi-level finite element modeling. *Comput. Methods Appl. Mech. Engrg.*, 155:181–192, 1998.

[165] D.E. Solas and C.N. Tome. Texture and strain localization prediction using a n-site polycrystal model. *Int. J. Plast.*, 17:737–753, 2001.

[166] P. Sparks and C. Oskay. The method of failure paths for reduced-order computational homogenization. *Int. J. Multiscale Com. Eng.*, 14, 2016.

[167] D. Spring and G. Paulino. A growing library of three-dimensional cohesive elements for use in ABAQUS. *Engng. Fract. Mech.*, 126:190–216, 2014.

[168] A. Staroselsky and L. Anand. Inelastic deformation of polycrystalline face centered cubic materials by slip and twinning. *J. Mech. Phys. Solids*, 46:671–696, 1998.

[169] A. Staroselsky and B. N. Cassenti. Creep, plasticity, and fatigue of single crystal superalloy. *Int. J. Solids Struct.*, 48:2060–2075, 2011.

[170] J.C. Stinville, N. Vanderesse, F. Bridier, P. Bocher, and T.M. Pollock. High resolution mapping of strain localization near twin boundaries in a nickel-based superalloy. *Acta Mater.*, 98:29–42, 2015.

[171] J.C. Stinville, W.C. Lenthe, J. Miao, and T.M. Pollock. A combined grain scale elasticplastic criterion for identification of fatigue crack initiation sites in a twin containing polycrystalline nickel-base superalloy. *Acta Mater.*, 103:461–473, 2016.

[172] Y. Sun, K. Maciejewski, and H. Ghonem. A damage-based cohesive zone model of intergranular crack growth in a Nickel-based superalloy. *Int. J. Damage Mech.*, 22: 905–923, 2013.

[173] R.W. Swindeman and Swindeman M.J. A comparison of creep models for Nickel base alloys for advanced energy systems. *Proceeding of ECCC Creep Conference, 12-14 September 2005, London*, 2005.

[174] F. Tahir, S. Dahire, and Y. Liu. Image-based creep-fatigue damage mechanism investigation of Alloy 617 at 950°C. *Mater. Sci. Eng. A*, 679:391–400, 2017.

[175] E.M. Taleff, W.P. Green, M.-A. Kulas, T. R. McNelley, and P.E. Krajewski. Analysis, representation, and prediction of creep transients in class I alloys. *Mater. Sci. Eng. A*, 410-411:32–37, 2005.

[176] G. I. Taylor. Plastic strain in metals. *J. Inst. Met.*, 62:307–324, 1938.

[177] P. Thamburaja and L. Anand. Polycrystalline shape-memory materials: effect of crystallographic texture. *J. Mech. Phys. Solids*, 49:709–737, 2001.

[178] M. Thomas, J. Groeber and S. Ghosh. Image-based crystal plasticity FE framework for microstructure dependent properties of ti6al4v alloys. *Mater. Sci. Eng. A*, 553: 164–175, 2012.

[179] S. Tian, J. Xie, X. Zhou, B. Qian, J. Jun, L. Yu, and W. Wang. Microstructure and creep behavior of FGH95 nickel-base superalloy. *Mater. Sci. Eng. A*, 528:2076–2084, 2011.

[180] D. D. Tjahjanto, P. Eisenlohr, and F. Roters. A novel grain cluster-based homogenization scheme. *Modelling Simul. Mater. Sci. Eng.*, 18:015006, 2010.

[181] T. C. Totemeier, H. Tian, D. E. Clark, and J. A. Simpson. Microstructure and strength characteristics of Alloy 617 welds. Technical report, Idaho National Laboratory, 2005.

[182] H.S. Turkmen, P.R. Dawson, and M.P. Miller. The evolution of crystalline stresses of a polycrystalline metal during cyclic loading. *Int. J. Plast.*, 18:941–969, 2002.

[183] H. Wang, P.D. Wu, C.N. Tome, and Y. Huang. A finite strain elasticviscoplastic self-consistent model for polycrystalline materials. *J. Mech. Phys. Solids*, 58:594–612, 2010.

[184] X. Wen. *Creep Behavior of High Temperature Alloys for Generation IV Nuclear Energy Systems*. PhD thesis, University of Cincinnati, 2014.

[185] J. Wright, L. Carroll, and R. Wright. Creep and creep-fatigue of Alloy 617 weldments. *Tech. Rep., Idaho National Laboratory*, 2014.

[186] J. K. Wright, L. J. Carroll, C. Cabet, T. M. Lillo, J.K. Benz, J. A. Simpson, W. R. Lloyd, J. A. Chapman, and R. N. Wright. Characterization of elevated temperature properties of heat exchanger and steam generator alloys. *Nucl. Eng. Des.*, 251:252–260, 2012.

[187] J. K. Wright, L. J. Carroll, J. A. Simpson, and R. N. Wright. Low cycle fatigue of Alloy 617 at 850°C and 950°C. *J. Eng. Mater. Technol.*, 135:031005, 2013.

[188] J. K. Wright, N. J. Lybeck, and R. N. Wright. Tensile properties of Alloy 617 bar stock. Technical report, Idaho National Laboratory, 2013.

[189] J.K. Wright, J.A. Simpson, R.N. Wright, L.J. Carroll, and T.L. Sham. Strain rate

sensitivity of alloys 800H and 617. In *Proceedings of the 2013 ASME Pressure Vessels & Piping Conference*, Paris, France, 2013.

[190] S. Yadegari, S. Turteltaub, and A. Suiker. Generalized grain cluster method for multiscale response of multiphase materials. *Comput. Mech.*, 56:193–219, 2015.

[191] H. Yan and C. Oskay. A three-field (displacement-pressure-concentration) formulation for couled transport-deformation problems. *Finite Elem. Anal. Des.*, 90:20–30, 2014.

[192] H. Yan and C. Oskay. Modeling the coupled transport-deformation response of titanium alloys subjected to thermo-mechanical environment. In *55th AIAA/ASME/ASCE/AHS/SC Structures, Structural Dynamics, and Materials Conference*, 2014.

[193] H. Yan and C. Oskay. Multi-yield surface modeling of viscoplastic materials. *Int. J. Multiscale Com. Eng.*, 15, 2017.

[194] H. Yan, C. Oskay, A. Krishnan, and L. R. Xu. Compression-after-impact response of woven fiber-reinforced composites. *Compos. Sci. Technol.*, 70:2128–2136, 2010.

[195] Hao Yan and Caglar Oskay. A viscoelasticviscoplastic model of titanium structures subjected to thermo-chemo-mechanical environment. *Int. J. Solids Struct.*, 5657: 29–42, 2015.

[196] H. Yang, M. Huang, and Z. Li. The influence of vacancies diffusion-induced dislocation climb on the creep and plasticity behaviors of Nickel-based single crystal superalloy. *Comp. Mat. Sc.*, 99:348–360, 2015.

[197] M.H. Yoo and J.K. Lee. Deformation twinning in H.C.P. metals and alloys. *Phil. Mag. A*, 63:987–1000, 1991.

[198] Z. Yuan and J. Fish. Multiple scale eigendeformation-based reduced order homogenization. *Comput. Methods Appl. Mech. Engrg.*, 198:2016–2038, 2009.

[199] Z. Yuan and J. Fish. Are the cohesive zone models necessary for delamination analysis. *Comput. Methods Appl. Mech. Engrg.*, 310:567–604, 2016.

[200] J. Yvonnet and Q.-C. He. The reduced model multiscale method (R3M) for the nonlinear homogenization of hyperelastic media at finite strains. *J. Comput. Phys.*, 223: 341–368, 2007.

[201] J. Yvonnet, D. Gonzalez, and Q.-C. He. Numerically explicit potentials for the homogenization of nonlinear elastic heterogeneous materials. *Comput. Methods Appl. Mech. Engrg.*, 198:2723–2737, 2009.

[202] J. Zhang. *High temperature deformation and fracture of materials*. Woodhead Publishing, 2010.

[203] M. Zhang, J. Zhang, and D.L. McDowell. Microstructure-based crystal plasticity modeling of cyclic deformation of Ti-6Al-4V. *Int. J. Plast.*, 23:1328–1348, 2007.

[204] S. Zhang and C. Oskay. Variational multiscale enrichment method with mixed boundary conditions for elasto-viscoplastic problems. *Comp. Mech.*, 55:771–787, 2015.

[205] S. Zhang and C. Oskay. Reduced order variational multiscale enrichment method for elasto-viscoplastic problems. *Comput. Methods Appl. Mech. Engg.*, 300:199–224, 2016.

[206] S. Zhang and C. Oskay. Reduced order variational multiscale enrichment method for thermo-mechanical problems. *Comput. Mech.*, pages 1–21, 2017.

[207] X. Zhang and C. Oskay. Eigenstrain based reduced order homogenization for polycrystalline materials. *Comput. Methods Appl. Mech. Engrg.*, 297:408–436, 2015.

[208] X. Zhang and C. Oskay. Polycrystal plasticity modeling of nickel-based superalloy IN 617 subjected to cyclic loading at high temperature. *Modelling Simul. Mater. Sci. Eng.*, 24:055009, 2016.

[209] X. Zhang and C. Oskay. Sparse and scalable eigenstrain-based reduced order homogenization models for polycrystal plasticity. *Comput. Methods Appl. Mech. Engrg.*, 326:241–269, 2017.

[210] X. Zhang and C. Oskay. Eigenstrain-based reduced order homogenization models for polycrystal plasticity: Addressing scalability. In *XIV International Conference on Computational Plasticity*. CIMNE, 2017.

[211] X. Zhang and Oskay C. Phan, T. V. Microstructural creep, fatigue and creep-fatigue modeling of Nickel-based superalloy Inconel 617 at high temperature. In *Proceedings of 2016 International Topical Meeting on High Temperature Reactor Technology*. American Nuclear Society, 2016.

[212] B. Zuchowski. Predictive capability for hypersonic structural response and life prediction: Phase II - detailed design of hypersonic cruise vehicle hot-structure. Technical report, AIR VEHICLE INTEGRATION AND TECHNOLOGY RESEARCH, 2012.